Title
Rational Material Architecture Design for Better Energy Storage

Author
Chen, Zheng

Publication Date
2012

Peer reviewed|Thesis/dissertation

UNIVERSITY OF CALIFORNIA

Los Angeles

Rational Material Architecture Design for Better Energy Storage

A dissertation submitted in partial satisfaction of the

requirements for the degree Doctor of Philosophy

in Chemical Engineering

by

Zheng Chen

2012

ABSTRACT OF DISSERTATION

Rational Material Architecture Design for Better Energy Storage

By

Zheng Chen

Doctor of Philosophy in Chemical Engineering

University of California, Los Angeles, 2012

Professor Yunfeng Lu, Chair

Human civilization relies on an abundant and sustainable supply of energy. Rapidly increasing energy consumption in past decades has resulted in a fossil-fuel shortage and ecological deterioration. Facing these challenges, humankind has been diligently seeking clean, safe and renewable energy sources, such as solar, wind, waves and tides, to offset the diminishing availability or to take place of fossil fuels. At the same time, the search for strategies to reduce fossil-fuel consumption and decrease CO_2 emission, such as to replace tradition vehicles by electrical vehicles (EVs), is demanded. However, the energy harvested from renewable sources must be stored prior to its connection to electric grids or delivery to customers, and EVs need sufficient on-board power sources. These essential

needs have made energy storage a critical component in the creation of sustainable society.

Among all energy storage technologies, electrochemical energy storage within batteries or electrochemical capacitors (ECs) is the most promising approach, since as-stored chemical energy can be effectively delivered as electrical energy with high energy density and power density, high efficiency, long service life and effective cost. However, the performance of current batteries and ECs are constrained by poor material properties, though great effort has been made to improve materials during the past few years. The objective of this dissertation is to address the limitation of current energy storage materials by rational architecture design according to the well-recognized principles and criteria. To achieve this goal, the research strategy is to design and fabricate multifunctional architectures by integrating distinct material structures and properties to address the limitation of traditional materials and create a new family of high-performance energy storage materials with desired properties.

Different types of energy storage architectures were investigated and compared with conventional structures to demonstrate such design concepts. First, hierarchically porous carbon particles with graphitized structures were designed and synthesized by an efficient aerosol-spray process. By comparison with commercially available activated carbon and CNTs, it was found that hierarchical pore architecture is important for providing high surface

area and fast ion transport, which leads to high capacitance and high power EDLC materials. Secondly, MnO_2/mesoporous carbon nanocomposites were designed. MnO_2 layers with different thicknesses were deposited on mesoporous carbon scaffolds with hierarchical pore structure and the charge storage performance of the composites was correlated to MnO_2 layer thickness. It was determined that a suitable thickness is critical to ensure good electronic conductivity, sufficient electrolyte diffusion and high capacitance. Thirdly, interpenetrating oxide nanowire/CNT network structures were designed and fabricated by an *in situ* hydrothermal reaction. The composition, CNT length, pore structure, V_2O_5 structure, electrode thickness and architecture are critical factors. Synergistic effects obtained between V_2O_5 nanowires and CNTs resulted in an optimal composition with the highest storage performance. Long CNTs led to robust flexible electrodes, while a hierarchical V_2O_5 structure enabled storage of both lithium and sodium ions at high rates. Thus, electrode architectures can be engineered to achieve high-rate, thick electrodes for bulk energy storage. Last, various architectures obtained through integrating nanocrystals and CNTs were designed and fabricated using ultrafine TiO_2 nanocrystals as a model system. Electrodes were fabricated by directly coating thin film TiO_2 on conductive Indium-Tin-Oxide (ITO) glass, by conformably coating nanocrystals on pre-formed CNT

papers, or by solvation-induced assembly between nanocrystals and CNTs. It was demonstrated that thick electrodes with high charge capacity, high rate performance and cycling stability rely on functional architecture that simultaneously provides high electronic conductivity, easy ion diffusion, abundant surface actives sites and robust structure and interfaces.

The general conclusion derived from these studies is that the energy storage performance of electrode materials can be significantly improved by constructing rational architectures that provide effective ion diffusion, good electronic conductivity, fast electrode reaction, robust structure and a stable interface, which normally cannot be obtained with conventional materials. This strategy also can be extended to other devices, such as batteries and fuel cells, providing a general design platform for high performance energy materials. Further exploration in this research direction will ultimately lead to high energy, high power, and long life energy storage devices for many applications, including portable electronics, EVs and grid-scale energy storage.

The dissertation of Zheng Chen is approved.

Bruce Dunn

Selim Senkan

Harold Monbouquette

Yunfeng Lu, Committee Chair

University of California, Los Angeles

2012

TABLE OF CONTENTS

LIST OF FIGURES

ACKNOWLEDGEMENTS

This thesis is my first step in the real world of science. The PhD study here at UCLA has equipped me with the most critical skills that I can use to continually seek for truth and knowledge. With this opportunity, I would like to thank many individuals who have been helping me to accomplish this dissertation, and supporting me along the way.

First, I am deeply grateful to Dr. Yunfeng Lu, who has been my thesis advisor, guide and philosopher. This PhD thesis would not have been possible without his strong support during the past more than five years. The dedicated and careful training I obtained from him in respect of fundamental knowledge and strategy in research and teaching, responsibility and attitudes has provided me with continual motivation and guidance to academic and professional success. I am indebted to him not only for the incredible research opportunity, but also for the chance of working with an advisor from whom I can follow and learn so much for my personal and professional development.

I also thank my doctoral committee members, Dr. Harold Monbouquette, Dr. Selim Senkan, and Dr. Bruce Dunn for their support of my doctoral candidacy. Their insightful questions and discussions along the way have helped me a lot over the years. Additional thanks to Dr. Harold Monbouquette and Dr. Bruce Dunn for letting me use of testing

equipments from their laboratories at the beginning of my research. Moreover, I would like to thank Dr. Bruce Dunn for the guidance and mentoring in the field of electrochemical energy storage; his suggestions and ideas have always been helpful for my research. I am also thankful to Dr. Dunn's student Veronica Augustyn who has been helping me a lot with characterization, analysis and writing.

Thank all the previous and current group members and friends in UCLA for sharing with me their experience and knowledge, through which I have been occasionally able to either generate new ideas or expedite the progress of the whole work. Especially, thank Dr. Zhenglong Yang, Dr. Qiangfeng Xiao, Dr. Daocheng Pan for their help and kind advice in the beginning of my PhD; thank Xiaolei Wang, Dr. Ding Weng, Dr. Longping Zhou, Dr. Fang Zhang, Dr. Hiesang Sohn for their help with my research and life in UCLA; thank Mr. Daniel Toso for the help with electron microscopic imaging for some of my samples.

Also, I would like to thank all the professors and staffs in the department that have been so nice, helpful and supportive all the time. Special thanks to Dr. Yi Tang for his help with my wife 's (Yanran Li) transfer from Rice University to UCLA, and providing her a great opportunity to study at UCLA, as well as being so supportive for her life and career; to Professor Yoram Cohen, Professor Robert Hicks and Professor Tatianna Segura for their

wonderful lectures; to John Berger, Miguel Perez and Alain C. De Vera for their always being so kind and patient to help me.

Finally, I am indebted to my parents, grandparents and brother, they have always been so supportive and encouraging. I am deeply grateful to them for their loving me so much and providing me such a great family, which provides me very important morals, values and philosophy. And specially, I would like to thank my wife Yanran Li, who is always on my side no matter what happen. Your support and love drive me forward.

VITA

2007	B. S., Chemical Engineering Tianjin University Tianjin, P. R. China
2007-2012	Teaching Assistant, Research Assistant Department of Chemical and Biomolecular Engineering University of California, Los Angeles, USA

PUBLICATIONS

1. **Zheng Chen,** Chi-Ping Liu, Fei Wei, Vidvuds Ozolins*, Yunfeng Lu*, Proton Conductive WO_3 for Energy Application, in preparation.
2. **Zheng Chen**, Veronica Augustyn, Bruce Dunn*, Yunfeng Lu*, Design High-Performance Bulk Energy Storage Architectures, in preparation.
3. Ranrang Wang, **Zheng Chen**, Yunfeng Lu*, Super-long Cu and CuO Nanotube for Energy Applications, in preparation.
4. **Zheng Chen**, Xiaolei Wang, Huihui Zhou, Yang Liu, Fei Wei, Mei Cai and Yunfeng Lu*, Carbon-Nanotube-Threaded Nanocrystal Architecture for High Performance Pseudocapacitors, *to be submitted*.
5. Xilai Jia, Ranran Wang, **Zheng Chen**, Fei Wei* and Yunfeng Lu*, Ultra-Stable Electrodes Built from Cross-linked Networks of Carbon Nanotubes and Oxide Nanowires, *to be submitted*.
6. Xilai Jia, **Zheng Chen**, Yiting Peng, Xiaolei Wang, Fei Wei*, Yunfeng Lu*, Building Robust Architectures of Carbon and Metal Oxide Nanocrystals towards High-Performance Anodes for Lithium Ion Batteries, ***ACS Nano***, 2012, *in press*.
7. Ling Fei, Yun Xu, **Zheng Chen**, Bin Yuan, Xiaofei Wu, Joshua Hill, Qianglu Lin, Shuguang Deng, Paul Andersen, Yunfeng Lu, Hongmei Luo*, Porous SnO_2 Helical Nanotubes and SnO_2 Sheets for Lithium-Ion Batteries, 2012, *submitted.*
8. Chunzhu Yan,§ **Zheng Chen**§ (***equal contribution***), Yiting Peng, Lin Guo, Yunfeng Lu*, Stable Lithium-ion Cathodes from Nanocomposites of VO_2 Nanowire and CNTs, ***Nanotechnology***, 2012, *in press*.
9. Qiangfeng Xiao, Hiesang Sohn, **Zheng Chen**, Daniel Toso, Matthew Mecklenburg, Hong Zhou, Eric Poirier, Anne Dailly, Mei Cai, Yunfeng Lu*, General Synthesis of Mesoporous Metal and Metal Alloy Particles by Aerosol-Assisted Confined Growth of Nanocrystals, ***Angew. Chem. Int. Ed.***, 2012, 51, 10546-10550.
10. **Zheng Chen**, Ding Weng, Xiaolei Wang, Yanhua Cheng, Ge Wang* and Yunfeng Lu*, Ready Fabrication of Thin-Film Electrodes from Building Nanocrystals for Micro-Supercapacitors, ***Chem. Comm***., 2012, 48, 3736-3738.
11. Hiesang Sohn, **Zheng Chen**, Yoon Seok Jung, Qiangfeng Xiao, and Yunfeng Lu*, Robust Fe_3O_4-Carbon Core-Shell Particles for High-Performance Li-Storage, ***J. Mater. Chem.***, 2012, submitted.
12. Xilai Jia§, **Zheng Chen**§ (***equal contribution***), Arnold Suwarnasarn, Benjamin M. Wu, Fei Wei* and Yunfeng Lu*, High-Performance Flexible Lithium-Ion Electrodes Based on

Robust Network Architecture, ***Energy Environ. Sci.***, 2012, 5, 6845-6849.

13. **Zheng Chen**, Dieqing Zhang, Xiaolei Wang, Xilai Jia, Fei Wei, Hexing Li and Yunfeng Lu[*], High-Performance Energy Storage Architectures from Carbon Nanotubes and Nanocrystals Building Blocks, ***Advanced Materials***, 2012, 24, 2030-2036.
14. Chao Lei, **Zheng Chen**, Meiqing Shen[*], Yunfeng Lu[*], Better Lithium-Ion Storage Materials Made through Hierarchical Assemblies of Active Nanocrystals and Nanorods, ***ACS Appl. Mater. Interfaces.*** 2012, submitted.
15. **Zheng Chen**, Veronica Augustyn, Xilai Jia, Qiangfeng Xiao, Bruce Dunn[*], Yunfeng Lu[*], High-Performance Sodium-ion Pseudocapacitors Based on Hierarchically Porous Nanowire Composites, ***ACS Nano***, 2012, 6(5), 4319-4327.
16. **Zheng Chen,** Ding Weng, Hiesang Sohn, Mei Cai[*], Yunfeng Lu[*], High-Performance Aqueous Supercapacitors Based on Hierarchically Porous Carbon, ***RSC Advances***, 2012, 2, 1755-1758.
17. Xiaolei Wang, Ge Li, **Zheng Chen**, Veronica Augustyn, Ge Wang[*], Bruce Dunn, Yunfeng Lu[*], High-Performance Supercapacitors Based on Nanocomposites of Nb_2O_5 Nanocrystals and Carbon Nanotubes, ***Advanced Energy Materials***, 2011, 1, 1089-1093.
18. Xilai Jia, Chunzu Yan, **Zheng Chen**, Ranran Wang, Qiang Zhang, Fei Wei[*], Yunfeng Lu[*], Direct Synthesis of Flexible $LiMn_2O_4$/CNT Nanocomposite Electrode for Lithium-ion Cathodes, ***Chem. Comm***., 2011, 47, 9669-9671.
19. **Zheng Chen**, Jing Wen, Chunzhu Yan, Lynn Rice, Hiesang Sohn, Mei Cai[*], Bruce Dunn and Yunfeng Lu[*], High-Performance Supercapacitors Based on Hierarchically Porous Graphite Particles, ***Advanced Energy Materials***, 2011,1, 551-556.
20. **Zheng Chen**, Veronica Augustyn, Jing Wen, Yuewei Zhang, Meiqing Shen[*], Bruce Dunn[*], Yunfeng Lu[*], High-Performance Supercapacitors Based on Intertwined CNT/V_2O_5 Nanowire Nanocomposites, ***Advanced Materials***, 2011, 23, 791-795.
21. Yiting Peng[§], **Zheng Chen**[§](***equal contribution***), Jing Wen, Qiangfeng Xiao, Ding Weng, Shiyu He[*], Hongbin Geng[*], Yunfeng Lu[*], Hierarchical Manganese Oxide/Carbon Nanocomposites for Supercapacitor Electrodes, ***Nano Research***, 2011, 4(2), 216-225.
22. **Zheng Chen**, Yaochun Qin, Ding Weng, Qiangfeng Xiao, Yiting Peng, Xiaolei Wang, Hexing Li[*], Fei Wei[*], Yunfeng Lu[*], Design and Synthesis of Hierarchical Nanowire Composites for Electrochemical Energy Storage, ***Advanced Functional Materials***, 2009, 19(21), 3420-3426.

Chapter 1: Introduction

1.1 Background

Nature and human society are driven by energy. The evolution of an ecosystem is supported by chemical energy stored in organic compounds such as carbohydrates, fats and proteins that are converted from sunlight by autotrophs (e.g. plants and algae).[1] Similarly, human activity and society development rely on chemical energy stored in food and electrical energy produced from fossil fuels (e.g. oil, coal and gas). To continue human civilization requires abundant and sustainable supply of energy. During the past decades, global energy consumption has been booming with steadily increased standard of living and quality of civilization. Rapidly increased energy consumption, however, has inevitably resulted in fossil-fuel shortage and ecological deterioration.[2, 3] Facing these challenges, humankind has been diligently seeking for alternative energy sources to offset the diminishing availability or to take place of fossil fuels (**Figure 1.1**), and at the same time, seeking for strategies to increase the efficiency of energy use.[4, 5]

In the respect of alternative sources, biomass conversion may be a potential way to

produce high-quality energy (e.g. alcohol, bio-diesel) from renewable sources, such as wood, sugar canes and crop residues. However, growth of biomass decreases total size of fertile land for crops and timber, raising the price of food and wood products. Moreover, to convert and collect biomass energy consumes too much energy and causes serious pollutions.[6-8] Hydropower is an economically effective energy source but it requires building huge dams at locations where special geological conditions have to be met.[9] Electricity produced from nuclear fission has been increasing in the past three decades, but recent failure of Fukushima Daiichi nuclear power plant caused by 2011 Tohoku earthquake in Japan has re-drawn a great concern about nuclear security.[10]

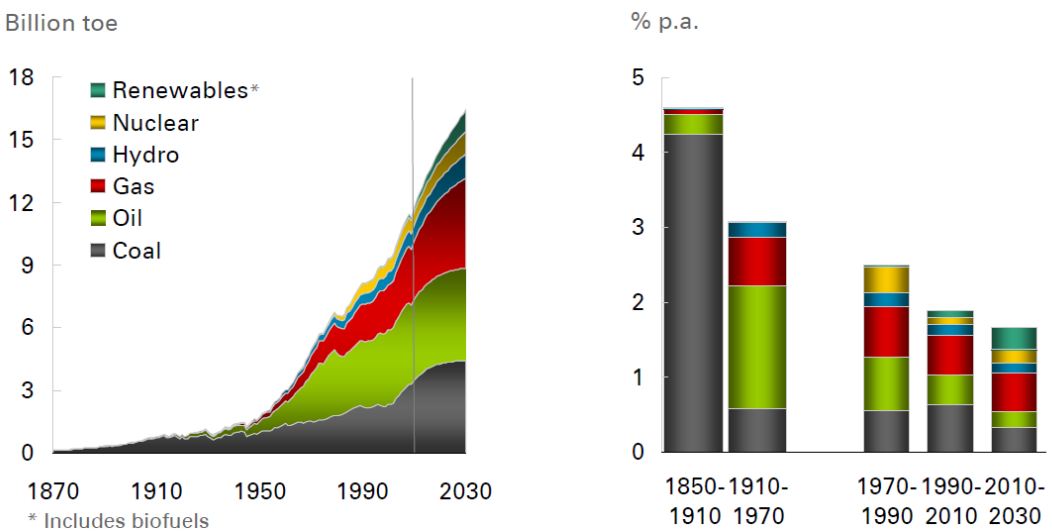

Figure 1.1 World commercial energy use (left) and contribution of each source to total energy growth (right).[4](toe: term of oil equivalent)

In this context, clean, safe and renewable sources such as solar radiation, wind, waves and tides are considered as more promising sources for energy production.[11] As predicted, increase of renewable energy will be a leading factor contributing to total energy growth by 2030 (**Figure 1.1**). However, these energies are variable with time and diffused in space. The energy harvested from these sources is in such intermittent nature and that must be stored prior to its connection to electric grids or delivery to customers. This requirement has drawn a huge demand for effective energy storage.

On the other hand, to increase the efficiency of energy use, a key step is to replace the current petroleum-based transportation infrastructure by electric transportation.[12, 13] Since energy conversion efficiency of electric motors is 4 to 5 times higher than that of normal engines (90% *vs*. 20%), the net energy consumption and CO_2 production from electric vehicles (EVs) is typically less than one-half of that from traditional vehicles.[14] Moreover, the electricity used to power electrical vehicles (EVs) can be produced from various renewable sources instead of fossil-fuel power plant, which further reduces the use of fossil fuels. However, widespread implementation of EVs also relies on successful on-board rechargeable electricity storage. In addition, other emerging applications such as advanced portable electronics and smart grids demand effective energy storage devices and systems.[3]

These growing needs have made energy storage an essential component of creating sustainable society.

1.2 Energy Storage Technologies

Our ancestors used fire wood and charcoal with stored chemical energy to light, cook food and make bronze wares, which created ancient civilization, while modern industries requires more complex and high-performance energy storage technologies. To date, various advanced strategies have been proposed for energy storage,[15, 16] including mechanical energy storage, electrostatic energy storage, hydrogen (H_2)-based chemical energy storage, and electrochemical energy storage. They favor different applications due to their individual characteristics.

Typical mechanical energy storage includes flywheel storage and compressed air storage. Flywheels use vacuum-housed high-speed rotor to reversibly convert electrical energy to kinetic energy; the flywheel's rotational speed is reduced or increased as electrical energy is generated or added.[17, 18] Common spinning speeds are in the range of 20,000 to over 50,000 rotations per minute.[19] The energy density (energy stored per unit mass or volume) is proportional to the mass and the square of the angular velocity of the rotor, the lighter the rotor and the higher the spinning speed, the higher the energy density. To reach high speed,

light and high-strength materials such as polymer-reinforced composites are used. Typical energy density may reach 100-130 Wh/kg based on the mass of rotor, while it decreases to ~10 Wh/kg if the whole heavy container is considered. This technology shows advantages of wide range of operation temperatures, high round-trip efficiency and long services life, but is limited by fast energy loss and potential safety issue from shattering.[20] On the other hand, compressed air energy storage is based on compression and expansion of gas to store or release kinetic energy, which is driven by turbo compressor or drives air engine to produce electricity.[21] It is only suitable for storage of a large amount of off-peak electric power when large cavern is available. For vehicle applications, this technology is constrained by low energy density, low efficiency, high-cost vessels and safety concern.[22]

Electrostatic energy storage using dielectrical capacitors shows high frequency response, but can only store a small amount of energy.[23] Therefore, they are only used in small electronics. Using polarized polymers may significantly improve the energy density, but it is too low to be used in large-scale storage.[24]

H_2-based chemical energy storage was considered as a critical technology to develop hydrogen economy. [25] For example, to develop H_2-powered fuel cells for vehicles and other applications. However, after almost two decades' effort, there has been no successful

strategy to store H_2 with a capacity, cost and operation condition that can meet general applications.[26]

1.3 Electrochemical Energy Storage

Among all energy storage endeavors, converting electrical energy into chemical energy stored within batteries or electrochemical capacitors (ECs) is probably the most promising approach, since as-stored chemical energy can be effectively delivered as electrical energy with a diversity of energy density and power density (power delivered per unit mass or volume), high efficiency, long service life, effective cost and environmental benignity.[3, 27, 28] Furthermore, batteries and ECs can be highly portable, enabling their broad use in portable electronics, electric vehicles, and other applications. Effectively assembling battery or EC stacks can easily create large-scale energy storage systems for utility applications. In fact, rapid market growth for portable electronics, electric vehicles and grid storage has placed high-performance batteries and ECs at the forefront of technical innovation.

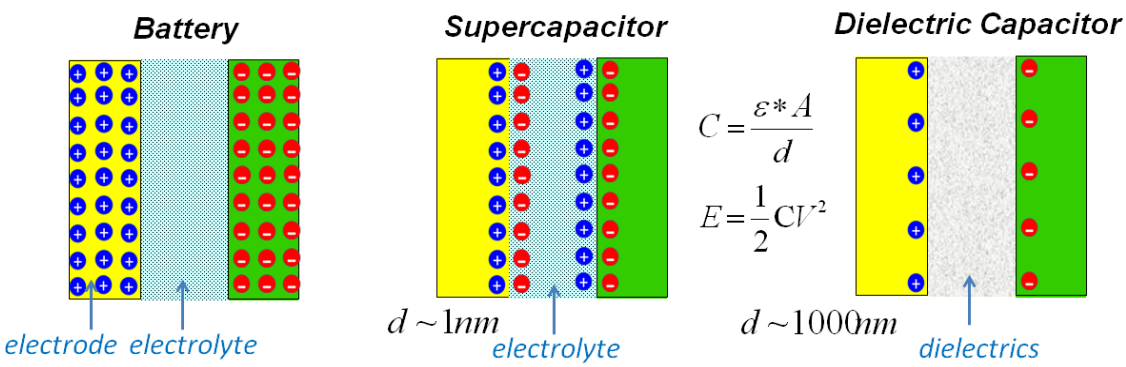

Figure 1.2 Simplified models of different energy storage devices.

The performance of these devices is determined by their structure and storage features. A simple comparison is presented in **Figure 1.2** where simplified device models are presented. Batteries can store a lot of energy using their whole electrode active materials where chemical reactions take place through the bulk of electrodes. ECs, called supercapacitors, store charge on the surface of their electrodes. Chemical or physical processes occur on the interface between electrode and electrolyte, so the total charge is smaller. But according to the equation ($C=\varepsilon*A/d$), since the distance (d) between this two surfaces is in the range of 1 nm, the energy density is still significant. Capacitors use dielectrics which generally have length scale of ~1000 nm; therefore the capacitance and energy density are very low. Therefore, capacitors are not used for major power sources in electronic devices.

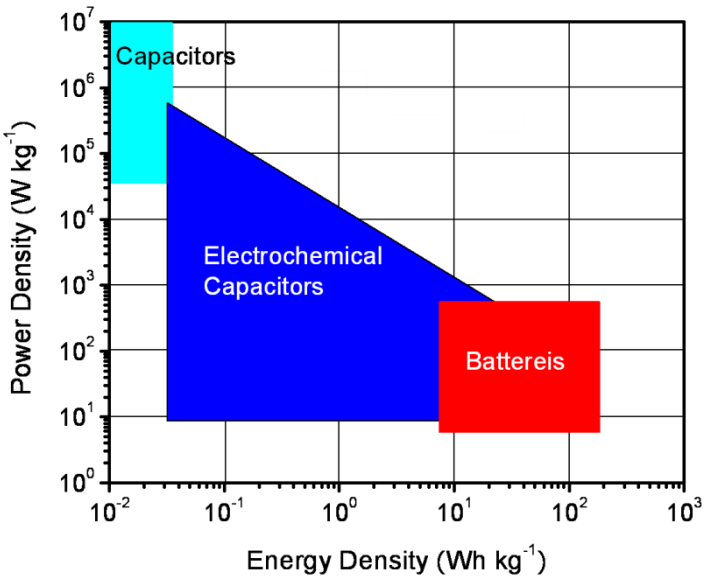

Figure 1.3 A general plot of power density against energy density for capacitors, electrochemical capacitors and batteries.

Generally, energy density and power density are used to quantify the performance of batteries and ECs. **Figure 1.3** shows a plot of power density versus energy density, also called a Ragone plot, for capacitors, ECs and batteries.[29] As illustrated, batteries, which operate based on redox reactions between their cathodes and anodes, offer high energy density but low power density. These features allow them to be used in ordinary electronics where energy density is of primary concern. Capacitors, on the other hand, which are operated based on charge accumulation on parallel electrodes separated by dielectrics, offer much higher power density but much lower energy density. In the aspect of lifetime, capacitors exhibit dramatically longer lifetimes (e.g., > 1,000,000 cycles) than batteries (e.g.,

1,000 cycles).[3, 27]

ECs exhibit storage performance intermediate that of capacitors and batteries. They are generally operated based on electrical double-layer capacitance or pseudocapacitance, and are referred to electrical double-layer capacitor (EDLC) and pseudocapacitor, respectively. Supercapacitors can deliver at least 1,000 times more energy than dielectric capacitors and 10 times more power than batteries. In addition, they often exhibit long cycling lives of over 500,000 cycles. Such superior performance is essential for various applications where fast charging, high power and long cycling life are required. Typical applications include energy recovery, energy harvesting from intermittent power sources, back-up power supply, heavy-duty loading and uninterruptible power supplies.[30]

1.3.1. Rechargeable Batteries

Rechargeable batteries can be divided into different categories according to their electrode materials, and mainly include lead-acid, nickel-cadmium, nickel-metal hydride and lithium-ion batteries.[31] Currently, lithium-ion batteries are the most widely used rechargeable batteries due to their high energy density, high cell voltage, low self-discharge, long cycling life and absence of memory effect. To illustrate the working principle of rechargeable batteries, we use lithium-ion battery as an example **(Figure 1.4)**. Such a

device contains a cathode and an anode, which are separated and soaked in an electrolyte. The energy is stored by reversible chemical reaction. During a discharge process, lithium ions are extracted from anode materials, such as graphite, and electrons are released at the same time. The electrons are driven to the cathode through external circuit. Lithium-ions diffuse from anode into the cathode through internal circuit (or electrolyte), and then react with cathode materials by combining electrons. As a result, the cell voltage decreases and energy is released. Reverse reactions take place during a charge process. So it can be determined that the following key processes take place in a battery process: 1) ion transport and diffusion; 2) electron transfer and 3) chemical reactions in solid-phase and on electrode/electrolyte interfaces. These complicated processes make the charge storage kinetics to be very slow.

Anode materials used for current commercial lithium-ion battery are mainly graphite, which can take a large amount of lithium ions in the form of LiC_6, of which the theoretical lithium storage capacity is 372 mAh/g. Cathode materials are dominated by lithium metal oxide such as $LiCoO_2$ and $LiMn_2O_4$, which give a lithium capacity of 120-150 mAh/g. Such combination leads to an energy density of 500-600 Wh/kg based on electrode materials or 100-150 Wh/kg if considering the whole device package.[32]

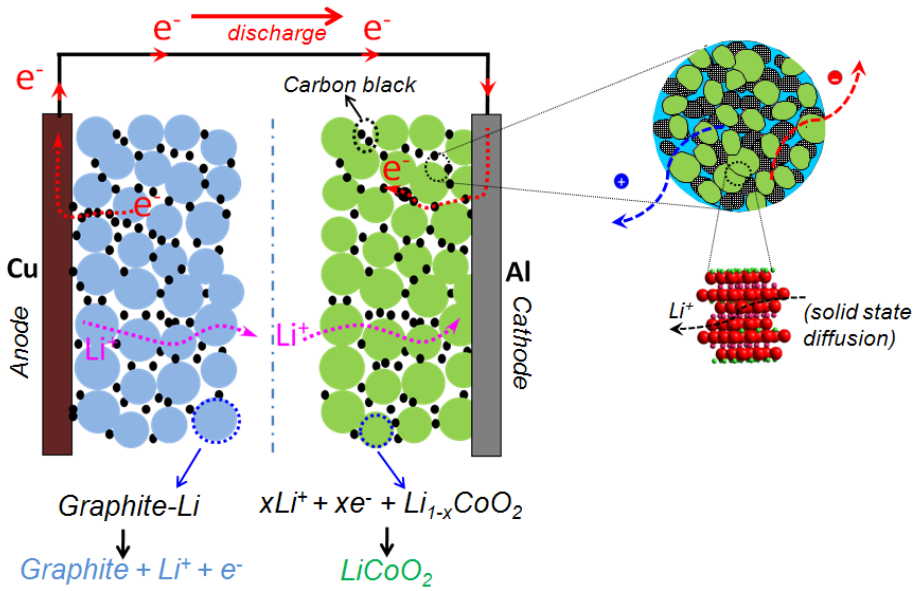

Figure 1.4 Operation principle of a lithium-ion battery (illustrated with a discharging process)

1.3.2. Electrical Double-Layer Capacitors (EDLCs)

For EDLCs, the device structure is similar to that of batteries; there are also two electrodes (a positive and a negative), a separator and electrolyte filled inside the cell, as shown in **Figure 1.4**. The energy storage is based on physical separation and accumulation of charged ions on the electrode/electrolyte interface. Porous materials (such as activated carbon) are normally used to provide large interface for more charge storage. During a charge process, negatively charged ion move to positive side and form a double layer, and electrons move through the external circuit to negative electrode, where positively charged

ions are accumulated over there (**Figure 1.5**).[27, 29, 30] As a result, the cell voltage increases and energy is stored. The most critical process that might limit the storage performance is ion transport. Since the electrode capacitance is independent with potential, a linear charge/discharge curve is obtained. Current commercial EDLCs use organic electrolyte and porous carbon electrode which can provide a capacitance of 100-150 F/g.[33, 34]

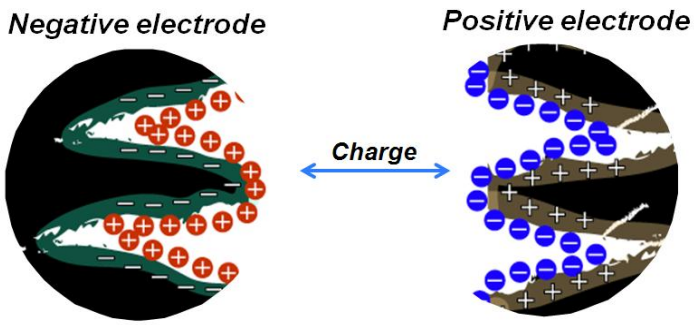

Figure 1.5. Working principle of EDLCs (illustrated with a charging process)

1.3.3. Pseudocapacitors

The other type of supercapacitor is pseudocapacitors, which store energy by fast faradic reactions. In these devices, the ions and electrons move in the same manner with EDLCs, but instead of forming double-layer on the electrode/electrolyte interface, redox reactions take place on the surface or near the surface of the electrodes (**Figure 1.6**).[27, 29, 30] Energy is also stored by chemical reaction which is similar to battery, but the reaction would only involve just the first a few or tens of nanometers of the electrode material and the process is

free of solid-state diffusion and phase change, which is similar to EDLCs. The most critical process that might limit the storage performance is ion transport and charge transfer. The best pseudocapacitor materials (RuO_2 xH_2O) so far can provide a capacitance of over 1000F/g.[35] It can be seen that the major electrode process of supercapacitors is ion transport and diffusion; pseudocapacitors have fast charge transfer and surface reactions, which enable fast charge/discharge and high power density.

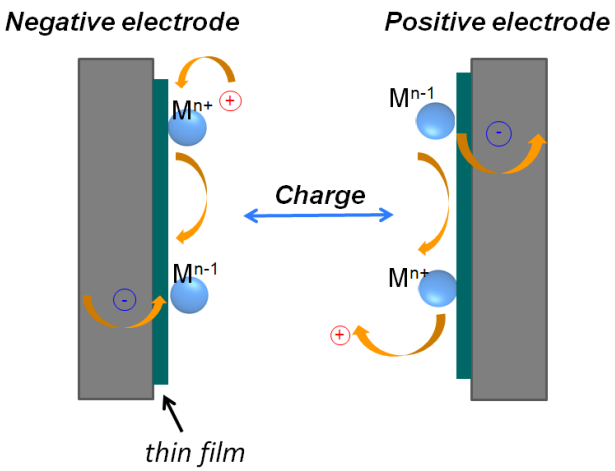

Figure 1.6. Working principle of pseudocapacitors (illustrated with a charging process).

1.4 Development of Electrochemical Energy Storage Materials

1.4.1 Carbon (EDLC) Materials

Conventionally, EDLC utilizes activated carbon as the electrode material; their capacitance comes purely from the electrostatic charge accumulated at the electrode/electrolyte interface. The energy density of an EDLC depends on the surface area

of the electrode material that is accessible to electrolyte ions which form electrical double layers at electrode/electrolyte interface.[36, 37] To date, the most advanced EDLCs based on activated carbons may provide capacitance of up to 150 F g^{-1} in organic electrolyte or 250 F g^{-1} in aqueous electrolyte, which approximately corresponds to energy densities of 35 and 8 Wh kg^{-1} (based on the weight of active materials for all energy and power densities hereinafter), respectively.[33, 34, 38] Such energy densities are significantly higher than those of dielectric-based capacitors (e.g., 10^{-2} Wh kg^{-1} for the best tantalum capacitors); however, they are much less than those of batteries (~ 100-150 Wh kg^{-1}).[32] Nevertheless, EDLCs are operated based on electrostatic charge accumulation, which allows rapid charge and discharge with high power density (e.g., 5 kW kg^{-1} at energy density of 5 Wh kg^{-1}).[39]

Towards better EDLCs, various carbon materials have been explored, including activated carbons,[40] carbon nanotubes (CNTs),[41] graphene,[42] templated carbons[43] and carbon aerogels.[44] These efforts have been focused on optimizing the materials' pore structure to enable faster ion transport and to increase their effective surface area. Electrical double layers can be readily formed on CNTs; however, capacitance of CNTs is generally low due to low surface area.[45] Graphene may provide higher surface area; however, it tends to form stacking structure with reduced surface area. Recently, activated graphene with high surface

area was reported with capacitance as high as 170 F g^{-1} in organic electrolyte, which is the highest capacitance ever obtained from carbon materials.[34] Compared to activated carbons that are low cost but have less controlled pore structure, templated carbons were synthesized with well-controlled pore structure. The highest capacitance achieved for templated carbons, however, is still less than 120 F g^{-1} in organic electrolyte[43] or 250 F g^{-1} in aqueous electrolyte.[38]

In addition, extensive efforts have also been devoted to developing better organic electrolytes with wider voltage windows and lower ion-transport resistance, since the energy density of EDLCs is proportional to the square of the cell voltage. However, implementation of such electrolytes also requires the fabrication of high-purity carbon materials in order to avoid side reactions occurring at high voltage.[46] In short, despite the extensive efforts made, advances in the field of EDLCs have been quite limited.

1.4.2 Redox-Active Materials (Batteries and Pseudocapacitors)

Batteries and pseudocapacitors share similar characteristics in terms of active materials, device structures and operations. A pseudocapacitor is similar to a high-power thin-film battery. Normally, battery charge/discharge processes show slow solid-state diffusions and may involve tedious bulk reaction and unfavorable phase transformation, which limits the

rate capability and charge/discharge life (cycling life). Nevertheless, by decreasing the size or increasing the porosity, battery electrodes may show significantly increased surface-area, which enables enhanced charge storage from surface redox reactions. If suitable electronic conductivity and structure/interface stability can be reached, these materials may be charged and discharged at increased rates, which is similar to pseudocapacitors. In this context, materials used for battery electrode can be also potential candidates for pseudocapacitors. One of the major efforts of my PhD research is to design high-performance materials architectures that could enable traditional redox materials with high capacity, high rate and long cycling life, through improving pseudocapacitive charge storage. In this dissertation, I will discuss all redox materials with a purpose of pseudocapacitor application, though some of them may be considered as conventional battery materials.

Pseudocapacitors rely on fast reversible faradic processes occurring on the surface of sub-surface of redox-active materials such as conductive polymers and metal oxides. Pseudocapacitance arises due to thermodynamic consideration between the charge acceptance (Δq) and the change in voltage ($\Delta \upsilon$), where the derivative ($dq/d\upsilon$) corresponds to the pseudocapacitance.[47] Compared to carbon materials, metal oxides may offer significantly higher capacitances. For example, hydrous ruthenium oxide ($RuO_2\,xH_2O$) has a specific

capacitance of over 720 F g^{-1} in 1 V acidic electrolytes owning to its excellent proton and electron conduction.[35] Transition metal oxides (e.g., MnO_2,[48] Co_3O_4,[49] TiO_2,[50] MoO_3[51] and Nb_2O_5[52]) also possess theoretical capacitances of up to 1000 F g^{-1}; however, the electrodes made from these oxides generally exhibit very low energy and power densities due to poor ionic and electronic conductivity. To circumvent this barrier, pseudocapacitors are generally prepared from thin-film electrodes or composite electrodes as detailed below.

Thin-Film Pseudocapacitors: To minimize ionic and electronic transport resistance, oxide thin films with thickness of nanometers to hundreds of nanometers were deposited on conductive substrates, exhibiting high gravimetric capacitances and high power.[50, 51, 53, 54] However, their performance decreases rapidly with increasing electrode thickness. With limited thickness, mass loading of active materials, and hence energy density, is extremely low, which precludes their practical application.[55] Recently, thin-film pseudocapacitors were made by coating oxides onto porous conductive substrates such as gold[56] and nickel;[57] their mass loading was improved to some degree but is still too low for actual application.

Composited Pseudocapacitors: To increase mass loading, composite electrodes were fabricated by introducing conductive agents, such as carbon black,[58, 59] graphene[60, 61] and CNTs.[62, 63] Such electrodes can be classified into two categories. The first category was

made by coating physical mixtures of active materials, polymeric binders, and conductive agents onto the current collectors. This method is simple, however, such electrodes generally exhibit mediocre storage performance. For example, MnO_2-based electrodes made with 30 wt-% acetylene black exhibit a capacitance of 228 F g^{-1} at a rate of 10 mV s^{-1}, which is significantly lower than the theoretical value of MnO_2.[58] Such mediocre performance can be attributed to poor electrode-structure control, in particular, poor control over the interfaces between active materials and conductive agents.

The second category of pseudocapacitors was made from nanocomposites of oxides and CNTs or graphene. Graphene and CNTs are lightweight and highly conductive materials with large open surface, excellent mechanical strength, and high chemical/electrochemical stability, and have been extensively used to form various nanocomposites. To form the nanocomposites, active materials were deposited on graphene[60, 61, 64] or CNTs[62, 63, 65] or within graphene layers or CNT networks though various techniques, such as sol-gel processing,[66] electrophoresis,[67] electrochemical deposition,[68, 69] electroless deposition,[62, 70] hydrothermal reaction[71, 72] and thermal evaporation.[73] Such nanocomposites possess well-controlled structure and interfaces, making the fabrication of high-performance pseudocapacitors possible. However, many of the nanocomposites reported are based on

SnO_2,[64, 65] Fe_3O_4,[74] Mn_3O_4[72] and other high capacitive materials,[75] where charge storage is based on conversion reactions in organic electrolytes. These nanocomposites exhibited impressive capacity of up to 1000 mAh g^{-1}, but at extremely slow charge/discharge rates (a few hours) and at low working potentials. Their tendency to form solid-electrolyte-interface (SEI) layers, as well as their phase transitions and large volume changes during charge and discharge, results in electrodes with short cycling life (e.g., < 100 cycles) and reduced efficiency.[76] In this context, such nanocomposites are more suitable for batteries rather than for supercapacitors where high power, high efficiency and long cycle life are required.

Finding other oxide nanocomposites, which don't form the SEI layers or undergo significant structural and volume changes during charge/discharge, is essential towards the development of high-performance pseudocapacitors. To date, nanocomposites of MnO_2,[60] Co_3O_4,[77] NiO[78] and RuO_2[79]aqueous electrolyte were extensively studied. RuO_2-based nanocomposites exhibit notably good performance; however, their high cost forbids their large-scale application. Nanocomposites based on Co_3O_4 and NiO may provide capacitances of over 1000 F g^{-1} in alkaline electrolytes, but their narrow voltage window (~ 0.3 V) results in low energy density. MnO_2 is low cost, abundant and environmentally benign; however, nanocomposites based on MnO_2 generally exhibit low capacitances of less

than 300 F g^{-1}. Adapting organic electrolytes with wider voltage windows may give high energy density, but even then, such nanocomposites would be still limited by their poor cycling stability.

1. 5 Design Criteria and Needs for Electrochemical Energy Storage Materials

As mentioned above, batteries and ECs share similar characteristics in terms of active materials, device structures and operations; energy is stored or liberated through reversible redox reactions occurring in two electrodes, which are accompanied by shuttling of ions and electrons between the cathodes and anodes. Therefore, to realize high energy and power densities, sufficient number of ions and electrons need to be rapidly shuttled between the two electrodes. To obtain long cycling life, the electrodes and device structure must keep stable during charge/discharge cycling. These principles imply that high-performance electrodes and devices should meet the following criteria: 1) Large amount of installed active materials for high energy capacity; 2) Rapid transport of ions and electrons; 3) Facile electrochemical reactions on surface and in the bulk of electrodes; 4) Mechanically robust electrode architecture and chemically stable electrode/electrolyte interface. However, none of the existing single materials can meet all these criteria. Typical porous carbon materials show insufficient charge storage density; oxide and phosphate materials usually have low electron

conductivity and low ion mobility; and most oxides have poor structure stability. These issues restrain the performance of current energy storage devices. Therefore, the seeking for high performance material architectures to circumvent these issues is highly demanded.

1.6 Thesis Objective and Research Scope

The objective of my dissertation is to address the limitation of current energy storage materials by rational structure design according to the above principles and criteria. The ultimate goal of this research is to develop high energy, high power, low cost and long life electrochemical energy storage devices for various applications, including portable electronics, EVs and grid-scale energy storage. To achieve this goal, my research strategy is to design and fabricate multifunctional architectures by integrating distinct material structures and properties to address the limitation of traditional materials and create a new family of high-performance energy materials with desired properties. Generally, my dissertation is dedicated to the following aspects: 1) understanding of novel charge storage behavior at nanoscale electrochemical interfaces, 2) design and efficient fabrication of new nano-architectured materials with tunable functionality and 3) integration of these materials into electrochemical devices and studying their performance to further guide the materials design.

Specifically, this dissertation includes the following research directions:

High-performance carbon materials for EDLC (Chapter 2, 3). Hierarchically porous carbon particles with graphitized structures were designed and synthesized with an efficient aerosol-spray process. By comparing with commercial activated carbon and CNTs, the surface area and pore structure were systematically studied to understand the parameters that determine the charge storage performance.

MnO_2/Mesoporous carbon nanocomposite (Chapter 4). MnO_2 thin-layers with different thicknesses were deposited on mesoporous carbon scaffold with hierarchical pore structure. The effect of layer thickness on the charge storage performance of the composites was correlated to electronic conductivity and electrolyte diffusion properties.

Interpenetrating oxide nanowire/CNT network structure (Chapter 5-7). Interpenetrating networks of layered structured V_2O_5 nanowire and CNT were fabricated by an *in-situ* hydrothermal reaction. The effects of CNT compositions, pore structure, electrode thickness were systematically studied. Synergistic effect between V_2O_5 nanowire and CNT was examined and resulted in a proper composition for highest storage performance. Different CNT lengths were also investigated and led to robust flexible electrodes; V_2O_5 structure was modified to store both lithium and sodium ions; electrode architectures were

engineered and leading to high-rate, thick electrodes for bulk energy storage.

Integrated nanocrystal and CNT architectures (Chapter 8-10). Ultrafine TiO_2 nanocrystals were synthesized and studied as a model system to investigate the electrode architecture effect. Electrodes were fabricated by directly coating thin film TiO_2 on conductive Indium-Tin Oxide (ITO) glass, by conformably coating nanocrystals on pre-formed CNT papers, and by salvation induced assembly between nanocrystals and CNT. Charge storage capacity, rate performance and cycling stability were compared and pseudocapacitive storage was investigated.

References

[1] http://en.wikipedia.org/wiki/Autotroph

[2] Armand, M.; Tarascon, J. M., Building better batteries. *Nature* **2008,** 451 (7179), 652-657.

[3] Simon, P.; Gogotsi, Y., Materials for electrochemical capacitors. *Nat Mater* **2008,** 7 (11), 845-854.

[4] BP Energy Outlook 2030, London, United Kingdom, January **2011**.

[5] BP Statistical Review of World Energy, London, United Kingdom, June **2012**.

[6] A. Demirbas, Biomass resource facilities and biomass conversion processing for fuels and chemicals, *Energy Conversion and Management* **2001**, 42(11), 1357-1378.

[7] M. F. Demirbas, M. Balat, H. Balat, Potential contribution of biomass to the sustainable energy development, *Energy Conversion and Management* **2009**, 50(7), 1746-1760.

[8] http://www.altenergy.org/renewables/biomass.html.

[9] http://www.eere.energy.gov/basics/renewable_energy/hydropower.html.

[10] http://en.wikipedia.org/wiki/Fukushima_Daiichi_Nuclear_Power_Plant.

[11] Top 5 Renewable Energy Sources of 2012, www.greenerideal.com.

[12] A. Faiz, C. S. Weaver, M. P. Walsh, Air Pollution from Motor Vehicles: Standards and Technologies for Controlling Emissions, **1996**, The World Bank, Washington, D. C.

[13] Electric car boom-Fiji Times Online, Fijitimes.com, March 4, **2010**.

[14] California Energy Commission's Demonstration of Neighborhood Electric Vehicles Consultant Report P600-02-020F, July 1, **2002**.

[15] Jensen, J.; Sorensen, B., Fundamentals of energy storage. *John Wiley and Sons, Inc.,New York, NY, USA* **1984**.

[16] Liu, C.; Li, F.; Ma, L.-P.; Cheng, H.-M., Advanced Materials for Energy Storage. *Advanced Materials* **2010,** 22 (8), E28-E62.

[17] S. Miller, Flywheel Fundamentals, *Environmental Science and Technology* **1994**, 28(2), 62A.

[18] B. Bolund, H. Bernhoff, M. Leijon, Flywheel energy and power storage systems, *Renewable and Sustainable Energy Reviews* **2007**, 11, 235-258.

[19] Davide Castelvecchi, Spinning into control: High-tech reincarnations of an ancient way of storing energy, *Science News* **2007**, 171(20), 312-313.

[20] http://en.wikipedia.org/wiki/Flywheel.

[21] S. J. Bauer, K. N. Gaither, S. S. Webb, C. Nelson, Compressed Air Energy Storage in Hard Rock Feasibility Study, Sandia Report, SAND2012-0540, February, **2012**.

[22] Distributed Energy Program: Compressed Air Energy Storage, United States Department of Energy, August **2006**.

[23] R. C. Dorf, J. A Svoboda, *Introduction to Electric Circuits* (5th ed.). *John Wiley and Sons, Inc., New York, NY, USA* **2001**.

[24] X. N. Xie, K. L. Lee, J. Z. Wang, K. P. Loh, Polarizable energy-storage membrane based on ionic condensation and decondensation, *Energy and Environmental Science* **2011**, 4, 3960-3965.

[25] J. Rifkin, The hydrogen Economy, *Tarcher/Putnam, Penguin Group Inc., New York, NY,*

USA **2002**.

[26] Yang R. T.; Wang Y. H. Catalyzed Hydrogen Spillover for Hydrogen Storage *J. Am. Chem. Soc.* **2009**, 131, 4224–4226.

[27] Winter, M.; Brodd, R. J., What Are Batteries, Fuel Cells, and Supercapacitors? *Chemical Reviews* **2004,** 104, (10), 4245-4270.

[28] Ibrahim, H.; Ilinca, A.; Perron, J., Energy storage systems—Characteristics and comparisons. *Renewable and Sustainable Energy Reviews* **2008,** 12, (5), 1221-1250.

[29] Kötz, R.; Carlen, M., Principles and applications of electrochemical capacitors. *Electrochimica Acta* **2000,** 45, (15-16), 2483-2498.

[30] John R. Miller, A. F. B., Electrochemical Capacitors: Challenges and Opportunities for Real-World Applications. *The Electrochemical Society Interface* **2008**, 53-57.

[31] T. B. Reddy, Linden's Handbook of Batteries, 4th Edition, The McGraw-Hill, Inc., *New York, NY, USA*, USA 2011.

[32] Rechargeable Li-ion OEM Battery Products, Panasonic.com, April 23, **2010**.

[33] J. Chmiola, G. Yushin, Y. Gogotsi, C. Portet, P. Simon, P. L. Taberna, *Science* **2006**, *313*, 1760.

[34] Y. Zhu, S. Murali, M. D. Stoller, K. J. Ganesh, W. Cai, P. J. Ferreira, A. Pirkle, R. M.

Wallace, K. A. Cychosz, M. Thommes, D. Su, E. A. Stach, R. S. Ruoff, *Science* **2011**, *14*, B70.

[35] Zheng, J. P.; Cygan, P. J.; Jow, T. R., Hydrous Ruthenium Oxide as an Electrode Material for Electrochemical Capacitors. *Journal of The Electrochemical Society* **1995,** 142, (8), 2699-2703.

[36] Liu, H.; Zhu, G., The electrochemical capacitance of nanoporous carbons in aqueous and ionic liquids. *Journal of Power Sources* **2007,** 171, (2), 1054-1061.

[37] Frackowiak, E., Carbon materials for supercapacitor application. *Phys. Chem. Chem. Phys.* **2007,** 9, 1774-1785.

[38] A. Kajdos, A. Kvit, F. Jones, J. Jagiello, G. Yushin, *Journal of the American Chemical Society* **2010**, *132*, 3252.

[39] Burke, A., Ultracapacitors: why, how, and where is the technology. *Journal of Power Sources* **2000,** 91, (1), 37-50.

[40] Kierzek, K.; Frackowiak, E.; Lota, G.; Gryglewicz, G.; Machnikowski, J., Electrochemical capacitors based on highly porous carbons prepared by KOH activation. *Electrochimica Acta* **2004,** 49, (4), 515-523.

[41] An, K. H.; Kim, W. S.; Park, Y. S.; Choi, Y. C.; Lee, S. M.; Chung, D. C.; Bae, D. J.; Lim,

S. C.; Lee, Y. H., Supercapacitors using single-walled carbon nanotube electrodes. *Advanced Materials* **2001,** 13, (7), 4.

[42] Stoller, M. D.; Park, S.; Zhu, Y.; An, J.; Ruoff, R. S., Graphene-Based Ultracapacitors. *Nano Letters* **2008,** 8, (10), 3498-3502.

[43] Li, H.-Q.; Liu, R.-L.; Zhao, D.-Y.; Xia, Y.-Y., Electrochemical properties of an ordered mesoporous carbon prepared by direct tri-constituent co-assembly. *Carbon* **2007,** 45, (13), 2628-2635.

[44] Hwang, S. W.; Hyun, S. H., Capacitance control of carbon aerogel electrodes. *Journal of Non-Crystalline Solids* **2004,** 347, (1-3), 238-245.

[45] Chunsheng Du, N. P., High power density supercapacitor electrodes of carbon nanotube films by electrophoretic deposition. *Nanotechnology* **2006,** 17, 5314-5318.

[46] Naoi, K., 'Nanohybrid Capacitor': The Next Generation Electrochemical Capacitors. *Fuel Cells* **2010**, 10(5), 825-833.

[47] Conway, B. E.; Birss, V.; Wojtowicz, J., The role and utilization of pseudocapacitance for energy storage by supercapacitors. *Journal of Power Sources* **1997,** 66, (1-2), 1-14.

[48] Toupin, M.; Brousse, T.; Belanger, D., Charge Storage Mechanism of MnO_2 Electrode Used in Aqueous Electrochemical Capacitor. *Chemistry of Materials* **2004,** 16, (16),

3184-3190.

[49] Wei, T.-Y.; Chen, C.-H.; Chang, K.-H.; Lu, S.-Y.; Hu, C.-C., Cobalt Oxide Aerogels of Ideal Supercapacitive Properties Prepared with an Epoxide Synthetic Route. *Chemistry of Materials* **2009,** 21, (14), 3228-3233.

[50] Brezesinski, T.; Wang, J.; Polleux, J.; Dunn, B.; Tolbert, S. H., Templated Nanocrystal-Based Porous TiO_2 Films for Next-Generation Electrochemical Capacitors. *Journal of the American Chemical Society* **2009,** 131, (5), 8.

[51] Brezesinski, T.; Wang, J.; Tolbert, S. H.; Dunn, B., Ordered mesoporous α-MoO_3 with iso-oriented nanocrystalline walls for thin-film pseudocapacitors. *Nat Mater* **2009**, (2), 146-151.

[52] Wang, X.; Li, G.; Chen, Z.; Augustyn, V.; Ma, X.; Wang, G.; Dunn, B.; Lu, Y., High-Performance Supercapacitors Based on Nanocomposites of Nb_2O_5 Nanocrystals and Carbon Nanotubes. *Advanced Energy Materials* **2011**, 1(6), 1089-1093.

[53] Toupin, M.; Brousse, T.; Belanger, D., Influence of Microstucture on the Charge Storage Properties of Chemically Synthesized Manganese Dioxide. *Chemistry of Materials* **2002,** 14, (9), 3946-3952.

[54] Pang, S.-C.; Anderson, M. A.; Chapman, T. W., Novel Electrode Materials for Thin-Film

Ultracapacitors: Comparison of Electrochemical Properties of Sol-Gel-Derived and Electrodeposited Manganese Dioxide. *Journal of The Electrochemical Society* **2000,** 147, (2), 444-450.

[55] Gogotsi, Y.; Simon, P., True Performance Metrics in Electrochemical Energy Storage. *Science* 334, (6058), 917-918.

[56] Lang, X.; Hirata, A.; Fujita, T.; Chen, M., Nanoporous metal/oxide hybrid electrodes for electrochemical supercapacitors. *Nat Nano* **2011**, 6, 232-236.

[57] Zhang, H.; Yu, X.; Braun, P. V., Three-dimensional bicontinuous ultrafast-charge and -discharge bulk battery electrodes. *Nat Nano* **2011**, 6, 277-281.

[58]. Wang, H.-Q.; Li, Z.-S.; Huang, Y.-G.; Li, Q.-Y.; Wang, X.-Y., A novel hybrid supercapacitor based on spherical activated carbon and spherical MnO_2 in a non-aqueous electrolyte. *Journal of Materials Chemistry* 20, (19).

[59] Kawaoka, H.; Hibino, M.; Zhou, H.; Honma, I., Enhancement of Specific Capacity of Manganese Oxide/Carbon Composite Synthesized by Sonochemical Method. *Electrochemical and Solid-State Letters* **2005,** 8, (5), A253-A255.

[60] Chen, S.; Zhu, J.; Wu, X.; Han, Q.; Wang, X., Graphene Oxide−MnO_2 Nanocomposites for Supercapacitors. *ACS Nano* 4, (5), 2822-2830.

[61] Yan, J.; Fan, Z.; Wei, T.; Qian, W.; Zhang, M.; Wei, F., Fast and reversible surface redox reaction of graphene-MnO_2 composites as supercapacitor electrodes. *Carbon* 48, (13), 3825-3833.

[62] Ma, S.-B.; Nam, K.-W.; Yoon, W.-S.; Yang, X.-Q.; Ahn, K.-Y.; Oh, K.-H.; Kim, K.-B., Electrochemical properties of manganese oxide coated onto carbon nanotubes for energy-storage applications. *Journal of Power Sources* **2008,** 178, (1), 483-489.

[63] Bordjiba, T.; Belanger, D., Direct Redox Deposition of Manganese Oxide on Multiscaled Carbon Nanotube/Microfiber Carbon Electrode for Electrochemical Capacitor. *Journal of The Electrochemical Society* **2009,** 156, (5), A378-A384.

[64] Paek, S.-M.; Yoo, E.; Honma, I., Enhanced Cyclic Performance and Lithium Storage Capacity of SnO_2/Graphene Nanoporous Electrodes with Three-Dimensionally Delaminated Flexible Structure. *Nano Letters* **2008,** 9, (1), 72-75.

[65] Zhang, H.-X.; Feng, C.; Zhai, Y.-C.; Jiang, K.-L.; Li, Q.-Q.; Fan, S.-S., Cross-Stacked Carbon Nanotube Sheets Uniformly Loaded with SnO_2 Nanoparticles: A Novel Binder-Free and High-Capacity Anode Material for Lithium-Ion Batteries. *Advanced Materials* **2009,** 21, (22), 2299-2304.

[66] Ko, J. M.; Kim, K. M., Electrochemical properties of MnO_2/activated carbon nanotube

composite as an electrode material for supercapacitor. *Materials Chemistry and Physics* **2009,** 114, (2–3), 837-841.

[67] Wang, Y.; Zhitomirsky, I., Electrophoretic Deposition of Manganese Dioxide-Multiwalled Carbon Nanotube Composites for Electrochemical Supercapacitors. *Langmuir* **2009**, 25 (17), 9684-9689.

[68] Nam, K.-W.; Lee, C.-W.; Yang, X.-Q.; Cho, B. W.; Yoon, W.-S.; Kim, K.-B., Electrodeposited manganese oxides on three-dimensional carbon nanotube substrate: Supercapacitive behaviour in aqueous and organic electrolytes. *Journal of Power Sources* **2009,** 188, (1), 323-331.

[69] Zhang, H.; Cao, G.; Wang, Z.; Yang, Y.; Shi, Z.; Gu, Z., Growth of Manganese Oxide Nanoflowers on Vertically-Aligned Carbon Nanotube Arrays for High-Rate Electrochemical Capacitive Energy Storage. *Nano Letters* **2008,** 8, (9), 2664-2668.

[70] Fischer, A. E.; Pettigrew, K. A.; Rolison, D. R.; Stroud, R. M.; Long, J. W., Incorporation of Homogeneous, Nanoscale MnO_2 within Ultraporous Carbon Structures via Self-Limiting Electroless Deposition: Implications for Electrochemical Capacitors. *Nano Letters* **2007,** 7, (2), 281-286.

[71] Li, L.; Qin, Z.-Y.; Wang, L.-F.; Liu, H.-J.; Zhu, M.-F., Anchoring alpha-manganese oxide

nanocrystallites on multi-walled carbon nanotubes as electrode materials for supercapacitor. *Journal of Nanoparticle Research* **2010**, 12, (7), 2349-2353.

[72] Wang, H.; Cui, L.-F.; Yang, Y.; Sanchez Casalongue, H.; Robinson, J. T.; Liang, Y.; Cui, Y.; Dai, H., Mn_3O_4–Graphene Hybrid as a High-Capacity Anode Material for Lithium Ion Batteries. *Journal of the American Chemical Society* **2010**, 132, (40), 13978-13980.

[73] Ji, L.; Tan, Z.; Kuykendall, T.; An, E. J.; Fu, Y.; Battaglia, V.; Zhang, Y., Multilayer nanoassembly of Sn-nanopillar arrays sandwiched between graphene layers for high-capacity lithium storage. *Energy & Environmental Science* **2011**, 4, (9), 3611-3616.

[74] Wang, J.-Z.; Zhong, C.; Wexler, D.; Idris, N. H.; Wang, Z.-X.; Chen, L.-Q.; Liu, H.-K., Graphene-Encapsulated Fe_3O_4 Nanoparticles with 3D Laminated Structure as Superior Anode in Lithium Ion Batteries. *Chemistry – A European Journal* **2011**, 17, (2), 661-667.

[75] Wang, B.; Wu, X.-L.; Shu, C.-Y.; Guo, Y.-G.; Wang, C.-R., Synthesis of CuO/graphene nanocomposite as a high-performance anode material for lithium-ion batteries. *Journal of Materials Chemistry* **2010**, 20, 10661-10664.

[76] Cabana, J.; Monconduit, L.; Larcher, D.; Palac ń, M. R., Beyond Intercalation-Based Li-Ion Batteries: The State of the Art and Challenges of Electrode Materials Reacting Through Conversion Reactions. *Advanced Materials* **2010**, 22, (35), E170-E192.

[77]Zhou, W.; Liu, J.; Chen, T.; Tan, K. S.; Jia, X.; Luo, Z.; Cong, C.; Yang, H.; Li, C. M.; Yu, T., Fabrication of Co_3O_4-reduced graphene oxide scrolls for high-performance supercapacitor electrodes. *Physical Chemistry Chemical Physics* **2011**, 13 (32), 14462-14465.

[78]Wang, H.; Liang, Y.; Mirfakhrai, T.; Chen, Z.; Casalongue, H.; Dai, H., Advanced asymmetrical supercapacitors based on graphene hybrid materials. *Nano Research* **2011**, 4, (8), 729-736.

[79]Kim, I.-H.; Kim, J.-H.; Lee, Y.-H.; Kim, K.-B., Synthesis and Characterization of Electrochemically Prepared Ruthenium Oxide on Carbon Nanotube Film Substrate for Supercapacitor Applications. *Journal of The Electrochemical Society* **2005,** 152, (11), A2170-A2178.

Chapter 2: Hierarchically Porous Graphitized Carbon Particles for Organic Electrolyte Supercapacitors

1. Introduction

Supercapacitors, a class of electrical-energy-storage devices with high power density (10^3-10^4 W kg^{-1}) and long cycling life (>100,000 cycles), hold great promise for a broad spectrum of applications, such as hybrid electric vehicles, power tools and mobile electronic devices.[1,2] However, current supercapacitors are still limited by low energy density; improving the energy density while maintaining high power density is essential to realize such great potentials. Since supercapacitors generally rely on electrical double-layer capacitance or pseudocapacitance, to realize high energy density requires sufficient number of ions to be absorbed on or inserted into the electrodes, while realizing high power density requires rapid transport of ions and electrons between the electrodes. To satisfy these criteria, the electrode materials should exhibit high ion-storage density, excellent electronic conductivity, and effective ion-transport capability.

The current electrode materials for supercapacitors are mainly activated carbons, carbon nanotubes (CNTs) and metal oxides. In this context, activated carbons possess high surface area, high microporosity and moderate electronic conductivity. Capacitances up to 300 F g^{-1} in aqueous electrolyte or 120 F g^{-1} in organic electrolyte may be achieved at low discharge

rates, which correspond to energy densities of ~10 and 30 Wh kg^{-1}, respectively. At high discharge rates, however, their storage performance radically deteriorates due to the lagged ion transport within their torturous microporous channels.[3] Carbon nanotubes (CNTs), on the other hand, possess excellent electronic conductivity and readily accessible external surfaces that can provide outstanding rate performance. However, CNTs generally possess low surface areas, which provide low specific capacitances of less than 100 F g^{-1} in aqueous electrolyte or 50 F g^{-1} in organic electrolyte, respectively.[4-7] Alternatively, metal oxides, such as RuO_2,[8] MnO_2[9] and V_2O_5[10] may provide much higher pseudocapacitance through faradic reactions. Except the cost-prohibitive RuO_2, however, such materials are intrinsically poor ionic and electronic conductors, which limit their high-power application. Much effort has been devoted to making better electrode materials recently. For example, high-surface-area carbons with more regulated pore channels, such as carbide-derived carbon and zeolite-templated carbon, were synthesized with capacitances up to 150 F g^{-1} and improved high-rate performance in organic electrolytes,[11-13] however, their synthesis is extremely ineffective. Similarly, surface functionalized CNTs may provide capacitances up to ~150 F g^{-1} in H_2SO_4,[14] however, such modified CNTs are easily degraded during cycling. Up to now, making high-performance supercapacitor materials remains challenging.

Herein, we report the design and fabrication of high-performance supercapacitors based on hierarchically porous graphite particles. As illustrated in **Figure 2.1**, our supercapacitor electrodes are constructed from such particles containing interconnected micro-, meso- and macro- pores. In comparison to the activated carbons with low rate capability, and CNTs with low capacitance, this unique structure provides the critical features required for high-performance electrodes: i) abundant micropores and small mesopores provide the electrode with high surface areas, resulting in large capacitance and high energy density, ii) small particle size and their hierarchically interconnected mesopores and macropores facilitate ion transport, which ensure high rate capability;[15,16] iii) graphitized carbon provides excellent electronic conductivity that is another key factor for high rate capability; iv) these carbon spheres can be densely packed into electrodes, which is of importance to ensure high volumetric energy density.

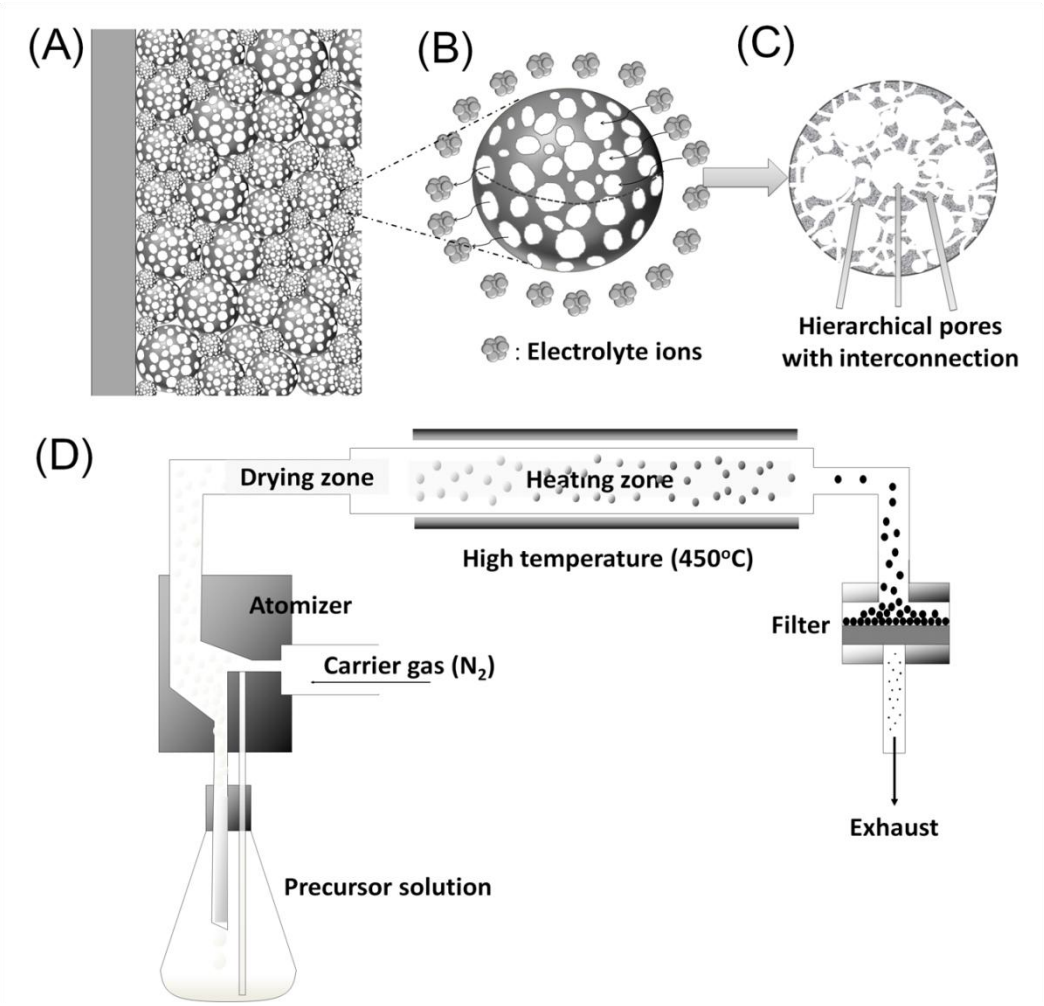

Figure 2.1 Schematic of an electrode based on porous graphitized particles and their synthesis: (A) An electrode made of densely packed carbon particles, (B) schematic of a hierarchically porous carbon particle enabling effective transport of electrolyte ions. (C) cross-view of the carbon particles showing interconnected hierarchical porous structure, and (D) an aerosol process used to synthesize the carbon particles.

2. Results and Discussion

The synthesis of such particles is based on a simple aerosol process.[17] As illustrated in **Figure 2.1**, we started with aqueous solutions containing sucrose, nickel nitrate, colloidal silica particles (template for the mesopores) and silicate clusters (template for the micropores and small mesopores); an atomization process using nitrogen as the carrier gas continuously generated aerosol droplets, which were passed through a heating zone and converted to nanocomposite particles. Subsequent carbonization in the presence of the nickel moieties *in-situ* converted the sucrose into graphitized carbon. Further removal of the templates resulted in graphitized, porous carbon particles with high surface area and hierarchical pores. It is important to point out that such a continuous synthesis approach can be suitable for scale-up.

Figure 2.2 shows the representative scanning electron microscope (SEM) and transmission electron microscope (TEM) images of the aerosol-carbon particles. It is shown in **Figure 2.2**A that most of the particles are densely packed. As the pressed pellets reached a density as high as 0.75 g cm^{-3}, which is much higher than that of commercial activated carbon with similar porosity (~0.5 g cm^{-3}) and CNT we used for this study (0.56 g cm^{-3}). For device applications, in order to increase overall device capacitance, it is generally

necessary to increase electrode porosity, which inevitably reduces the electrode density.[18] Therefore, a high gravimetric capacitance is often achieved by compromising rate capability and volumetric capacitance. The capability to synthesize high-surface-area carbon with high packing density is therefore essential to ensure both high gravimetric and volumetric densities.

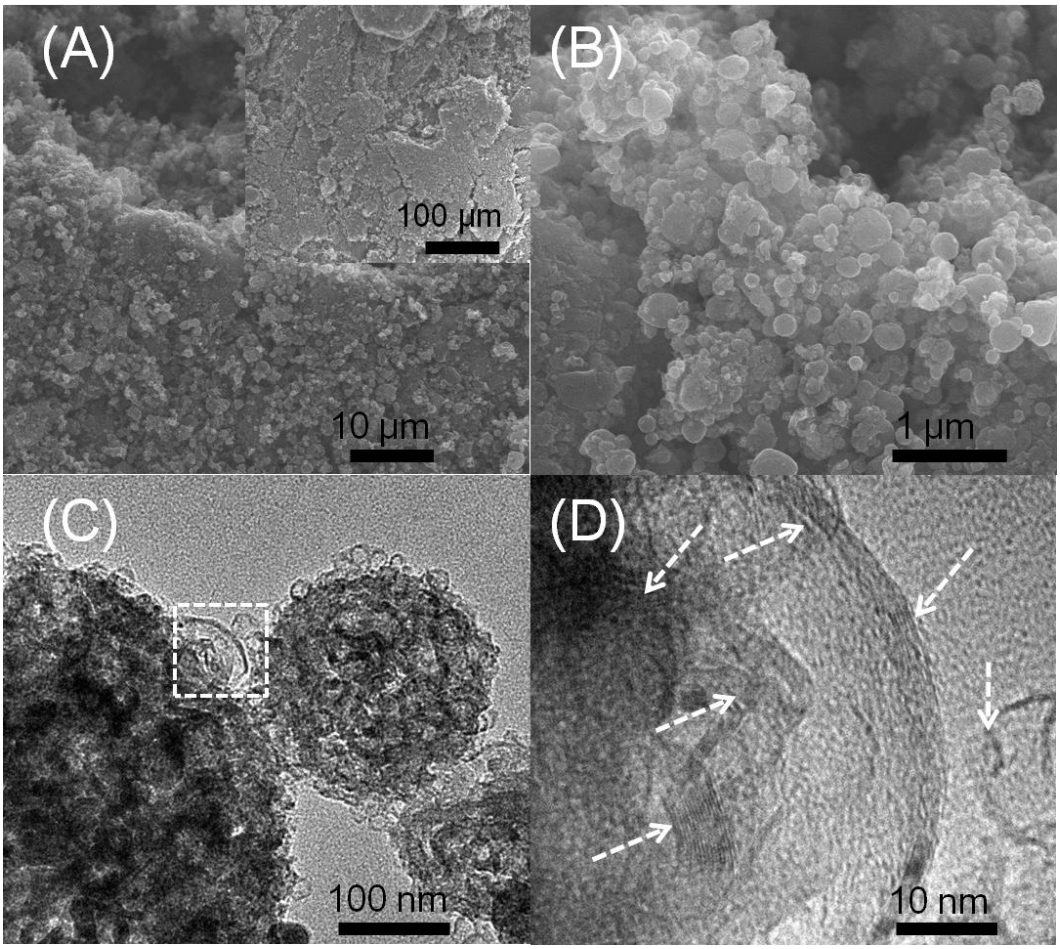

Figure 2.2 SEM and TEM images of the hierarchically porous aerosol-carbon particles: A) a low-magnification SEM image showing densely packed particles,

(B) a high-magnification SEM image showing spherical morphology with diameter ranging from 50 to 300 nm, (C) a TEM image of the hierarchically porous aerosol-carbon particles, (D) high-magnification TEM showing the graphitized carbon structure.

High-magnification SEM shows that these particles are polydisperse with diameters ranging from 50 to 300 nm (Figure 1B), which are much smaller than that of activated carbon normally used in commercial devices (5-20 μm). TEM image (Figure 1C) reveals a highly porous sponge- or foam-like pore structure with interconnected mesopores and micropores. The diameters of the mesopores are around 10-20 nm, which is consistent with the size of the colloidal silica template used (average diameter of 13 nm). The formation of micropores and small mesopores below 3 nm in diameter is due to the removal of silica clusters that were uniformly distributed within the carbon framework.[19] High-resolution TEM (Figure 1D) image suggests that the "bubbles" observed in **Figure 2.2**C are graphite shells formed by the catalytic carbonization of sucrose.[20] The formation of such graphite shells, which improve the electrode conductivity, is further confirmed by their appreciable (002) graphite x-ray diffraction peak (**Figure 2.3**).

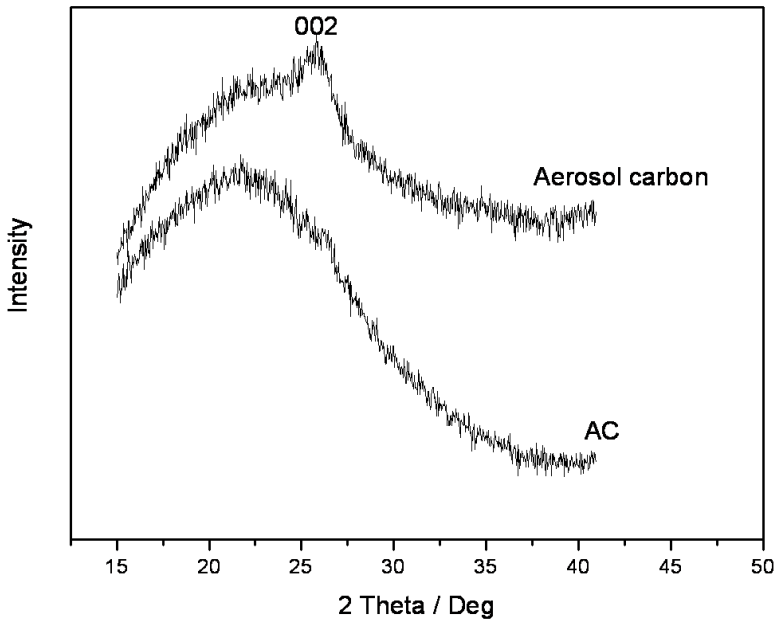

Figure 2.3 XRD patterns of aerosol-carbon and AC.

Pore structure of the aerosol-carbon particles was investigated using nitrogen sorption experiments. **Figure 2.4** shows nitrogen sorption isotherms and pore size distributions of the particles, which clearly suggest the coexistence of micropores and mesopores. The first nitrogen-uptake step, at a relative pressure below 0.2, is contributed by the micropores mainly templated from silica clusters. The second nitrogen-uptake step, at a relative pressure between 0.6 and 0.9, is attributed to the mesopores templated from colloidal silica particles. These mesopores are narrowly distributed and centred at 11 nm, which is consistent with the size of the colloidal silica template. These particles exhibit a high pore volume of 2.02 cm^3 g^{-1} and Brunauer–Emmett–Teller (BET) surface area of 1522 m^2 g^{-1}, of which ~80% (1208

m^2 g^{-1}) is contributed by external surface, as calculated from the *t*-plot method. To better understand how such pore structure affects energy storage performance, commercial activated carbon (AC) and multi-walled CNTs were also studied for comparison. As shown in **Figure 2.4**, the AC shows typical type I isotherms with uptake at low relative pressure, suggesting a microporous structure (pore diameter < 2 nm) with an extremely high surface area of 2549 m^2 g^{-1} of which ~64 % (1627 m^2 g^{-1}) is contributed by the external surface. As expected, the CNTs have quite limited surface area (156 m^2 g^{-1}) with some mesoporous structure resulting from stacking of the nanotubes. The external surface area (123 m^2 g^{-1}) accounts for ~79% of the total CNTs surface area.

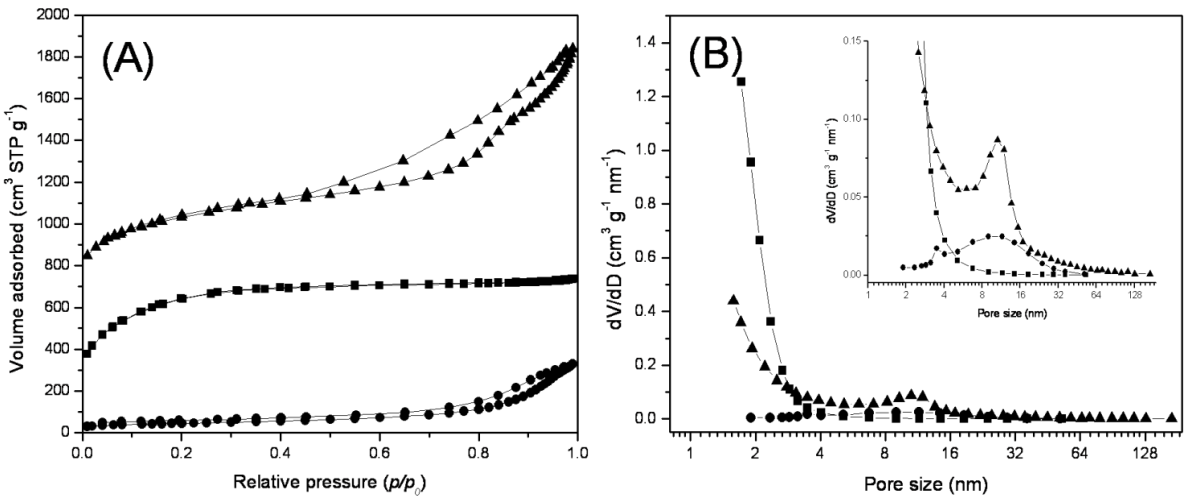

Figure 2.4 Nitrogen sorption isotherms (A) and pore size distributions (B) of the hierarchically porous aerosol-carbon particles (▲), AC (■) and CNTs (●).

This unique hierarchical pore structure endows the particles with outstanding capacitive performance. **Figure 2.5** compares cyclic voltammetry (CV) plots of the aerosol-carbon particles, AC and CNT electrodes at potential sweep rates of 5 (**Figure 2.5A**) and 50 mV s^{-1} (**Figure 2.5B**) in three-electrode cells using platinum foil as the counter electrode, silver wire as the quasi-reference electrode[21] and 1 M NEt_4BF_4 in propylene carbonate (PC) as the electrolyte. At a potential sweep rate of 5 mV s^{-1}, all CV curves show typical capacitive behavior, as evidenced by their nearly rectangular voltammograms. For AC electrode, the CV plot is fully developed at positive polarization, which is associated with solvated BF_4^- (1.35 nm) adsorption. The CV plot shows obvious distortion at negative polarization, though, which is associated with adsorption of solvated NEt_4^+ (1.40 nm). Generally, commercial activated carbons have abundantly irregular micropores and small mesopores in the range of 0.3-4 nm with narrow bottlenecks that limit ion transport and adsorption. In addition, at sweep rates as low as 5 mV s^{-1}, ohmic drop across the electrode is not significant. Therefore, such an asymmetric CV characteristic could be attributable to a micropore-size effect on electrode kinetics, which has been recently confirmed on carbide-derived carbons in the same electrolyte system.[21] When potential sweep rates reach 50 mV s^{-1} (**Figure 2.5B**), CV plots of the AC electrode distort dramatically over the whole potential range. Such

behavior can be ascribed to both the increased ohmic drop and the limited ion transport within their tortuous pore structure.

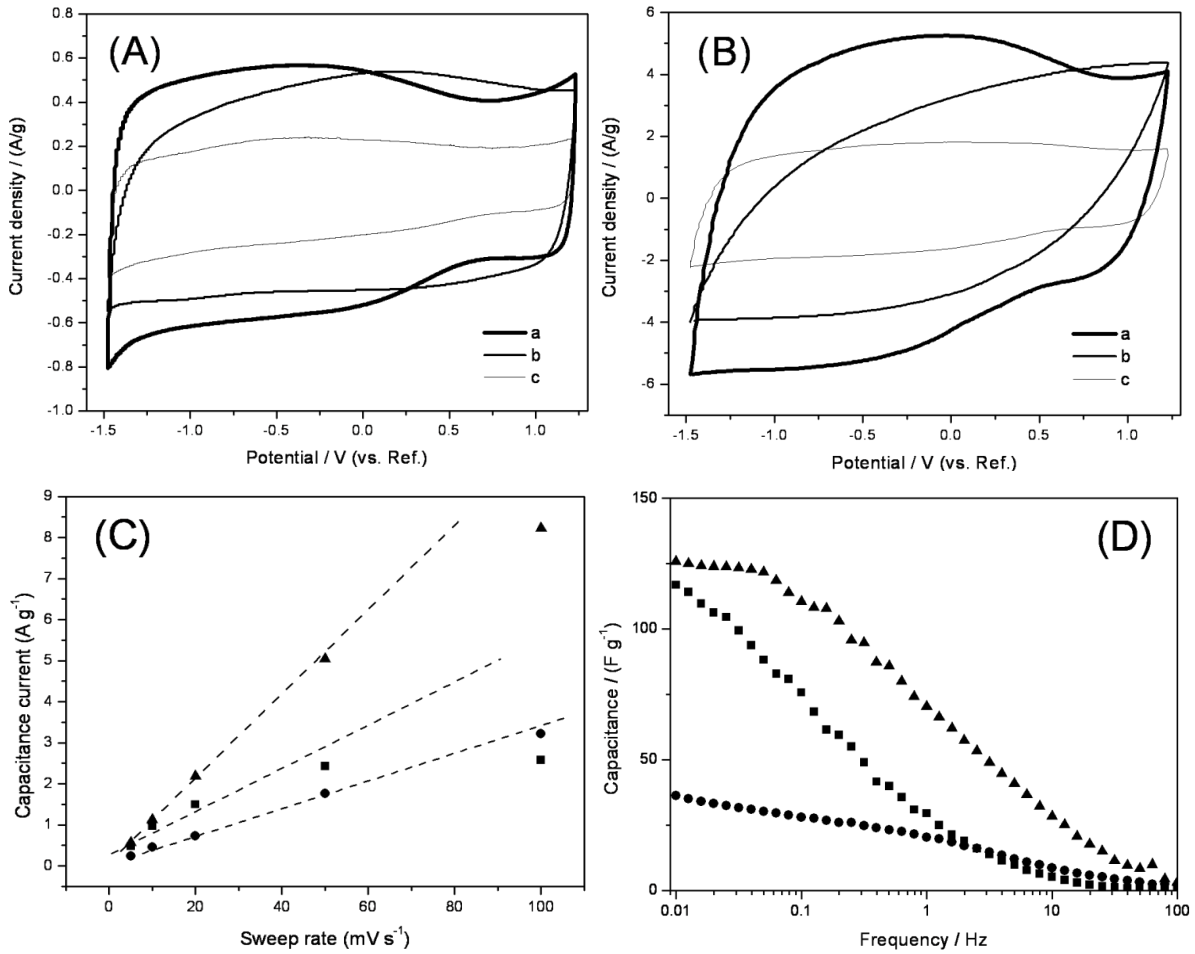

Figure 2.5. Cyclic voltammograms of various carbon electrodes at scan rate of (A) 5 mV s^{-1} and (B) 50 mV s^{-1} (a: aerosol-carbon particle; b: AC; c: CNTs); (C) capacitance current dependence on potential sweep rates at potential of -0.4 V (*vs*. Ref.): and capacitance-frequency dependence of the aerosol-carbon particles (▲), AC (■) and CNTs (●).

By comparison, at both potential sweep rates, the CV plots of the aerosol-carbon- and CNT- based electrodes show symmetric characteristics at both positive and negative polarizations, suggesting facile ion transport and adsorption behavior. Although there are broad humps at potentials below 0.5 V on the CV curves of the aerosol-carbon electrodes, the charge and discharge processes are defined to not be limited by any kinetics issue since the voltammetric response is very fast. **Figure 2.5**C shows the voltammetric current (i.e., the current value at potential of -0.4 V) dependence on potential sweep rate. Unlike the AC electrodes, a perfect linear plot can be seen at sweep rates ranging from 5 to 50 mV s^{-1} for the aerosol-carbon electrodes, confirming that their currents are purely capacitive in nature. Note that, due to the large ohmic drop, the current response at high sweep rate of 100 mV s^{-1} is nonlinear. This phenomenon was not observed for CNT electrodes due to their better conductivity and lower porosity. For both the aerosol-carbon and CNT electrodes, only limited distortion of CV curves can be observed when the sweep rate increases to 100 mV s^{-1} (**Figure 2.6**), demonstrating very high rate-capability. We attribute this excellent capacitive performance to facile ion transport in their open pore structures and good electrode conductivity.

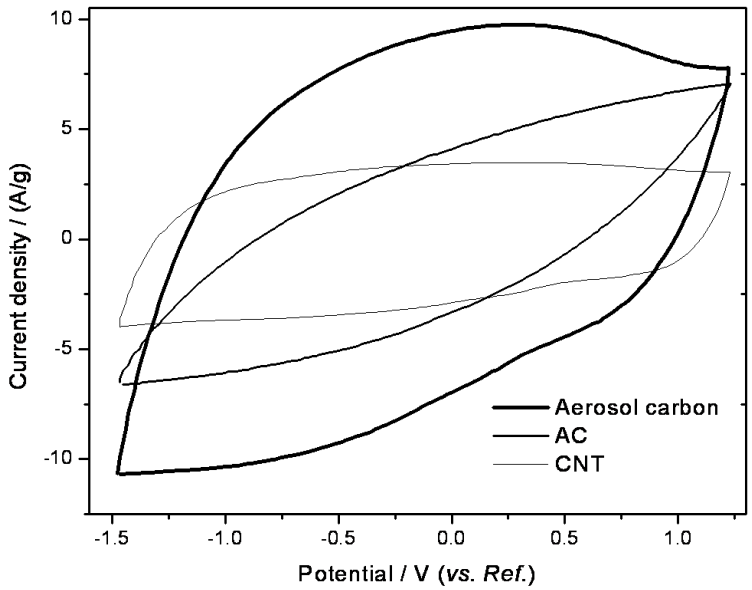

Figure 2.6. Cyclic voltammograms of various carbon electrodes at scan rate of 100 mV s^{-1}.

The facilitated ion-transport kinetics within hierarchical pore channels was further studied by electrochemical impedance spectroscopy (EIS). **Figure 2.5**D compares capacitance dependence on frequency (10 mHz to 100 kHz) of each electrode. Clearly, the capacitance gradually decreases with increasing frequency, which is a common feature for porous carbon electrodes. The CNT electrodes exhibit slow capacitance drops due to fast ion transport and adsorption on their surface. Similarly, because of their open pore structure, the capacitance of aerosol-carbon electrodes approaches saturation at frequencies close to 0.1 Hz, meaning that their ion-adsorption can reach equilibrium in 10 s. By comparison, the AC electrodes show no sign of saturation at frequencies as low as 0.001 Hz, indicating slow

electrolyte ions diffusion within their tortuous pore structure. Also, aerosol-carbon electrodes retain over 60% of their maximum capacitance at a frequency of 1 Hz, about three times higher than that of AC electrodes. This result further confirms the importance of creating easy ion-transport pathways in pursuit of high-rate supercapacitor electrodes.

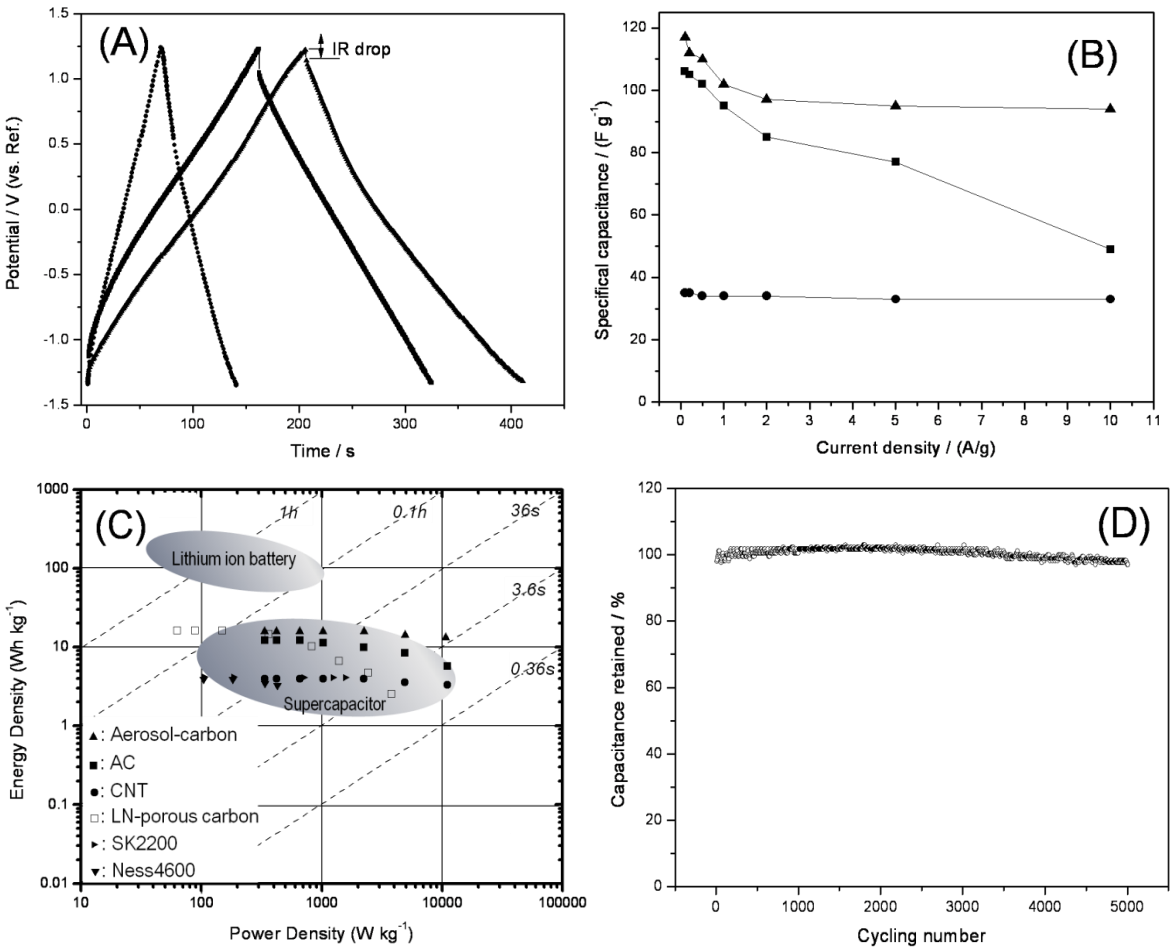

Figure 2.7. Constant current charge/discharge curves of different electrodes at current density of 1 A g^{-1} (A)**,** specific capacitance as a function of current density (B) and Ragone plots of

various carbon electrodes (C) (aerosol-carbon particles: ▲; AC: ■; CNTs: ●; LN-porous carbon: □; SK2200: ►; Ness4600: ▼), and long-term cycling performance of symmetric supercapacitor made from aerosol carbon particles (D).

To further quantify their specific capacitances, galvanostatic charge/discharge tests were performed, and specific capacitances C_s (F g^{-1}) were calculated from the discharge curves of galvanostatic profiles. For example, as shown in **Figure 2.7A**, at a current density of 1 A g^{-1} the CNT-, AC- and aerosol-carbon- based electrodes show capacitances of 34, 95, and 102 F g^{-1}, respectively. The aerosol-carbon electrodes display a more pronounced ohmic loss (*IR* drop) than the CNTs electrodes, but the *IR* drop is much less than that of the AC electrodes. Calculated from the *IR* drop, the maximum power density of the aerosol-carbon electrodes (55 kW kg^{-1}) reach ~70% of the CNT electrode (78 kW kg^{-1}), which is 2.2 times that of the AC electrodes (25 kW kg^{-1}). Different current densities from 0.1 to 10 A g^{-1} were used to further investigate the rate capability (**Figure 2.7B**). The CNT electrodes keep ~95 % of its initial C_s (35 F g^{-1}) as current density increase from 0.1 to 10 A g^{-1}. Although showing a much higher C_s of 106 F g^{-1} at current density of 0.1 A g^{-1}, the AC electrodes have only 45 % capacitance retention (50 F g^{-1}) at 10 A g^{-1}. By comparison, the aerosol-carbon electrodes

show a high C_s of 115 F g^{-1} at a current density of 0.1 A g^{-1}, and retain 83 % of this capacitance (95 F g^{-1}) at 10 A g^{-1}, displaying excellent high-rate performance. Such capacitive performance is superior to the pore-opened single-walled CNTs with surface area of 2200 m^2 g^{-1}[22] and chemically modified graphene with surface area of 705 m^2 g^{-1}.[23] Note that recent carbide-derived carbon exhibits somewhat greater capacitances in acetonitrile, which has lower viscosity and 5 times higher ionic conductivity than PC and is an electrolyte solvent generally known to lead to higher capacitance.[22]

Consistent with electrochemical studies, these hierarchical aerosol-carbon particles exhibit outstanding device performance. In this work, symmetric supercapacitors were assembled to evaluate energy and power performance. The AC supercapacitor possesses a gravimetric energy density of 27 Wh kg^{-1} at a power output of 270 W kg^{-1} when only considering the mass of electrode active materials, however, its energy density drops to 12 Wh kg^{-1} at a power density of 20 kW kg^{-1}. The CNT supercapacitor shows good rate capability but low energy density due to its low capacitance. In comparison, the aerosol-carbon supercapacitor reaches a gravimetric energy density of 30 Wh kg^{-1} at a power density of 270 W kg^{-1}, or 24 Wh kg^{-1} at 25 kW kg^{-1}. If considering the material density, our

aerosol-carbon has a maximum volumetric energy density of 22.5 Wh L^{-1} which is about 2 times of that of AC (13.5 Wh L^{-1}). It still has 18 Wh L^{-1} at 18.8 kW L^{-1}, even significantly higher than AC (6 Wh L^{-1} at 10 kW L^{-1}). For better comparison, all the energy and power density are normalized to the mass of whole device using a packaging factor of 0.4.[24] **Figure 2.7**C shows the Ragone plot, which displays the energy density dependence on the power output of various symmetric supercapacitors. The aerosol-carbon supercapacitor shows superior performance to other devices. In particular, at 4 s of charge/discharge, the energy density of the aerosol-carbon supercapacitor is about 2 and 3 times higher than that of the AC and CNT supercapacitors, respectively. Compared with the state-of-the-art supercapacitors, our aerosol-carbon-based devices outperform many other prototypes and commercial devices as well, including those based on ACs, pore-opened CNTs,[22] LN-porous carbon,[25] SK2200,[26] and Ness4600.[26] Besides their high energy and high power performance, aerosol-carbon supercapacitors exhibit outstanding cycling stability. **Figure 2.7**D shows the results of long-term cycling tests at a current density of 2 A g^{-1}, suggesting capacitance retention of ~98% after 5000 cycles of charge and discharge.

3. Conclusion

In summary, we have synthesized a class of graphitized porous carbon particles using a continuous, scalable approach. Such carbons contain hierarchical pore structure and graphitized shells, providing a new material platform for high-performance supercapacitors with high packing density. This new family of porous carbons could also be adapted for battery electrodes, fuel-cell catalyst supports and other applications.

4. Experimental Section

4.1 Synthesis of porous graphitized carbon nanoparticles

For the synthesis of the graphitized carbon particles, aqueous solutions containing de-ionized water (40 mL), sucrose (12 g), nickel (II) nitrate hexahydrate (10 g), HCl (20 g, 0.1 M) and silicate templates including colloidal silica (20 g) (AS 30%, Nissan Chemicals. Inc.) and of TEOS (16 g) were sent through an atomizer using nitrogen as carrier gas. The atomizer dispersed the solution into aerosol droplets, which were then passed through a ceramic tube that was heated to 450 °C. Continuous solvent evaporation at the air/liquid interface of the aerosol droplets enriched the sucrose and silica, resulting in the formation of spherical silica/sucrose/nickel moiety nanocomposite particles. The particles were then collected on a membrane filter in a press, and subsequent carbonization to 900 °C of the

composite nanoparticles under N_2 atmosphere resulted in the formation of spherical silica/carbon/nickel composite nanoparticles. 1 M HCl and 5 M NaOH were used in sequence to remove the nickel and silica respectively, which produced the porous carbon particles with graphitized shell structures.

4.2. AC and CNTs

Commercially available activated carbon (Yihuan Carbon Co., Ltd. Fuzhou, China) after vacuum-dry was used for comparison. Multi-walled CNTs were synthesized using a catalytic chemical vapor deposition in a nano-agglomerate fluidized bed.[27] Before electrode fabrication, CNTs were functionalized by attaching carboxylic groups on the surface using a method similar to that developed by Gao and co-workers.[28]

4.3 Characterization

Nitrogen sorption isotherms were measured at 77 K with a Micromeritics ASAP 2020 analyzer (Micromeritics Instrument Corporation, Norcross, GA). Specific surface areas (S_{BET}) were calculated by the Brunauer-Emmett-Teller (BET) method using the adsorption branch in a relative pressure range from 0.04 to 0.25. Scanning electron microscopy (SEM)

experiments were conducted on a JEOL JSM-6700 FE-SEM (JEOL Ltd., Japan). Transmission electron microscopy (TEM) experiments were conducted on a Philips CM120 operated at 120 kV (Philips/FEI Inc., Eindhoven, The Netherlands).

4.4 Electrode Fabrication and Electrochemical Measurements

The aerosol-carbon particles, AC and CNTs were assembled onto nickel foam current collectors. Briefly, 85% of the electrochemically active material, 5% carbon black, and 10% poly(vinylidene fluoride) (PVDF) dispersed in N-methylpyrrolidinone (NMP) were mixed to form slurries. The homogenous slurries were coated on nickel foam substrates and dried at 80 ^{o}C for 10 min under vacuum. As-formed electrodes were then pressed at a pressure of 2 MPa and further dried under vacuum at 100 ^{o}C for another 12 h. Electrodes were obtained by coating an active mass of 1~3 mg on each current collector (0.5 cm * 0.5 cm).

The electrochemical measurements were carried out on a Solartron 1860/1287 Electrochemical Interface (Solartron Analytical, Oak Ridge, TN). The electrolyte solution was a 1 M tetraethylammonium tetrafluoroborate (NEt_4BF_4) in propylene carbonate (PC) solution and platinum foil was used as the counter electrode. Silver wire was used as a quasi-reference electrode. CV measurements were carried out in an argon-filled glove box

using cutoff voltages of -1.5 and 1.2 V versus Ag. The specific capacitance, C_s (F g^{-1}) of the electrode materials was calculated from the discharge curve of galvanostatic cycles, according to $C = I/(dV/dt) \approx I/(\Delta V/\Delta t)$, where I is the constant discharge current density, E is the cell voltage, and dV/dt is the slope of the discharge curve. The EIS tests were operated in the frequency range of 10 mHz – 100 kHz with 10 mV AC amplitude. The gravimetric capacitance, C was also calculated according to $C= 1/[2\pi f \text{ Im(Z)M}]$, where f is the operating frequency (Hz), Im(Z) is the imaginary part of the electrode resistance (ohm), and M (g) is the mass of electrode.

To make 2032 type coin cells, glass fiber (GF/D) from Whatman was used as a separator. The cells were assembled in a glovebox under an argon atmosphere. Charge and discharge measurements and long-term cycling tests were carried out by LAND CT2000 (Wuhan Jinnuo Electronics, Ltd., Wuhan, China) at different current densities. Symmetric cells were charged and discharged between 2.7 and 0 V. The specific capacitance, and power and energy density were calculated based on the total mass or volume of anode and cathode materials. Energy density was calculated using $E=1/2\ CV^2$, where C is the total cell capacitance and V is the cell operation potential. The maximum power density was calculated by $P_{max}= V^2/(4ESR*M)$, where ESR is the equivalent series resistance and M (g) is

the total mass of anode and cathode materials.

References:

[1] P. Simon, Y. Gogotsi, *Nat. Mater.* **2008**, *7*, 845.

[2] J. R. Miller, A. F. Burke, *Electrochem. Soc. Interface* **2008**, *17*, 53.

[3] E. Frackowiak, *Phys. Chem. Chem. Phys.* **2007**, *9*, 1774.

[4] C. M. Niu, E. K. Sichel, R. Hoch, D. Moy, H. Tennent, *Appl. Phys. Lett.* **1997**, *70*, 1480.

[5] M. Kaempgen, J. Ma, G. Gruner, G. Wee, S. G. Mhaisalkar, *Appl. Phys. Lett.* **2007**, *90*, 264104.

[6] C. S. Du, N. Pan, *Nanotechnology* **2006**, *17*, 5314.

[7] M. Kaempgen, C. K. Chan, J. Ma, Y. Cui, G. Gruner, *Nano Lett.* **2009**, *9*, 1872.

[8] J. P. Zheng, P. J. Cygan, T. R. Jow, *J. Electrochem. Soc.* **1995**, *142*, 5.

[9] M. Toupin, T. Brousse, D. Belanger, *Chem. Mater.* **2002**, *14*, 3946.

[10] Z. Chen, Y. C. Qin, D. Weng, Q. F. Xiao, Y. T. Peng, X. L. Wang, H. X. Li, F. Wei, Y. F. Lu, *Adv. Funct. Mater.* **2009**, *19*, 3420.

[11] J. Chmiola, G. Yushin, Y. Gogotsi, C. Portet, P. Simon, P. L. Taberna, *Science* **2006**, *313*, 1760.

[12] Y. Korenblit, M. Rose, E. Kockrick, L. Borchardt, A. Kvit, S. Kaskel, G. Yushin, *ACS Nano* **2010**, *4*, 1337.

[13] H. Itoi, H. Nishihara, T. Kogure, T. Kyotani, *J. Am. Chem. Soc.* **2011**, *133*, 1165.

[14] S. W. Lee, B. S. Kim, S. Chen, Y. Shao-Horn, P. T. Hammond, *J. Am. Chem. Soc.* **2009**, *131*, 671.

[15] D.W. Wang, F. Li, M. Liu, G. Q. Lu, H. M. Cheng, *Angew. Chem. Int. Ed.* **2008**, *47*, 373.

[16] C. Portet, G. Yushin, Y. Gogotsi, *J. Electrochem. Soc.* **2008**, *155*, A531.

[17] J. E. Hampsey, Q. Hu, L. Rice, J. Pang, Z. Wu, Y. Lu, *Chem. Comm.* **2005**, *28*, 3606.

[18] C. Portet, M. A. Lillo-Rodenas, A. Linares-Solano, Y. Gogotsi, *Phys. Chem. Chem. Phys.* **2009**, *11*, 4943.

[19] J. B. Pang, Q. Y. Hu, Z. W. Wu, J. E. Hampsey, J. B He and Y. F. Lu, , *Microporous Mesoporous Mater.* **2004**, *74*, 6.

[20] H. S. Bengaard, J. K. Nørskov, J. Sehested, B. S. Clausen, L. P. Nielsen, A. M. Molenbroek, J. R. Rostrup-Nielsen, *J. Catal.* **2002**, *209*, 365.

[21] R. Lin, P. L. Taberna, J. Chmiola, D. Guay, Y. Gogotsi, P. Simon, *J. Electrochem. Soc.* **2009**, *156*, A7.

[22] T. Hiraoka,, A. Izadi-Najafabadi, T. Yamada, D. N. Futaba, S. Yasuda, O. Tanaike, H.Hatori, M. Yumura, S. lijima, K. Hata, *Adv. Funct. Mater.* **2010**, *20*, 422.

[23] M. D. Stoller, S. Park, Y. Zhu, J. An, R. S. Ruoff, *Nano Lett.* **2008**, *8*, 3498.

[24] Z. Chen, V. Augustyn, J. Wen, Y. Zhang, M. Shen, B. Dunn, Y. Lu, *Adv. Mater.* **2011**, *23*, 791.

[25] E. Raymundo-Piñero, M. Cadek, F. Beguin, *Adv. Funct. Mater.* **2009**, *19*, 1032.

[26] A. F. Burke, Proc. IEEE Veh. Power Propulsion Conf. (VPPC"05), **2005**, 356.

[27] F. Wei, Q. Zhang, W. Z. Qian, H. Yu, Y. Wang, G. H. Luo, G. H. Xu, D. Z. Wang, *Powder Technol*. **2008**, *183*, 10.

[28] C. Gao, C. D. Vo, Y. Z. Jin, W. W. Li, S. P. Armes, *Macromolecules* **2005**, *38*, 8634.

Chapter 3: Hierarchically Porous Graphitized Carbon Particles for aqueous Supercapacitors

1. Introduction

Supercapacitors, a class of electrical energy storage devices with high power density (10^3-10^4 W kg^{-1}) and long cycling life (>100,000 cycles), hold great promise for a broad spectrum of applications, such as hybrid electric vehicles, power tools and mobile electronic devices. However, current applications of supercapacitors are still limited by low energy density; developing better electrode materials leading to improved device energy density has been an essential but challenging topic.[1-3]

In this context, carbon materials, such as activated carbons, mesoporous carbon and carbon nanotubes, have been extensively investigated.[4-6] Activated carbons may respectively provide capacitances up to 300 F g^{-1} in aqueous electrolyte or 120 F g^{-1} in organic electrolyte at low discharge rates. However, their storage performance radically deteriorates at high discharge rates due to the lagged transport of ions within their torturous microporous channels.[7, 8] Mesoporous carbons, on the other hand, exhibit uniform pore geometry and larger pore size; however, they did not show exciting improvement in either energy or power density, possibly due to unfavourable ion transport within their long-range

pore channels.[9,10] Carbon nanotubes possess excellent electronic conductivity and readily accessible external surfaces that can provide outstanding rate performance. However, carbon nanotubes generally possess low surface areas, which provide low specific capacitances of less than 100 F g^{-1} in aqueous electrolyte or less than 50 F g^{-1} in organic electrolyte, respectively.[11-13] Recently, high-surface-area microporous carbons with regulated pore channels, such as carbide-derived carbon and zeolite-templated carbon, were synthesized with capacitances up to 150 F g^{-1} and improved high-rate performance in organic electrolytes,[8,14,15] however, their synthesis is extremely ineffective.

Recently, we developed a continuous aerosol process leading to the formation of hierarchically porous graphitized carbon particles. The synthesis of such carbon particles is quite simple and efficient.[16, 17] Briefly, the synthesis was started with an aqueous solution containing sucrose, nickel nitrate, colloidal silica particles and silicate clusters; an atomization process using nitrogen as the carrier gas continuously generated aerosol droplets, which were passed through a heating zone and converted to nanocomposite particles. Subsequent carbonization in the presence of the nickel moieties *in-situ* converted the sucrose into graphitized carbon.[18] Further removal of the templates resulted in graphitized, porous carbon particles with high surface area and hierarchical pores.

Such carbon materials exhibited impressive cycling stability in organic electrolyte and significantly improved energy and power density comparing with the commercial activated carbons and carbon nanotubes. However, the achievement of such performance relies on utilizing high-cost electrolytes and cell-fabrication process; moreover, the use of flammable solvents and electrolytes presents potential safety issues that may prevent their widespread applications. Herein, we explore the use of such hierarchically porous graphitized carbon for aqueous-electrolyte based devices. Owing to the unique structure, such as high surface area, small particle size, hierarchically porous architecture and conductive graphitic framework, such graphitized carbon material may provide large double layer area, fast ion transport and efficient charge harvesting in aqueous electrolytes. In this work, asymmetric supercapacitors with high energy density that is close to those of the organic devices were successfully fabricated, offering a new method towards cost-effective energy storage.

2. Results and Discussions

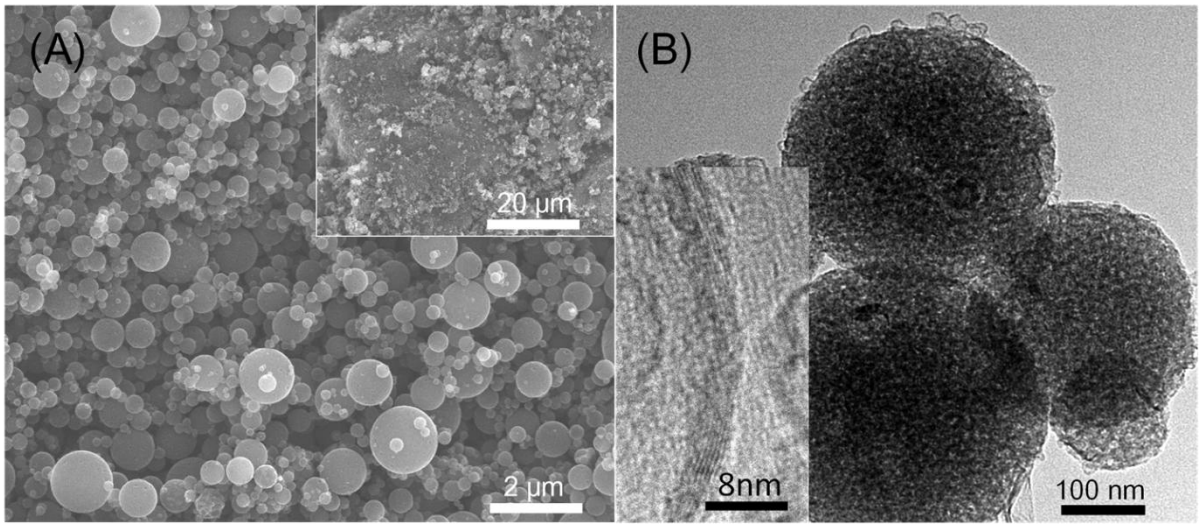

Figure 3.1. SEM and TEM images of the hierarchically porous aerosol-carbon particles.

Figure 3.1A shows representative scanning electron microscope (SEM) images of the carbon particles. Such particles are polydisperse with diameters mainly ranging from 50 to 300 nm, which are much smaller than that of activated carbon normally used in commercial supercapacitor devices (5-20 μm). Transmission electron microscope (TEM) image (**Figure 3.1B**) reveals a highly porous sponge- or foam-like pore structure with interconnected mesopores and micropores. High-resolution TEM (inset, **Figure 3.1B**) image suggests that the "bubbles" observed around each particle are graphite shells formed by the catalytic carbonization of sucrose.[18] Raman spectrum of the carbon particles clearly show two bands, at around 1345 cm^{-1} (D band) and 1583 cm^{-1} (G band), with a relatively intensity ratio (I_D/I_G) of ~2, which further confirms the existence of a large amount of graphitized carbon (**Figure**

3.2). In addition, an interconnected mesopore and micropore structure can also be observed. Nitrogen sorption isotherms and pore size distributions of the particles clearly suggest the coexistence of micropores and mesopores (**Figure 3.3**). The mesopores are narrowly distributed and centred at 11 nm, which is consistent with the size of the colloidal silica template. These particles exhibit a large pore volume of 2.02 cm^3 g^{-1} and Brunauer–Emmett–Teller (BET) surface area (S_{BET}) of 1522 m^2 g^{-1}, of which ~80% (1208 m^2 g^{-1}) is contributed by external surface, as calculated from the *t*-plot method. Such carbon architecture provides an ideal platform for fast ion transport and double layer formation, and thus is of great interest for capacitive energy storage.

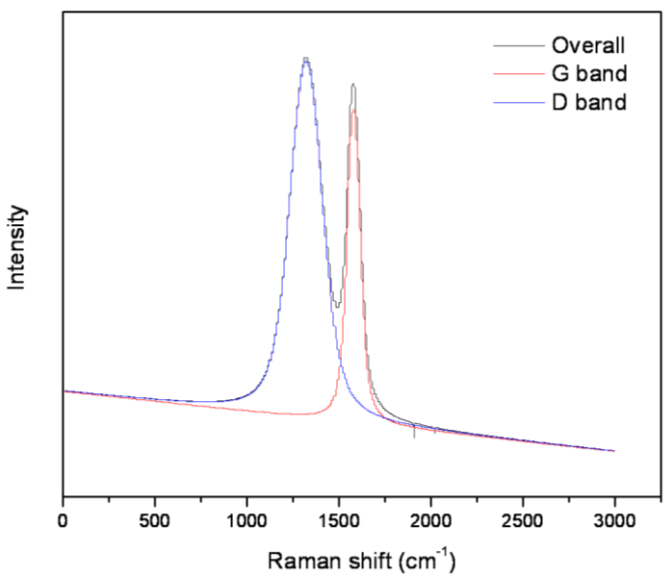

Figure 3.2. Raman spectrum of the porous graphitized carbon particles.

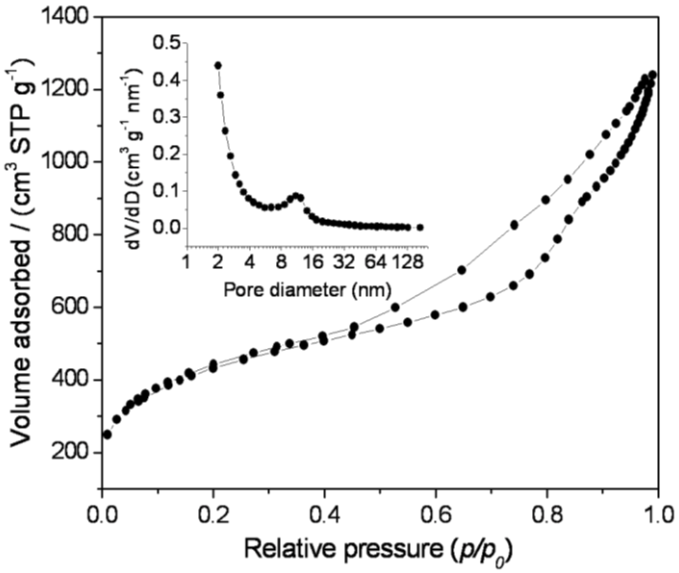

Figure 3.3. Nitrogen sorption isotherms and pore size distributions (inset) of the hierarchically porous aerosol-carbon particles.

Capacitive performance of the particles was first examined in 3 M KOH, an alkaline electrolyte commonly used for carbon-NiO-based hybrid capacitors.[19] **Figure 3.4A** shows their typical cyclic voltammetry (CV) curves at potential scan rates from 10 to 100 mV s^{-1} in a three-electrode cell using a platinum foil as the counter electrode and an Hg/HgO as the reference electrode. The cut-off potential was defined to be -0.9 and 0.1 V (vs. ref.) for stable and reversible cycling. The CV curves exhibit near-rectangular shapes even at high scan rates, suggesting a pure double-layer charge storage behavior with excellent rate-capability. The normalized specific capacitance C_s (F g^{-1}) was calculated from the discharge

curves of galvanostatic charge/discharge profiles at current densities from 0.5 to 10 A g^{-1} (**Figure 3.5**).

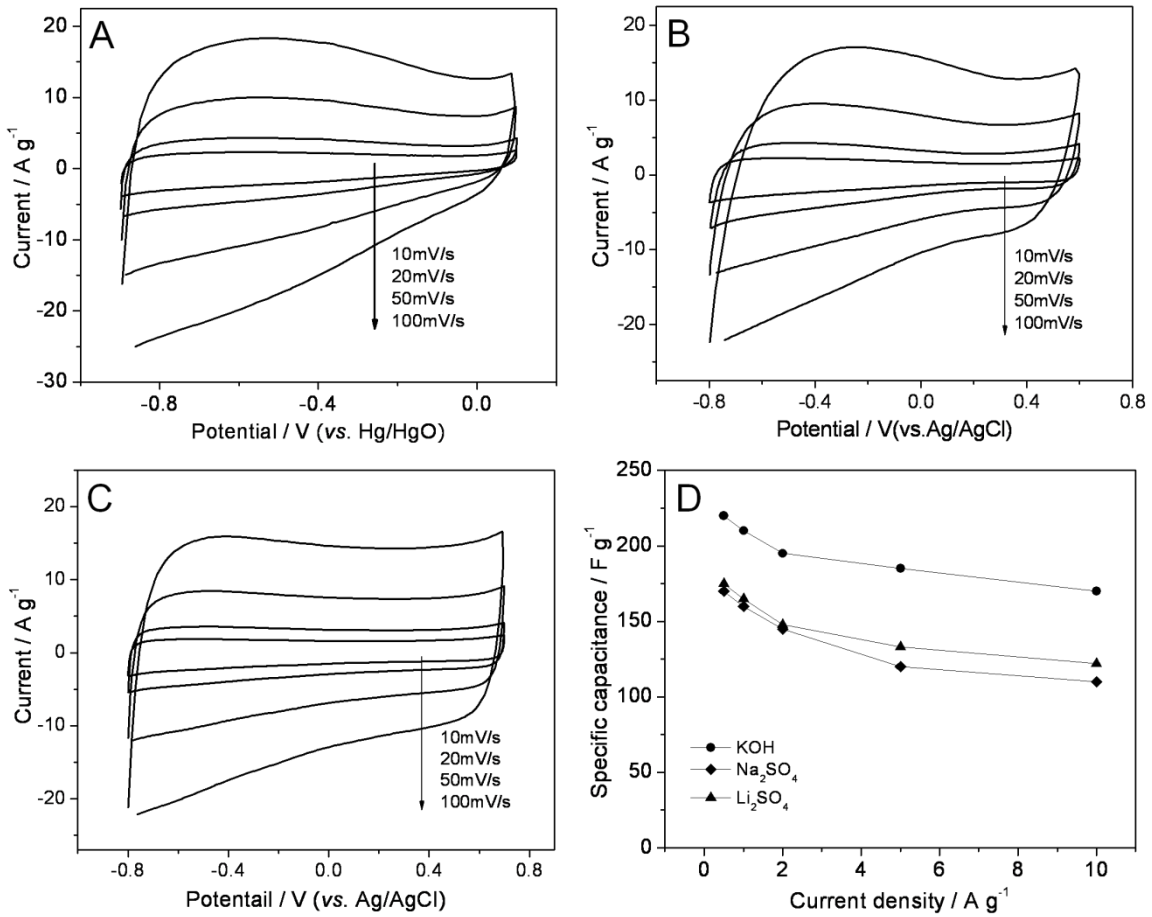

Figure 3.4. Cyclic voltammograms of aerosol carbon electrodes at potential sweep rate from 10 to 100 mV s^{-1} in 3 M KOH (A), 1 M Na_2SO_4 (B) and 1 M Li_2SO_4 (C); Dependence of specific capacitance and charge/discharge current density for aerosol carbon electrodes in different electrolytes (D).

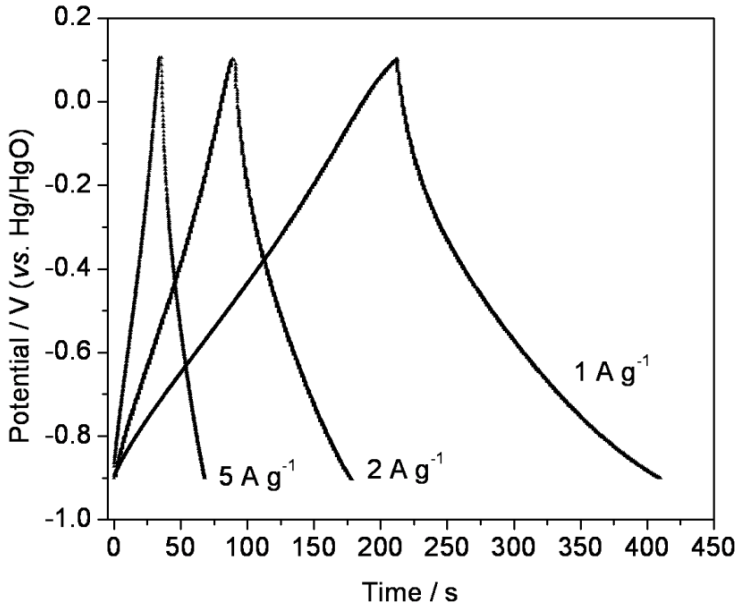

Figure 3.5. Galvanostaic charge/discharge curves of porous graphitized carbon electrodes at different current densities in 3 M KOH aqueous electrolyte.

It was found that the electrode possesses a C_s of 220 F g^{-1} at the current density of 0.5 A g^{-1} and retains about 73 % of this capacitance (160 F g^{-1}) at a high current density of 10 A g^{-1}. In comparison, a commercial activated carbon (S_{BET} = 1900 m^2 g^{-1}) shows a C_s of 250 F g^{-1} at 0.5 A g^{-1} and 105 F g^{-1} at 10 A g^{-1}, a moderate rate performance commonly observed for activated carbons.[20] In addition, in comparing with the carbon materials reported recently, such as activated hierarchical porous carbon (S_{BET} = 1660 m^2 g^{-1}, C_s = 180 F g^{-1}),[21] partially graphitic ordered mesoporous carbon (S_{BET} = 1300 m^2 g^{-1}, C_s = 155 F g^{-1}), nitrogen-enriched porous carbon (33 to 153 F g^{-1}),[22] and modified graphene (S_{BET} = 950 m^2 g^{-1}, C_s = 101 F

g^{-1}),[23] this unique carbon materials also show significantly improved performance. Such a high capacitance and high rate-capability is ascribed to the large accessible surface area and hierarchically porous structure which together provide efficient ion-adsorption and fast charge transport. Note that mesoporous carbon nanospheres (S_{BET} = 2396 m^2 g^{-1}) can provide a similar high capacitance and rate capability in a similar testing condition, however, the synthesis is extremely inefficient.[15]

Besides the alkaline electrolyte, capacitive performance of the carbon particles was also evaluated in 1 M Na_2SO_4 and 1 M Li_2SO_4 aqueous electrolytes, the electrolytes commonly used for carbon//MnO_2[24] and carbon//$LiMn_2O_4$[25] asymmetric supercapacitors. The carbon electrodes were tested in three-electrode cells using a platinum foil as the counter electrode and an Ag/AgCl as the reference electrode. Highly reversible charge and discharge behavior was also observed at a potential window from -0.8 to 0.6 V (vs. ref.). Similar to that in alkaline electrolytes, the electrodes show ideal CV curves with excellent rate performance in both electrolytes (**Figure 3.4B, C**). Notably, the curvature of the CV curves in the three electrolytes shows different features, which is due to the size difference of electrolyte ions adsorbed on the electrode surface. According to galvanostatic charge/discharge tests, the electrode shows a capacitance of 170 F g^{-1} at a current density of 0.5 A g^{-1} and 115 F g^{-1} at 10

A g^{-1} in 1 M Na_2SO_4, and a capacitance of 175 F g^{-1} at 0.5 A g^{-1} and 122 F g^{-1} at 10 A g^{-1} in 1 M Li_2SO_4, respectively (**Figure 3.4D**). Due to a lower electrolyte concentration and larger anions, these capacitance values are relatively lower than that in KOH electrolyte. Nevertheless, the rate-capability for all electrodes is similar (~70% of initial capacitance was retained at 10 A g^{-1}), which suggests a rapid ion response of such carbon electrodes in all the electrolytes.

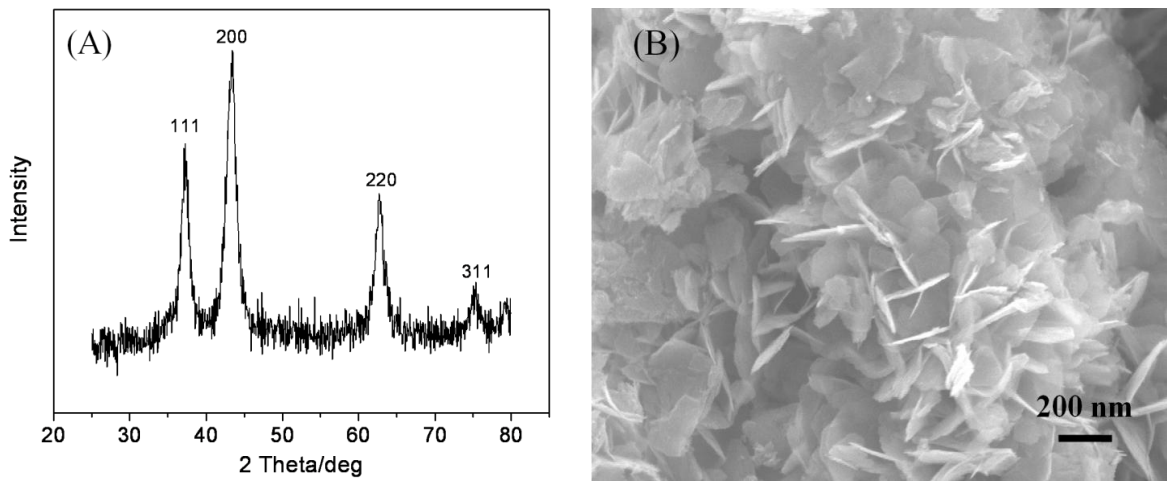

Figure 3.6. XRD pattern (A) and SEM image (B) of NiO nano-flakes.

To further demonstrate their device applications, prototype coin-type devices were assembled using nickel oxide (NiO) as the positive material and the aerosol carbon particles as the negative material. In such devices, the carbon electrodes store charges by electrical-double layer process, while the oxide electrodes are based on redox reaction. To

match the high rate-capability of the carbon electrode, a high-rate NiO electrode was also fabricated from nano-flakes of NiO (~ 10 nm thick) synthesized using a chemical deposition process (**Figure 3.6**).[26] As-synthesized NiO flakes show a surface-redox process according to the CV curve shown in **Figure 3.7A.** The electrochemical reaction occurs at the NiO electrode can be expressed by $NiO + OH^- \leftrightarrow NiOOH + e^-$.[26, 27] Two pairs of peaks appear symmetrically in the CV curve, indicating a good reversibility of this reaction. Galvanostatic charge/discharge was used to further quantify the capacitance of NiO electrode; the C_s was calculated to be ~800 F g^{-1} at a potential window from 0.1~0.5 V and a current density of 0.5 A g^{-1}. According to a charge balance between positive and negative electrodes, an optimal negative-to-positive mass ratio was determined to be 3.6:1[24] in this asymmetric supercapacitor.

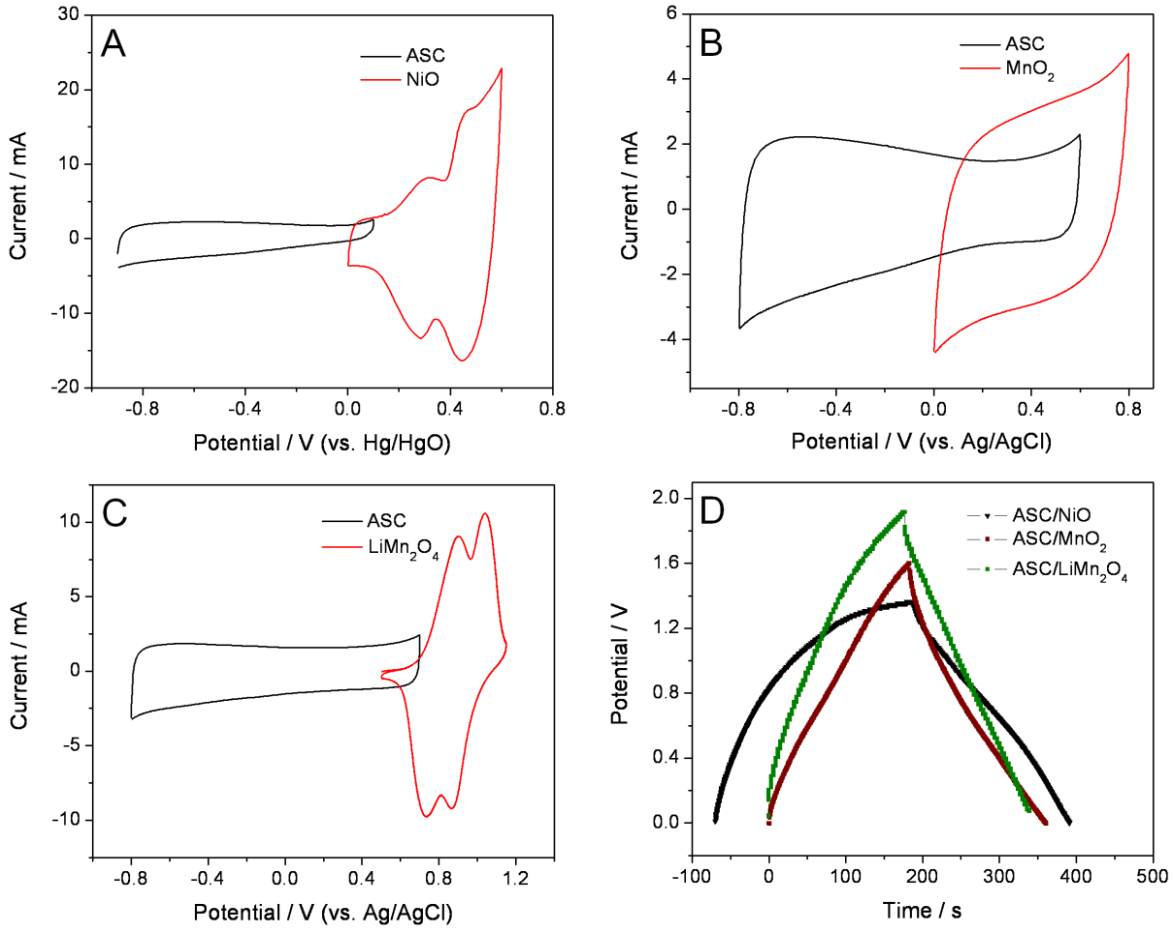

Figure 3.7. Typical CV curves of aerosol carbon electrodes in combination of NiO (A), MnO_2 (B) and $LiMn_2O_4$ (C) electrodes in different electrodes; comparison of charge/discharge potential window of different prototypes (D).

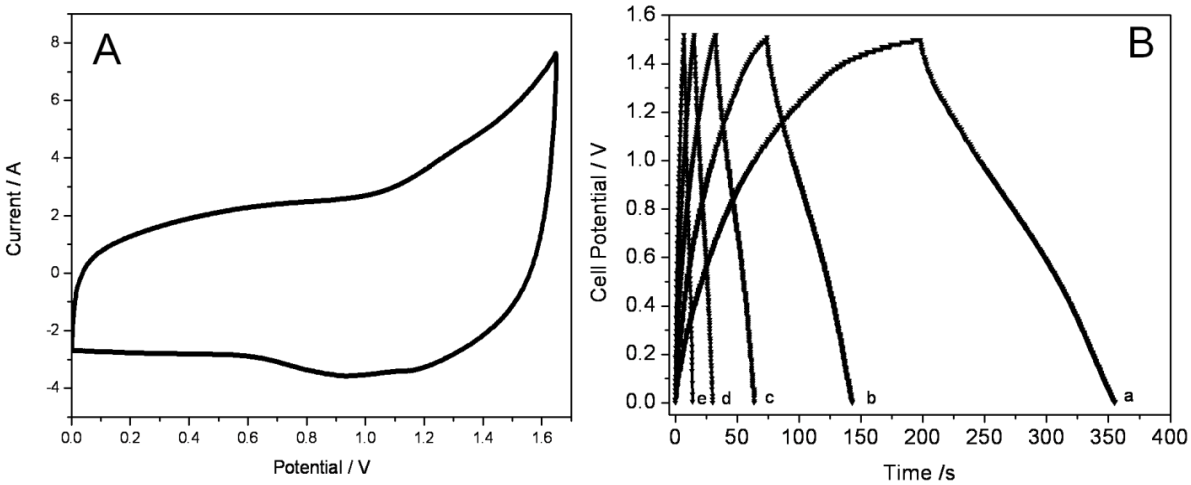

Figure 3.8. CV of a prototype asymmetric carbon/NiO device at 2 mV s^{-1} using porous carbon particles as anode and NiO as cathode (A); and galvanostaic charge-discharge curves at various current density (a: 1.5 mA cm^{-2}; b: 3.1 mA cm^{-2}; c: 6.2 mA cm^{-2}; d: 12.5 mA cm^{-2}; d: 24.6 mA cm^{-2}) of NiO-aerosol carbon in 3 M KOH (B).

Considering the working potential for graphitized carbon anode and NiO cathode are -0.9-0.1 V and 0-0.5 V, respectively, a maximum operation potential of the full cell was achieved at 1.4 V, which was confirmed by galvanostatic charge/discharge of the assembled prototype cells (**Figure 3.7A, C and Figure 3.8**). For a device at optimal configuration, it reached a capacitance of ~ 80 F g^{-1} at a discharge current density of 0.25 A g^{-1}, corresponding to an energy density of 25.0 Wh kg^{-1} at a power density of 180 W kg^{-1} (based on the total weight of cathode and anode active materials). This device could still possess an energy

density of 8.5 Wh kg^{-1} even at a power density of 6000 W kg^{-1}, suggesting a very high rate-capability. In addition, long-term cycling test shows that the device still retains ~75% of the initial capacity after 2000 cycles under a current density of 5 A g^{-1}, suggesting a good cycling stability of the cell.(**Figure 3.9**) Comparing with the symmetric supercapacitor based on the hierarchical porous carbon (**Figure 3.10**), Maxsorb activated carbon, chemically modified graphene,[23] or asymmetric capacitors based on hierarchically porous NiO and carbon,[28] this asymmetric capacitor represents a significant improvement in terms of energy and power density, thus demonstrating the superiority of using our aerosol carbon for high-performance asymmetric devices.

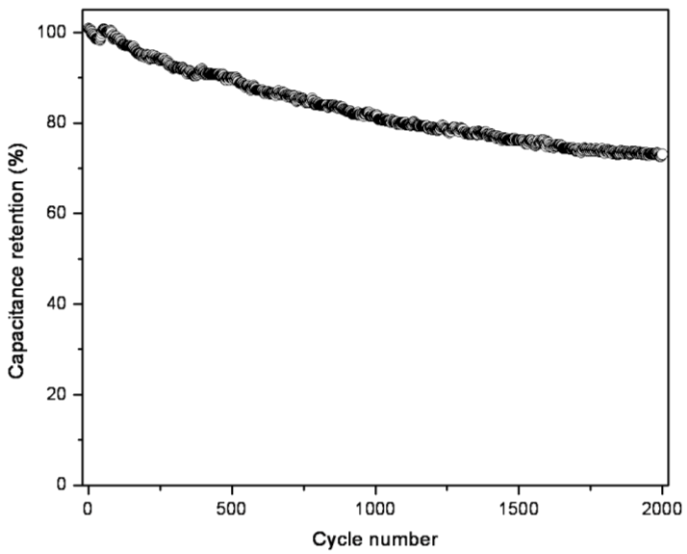

Figure 3.9. Cycling performance of the Carbon/NiO asymmetric capacitor.

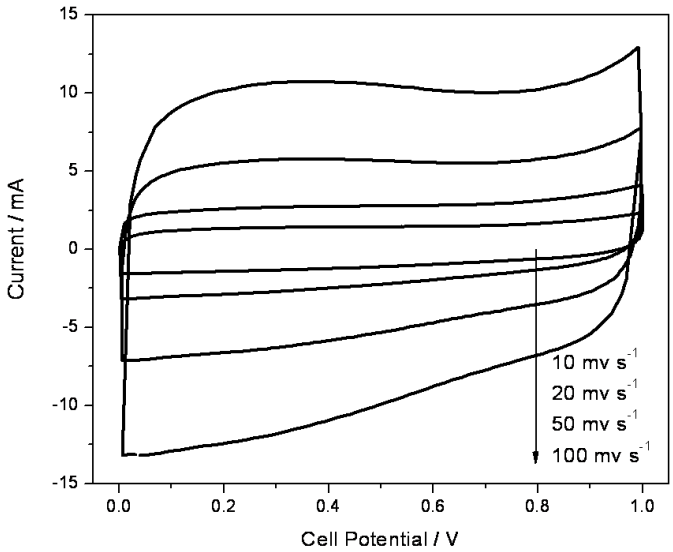

Figure 3.10. CVs of symmetric supercapacitor with porous carbon particle electrodes.

Successful implementation of our hierarchically porous carbon electrodes in other devices was also demonstrated using manganese oxide (MnO_2) and lithium manganese oxide ($LiMn_2O_4$) as the cathode materials. Nano-sized MnO_2 (**Figure 3.11**) and $LiMn_2O_4$ (**Figure 3.12**) were synthesized according to our previous work[29] or reported method with some modification.[30] **Fig. 3.4B** shows typical CV plot of MnO_2 in 1 M Na_2SO_4 together with a graphitized carbon electrode. The electrochemical reaction occurs at the MnO_2 electrode can be expressed by $MnO_2 + xNa^+ + xe^- \leftrightarrow MnOONa_x$.[31] The MnO_2 electrodes show ideal pseudocapacitive behavior with a specific capacitance of ~150 F g^{-1} between a potential window from 0 to 0.8 V, which agrees well with the previous reports.

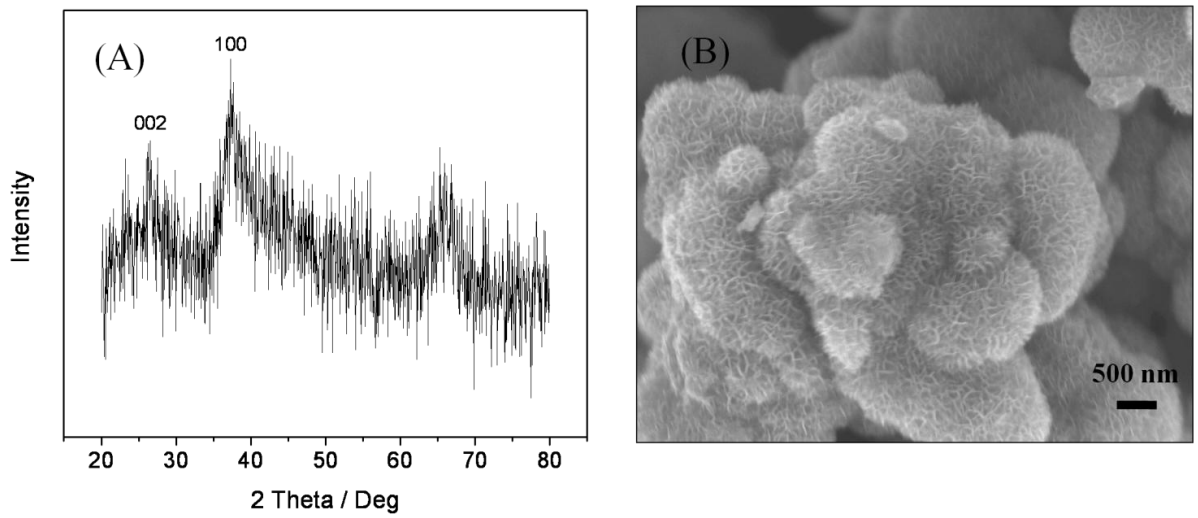

Figure 3.11. XRD pattern (A) and SEM image (B) of MnO_2/C nanocomposite for asymmetric carbon/MnO_2 devices.

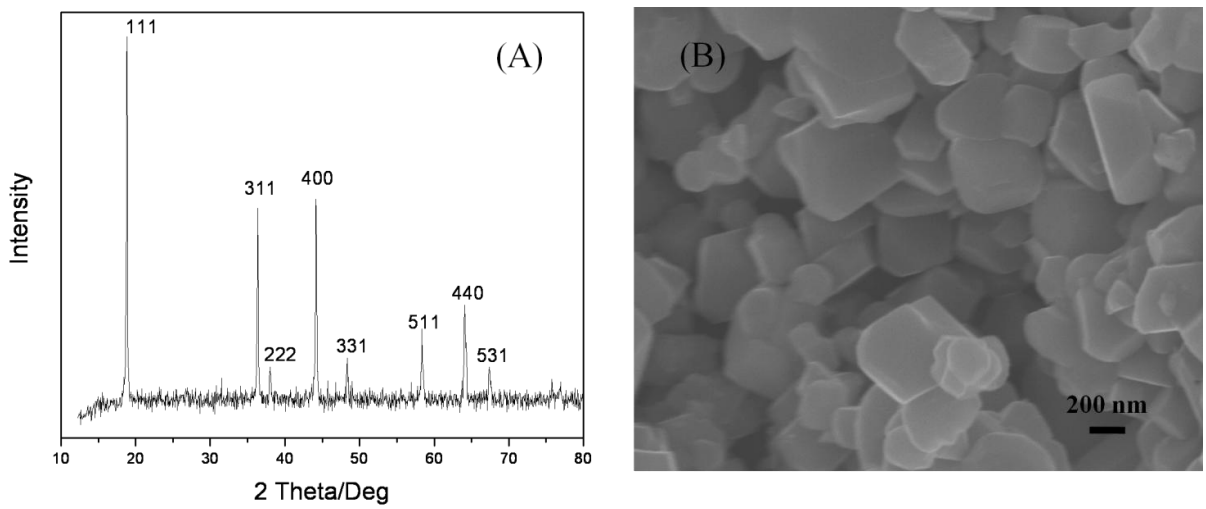

Figure 3.12. XRD pattern (A) and SEM image (B) of $LiMn_2O_4$ nanoparticles for asymmetric carbon/$LiMn_2O_4$ devices.

The electrochemical reaction occurs at the $LiMn_2O_4$ electrode can be expressed by $LiMn_2O_4 + xLi^+ + xe^- \leftrightarrow Li_xMn_2O_4$.[32] Slightly different from the MnO_2 electrodes, the $LiMn_2O_4$ electrodes store charge by lithium intercalation reaction, which gives a charge capacity of 95 mAh g^{-1} (averaged to be 700 F g^{-1}) at potential between 0.6 and 1.1V (**Figure 3.7C**). Similar to the above carbon//NiO asymmetric cells, in combination with the carbon electrodes, therefore, asymmetric devices can provide a maximum cell voltage of 1.6 and 1.9 V when using MnO_2 and $LiMn_2O_4$ as cathode, respectively (**Figure 3.7D**). At a slow rate (0.1 mA cm^{-2}), optimal asymmetric carbon/MnO_2 and carbon/$LiMn_2O_4$ devices provided an energy density of ~14 and 32 Wh kg^{-1}, respectively. The energy density of the cells decreased to 4.2 and 4.5 Wh kg^{-1}, respectively, at high rate (5 mA cm^{-1}), revealing that the structure of the oxides need to be further tuned for high-rate application. Nevertheless, such high energy densities approach those of the organic electrolyte-based devices, and are significantly higher than those of the carbon-based symmetric devices in aqueous electrolytes. These results further reveal the great potentials of using such aerosol carbons as the anodes for hybrid capacitive energy storage. Further effort to make high-rate MnO_2 and $LiMn_2O_4$ bulk electrodes will enable us to fabricate these high-energy supercapacitors with improved power density.

3. Conclusions

In summary, we have showed excellent capacitive performance of hierarchically porous carbon in aqueous electrolytes, where high-energy asymmetric supercapacitors were fabricated using this carbon material as anodes. The appealing capacitive performance is attributed to its unique structure that provides large double layer capacitance, fast ion transport and efficient charge harvesting capability. This new family of porous carbons offers great opportunity to fabricate high-energy and safer supercapacitor devices at low cost.

4. Experimental

4.1 Synthesis of hierarchically porous graphitized carbon particles

In a typical synthesis, aqueous solutions containing 40 mL of de-ionized water, 12 g of sucrose, 10 g of nickel nitrate, 20 g of 0.1 M HCl and silicate templates (20 g of colloidal silica particles (AS 30%, Nissan Chemicals. Inc.) and 16 g of TEOS) were sent through an atomizer using nitrogen as carrier gas. The atomizer dispersed the solution into aerosol droplets, which were then passed through a ceramic tube that was heated to 450 °C. Continuous solvent evaporation at the air/liquid interface of the aerosol droplets enriched the sucrose and silica, resulting in the formation of spherical silica/sucrose/nickel moiety

nanocomposite particles. The particles were then collected on a membrane filter in a press, and subsequent carbonization to 900 °C of the composite nanoparticles under N_2 atmosphere resulted in the formation of spherical silica/carbon/nickel composite nanoparticles. 1 M HCl and 5 M NaOH were used in sequence to remove the nickel and silica respectively, which produced the porous carbon particles with graphitized shell structure.

4.2 Material characterization

The X-ray diffraction measurements were taken on Panalytical X'Pert Pro X-ray powder diffractometer using the copper Kα radiation (λ=1.54 Å). Nitrogen sorption isotherms were measured at 77K with a Micromeritics ASAP 2020 analyzer. All the samples were degassed in vacuum at 180℃ for three hours. The specific surface areas (S_{BET}) were calculated by the Brunauer-Emmett-Teller (BET) method using adsorption branch in a relative pressure range from 0.04 to 0.25. The pore size distributions (D_p) were derived from the adsorption branches of isotherms using the Barrett-Joyner-Halenda (BJH) model. Scanning electron microscopy (SEM) experiments were conducted on a JEOL JSM-6700 FE-SEM. Transmission electron microscopy (TEM) experiments were conducted on a Philips CM120 operated at 120 kV. The Raman spectrum was recorded by a Jobin Yvon micro-Raman

spectroscope (Super LabRam II) with a mode of 50 ×objective (8 mm), a holographic grating (1800 g mm^{-1}), 1024 × 256 pixels charge-coupled device detector and 5 mW He-Ne laser at 632.8 nm as an excitation line. Each Raman spectrum was obtained using three accumulations, and the acquisition time in each case was typically 8 s.

4.3 Electrochemical test

All the electrodes were prepared by a slurry-coating process using nickel foam as substrates. Briefly, 80% of the testing materials, 10% carbon black, and 10% poly(vinylidene fluoride) (PVDF) dispersed in N-methylpyrrolidinone (NMP) were mixed to form slurries. The slurries were ultrasonically treated at 60℃ for 0.5 h, coated on a nickel foam substrates, and dried at 80℃ for 10 min under vacuum. As formed electrodes were then pressed at a pressure of 2 M Pa and further dried under vacuum at 100℃ for 12 h. The electrochemical measurements were conducted in a Solartron 1287 electrochemistry workstation. The specific capacitance (C) of the electrode materials were derived from $C = I/(dE/dt) \approx I/(\Delta E/\Delta t)$, where I is the constant discharge current density, E is cell voltage, and dE/dt is slope of the discharge curve.

References

1. A. Burke, *J. Power Sources*, 2000, **91**, 37-50.

2. J. R. Miller and P. Simon, *Science*, 2008, **321**, 651-652.

3. J. R. Miller and A. F. Burke., *Electrochem. Soc. Interface*, 2008, 53-57.

4. E. Frackowiak and F. Béguin, *Carbon*, 2001, **39**, 937-950.

5. P. Simon and J. R. Miller, *Electrochem. Soc. Interface*, 2008, 38-43.

6. P. Simon and Y. Gogotsi, *Nat Mater*, 2008, **7**, 845-854.

7. D. W. Wang, F. Li, M. Liu, G. Q. Lu and H. M. Cheng, *Angew. Chem. Int. Ed.*, 2008, **47**, 373-376.

8. A. Kajdos, A. Kvit, F. Jones, J. Jagiello and G. Yushin, *J. Am. Chem. Soc.*, **132**, 3252-3253.

9. D. Carriazo, F. Picó, M. C. Gutiérrez, F. Rubio, J. M. Rojo and F. d. Monte, *J. Mater. Chem.*, 2010, **20**, 773-780.

10. H. J. Liu, W. J. Cui, L. H. Jin, C. X. Wang and Y. Y. Xia, *J. Mater. Chem.*, 2009, **19**, 3661-3667.

11. C. Du, N. Pan, *Nanotechnology*, 2006, **17**, 5314-5318.

12. M. Kaempgen, J. Ma, G. Gruner, G. Wee and S. G. Mhaisalkar, *Appl. Phys. Lett.*, 2007, **90**, 264104.

13. S. W. Lee, B. S. Kim, S. Chen, Y. Shao-Horn and P. T. Hammond, *J. Am. Chem. Soc.*, 2009, **131**, 671-679.

14. J. Chmiola, G. Yushin, Y. Gogotsi, C. Portet, P. Simon and P. L. Taberna, *Science*, 2006, **313**, 1760-1763.

15. Z. Lei, N. Christov, L. L. Zhang and X. S. Zhao, *J. Mater. Chem.*, 2011, **21**, 2274-2281.

16. Z. Chen, J. Wen, C. Yan, L. Rice, H. Sohn, M. Shen, M. Cai, B. Dunn and Y. Lu, *Adv. Energy Mater.*, 2011, **1**, 551-556.

17. J. E. Hampsey, Q. Hu, L. Rice, J. Pang, Z. Wu and Y. Lu, *Chemical Comm.*, 2005, **28**, 3606-3608.

18. H. S. Bengaard, J. K. Nørskov, J. Sehested, B. S. Clausen, L. P. Nielsen, A. M. Molenbroek and J. R. Rostrup-Nielsen, *J. Catal.*, 2002, **209**, 365-384.

19. V. Ganesh, S. Pitchumani and V. Lakshminarayanan, *J. Power Sources*, 2006, **158**, 1523-1532.

20. E. Frackowiak, *Phys. Chem. Chem. Phys.*, 2007, **9**, 1774-1785.

21. W. Xing, C. C. Huang, S. P. Zhuo, X. Yuan, G. Q. Wang, D. Hulicova-Jurcakova, Z. F. Yan and G. Q. Lu, *Carbon*, 2009, **47**, 1715-1722.

22. D. Hulicova-Jurcakova, M. Kodama, S. Shiraishi, H. Hatori, Z. H. Zhu and G. Q. Lu., *Adv. Funct. Mater.*, 2009, **19**, 1800-1809.

23. M. D. Stoller, S. Park, Y. Zhu, J. An and R. S. Ruoff, *Nano Lett.*, 2008, **8**, 3498-3502.

24. V. Khomenko, E. Raymundo-Piñero and F. Béguin, *J. Power Sources*, 2006, **153**, 183-190.

25. Y. G. Wang and Y. Y. Xia, *Electrochem. Comm.*, 2005, **7**, 1138-1142.

26. J. W. Lang, L. B. Kong, W. J. Wu, Y. C. Luo and L. Kang, *Chem. Commun.*, 2008, **35**, 4213-4215.

27. J.-H. Kim, S. H. Kang, K. Zhu, J. Y. Kim, N. R. Neale and A. J. Frank, *Chem. Comm.*, 2011, **47**, 5214-5216.

28. D. W. Wang, F. Li and H. M. Cheng, *J. Power Sources*, 2008, **185**, 1563-1568.

29. Y. Peng, Z. Chen, J. Wen, Q. Xiao, D. Weng, S. He, H. Geng and Y. Lu, *Nano Res.*, 2011, 4, 216-225.

30. K. M. Shaju and P. G. Bruce, *Chem. Mater.*, 2008, **20**, 5557-5562.

31. M. Toupin, T. Brousse and D. Belanger, *Chem. Mater.*, 2004, **16**, 3184-3190.

32. A. Eftekhari, *Electrochimica Acta*, 2001, 47, 495-499.

Chapter 4: Hierarchical Manganese Oxide/Carbon Nanocomposites for Supercapacitor Electrodes

1. Introduction

Supercapacitors are emerging as a class of high-power energy-storage devices[1–4]; their broader uses, however, are still limited by their energy density[5–7]. Generally, a supercapacitor is based on the electrical double layers formed along carbon electrodes, which may provide capacitance of up to 300 F/g in an aqueous electrolyte[8, 9]. Oxides of transition metals, such as RuO_2 [10–12], MnO_2 [13–16], NiO [17, 18], Co_3O_4 [19] and V_2O_5 [20, 21], possess significantly higher capacitances; however, harvesting such capacitance has been limited by their low conductivity and redox kinetics. To address such intrinsic limitations, a common strategy is to integrate low-dimensional oxide materials with conductive components, such as carbon, which has led to the development of various nanocomposites with significantly improved energy density [22–24]. Nevertheless, many essential questions about such composites, such as how the structure, composition and interfaces of the composites may affect the capacitive performance, remain open.

We report herein the synthesis of MnO_2/carbon nanocomposites with controlled structure and composition and the study of the role of these properties in determining capacitive

performance. MnO_2 is currently considered as one of the most promising redox components for supercapacitor applications owning to its high capacitance, low cost and low toxicity. To date, various MnO_2/carbon composites have been synthesized, such as composites with planar graphite [25], acetylene black [26, 27], ordered mesoporous carbon [28, 29], carbon nanotubes [30–33], and carbon aerogels and nanofoams [34]. These have generally been synthesized by physical mixing of MnO_2 with carbon [31], or electrochemically or chemically depositing MnO_2 on carbon substrates [32, 33]. Among these synthesis methods, the chemical deposition of MnO_2 through self-limiting redox reactions of $KMnO_4$ and carbon is of particular interest [25–29]. In such a synthesis, carbon substrates are exposed to $KMnO_4$ solution at room temperature or an elevated temperature, and a spontaneous redox reaction described as

$$4MnO_4^- + 3C + 2H_2O \rightarrow 4MnO_2 + 3CO_2 + 4OH^- \quad (1)$$

occurs producing MnO_2 on the sacrificial carbon substrates [35]. The resulting MnO_2 layer reduces the diffusion of the MnO_4^- ions, generating conformal MnO_2 coatings on the conductive carbon substrates. Such a self-limiting growth confers several major advantages, such as intimate interfaces between the oxide and the carbon, nanosized oxide particles, and controllable oxide thickness.

Nevertheless, the structure and composition of such MnO_2/carbon composites are governed by transport of the $KMnO_4$ in solution and its reaction with carbon, which is very rapid even at room temperature. Note that the diffusion of $KMnO_4$ in porous carbon substrates, such as activated carbon and mesoporous carbons, is generally slow in comparison with the fast reaction kinetics [36, 37]. The rapid reactions result in the preferential formation of MnO_2 layers located on the exterior of the carbon substrates, blocking inwards diffusion and reaction of $KMnO_4$. This technical difficulty inevitably leads to a low MnO_2 loading in the composites, which is detrimental for overall capacitance. Moreover, the formation of MnO_2 is often associated with reduced pore accessibility and electron conductivity. In fact, it has been observed that increasing the oxide loading in such carbon composites by further promoting the redox reaction resulted in a reduction in the overall capacitance [38]. Therefore, the synthesis of MnO_2/carbon composites with higher oxide loading and controlled pore structure for fast transport of ions, which retain the carbon framework needed for electron conductivity is essential to ensure a satisfactory capacitance performance.

To address this challenge, carbon substrates with hierarchical pores (pores with multiple-length-scale diameters) rather than uniform pores were used in this work. The presence of large pores ensures the effective transport of $KMnO_4$ to the substrate interior,

while the mesopores provide high surface area for effective reaction. Such a structure allows the formation of composites with high oxide loadings that are homogenously and intimately coated on the sacrificial carbon scaffold. Moreover, the resulting nanocomposites still retain an interconnected porous structure, which facilitates effective electrolyte diffusion and charge transport and ensures higher specific capacitance and better rate capability. Resulting from this unique design, nanocomposites with MnO_2 loadings of up to 80 wt.% have been achieved, which is a significant advance on the current state of the art. For the first time, electrochemical impedance spectroscopy has been used to study the synergic effects between the MnO_2 mass loading and conductive carbon scaffold, providing insights leading to better capacitance performance.

2. Results and Discussion

2.1 Composition and structure of the composites

The structure and composition of the nanocomposites were found to depend strongly on the reaction conditions. **Figure 4.1(a)** compares the thermogravimetric analysis (TGA) traces of the carbon substrate and a representative composite synthesized using 0.1 M $KMnO_4$ at 50 ℃ with a reaction time of 120 min (denoted as MnO_2/carbon-120). The

carbon substrate lost 99.7 % of its weight at 640 ℃, while the TGA curve of MnO_2/carbon-120 can be divided into three regions. The weight loss (~15%) below 200 ℃ can be ascribed to the removal of adsorbed water. It is worth mentioning that the weight loss for MnO_2/carbon-10 in this region was slightly less (~ 11%), which is due to its thinner MnO_2 coating that retains less interlayer hydration [39]. The weight loss between 200 ℃ and 400 ℃ corresponds to the combustion of residual carbon catalyzed by MnO_2 and its derivatives [40]. At the same time, the layered structure transformed to a thermodynamically stable tunnel structure [41, 42], and in addition δ-MnO_2 decomposed to Mn_3O_4 with release of oxygen at around 400 ℃, which also contributed to the weight loss. Above 500 ℃, residual carbon underwent combustion and Mn_3O_4 was transformed to Mn_2O_3 [43].

Based the TGA analysis, the MnO_2 contents of the composites synthesized with reaction times of 1, 5, 10, 30, 60, 120 and 240 min are compared in **Figure 4.1(b)**. It was found that the MnO_2 content increased rapidly to 46 wt.% within minutes and more slowly subsequently, due to the self-limiting growth mechanism, reaching 67 and 83 wt.% after 60 and 240 minutes of the reaction, respectively. The rapid formation of MnO_2 can be attributed to the large carbon/$KMnO_4$ contact area and rapid $KMnO_4$ diffusion and reaction kinetics.

Composites with 83 wt.% of MnO_2 were obtained; this is significantly higher than those prepared using mesoporous carbon or activated carbon as the sacrificed substrates (~ 40 wt.%)[34]. To be best of our knowledge, this content is higher than that of materials prepared using other carbon scaffolds [29, 31].

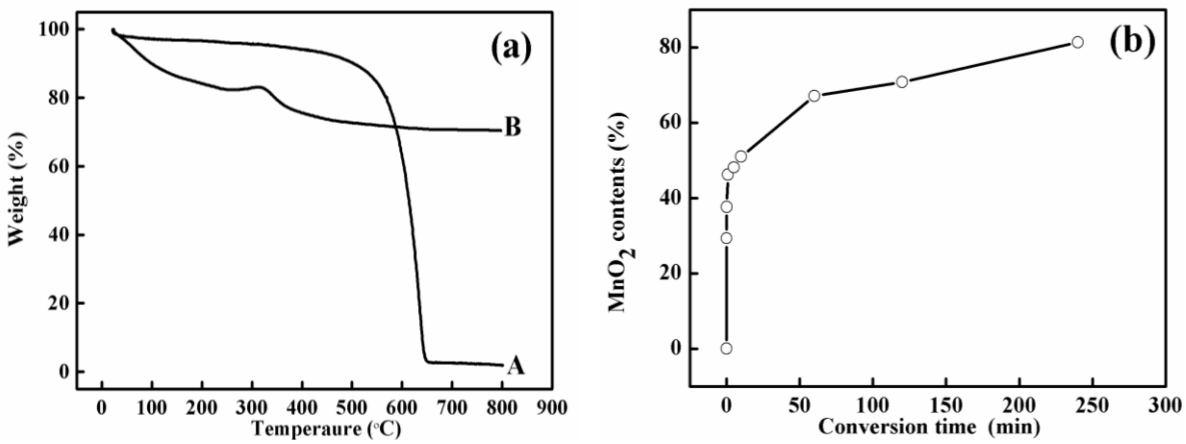

Figure 4.1 (a) Thermogravimetric analysis (TGA) curves of (A) the carbon substrate and (B) MnO_2/carbon-120 in air (100 mL/min) (b) Dependence of the MnO_2 content on the reaction time of the carbon substrates with $KMnO_4$ solution as measured by TGA.

The structure of the composites was characterized using scanning electron microscopy (SEM), transmission electron microscopy (TEM), X-ray diffraction (XRD) and other techniques. **Figure 4.2(a)** shows a representative SEM image of the hierarchical carbon substrate showing the presence of macropores with diameter from 70–100 nm. Their

mesoporous structure is clearly revealed under TEM observation (**Figure 4.2(c)**). These mesoporous channels have uniform diameters in the range 6–8 nm, which is consistent with the use of F127 surfactant as the template [44]. Upon reaction with $KMnO_4$ for 120 min, the composite exhibited a rougher morphology whilst retaining the macroporous structure, and deposition of MnO_2 particles was also observed (**Figure 4.2(b)**). TEM images (**Figure 4.2(d)**) confirmed the retention of macropores necessary for effective electrolyte transport; the ordered carbon mesoporous texture was destroyed; however, and disordered pores are clearly present in the composite. A high-resolution TEM (HRTEM) image (**Figure 4.2(d)**) suggests that the MnO_2 in the composites is polycrystalline, which is confirmed by XRD. The diffraction peaks in this figure marked Bir (birnessite) and Bur (buserite) are characteristic of two different types of layered δ-MnO_2 [45]: the sharp peaks occur at 2θ values of 12.5 °(002) and 25 °(212) can be assigned to Na-birnessite and the peak at a 2θ value of 17° to Na-buserite, with these layered structures having an interlayer separation of 0.7 Å and 1 Å, respectively [46]. The reflection marked Feit at a 2θ value of 19.1° (002) represents feitknechtite (β-MnOOH) derived from a phase transformation which depends on the MnO_4^-/Mn^{2+} ratio [47].

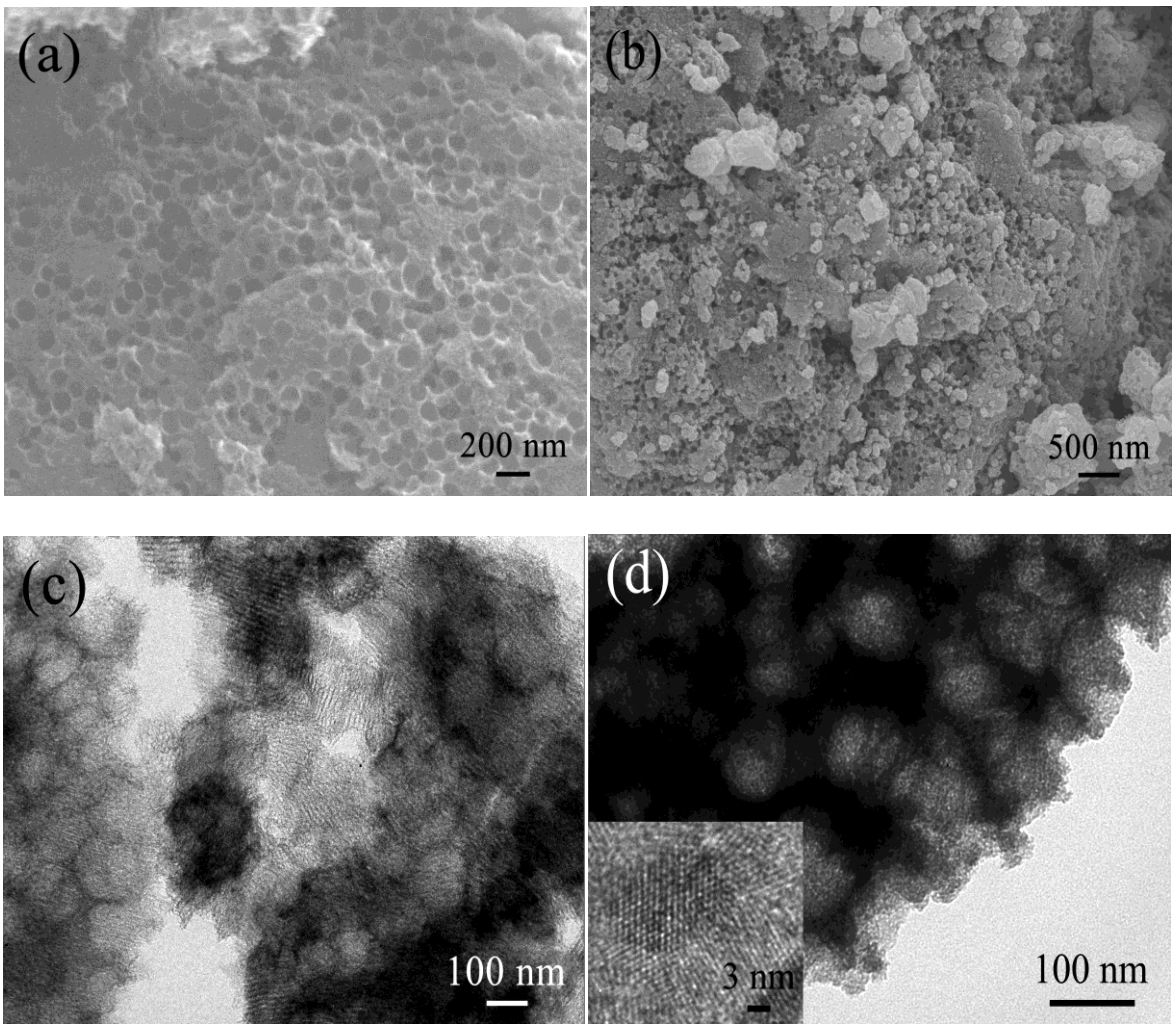

Figure 4.2 SEM images of (a) the carbon substrate and (b) MnO_2/carbon-120; TEM images of (c) the carbon substrate and (d) MnO_2/carbon-120 (inset, high-resolution TEM of the MnO_2 within the composite).

The pore structure of the nanocomposites was further probed using the nitrogen sorption technique. **Figure 4.3(a)** shows the nitrogen sorption isotherms and pore size

distribution of the carbon substrate, clearly suggesting a hierarchical pore structure. The significant nitrogen uptake at relative pressures below 0.3 is consistent with the microporous to mesoporous structure (2–3 nm in pore diameter) created by removal of silicate clusters [48]. In addition, the isotherm curves show two substantial hysteresis loops which confirm the bimodal porosity in the meso- and macro- range, which are associated with mesoporous channels templated by the F127 surfactant and macropores templated by the silica colloids, respectively. For comparison, MnO_2/carbon-120 shows significantly different isotherms (**Figure 4.3(b)**). The uptake at low relative pressure is significantly lower, suggesting a reduced microporosity and mesoporosity; significant uptake at high relative pressure (P/P_0) is still retained, suggesting retention of the macroporosity. In particular, the presence of the hysteresis loop concluding at a relative pressure of 0.8 indicates that the macropores are connected through a mesoporous network, forming hierarchically connected pore channels.

The above studies confirm the successful synthesis of MnO_2/carbon nanocomposites with a hierarchically porous network and tunable oxide content. The relationship between the exact location of the carbon and the oxide within the nanocomposites is unclear. Since the redox reaction was initiated from the pore surface of the carbon substrates, the rapid reaction resulted in the carbon framework becoming wrapped with a layer of MnO_2. Such a

reaction may create porous nanocomposites in which the frameworks possess a “cable-like” structure made with a residual carbon core and an oxide exterior layer. Such a structure will be highly beneficial for harvesting the capacitance of the oxide; however, it is difficult to observe directly using electron microscopy and other techniques.

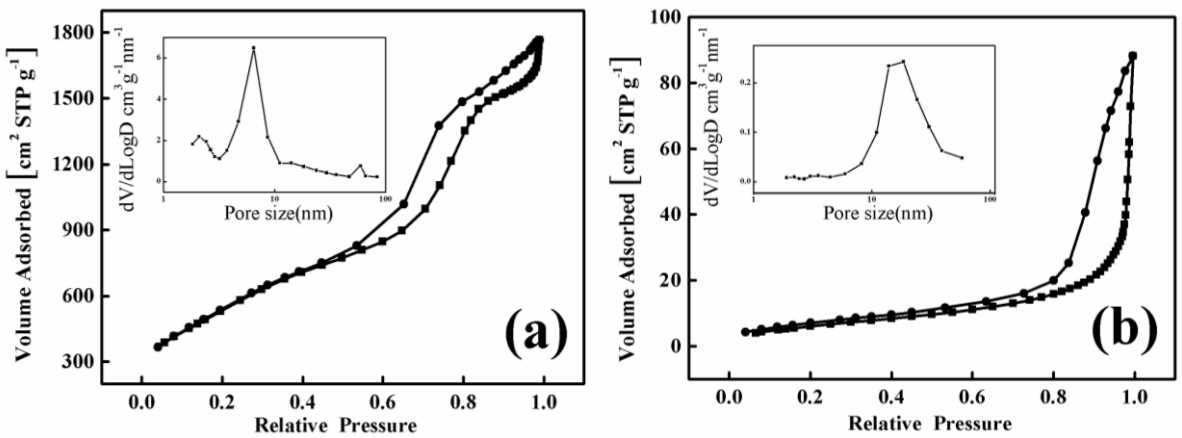

Figure 4.3 Nitrogen sorption isotherms and pore size distributions (insets) of (a) the hierarchical carbon substrate and (b) MnO_2/carbon-120 nanocomposite.

2.2 Capacitive performance of MnO_2/carbon nanocomposites

The synthesis of MnO_2/carbon nanocomposites with a hierarchically porous network and tunable oxide content provides a unique material platform for a study of capacitance. **Figure 4.4(a)** shows the cyclic voltammetry (CV) curves of the carbon electrode. CV curves with nearly symmetrical rectangular shape were observed at potential scan rates of 5,

10 and 20 mV/s, owning to the connective pore structure and good conductivity. The MnO_2/carbon-120 electrode showed an obvious polarization, indicated by the distorted CV curve as the scan rate was increased to 20 mV/s (**Figure 4.4(b)**). The polarization is believed to be due to the increased electron and transport resistance mentioned above. Nevertheless, with a mass loading of 70 wt.% MnO_2, the specific capacitance increased to 218 F/g at a current density of 0.1 A/g, which was three times of that of the carbon substrate (**Figure 4.4 (c)** and 4.**4(d)**).

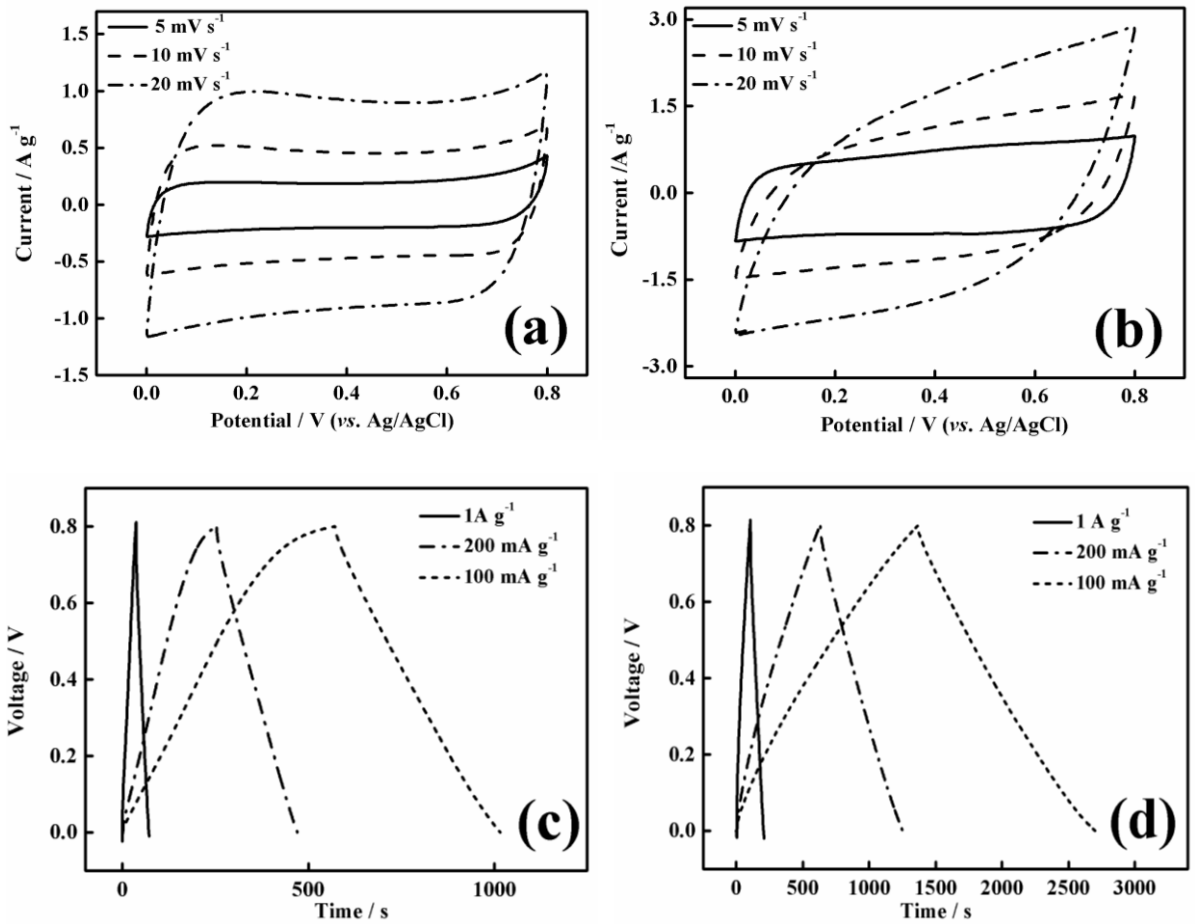

Figure 4.4 Cyclic voltammograms of electrodes made from (a) hierarchical carbon substrate and (b) MnO_2/carbon-120 at potential sweep rates of 5, 10 and 20 mV/s in 1 M Na_2SO_4 aqueous electrolyte at room temperature; Typical charge and discharge curves of the (c) carbon and (d) MnO_2/carbon-120 electrodes at different current densities of 0.1, 0.2 and 1 A/g.

It is well known that the capacitance generally decreases with increasing current density due to the polarization from electrolyte transport, ion diffusion or charge transfer [49, 50]. To investigate the relation between the rate capability and the oxide content, galvanostatic charge and discharge (GC) tests at various current densities were conducted (**Figure 4.5**). Owing to the favorable pore connectivity and good conductivity, the carbon electrode retained 81% (a decrease from 71 F/g to 58 F/g) of its capacitance as the current density was increased from 0.1 to 2 A/g. After introducing the oxide with its high specific capacitance, the nanocomposites exhibited improved capacitance. For example, the MnO_2/carbon-5 electrode, with 48 wt.% MnO_2 content, gave a moderate specific capacitance of 164 F/g at a current density of 0.1 A/g; 79 % capacitance was retained (130 F/g) at a current density of 2 A/g, exhibiting a good rate capability. The MnO_2/carbon-120 electrode, with 70 wt.%

MnO_2 content, showed an even higher capacitance of 218 F/g at 0.1 A/g and good capacitance retention of 70 % at 2 A/g. This value is about twice that of the capacitance of the MnO_2/carbon nanofoam composite prepared by a similar approach (110 F/g at 2 mV/s) [51]. However, further increasing the MnO_2 content resulted in a deterioration in the capacitance of the nanocomposites. For example, although the MnO_2/carbon-240 electrode has the highest MnO_2 loading (83 wt.%), its overall capacitance was only 166 F/g at 0.1 A/g; only 40 % of its capacitance was released at a current density of 2 A/g, which is similar to that for a pure MnO_2 electrode. The deterioration in capacitance performance is due to the reduced electron conductivity (less residual carbon skeleton) and increased ion diffusion resistance (thicker MnO_2 layer).

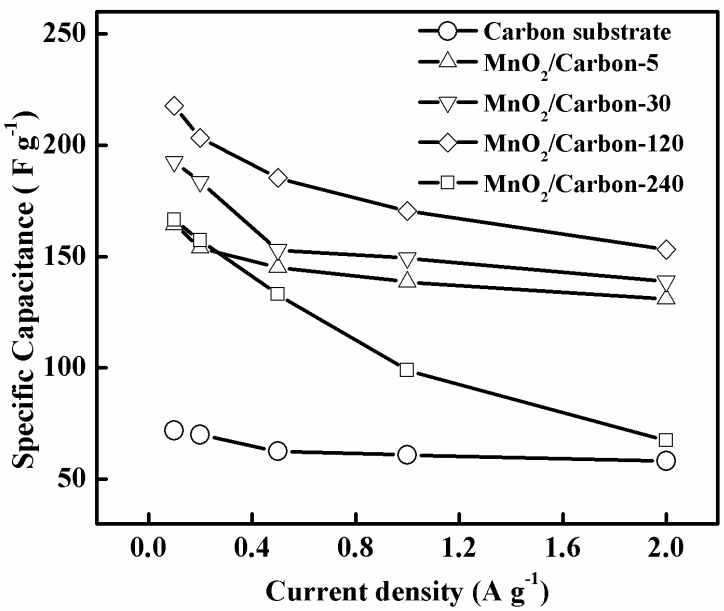

Figure 4.5 Gravimetric capacitance of the carbon substrate and composites with different

MnO_2 content measured at charge–discharge current densities of 0.1, 0.2, 0.5, 1, and 2 A/g in 1 M Na_2SO_4 aqueous electrolyte at room temperature.

To further understand the galvanostatic charge and discharge results, EIS was used to quantify their conductive and diffusive behavior. **Figure 4.6** shows Nyquist plots of the composite electrodes with different oxide content, all of which have a comparable ohmic resistance. Polarization resistance (or charge transfer resistance R_p) of the electrode, shown in the high frequency region, increased gradually as the oxide content was increased. The MnO_2/carbon-240 electrode has an R_p of ~14 Ω calculated from the diameter of the semicircle, which is significantly higher than that of the MnO_2/carbon-120, MnO_2/carbon-30, and MnO_2/carbon-5 electrodes (10, 3, and 2 Ω, respectively). Assuming a bulk resistivity of MnO_2 of 5×10^5 Ω cm, a pure birnessite MnO_2 electrode with the same thickness (~20 μm) as the composite electrode will have a resistance of 1000 Ω [34]. It is clear that the carbon framework in the composites does serve as an effective conductive pathway, dramatically reducing the resistance. Note that with increasing MnO_2 content, the slope of the Nyquist plot in the low frequency region decreased gradually, indicative of the increasing Warburg resistance (or diffusion resistance). These results are in good agreement with the CV and

galvanostatic charge/discharge results, verifying that higher MnO_2 content leads to larger charge transfer resistance and diffusion resistance. Therefore, to achieve good capacitance performance, it is necessary to maintain a connective carbon framework for good conductivity, and a high MnO_2 content for high specific capacitance.

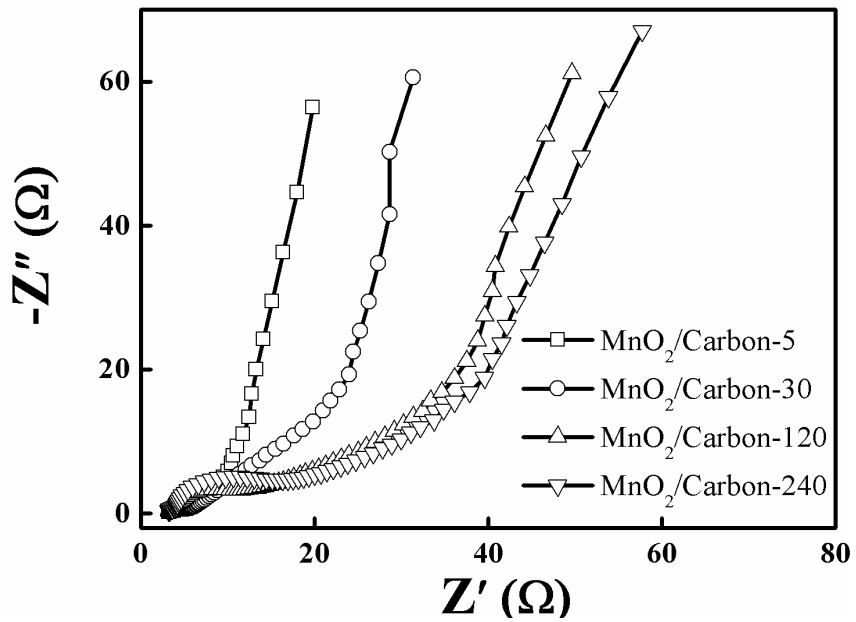

Figure 4.6 Nyquist plot from impedance spectroscopic analysis of the MnO_2/carbon-5 nanocomposite (□), MnO_2/carbon-30 nanocomposite (○), MnO_2/carbon-120 nanocomposite (△) and MnO_2/carbon-240 nanocomposite (▽).

Besides the improved capacitance and good rate performance, the unique composite structure creates robust oxide/carbon interfaces, which endows the nanocomposites with

outstanding cycling stability. Using MnO_2/carbon-120 as an example, **Figure 4.7** shows the charge–discharge cycles at a constant current density of 1 A/g in 1 M Na_2SO_4 electrolyte. The cycling performance is shown in the inset plot, which gives the galvanostatic cycling (GC) plots from the 91st to 100th cycles. As shown, the electrode retained a very stable capacitance over 100 cycles (the capacitance decays by only 0.1%), suggesting a good electrochemical cycling stability.

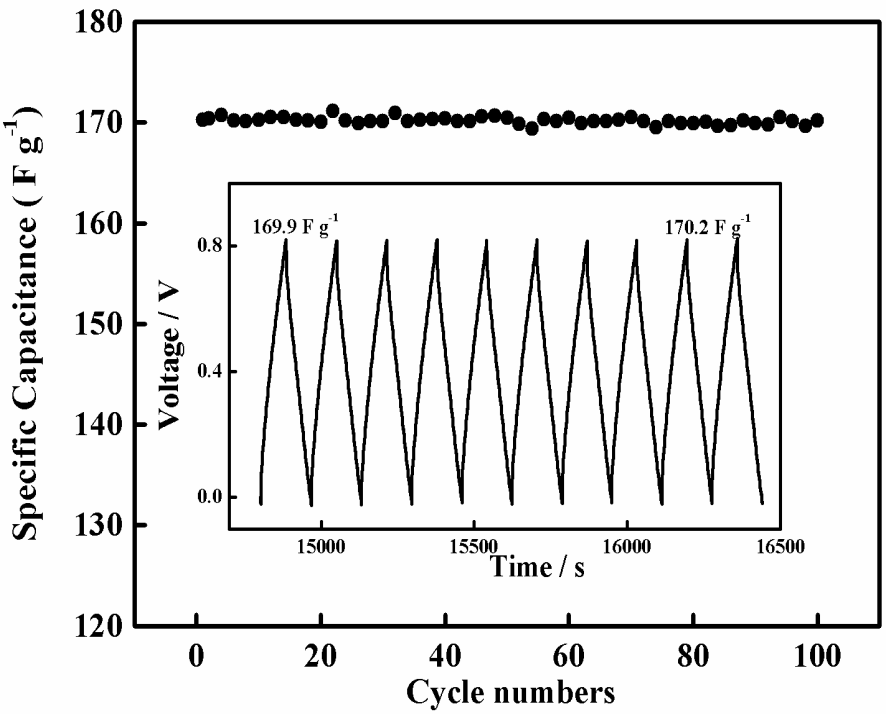

Figure 4.7 Cycling stability and typical charge and discharge curves (insert) of the MnO_2/carbon-120 nanocomposite at a current density of 1 A/g in 1 M aqueous sodium sulfate electrolyte at room temperature.

3. Conclusion

We have developed a general approach to synthesize MnO_2/carbon nanocomposites with hierarchically porous structure and controllable MnO_2 loading using hierarchical carbon as the sacrificed substrate. Such unique porous substrates enable the formation of nanocomposites with high MnO_2 loading and capacitance. An EIS study suggests that increasing the MnO_2 loading also reduces the conductivity of the composites. Optimizing the MnO_2 loading and conductivity of the nanocomposites provides high specific capacitance and excellent rate capability. The fundamental understanding gained in this work will promote the design and fabrication of high-performance supercapacitors for a large variety of applications.

4. Experimental

4.1 Synthesis of carbon substrate and MnO_2/carbon nanocomposites

The porous carbon substrates were synthesized by an assembly process using phenolic resol as the carbon precursor. Tri-block copolymer F127 (*Mw* = 12600, $PEO_{106}PPO_{70}PEO_{106}$, where PEO and PPO are poly(ethylene oxide) and poly(propylene oxide), respectively) was used as a soft template; silicate clusters formed by hydrolysis and condensation reactions of tetraethyl orthosilicate (TEOS) and colloidal silica particles

(70–100 nm in diameter) were used as the hard template. Briefly, F127 (1.6 g), 0.2 M HCl (1.0 g), ethanol (8 g), TEOS (2.08 g) and colloidal silica (1.5 g) were mixed in a flask and vigorously stirred for 4 h. The mixture was transferred to a glass dish and after evaporation of the solvent for 12 h at room temperature; the mixture was put into an oven at 100 ℃ for 24 h to affect the thermo-polymerization. The samples were then carbonized in a tubular furnace under nitrogen flow. The samples were heated from room temperature to 350 ℃ at 2 ℃/min, kept at 350 ℃ for 2 h and heated to 500 ℃ at 1 ℃ /min, followed by heating to 900 ℃ at 10 ℃/min and holding at 900 ℃ for 2 h. After carbonization, the as-formed carbon/silica composites were soaked with 5 wt.% HF for 12 h to remove the silica, converting the composites into hierarchical porous carbons. For comparison, ordered mesoporous carbon (OMC) with a uniform pore structure was also synthesized according to the method reported by Zhao et al. [44].

The synthesis of MnO_2/carbon composites was conducted by a procedure adapted from the literature [25]. Briefly, 0.08 g of carbon substrate was soaked in 25 mL of Na_2SO_4 solution (0.1 M) at 50 ℃ in vacuum and stirred with 25 mL solution containing 0.1 M $KMnO_4$ and 0.1 M Na_2SO_4 for 1, 5, 10, 30, 60, 120, or 240 min. The products were then washed with deionized water and dried at 80 ℃ in vacuum for 24 h; the products are denoted

MnO_2/carbon-time (e.g., MnO_2/carbon-240).

4.2. Material and electrode characterization

X-ray diffraction patterns were recorded on a PANalytical X'Pert Pro X-ray powder diffractometer using copper Kα radiation (λ = 1.54 Å). Nitrogen sorption isotherms were measured at 77 K with a Micromeritics ASAP 2020 analyzer. The samples were degassed in vacuum at 180 ℃ for 3 h before measurements were taken. The specific surface areas were calculated by the Brunauer–Emmett–Teller (BET) method using the adsorption branch in the relative pressure range from 0.04 to 0.25. The pore size distributions (Dp) were derived from the adsorption branch using the Barrett–Joyner–Halenda (BJH) model. Thermogravimetric analysis (TGA) was carried out in a PerkinElmer analyzer from 25 ℃ to 800 ℃ with a heating rate of 10 ℃/min and air flow rate of 100 ml/min. Scanning electron microscopy (SEM) images were obtained using a JEOL JSM-6700 FE-SEM. Transmission electron microscopy (TEM) images were obtained using a Philips CM120 microscope operated at 120 kV. High-resolution transmission electron microscopy (HRTEM) experiments were conducted on a Titan 300 kV S/TEM operated at 300 kV.

The electrodes were assembled on nickel foam collectors. Briefly, 80 wt.% of the test material, 10 wt.% of carbon black, and 10 wt.% of poly(vinylidene fluoride) dispersed in

N-methylpyrrolidinone were mixed to form a slurry. The slurry was ultrasonically treated at 60 ℃ for 0.5 h, coated on a nickel foam substrate, and dried at 80 ℃ for 10 min under vacuum. As formed electrodes were then subjected to a pressure of 2 MPa and further dried under vacuum at 100 ℃ for 12 h. The electrochemical measurements were conducted using a Solartron 1860 electrochemistry workstation. Cyclic voltammetry measurements were conducted in 1 M Na_2SO_4 aqueous solution at room temperature using a platinum wire as the counter electrode and an Ag/AgCl electrode as the reference electrode. Electrochemical impedance spectroscopy (EIS) measurements were conducted on a Solartron 1287 using a sinusoidal signal with an AC voltage of 13 mV amplitude in the frequency range from 1 × 105 to 1 × 10^{-2} Hz. The specific capacitance (C) of the electrode materials were derived using the equation $C = I/(dE/dt) \approx I/(\Delta E/\Delta t)$, where I is the constant discharge current density, E is the cell voltage, and dE/dt is the slope of the discharge curve.

References:

[1] Kötz, R.; Carlen, M. Principles and applications of electrochemical capacitors. *Electrochim. Acta*. **2000**, *45*, 2483–2498.

[2] Conway, B. E. *Electrochemical Supercapacitors: Scientific Fundamentals and Technological Applications*; Kluwer Academic/Plenum: New York, 1999.

[3] Huggins, R. A.; Parsons, R. Supercapacitors. *Phil. Trans. R. Soc. Lond. A*. **1996**, *354*,

1555–1566.

[4] Liu, H.; Mao, C.; Lu, J.; Wang, D. Electronic power transformer with supercapacitors storage energy system. *Electr. Pow. Syst. Res*. **2009**, *79*, 1200–1208.

[5] Raymundo-Piñero, E.; Cadek, M.; Béguin, F. Tuning carbon materials for supercapacitors by direct pyrolysis of seaweeds. *Adv. Funct. Mater*. **2009**, *19*, 1032–1039.

[6] Arico, A. S.; Bruce, P.; Scrosati, B.; Tarascon, J.-M.; van Schalkwijk, W. Nanostructured materials for advanced energy conversion and storage devices. *Nat. Mater*. **2005**, *4*, 366–377.

[7] Chmiola, J.; Yushin, G.; Gogotsi, Y.; Portet, C.; Simon, P.; Taberna, P. L. Anomalous increase in carbon capacitance at pore sizes less than 1 nanometer. *Science*. **2006**, *313*, 1760–1763.

[8] Centeno, T. A.; Stoeckli, F. On the specific double-layer capacitance of activated carbons, in relation to their structural and chemical properties. *J. Power Sources* **2006**, *154*, 314–320.

[9] Frackowiak, E. Carbon materials for supercapacitor application. *Phys. Chem. Chem. Phys*. **2007**, *9*, 1774–1785.

[10] Zheng, J. P.; Cygan, P. J.; Jow, T. R. Hydrous ruthenium oxide as an electrode material for electrochemical capacitors. *J. Electrochem. Soc*. **1995**, *142*, 2699–2703.

[11] Subramanian, V.; Hall, S. C.; Smith, P. H.; Rambabu, B. Mesoporous anhydrous RuO_2 as a supercapacitor electrode material. *Solid State Ionics* **2004**, *175*, 511–515.

[12] Wang, Y. G.; Wang, Z. D.; Xia, Y. Y. An asymmetric supercapacitor using RuO_2/TiO_2

nanotube composite and activated carbon electrodes. *Electrochim. Acta* **2005**, *50*, 5641–5646.

[13] Toupin, M.; Brousse, T.; Belanger, D. Influence of microstucture on the charge storage properties of chemically synthesized manganese dioxide. *Chem. Mater*. **2002**, *14*, 3946–3952.

[14] Pang, S. C.; Anderson, M. A.; Chapman, T. W. Novel electrode materials for thin-film ultracapacitors: Comparison of electrochemical properties of sol–gel-derived and electrodeposited manganese dioxide. *J. Electrochem. Soc*. **2000**, *147*, 444–450.

[15] Chang, J.; Lee, S.; Ganesh, T.; Mane, R. S.; Min, S.; Lee, W.; Han, S. H. Viologen-assisted manganese oxide electrode for improved electrochemical supercapacitors. *J. Electroanal. Chem*. **2008**, *624*, 167–173.

[16] Subramanian, V.; Zhu, H.; Wei, B. Nanostructured MnO_2: Hydrothermal synthesis and electrochemical properties as a supercapacitor electrode material. *J. Power Sources* **2006**, *159*, 361–364.

[17] Liu, K. C.; Anderson, M. A. Porous nickel oxide/nickel films for electrochemical capacitors. *J. Electrochem. Soc*. **1996**, *143*, 124–130.

[18] Lang, J. W.; Kong, L. B.; Wu, W. J.; Luo, Y. C.; Kang, L. Synthesis, characterization, and electrochemical properties of $Ni(OH)_2$/ultra-stable Y zeolite composite. *J. Mater. Sci*. **2009**, *44*, 4466–4471.

[19] Lin, C.; Ritter, J. A.; Popov, B. N. Characterization of sol–gel-derived cobalt oxide xerogels as electrochemical capacitors. *J. Electrochem. Soc*. **1998**, *145*, 4097–4103.

[20] Reddy, R. N.; Reddy, R. G. Porous structured vanadium oxide electrode material for

electrochemical capacitors. *J. Power Sources* **2006**, *156*, 700–704.

[21] Hu, C. C.; Huang, C. M.; Chang, K. H. Anodic deposition of porous vanadium oxide network with high power characteristics for pseudocapacitors. *J. Power Sources* **2008**, *185*, 1594–1597.

[22] Sato, Y.; Yomogida, K.; Nanaumi, T.; Kobayakawa, K.; Ohsawa, Y.; Kawai, M. Electrochemical behavior of activated-carbon capacitor materials loaded with ruthenium oxide. *Electrochem. Solid-State Lett*. **2000**, *3*, 113–116.

[23] Kim, I. H.; Kim, J. H.; Lee, Y. H.; Kim, K. B. Synthesis and characterization of electrochemically prepared ruthenium oxide on carbon nanotube film substrate for supercapacitor applications. *J. Electrochem. Soc*. **2005**, *152*, A2170–A2178.

[24] Chen, Z.; Qin, Y.; Weng, D.; Xiao, Q.; Peng, Y.; Wang, X.; Li, H.; Wei, F.; Lu, Y. Design and synthesis of hierarchical nanowire composites for electrochemical energy storage. *Adv. Funct. Mater*. **2009**, *19*, 3420–3426.

[25] Wu, M.; Snook, G. A.; Chen, G. Z.; Fray, D. Redox deposition of manganese oxide on graphite for supercapacitors. *J. Electrochem. Commun*. **2004**, *6*, 499–504.

[26] Huang, X.; Yue, H.; Attia, A.; Yang, Y. Preparation and properties of manganese oxide/carbon composites by reduction of potassium permanganate with acetylene black. *J. Electrochem. Soc*. **2007**, *154*, A26–A33.

[27] Ma, S. B.; Lee, Y. H.; Ahn, K. Y.; Kim, C. M.; Oh, K. H.; Kim, K. B. Spontaneously deposited manganese oxide on acetylene black in an aqueous potassium permanganate solution. *J. Electrochem. Soc*. **2006**, *153*, C27–C32.

[28] Zhu, S.; Zhou, H.; Hibino, M.; Honma, I.; Ichihara, M. Synthesis of MnO_2 nanoparticles

confined in ordered mesoporous carbon using a sonochemical method. *Adv. Funct. Mater*. **2005**, *15*, 381–386.

[29] Dong, X.; Shen, W.; Gu, J.; Xiong, L.; Zhu, Y.; Li, H.; Shi, H. J. MnO_2-embedded-in-mesoporous-carbon-wall structure for use as electrochemical capacitors. *J. Phys. Chem. B*. **2006**, *110*, 6015–6019.

[30] Zhang, H.; Cao, G.; Wang, Z.; Yang, Y.; Shi, Z.; Gu, Z. Growth of manganese oxide nanoflowers on vertically-aligned carbon nanotube arrays for high-rate electrochemical capacitive energy storage. *Nano Lett*. **2008**, *8*, 2664–2668.

[31] Raymundo-Pińero, E.; Khomenko, V.; Frackowiak, E.; Béguin, F. Performance of manganese oxide/CNTs composites as electrode materials for electrochemical capacitors. *J. Electrochem. Soc*. **2005**, *152*, A229–A235.

[32] Lee, C. Y.; Tsai, H. M.; Chuang, H. J.; Li, S. Y.; Lin, P.; Tsen, T. Y. Characteristics and electrochemical performance of supercapacitors with manganese oxide–carbon nanotube nanocomposite electrodes. *J. Electrochem. Soc*. **2005**, *152*, A716–A720.

[33] Fan, Z.; Chen, J.; Wang, M.; Cui, K.; Zhou, H.; Kuang, Y. Preparation and characterization of manganese oxide/CNT composites as supercapacitive materials. *Diam. Relat. Mater*. **2006**, *15*, 1478–1483.

[34] Fischer, A. E.; Pettigrew, K. A.; Rolison, D. R.; Stroud, R. M.; Long, J. W. Incorporation of homogeneous, nanoscale MnO_2 within ultraporous carbon structures via self-limiting electroless deposition: Implications for electrochemical capacitors. *Nano Lett*. **2007**, *7*, 281–286.

[35] Chu, H. Y.; Lai, Q. Y.; Wang, L.; Lu, J. F.; Zhao, Y. Preparation of MnO_2/WMNT

composite and MnO_2/AB composite by redox deposition method and its comparative study as supercapacitive materials. *Ionics* **2009**, *16*, 233–238.

[36] Wang, D. W.; Li, F.; Liu, M.; Lu, G.; Cheng, H. M. 3D Aperiodic hierarchical porous graphitic carbon material for high-rate electrochemical capacitive energy storage. *Angew. Chem. Int. Ed*. **2008**, *47*, 373–376.

[37] Jiao, F.; Bruce, P. G. Mesoporous crystalline β-MnO_2-reversible positive electrode for rechargeable lithium batteries. *Adv. Mater*. **2007**, *5*, 657–660.

[38] Jin, X.; Zhou, Wu.; Zhang, S.; Chen, G.Z. Nanoscale microelectrochemical cells on carbon nanotubes. *Small* **2007**, *3*, 1513–1517.

[39] Feng, Q.; Sun, E. H.; Yanagisawa, K.; Yamasaki, N. Synthesis of birnessite-type sodium manganese oxides by solution reaction and hydrothermal methods. *J. Ceram. Soc. Jpn*. **1997**, *105*, 564–568.

[40] Shen, B.; Qinlei. Study on MSW catalytic combustion by TGA. *Energy Convers. Manage*. **2006**, *47*, 1429–1437.

[41] Liu, L.; Feng, Q.; Yanagisawa, K.; Wang, Y. Characterization of birnessite-type sodium manganese oxides prepared by hydrothermal reaction process. *J. Mater. Sci. Lett*. **2000**, *19*, 2047–2050.

[42] Feng, Q.; Yanagisawa, K.; Yamasaki, N. Synthesis of birnessite-type potassium manganese oxide. *J. Mater. Sci. Lett*. **1997**, *16*, 110–112.

[43] Sharma, R. K.; Oh, H. S.; Shul, Y. G.; Kim, H. Growth and characterization of carbon-supported MnO_2 nanorods for supercapacitor electrode. *Phys. Rev. B: Condens. Matter* **2008**, *403*, 1763–1769.

[44] Liu, R.; Shi, Y.; Wan, Y.; Meng, Y.; Zhang, F.; Gu, D.; Chen, Z.; Tu, B.; Zhao, D. Triconstituent co-assembly to ordered mesostructured polymer–silica and carbon–silica nanocomposites and large-pore mesoporous carbons with high surface areas. *J. Am. Chem. Soc*. **2006**, *128*, 11652–11662.

[45] Vol'khin, V. V.; Pogodina, O. A.; Leont'eva, G. V. Nonstoichiometric compounds based on manganese(III, IV) oxides with the birnessite structure. *Russ. J. Gen. Chem*. **2002**, *72*, 173–177.

[46] Devaraj, S.; Munichandraiah, N. Effect of crystallographic structure of MnO_2 on its electrochemical capacitance properties. *J. Phys. Chem. C*. **2008**, *112*, 4406–4417.

[47] Luo, J.; Huang, A.; Park, S. H.; Suib, S. L.; O'Young, C. Crystallization of sodium β-birnessite and accompanied phase transformation. *Chem. Mater*. **1998**, *10*, 1561–1568.

[48] Hu, Q.; Lu, Y.; Meisner, G. P. Preparation of nanoporous carbon particles and their cryogenic hydrogen storage capacities. *J. Phys. Chem. C*. **2008**, *112*, 1516–1523.

[49] Brock, S. L.; Duan, N.; Tian, Z. R.; Giraldo, O.; Zhou, H.; Suib, S. L. A review of porous manganese oxide materials. *Chem. Mater*. **1998**, *10*, 2619–2628.

[50] Toupin, M.; Brousse, T.; Belanger, D. Charge storage mechanism of MnO_2 electrode used in aqueous electrochemical capacitor. *Chem. Mater*. **2004**, *16*, 3184–3190.

[51] Guzman, R. N. D.; Awaluddin, A.; Shen, Y.; Tian, Z.; Suib, S. L.; Ching, S.; O'Young, C. Electrical resistivity measurements on manganese oxides with layer and tunnel structures: Birnessites, todorokites, and cryptomelanes. *Chem. Mater*. **1995**, *7*, 1286–1292.

[52] Feng, Q; Yanagisawa, K; Yamasaki, N. Synthesis of birnessite-type potassium manganese oxide. *J. Mater. Sci. Lett*. **1997**, *16*, 110–112.

[53] Luo, J.; Huang, A.; Park, S. H.; Suib, S. L.; O'Young, C. Crystallization of sodium-birnessite and accompanied phase transformation. *Chem. Mater*. **1998**, *10*, 1561-1568.

Chapter 5: Design and Synthesis of Hierarchical Nanowire Composites for Electrochemical Energy Storage

1. Introduction

Electrochemical capacitors have been attracting numerous interests because they can instantaneously provide higher power density compared to batteries and higher energy density compared to the conventional dielectric capacitors. Such outstanding properties make them excellent candidates for hybrid electric vehicles, computers, mobile electric devices and other applications.[1,2] Generally, an electrochemical capacitor may be operated based on the electrochemical double-layer capacitance (EDLC) formed along an electrode/electrolyte interface, or a pseudocapacitance resulted from a fast reversible faradic process of redox-active materials (e.g., metal oxides and conductive polymers). For an EDLC-based capacitor, the rapid charge/discharge process provides the capacitor with a high power density, yet the energy density is limited by its effective double-layer area. To date, a large number of high-surface-area materials, such as activated carbon, templated carbon, and carbon nanotubes (CNTs), have been extensively studied. Activated carbons, with surface areas from 1000-2500 m^2 g^{-1}, are the most commonly used materials, which may provide a

capacitance up to 320 F g^{-1} at low potential scanning rate. However, the capacitance may drop dramatically at high scanning rates because of their tortuous pore structure and high microporosity.[3] The templated carbons, on the other hand, exhibit uniform pore geometry and larger pore size; however, they did not show any exciting improvement in either energy or power performance.[4] For comparison, multi-walled CNTs show capacitances up to 135 F g^{-1} [5] and single-wall CNTs show capacitances up to 180 F g^{-1},[6] which are still low for an actual device application. Compared with the EDLC-based capacitors, pseudocapacitors based on transition metal oxides or conducting polymers, such as RuO_2,[7] MnO_2,[8] NiO,[9] Co_3O_4,[10] V_2O_5,[11] and polyaniline,[12] may provide much higher specific capacitances up to one thousand F per gram of the active material. Nonetheless, their actual applications are still limited by high cost, low operation voltage, or poor rate capability, mostly because of inefficient mass transport or of slow faradic redox kinetics.

To design a better electrochemical capacitor with both high energy and power density, a common strategy is to construct a hybrid capacitor that integrates both the electric double-layer capacitance and pseudocapacitance within a single electrode. For example, Sato *et al*. loaded ruthenium oxide onto activated carbon, resulting in a capacity of 308 F g^{-1} at 7.1 wt % ruthenium loading and a low scanning rate of 2 mV s^{-1}.[13] Dong *et al*. reported

the composite of MnO_2 and the templated carbon with a capacitance of 156 F g^{-1} at 20 wt-% MnO_2 loading and a scanning rate of 50mV s^{-1}, which is about two times of that of the constituent carbon.[14] Kim *et al.* dispersed ruthenium oxide nanoparticles on carboxylated CNTs and obtained a total capacitance of 304 F g^{-1} at a RuO_2 loading amount of 50 wt-%.[15] Similarly, composites prepared by electrodepositing MnO_2 on vertically aligned CNT arrays exhibit a capacitance up to 199 F g^{-1} (or 305 F cm^{-3}) with long cycle life; however, the complex fabrication process may limit their actual use.[16]

In spite of extensive research and effort, making supercapacitors with high energy and power density still remains challenging. Herein, we report the synthesis of novel supercapacitor materials based on the composites of low-cost, interpenetrating CNTs and V_2O_5 nanowires, as illustrated in the **Figure 5. 1**. This unique architecture provides several major advantages: 1) the small dimension of the CNTs and the nanowires provide high surface areas, leading to a high EDLC and better utilization of the V_2O_5 active sites (higher specific pseudocapacitance); 2) the interpenetrating nanotube/nanowire structure creates hierarchical porous channels, enabling effective electrolyte transport and active-site accessibility; (3) the nanowires are intimately intertwined with highly conductive CNTs, facilitating a faster electron transport and efficient current collection. Experimentally, these

novel composites were readily synthesized using a one-pot hydrothermal approach. Briefly, multi-wall CNTs were firstly modified to attach carboxylic groups on the surface. Hydrothermal reaction of vanadium-oxide precursors in the presence of the modified CNTs led to the formation of the composites. Note that V_2O_5/CNT composites were prepared by depositing a thin layer of V_2O_5 (6 nm thick) on a CNT film, exhibiting a high Li-ion capacitance up to 910 F g^{-1} at a scan rate of 10mV s^{-1}.[17] However, such composite thin films with extremely low V_2O_5 loadings may not be suitable for practical applications. This work provides a simple but effective synthesis route and structure design towards better supercapacitors.

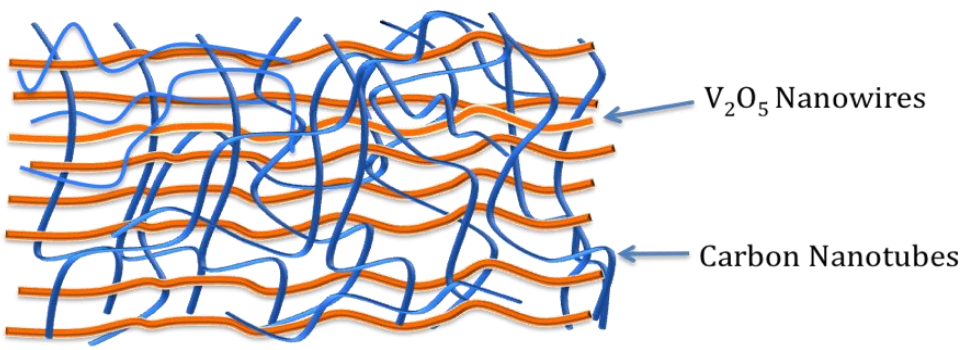

Figure 5.1 Schematic of forming supercapacitor material based on interpenetrating networks of CNTs and V_2O_5 nanowire.

2. Results and Discussion

2.1. Characterization of V_2O_5 nanowire/CNT composite

To systematically study the structure of the composites, we firstly studied the structure and morphology of the CNTs and the V_2O_5 nanowires. **Figure 5.2** shows representative SEM (A) and TEM (B) images of the CNTs, revealing a porous network of entangled CNTs of which diameters are around 20-30 nm and lengths up to micrometers. Similarly, the diameter of the V_2O_5 nanowires is around 20-50 nm and length is up to tens of micrometers (SEM image, **Figure 5.2C**). High resolution TEM image (**Figure 5.2D**) indicates the nanowires contain an ordered layered structure; selective area electron diffraction (SAED) pattern (Inset, **Figure 5.2D**) suggests that they are single crystalline. *In-situ* growth of the V_2O_5 nanowires within the porous CNT networks led to the formation of flexible, dark-brown nanocomposites (**Figure 5.3A**), of which the V_2O_5 loading can be readily controlled by tuning the ratio of CNTs to the V_2O_5 precursor used. **Figure 5.2**E shows a SEM image of a representative composite with 33 wt-% of CNTs (CVC-2), showing a continuous fibrous structure with pores up to micrometers in diameter.

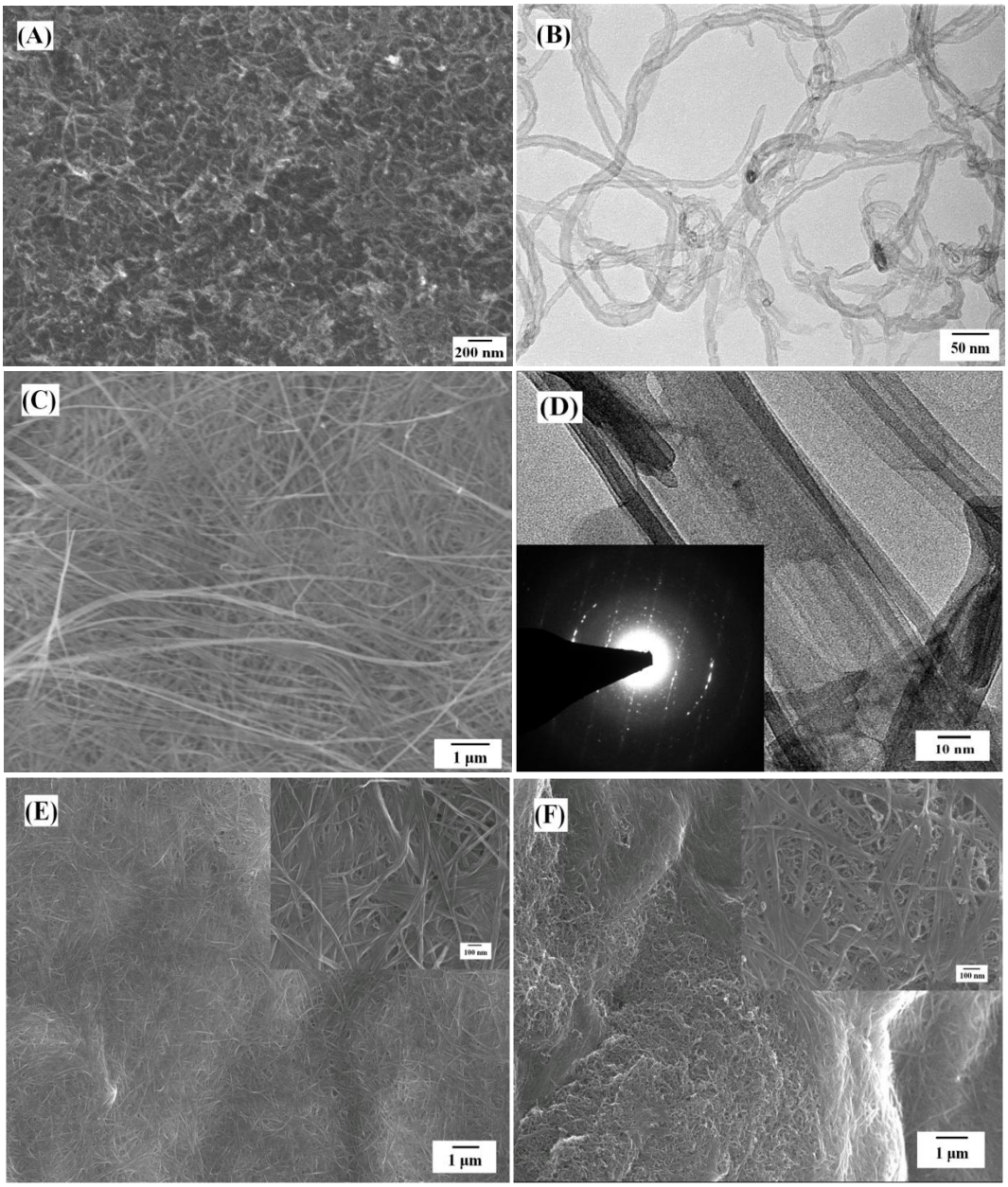

Figure 5.2 SEM (A) and TEM (B) images of the modified CNTs; SEM (C), TEM (D) images and selective area electron diffraction (SAED, Insert) of the V_2O_5 nanowires; SEM images of CVC-2 before (E) and after (F) etching showing an interpenetrating structure.

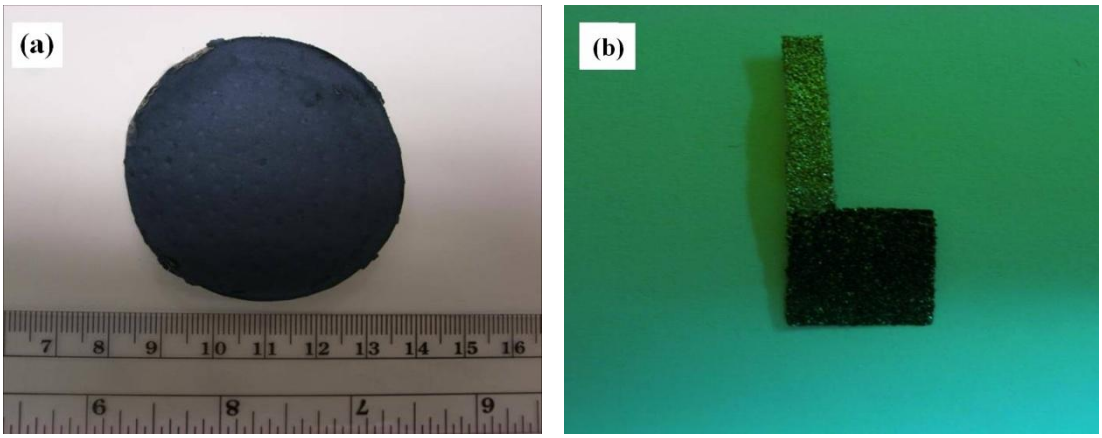

Figure 5.3 Photographs of (a) CVC-2 nanocomposite film collected by filtration of the hydrothermal product and (b) a single electrode made from the composite.

Figure 5.4A shows nitrogen sorption isotherms of the CNTs, V_2O_5 nanowires and CVC-2, all of which are similar in shape. The CNTs show a surface area of 150 $m^2 g^{-1}$, pore volume of 0.488 $cm^3 g^{-1}$, and an average pore diameter of 12.5 nm (**Figure 5.4B**). The V_2O_5 nanowires show a lower surface area of 83 $m^2 g^{-1}$, larger pore diameter of 26.7 nm, and a pore volume 0.552 $cm^3 g^{-1}$. The CVC-2 exhibits a comparable surface area of 125 $m^2 g^{-1}$ and average pore size of 15.2 nm, suggesting the composite is hierarchically porous. The composites with different CNT loadings show the similar porous fibrous structure (**Figure 5.5**, **Table 1**); the morphology of the composites with high CNT content is generally less uniformed with more CNTs exposed on the surface. Such hierarchical structure is essential to ensure a good capacitance performance, since the large pore channels allow rapid

electrolyte transport; while the small ones provide the composites with higher surface areas and more surface active sites.

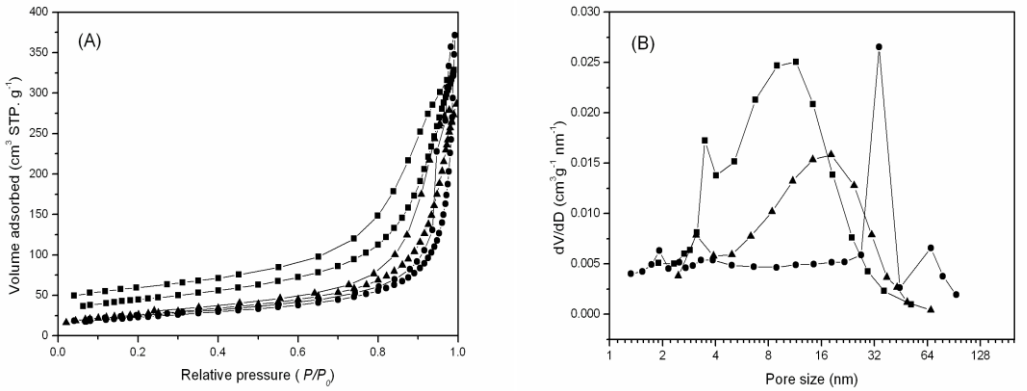

Figure 5.4 Nitrogen sorption isotherms (A) and pore size distributions (B) of CNTs (■), V_2O_5 nanowires (●) and CVC-2(▲).

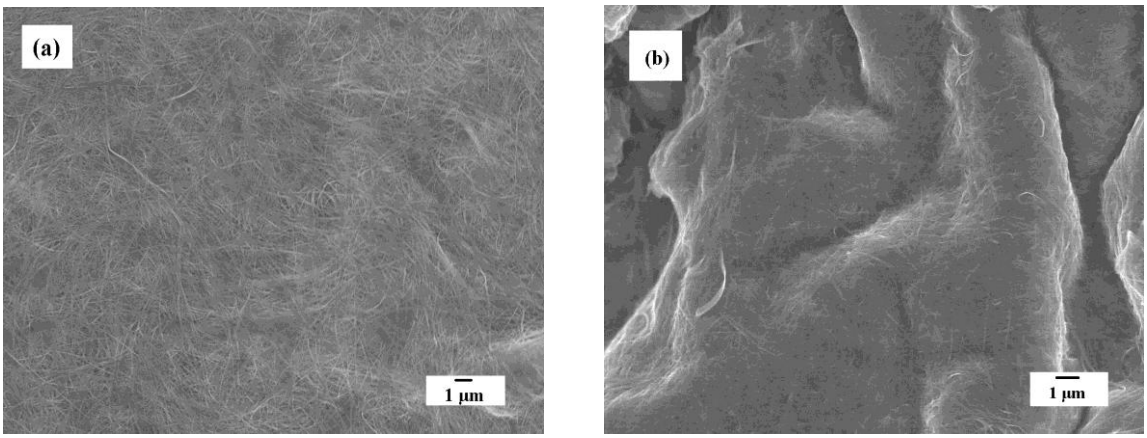

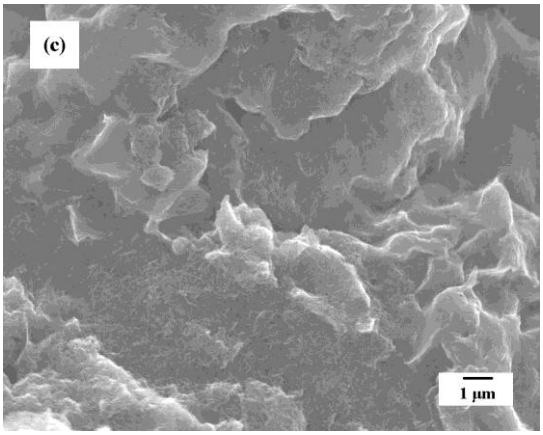

Figure 5.5 SEM images of nanocomposites with different compositions: (a) CVC-1, (b) CVC-3 and (c) CVC-4.

Table 1. Surface area, pore volume and pore size of the CNTs, V_2O_5 nanowires and their composites.

Samples	Surface area ($m^2\ g^{-1}$)	Pore volume ($cm^3\ g^{-1}$)	Average pore size (nm)
CNTs	156	0.488	12.5
CVC-1	108	0.639	20.9
CVC-2	125	0.445	15.2
CVC-3	144	0.645	17.8
CVC-4	142	0.486	13.7
V_2O_5-nanowire	83	0.552	26.7

Furthermore, *in-situ* growth of the nanowires within the CNT network leads to an interpenetrating network structure. X-ray diffraction (XRD, see **Figure 5.6**) indicates that the free-growth V_2O_5 nanowires are highly crystalline with well-defined (*00l*) reflections at

two-theta degree of 9.1, 13.5, 25.5, 32.5 and 42.0, consistent well with the lamellar structure shown in the **Figure 5.2D**. The CVC-2 composites show similar reflections but with significantly lower intensity, indicating the nanowires grown within the composites contain smaller crystalline domains. Partial removal of the nanowires using 1 wt-% HF solution exposed the constituent CNT networks on the composite surface (**Figure. 5.2F**), further confirming the interpenetrating network structure. Such interpenetrating network structure creates intimate contact of the CNT and nanowire networks, enabling rapid charge transport to the current collector through the highly conductive CNT network.

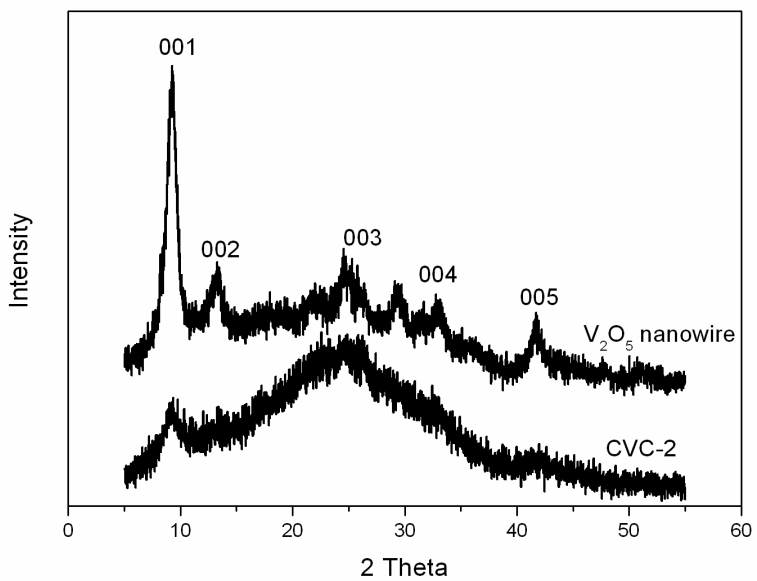

Figure 5.6 XRD patterns of the V_2O_5 nanowires and CVC-2 composite.

2.2. Electrochemical testing of V_2O_5 nanowire/CNT composite

Such a unique hierarchical architecture endows the composites with high capacitance and rate capability. **Figure 5.7** shows cyclic voltammograms (CVs) of the CNT, nanowire, and CVC-2 electrodes. The CNT electrode shows vague peaks at 0.12 V and 0.05 V, which are attributed to the anodic oxidation and cathodic reduction of the surface carboxyl groups.[18] The nanowire electrode shows two broad peaks of anodic oxidation (0.50 and -0.05 V) and reduction (0.35 and -0.10 V), which are typical for the crystalline V_2O_5.[11] For comparison, the composite electrode shows a rectangular-shape CV curve with a much larger area indicating a much higher capacitance. Furthermore, the redox peaks (anodic peaks at 0.51, -0.10 -0.40 V, cathodic peaks at 0.37, -0.28, -0.42) are much better defined, suggesting a more pronounced contribution of redox capacitance to the overall capacitance.[19] Such three-redox pairs are rare in a V_2O_5-Na_2SO_4 aqueous electrolyte system, which may be due to the ion (e.g., Na^+) insertion and de-insertion reactions at different energy states.[20] Moreover, as shown in **Figure 5.7**c, the current of the nanocomposite electrode responses to the switching potential rapidly, particularly at the potential switching point of 0.8 V, indicating the composite electrode exhibits a lower equivalent series resistance *(ESR)* than that of the nanowire electrode. A small *ESR* is vital to achieve a high rate capability and power density, since the maximum power density (P_{max}) of a capacitor is generally

determined by $P_{max} = V_i^2/4R$, where V_i is the initial voltage and R is the *ESR* from electrode materials, electrolyte, and the contact resistance between electrode and current collector.

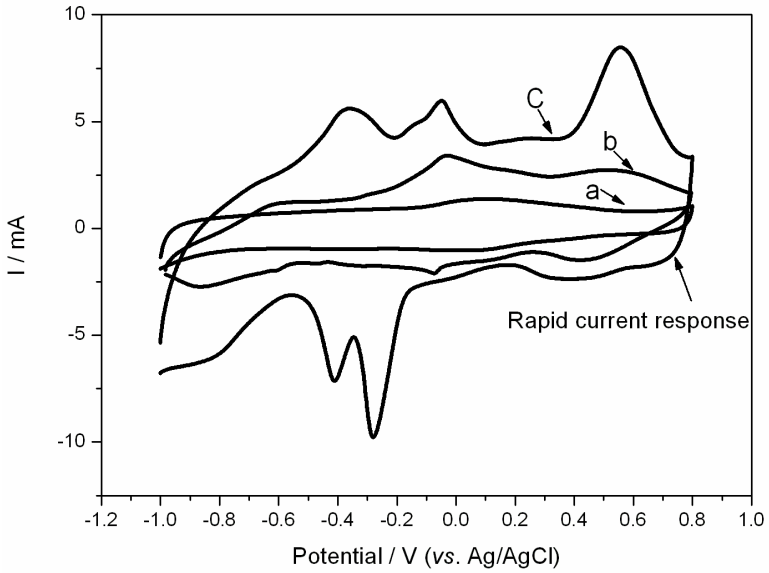

Figure 5.7 Cyclic voltammograms (CV) of CNT (a), V_2O_5 (b) nanowire and CVC-2 (c) electrodes at a scanning rate of 10 mV s^{-1} in 1 M Na_2SO_4 aqueous solution at room temperature.

To further quantify their specific capacitance, galvanostaic charge-discharge curves were measured in the same working cells. **Figure 5.8** shows the charge-discharge curves of the CNT, nanowire and CVC-2 electrodes at the current density of 1 A g^{-1}. The CNT electrode shows nearly linear charge and discharge curve, an indication of an ideal EDLC behaviour with a specific capacitance of 75 F g^{-1}. The nanowire electrode shows similar

charge-discharge curves with a slightly increased curvature, indicating that EDLC is still the primary contribution to the overall capacitance, which is 146 F g^{-1}. Note that V_2O_5 may provide a pseudocapacitance as high as 530 F g^{-1}, poor conductivity of the nanowires may attribute to the poor use of its pseudocapacitance. Intimately weaving these poorly conductive nanowires with the highly conductive CNTs into the composites led to dramatically increased capacitances. Indeed, the charge-discharge plots of the composite electrode displays a pronounced transition between the two linear ranges, indicating the capacitance is contributed from both EDLC and pseudocapacitance. The specific capacitance calculated is around 313 F g^{-1}, which is significantly higher than that of the CNTs (75 F g^{-1}) and the V_2O_5 nanowires (146 F g^{-1}). Since the surface area of the composite (125 m^2 g^{-1}) is less than that of the CNTs (150 m^2 g^{-1}), such a high capacitance should be attributed from the synergic effect of the composite constituents with the unique hierarchical structure. Considering the energy density of a capacitor is generally determined by $E=CV_i^2/2$, where C is the capacitance, composites with high capacitance are of great interest for high-energy-density device applications. To the best of our knowledge, although it is still lower than those of high-cost ruthenic-oxide- or ruthenic-acid- based supercapacitors, this is the highest capacitance reported among the macroscopic V_2O_5- [11] and MnO_2- based

supercapacitors.[8,14,16]

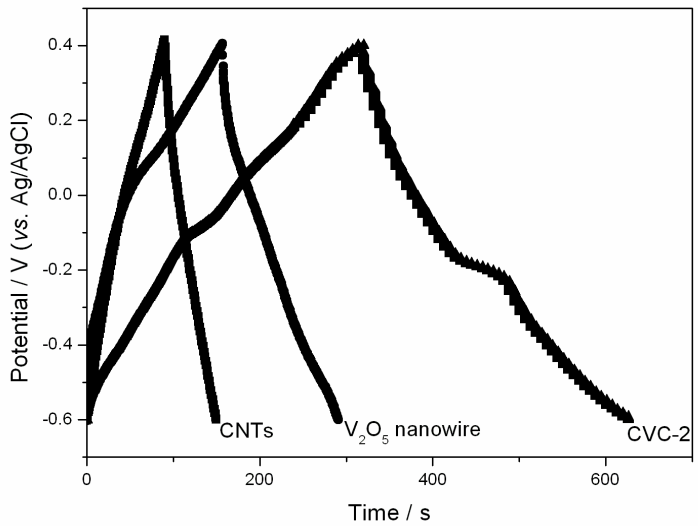

Figure 5.8 Galvanostaic charge-discharge curves of CNT, V_2O_5 nanowire and CVC-2 electrodes at charge-discharge current density of 1 A g^{-1}.

To further quantify their rate performance, CV studies at different scanning rates were conducted. **Figure 5.9** shows CV curves of the CNT, V_2O_5 nanowire and CVC-2 electrodes at scanning rates from 5 to 100 mV s^{-1}. Due to its excellent conductivity and porous structure, the CNT electrode shows excellent power performance,[5] evidenced from their rectangular shape of the CV curves at the high scanning rates (see **Figure 2.9A**). Consistent with its poor conductivity, the nanowire electrode shows a poor rate capability evidenced from its highly distorted CV curves at high scanning rates (**Figure 5.9B**). As expected, CV

curves of the composite electrode CVC-2 maintain the rectangular shape even at high scanning rates (**Figure 5.9C**), which is more pronounced for the composites with higher content of CNTs (**Figure 5.10**). Compared with the CV cures of the CNT electrode, the slight shape distortion is due to the overlapping effect of the two different energy-storage mechanisms, nevertheless, this study fully confirms the excellent rate performance of the composites.

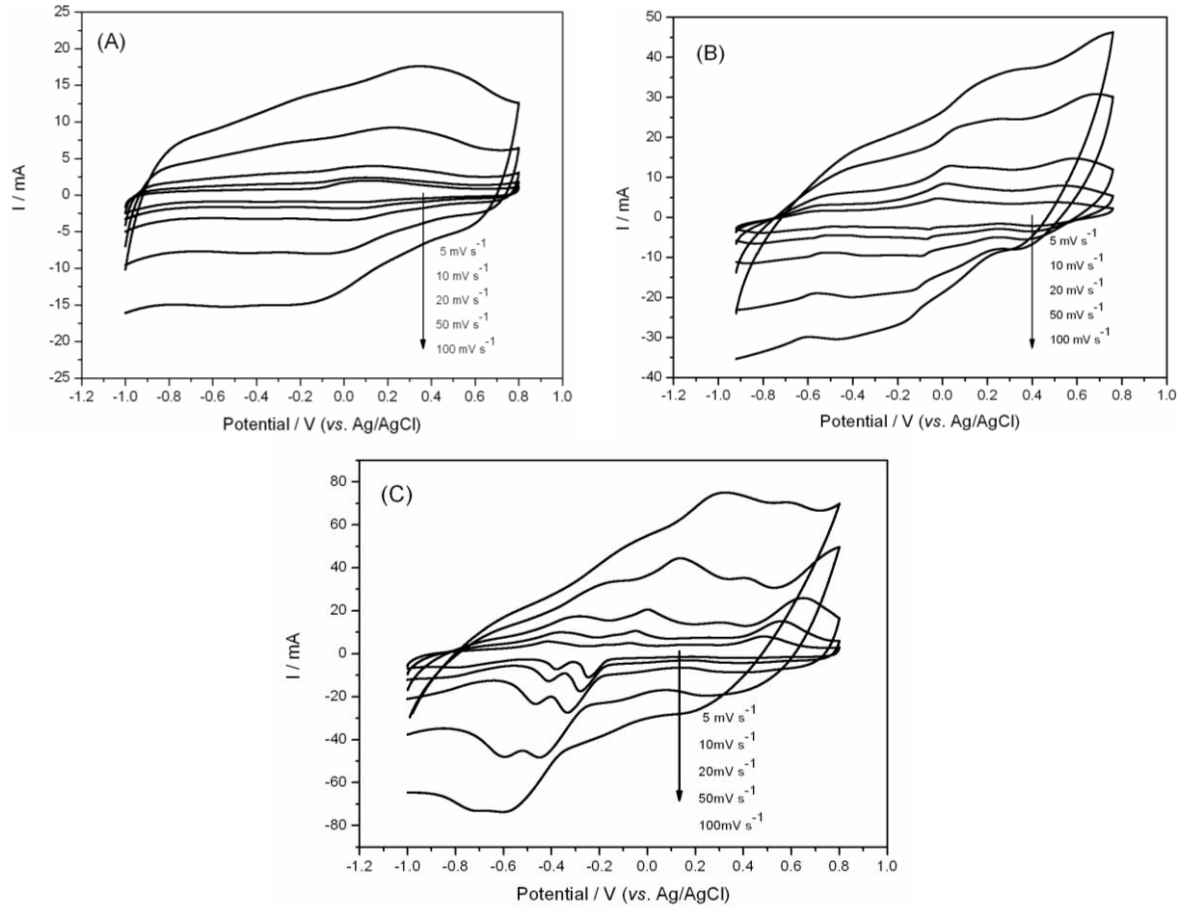

Figure 5.9 CV curves of the CNT (A) and V_2O_5 nanowire (B) and CVC-2 (C) electrodes at various potential scanning rates from 5 to 100 mV s^{-1} in 1 M Na_2SO_4 aqueous solution at

room temperature.

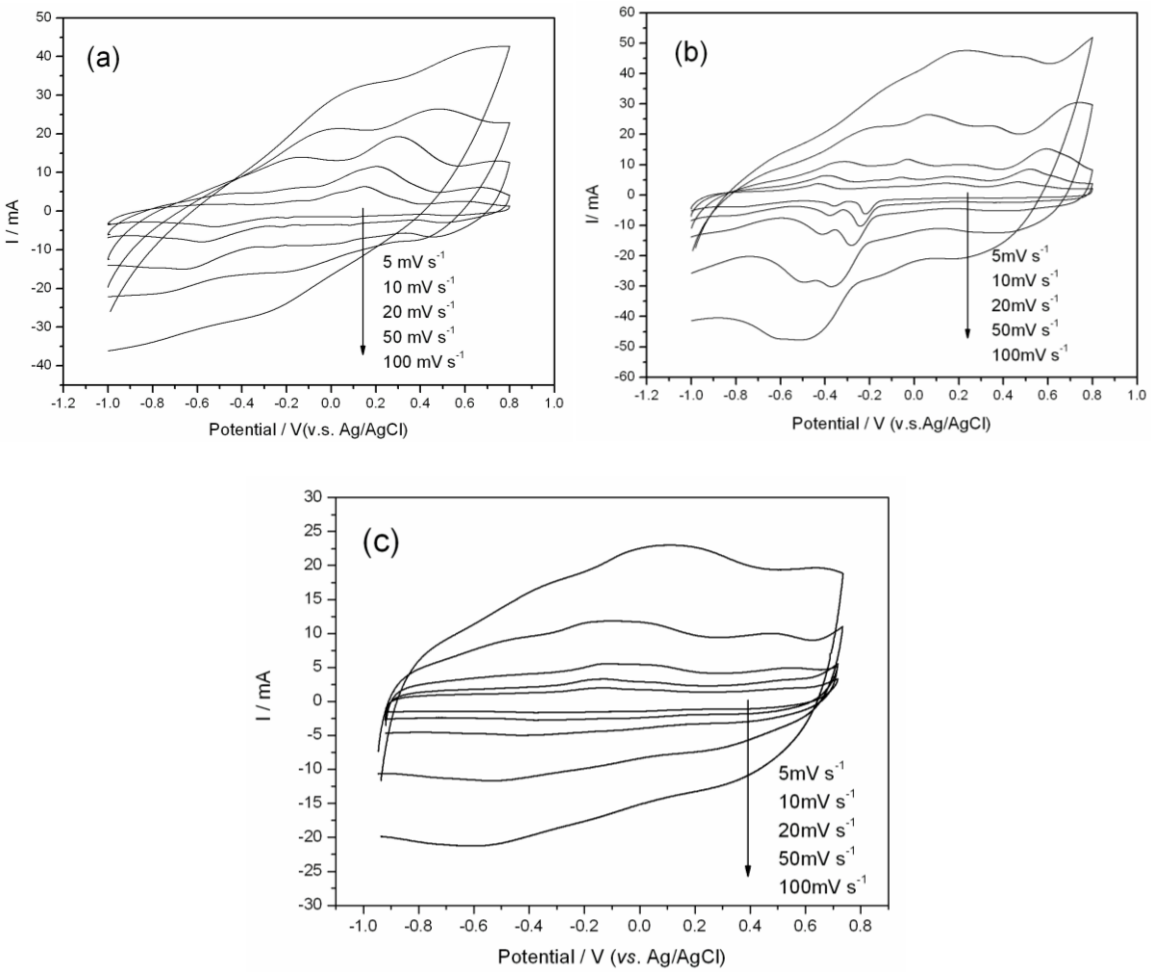

Figure 5.10 CV curves of (a) CVC-1, (b) CVC-3 and (c) CVC-4 electrodes at different potential scanning rates in 1 M aqueous Na_2SO_4 solution at room temperature.

In short, the unique composite structure integrates the high rate performance of the CNT constituent with the high capacitance of the V_2O_5 constituent, leading to the synergic energy

storage materials. Nevertheless, CNTs have low energy density whereas V_2O_5 has poor rate performance; optimization of the composition is therefore essential towards high capacitance performance. **Figure 5.11** compares the overall specific capacitance *vs.* current density of the composites with different CNT contents. The CVC-2 electrode shows the highest specific capacitance at different current densities. It affords a capacitance of 440 F g^{-1} at the current density of 0.25 A g^{-1} and preserves about 50% capacitance retention (200 F g^{-1}) even at the current density of 10 A g^{-1}. For comparison, the CNT electrode shows more than 60% capacitance retention at the same condition; however, its overall capacitance is low (55 F g^{-1} at the current density of 10 A g^{-1}). Similarly, although the V_2O_5 nanowire electrode shows a high capacitance at low discharge rates (e.g., 388 F g^{-1} at the current density of 0.25 A/g), only 20 % of the capacitance is retained at the current density of 10 A g^{-1}, showing a poor rate capability. The inserted plot in the **Figure 5.11** illustrates the V_2O_5-based specific capacitances of the composites *vs.* the V_2O_5 content at the current density of 1 A g^{-1}. The composite electrodes consistently show much higher specific capacitance than that of the pure V_2O_5 electrode, indicating that the CNT scaffold indeed facilitates the harvest of the V_2O_5 pseudocapacitance. The CVC-2 electrode exhibits the highest overall capacitance and V_2O_5-based specific capacitance. These charge-discharge behaviours are in good

consistence with the results from the cyclic voltammograms, further suggesting that improving conductivity of capacitor materials is essential towards designing better electrochemical capacitors.

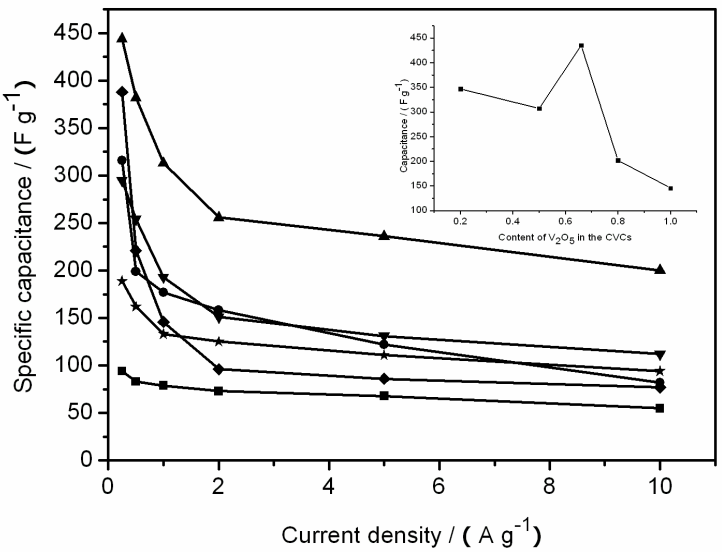

Figure 5.11 Gravimetric capacitance of the composite electrodes with different CNT contents at different current densities: CNT electrode (■), V_2O_5 nanowire electrode (◆), CVC-1 (●), CVC-2 (▲), CVC-3 (▼) and CVC-4 (★).

2.3. Device application of V_2O_5 nanowire/CNT composite

To further evaluate these nanocomposites for real device application, we assembled an asymmetric supercapacitor using CVC-2 as the anode and MnO_2/carbon composite as the cathode (see Experimental section for the preparation of MnO_2/C electrode). The typical

cyclic voltammogram of the MnO_2/C electrode are given in **Figure 5.12A**. The rectangular-shaped CV plot indicates the ideal capacitive behavior of the electrode. Galvanostaic charge-discharge curves of MnO_2/C electrode at current density of 0.1 A g^{-1} reveals that the electrode material can provide a specific capacitance of 145 F g^{-1}, as calculated from **Figure 5.12B**.

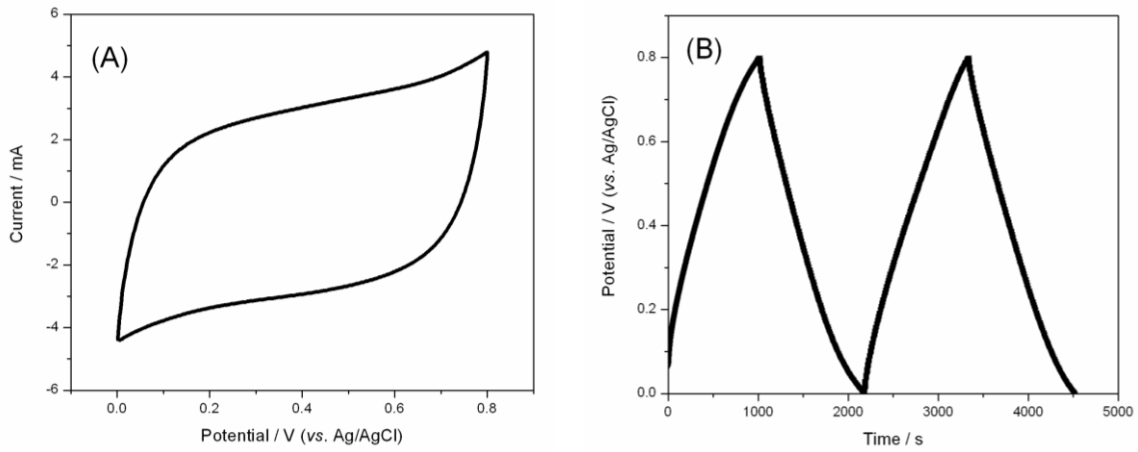

Figure 5.12 (A) CV curves of mesoporous carbon supported MnO_2 (MnO_2/C) at scanning rate of 10 mV s^{-1} in 1 M aqueous Na_2SO_4 solution and (B) Galvanostaic charge-discharge curves of MnO_2/C at current density of 0.1 A g^{-1} at room temperature.

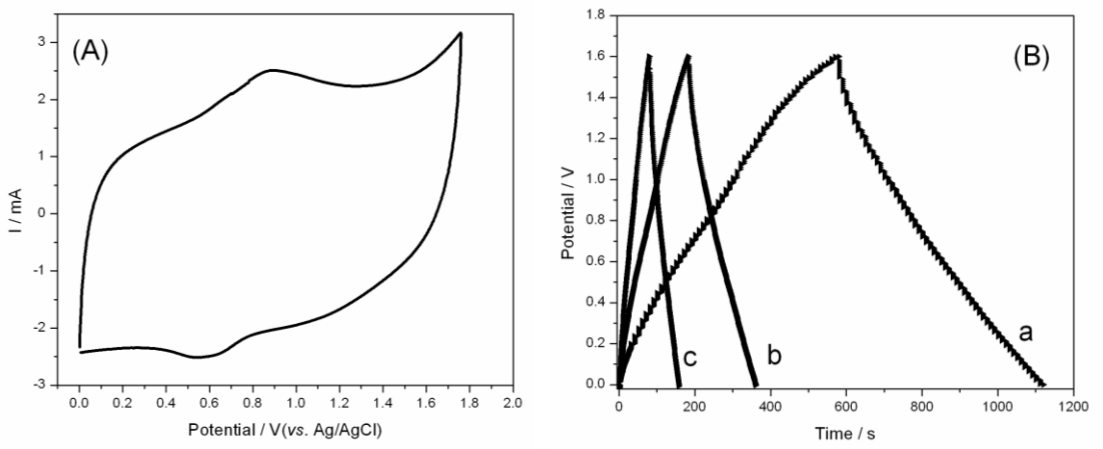

Figure 5.13 (A) CV curve of asymmetric supercapacitor consists of CVC-2 as anode and MnO_2/C as cathode at scanning rate of 10 mV s^{-1}; and (B) Galvanostaic charge-discharge of the asymmetric supercapacitor at different current densities (a-0.64 mA cm^{-2}, b-3.2 mA cm^{-2}, and c-6.4 mA cm^{-2}) in 1 M aqueous Na_2SO_4 solution at room temperature.

For the asymmetric supercapacitor consists of the CVC-2 and MnO_2/C electrodes, an ideal capacitive behavior was observed from 0~1.6 V in 1 M Na_2SO_4 (**Figure 5.13A**). A capacitance of 45 F g^{-1} (based on the total weight of the anode and cathode materials) was achieved at the discharge current density of 0.64 mA cm^{-2}, corresponding to an energy density of 16 Wh kg^{-1} at power density of 75 W kg^{-1}. The device still possesses an energy density of 5.5 Wh kg^{-1} even at power density of 3750 W kg^{-1} and retains more than 90% of the initial capacitance after 100 cycles of charge and discharge, indicative of high power

performance and good cycling stability. **Figure 5.14** shows the Ragone plot derived from the constant-current charges and discharges (**Figure 5.13B**) of the asymmetric supercapacitor, in comparison with some advanced aqueous-based supercapacitors from recent literature. The energy and power performance of this asymmetric supercapacitor are highly competetive with Ni–MH batteries and significantly improved over the current electrochemical capacitors. Considering the specific capacitance of the cathode materials (MnO_2/C) is below 150 F g^{-1} (**Figure 5.12**), an even higher energy density could be realized if a better cathode material is available. Moreover, considering that the CNT, V_2O_5 precursor, and processing can be achieved at the cost comparable to that of traditional carbon-based devices; these composites hold great promises as the next generation electrical energy storage materials.

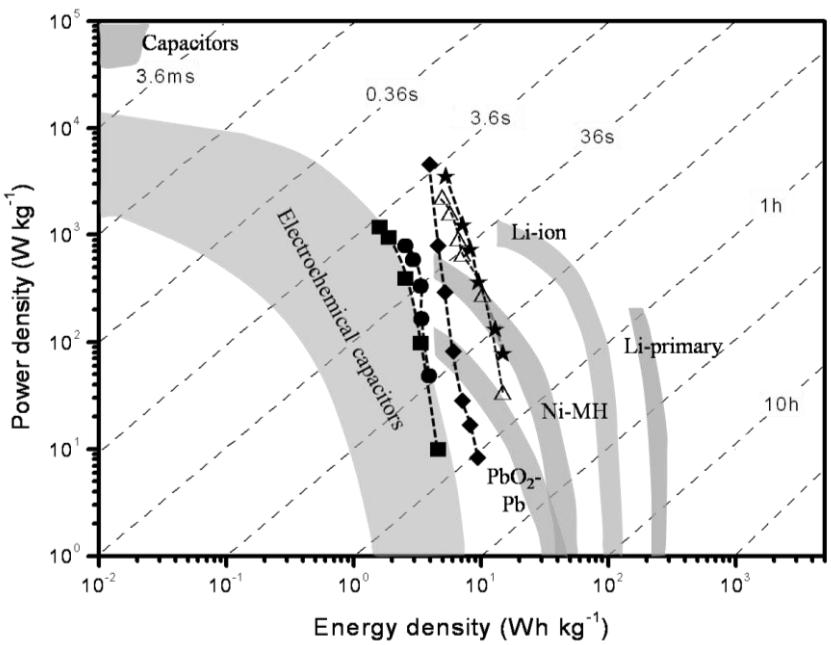

Figure 5.14 Ragone plot of the asymmetric supercapacitor (★) consisting of an CVC-2 anode and MnO_2/carbon cathode in comparison with carbon-based supercapacitors from active carbon (■),[21] mesoporous carbon CMK-3 (●),[22] hierarchical porous graphitic carbon (◆),[23] and phosphorus-enriched carbon (△).[24]

3. Conclusions

In summary, we have developed a class of supercapacitor composites based on confined growth of V_2O_5 nanowires within a conductive porous CNT scaffold. The hierarchically porous, interpenetrating network structure provides the composites with high capacitance and excellent rate performance. This design concept can be generalized towards other capacitor composites containing other low-dimensional metal oxides, such as MnO_2, Co_3O_4 and NiO, opening a new avenue for a large spectrum of device applications.

4. Experimental Section

Synthesis of the CNT/V_2O_5 Composites: Multi-wall carbon nanotubes (CNTs) were functionalized to attach carboxylic groups on the surface using a method similar to Gao [25]. Briefly, pristine CNTs (12.0 g), HNO_3 (65%, 100 mL) and H_2SO_4 (98%, 300 mL) were mixed

in a flask, vigorously stirred and reflux for 100 min. The mixture was diluted with deionized water, filtered, and re-dispersed in water. This process was repeated until the pH of the filtrate is around neutral. Then modified CNTs were dried in vacuum oven for 24 h at 80 ℃. A hydrothermal method similar to that of Xiong [26] was used to synthesize the composites. Briefly, appropriate amount of the modified CNTs, HCl (2 M, 0.5 mL), ammonium metavanadate (NH_4VO_3, 0.15 g) and surfactant P123 ($EO_{20}PO_{70}EO_{20}$, where EO and PO is ethylene oxide and propylene oxide, respectively, 0.25 g) were mixed under ultrasonication for 10 min. After stirring for 1 h, the mixtures were transferred to a 20 mL Telflon-lined autoclave and heated to 120 ℃ for 24 h. The resulted precipitates were filtered and rinsed with water and acetone for several times and dried at 80 ℃ for 12 h under vacuum. The amounts of CNTs used were varied from 0.037, 0.078, 0.15 to 0.6 g, resulting in the composites with 20, 33, 50, and 67 wt-% of the CNTs, which were denoted as CVC-1, CVC-2, CVC-3 and CVC-4, respectively.

Synthesis of mesoporous carbon supported MnO_2 (MnO_2/C): Mesoporous carbon was synthesized according to the method reported by Pang *et al* [27], using sucrose as carbon source and silica cluster and colloid as templates. Growth of MnO_2 onto the mesoporous carbon was realized according to the method reported by Long *et al* [28]. Simply,

as-prepared mesoporous carbon (0.1 g) was soaked into a flask containing $KMnO_4$ aqueous solution (0.1 M, 100 mL) under vacuum for 10 min. The mixture was kept stirring at 50 ℃ for 2 h for direct growth of MnO_2 onto the carbon surface. After reaction, the as-derived powder was washed by deionized water for several times and dried at vacuum at 80 ℃ for 12 h.

Material and Electrode Characterization: The X-ray diffraction measurements were taken on Panalytical X'Pert Pro X-ray powder diffractometer using the copper Kα radiation (λ=1.54 Å). Nitrogen sorption isotherms were measured at 77 K with a Micromeritics ASAP 2020 analyzer. The samples were degassed in vacuum at 180 ℃ for three hours. The specific surface areas (S_{BET}) were calculated by the Brunauer-Emmett-Teller (BET) method using adsorption branch in a relative pressure range from 0.04 to 0.25. The pore size distributions (D_p) were derived from the adsorption branches of isotherms using the Barrett-Joyner-Halenda (BJH) model. Scanning electron microscopy (SEM) experiments were conducted on a JEOL JSM-6700 FE-SEM. Transmission electron microscopy (TEM) experiments were conducted on a Philips CM120 operated at 120 kV.

The V_2O_5 nanowire/CNT composites or MnO_2/C were assembled onto foam nickel collectors to fabricate porous electrodes (see photograph of V_2O_5 nanowire/CNT electrode in

Fig. S1b). Briefly, 80% of the testing materials, 10% carbon black, and 10% poly(vinylidene fluoride) (PVDF) dispersed in N-methylpyrrolidinone (NMP) were mixed to form slurries. The slurries were ultrasonically treated at 60℃, coated on a nickel foam substrate, and dried at 80 ℃ for 10 min under vacuum. As formed electrodes were then pressed at a pressure of 2 M Pa cm^{-2} and further dried under vacuum at 100 ℃ for 12 h. The electrochemical measurements were conducted in a Princeton VMP3 electrochemistry workstation. Cyclic voltammetry measurements were conducted in 1 M Na_2SO_4 aqueous solution at room temperature using a platinum wire as the counter electrode and an Ag/AgCl electrode as the reference electrode. The specific capacitance (*C*) of the electrode materials were derived from $C = I/(dE/dt) \approx I/(\Delta E/\Delta t)$, where *I* is the constant discharge current density, *E* is cell voltage, and *dE/dt* is slope of the discharge curve.

Reference

[1] B. E. Conway, *Electrochemical Supercapacitors, Scientific Fundamentals and Technological Applications*. Kluwer Academic/Plenum, New York **1999**.

[2] J. R. Miller, A. F. Burke, *The Electrochemical Society Interface* **2008**, *17*, 53.

[3] a) T. A. Centeno, F. Stoeckli, *J. Power Source* **2006**, *154*, 314. b) E. Frackowiak, *Phys.*

Chem. Chem. Phys. **2007**, *9*, 1774.

[4] a) K. Jurewicz, C. Vix-Guterl, E. Frackowiak, S. Saadallah, M. Reda, J. Parmentier, J. Patarin, F. Béguin, *J. Phys. Chem. Solids* **2004**, *65*, 287. b) A. B. Fuertes, G. Lota, T. A. Centeno, E. Frackowiak, *Electrochim. Acta* **2005**, *50*, 2799. c) H. Q. Li, R. L. Liu, D. Y. Zhao, Y. Y. Xia, *Carbon* **2007**, *45*, 2628.

[5] a) C. S. Du, N. Pan, *Nanotechnology* **2006**, *17*, 5314. b) G. Lota, K. Lota, E. Frackowiak, *Electrochem. Comm.* **2007**, *9*, 1828.

[6] a) K. H. An, W. S. Kim, Y. S. Park, Y. C. Choi, S. M. Lee, D. C. Chung, D. J. Bae, S. C. Lim, Y. H. Lee, *Adv. Mater.* **2001**, *13*, 497. b) D. N. Futaba, K. Hata, T. Yamada, T. Hiraoka, Y. Hayamizu, Y. Kakudate, O. Tanaike, H. Hatori, M. Yumura, S. Iijima, *Nat. Mater.* **2006**, *5*, 987.

[7] a) J. P. Zheng, P. J. Cygan, T. R. Jow, *J. Electrochem. Soc.* **1995**, *142*, 2699. b) C. C. Wang, C. C. Hu, *Electrochim. Acta* **2005**, *50*, 2573. c) V. Subramanian, S. C. Hall, P. H. Smith, B. Rambabu, *Solid State Ionics* **2004**, *175*, 511.

[8] a) S. C. Pang, M. A. Anderson, T. W. Chapman, *J. Electrochem. Soc.* **2000**, *147*, 444. b) M. Toupin, T. Brousse, D. Bélanger, *Chem. Mater.* **2004**, *16*, 3184. c) M. Nakayama, T. Kanaya, R. Inoue, *Electrochem. Comm.* **2007**, *9*, 1154. d) V. Subramanian, H. W. Zhu, B. Q.

Wei, *J. Power Source* **2006**, *159*, 361.

[9] a) K. C. Liu, M. A. Anderson, *J. Electrochem. Soc.* **1996**, *143*, 124. b) K. W. Nam, K. B. Kim, *J. Electrochem. Soc.* **2002**, *149*, 346. b) J. W. Lang, L. B. Kong, W. J. Wu, Y. C. Luo, L. Kang, *Chem. Comm.* **2008**, *35*, 4213.

[10] C. Lin, J. A. Ritter, B. N. Popov, *J. Electrochem. Soc.* **1998**, *145*, 4097.

[11] a) R. N. Reddy, R. G. Reddy, *J. Power Sources* **2006**, *156*, 700. b) Z. J. Lao, K. Konstantinov, Y. Tournaire, S. H. Ng, G. X. Wang, H. K. Liu, *J. Power Sources* **2006**, *162*, 1451.

[12] a) Y. G. Wang, H. Q. Li, Y. Y. Xia, *Adv. Mater.* **2006**, *18*, 2619. b) S. R. Silvakumar, W. J. Kim, J. A. Choi, D. R. MacFarlance, M. Forsyth, D. W. Kim, *J. Power Sources* **2007**, *171*, 1062.

[13] Y. Sato, K. Yomogida, T. Nanaumi, K. Kobayakawa, Y. Ohsawa, M. Kawai, *Electrochem. Solid-State Lett.* **2000**, *3*, 113.

[14] X. P. Dong, W. H. Shen, J. L. Gu, L. M. Xiong, Y. F. Zhu, H. Li, J. Lin, Shi, *J. Phys. Chem. B* **2006**, *110*, 6015.

[15] I. H. Kim, J. H. Kim, Y. H. Lee, K. B. Kim, *J. Electrochem. Soc.* **2005**, *152*, 2170.

[16] H. Zhang, G. P. Cao, Z. Y. Wang, Y. S. Yang, Z. J. Shi, Z. N. Gu, *Nano Lett.* **2008**, *8*,

2664.

[17] I. H. Kim, J. H. Kim, B. W. Cho, Y. H. Lee, K. B. Kim, *J. Electrochem. Soc.* **2006**, *153*, A989.

[18] E. Frackowiak, *App. Phys. Lett.* **2000**, *77*, 2421.

[19] W. Sugimoto, H. Iwata, Y. Yasunaga, Y. Murakami, Y. Takasu, *Angew. Chem. Int. Ed.* **2003**, *42*, 4092.

[20] a) F. Huguenin, E. M. Girotto, G. Ruggeri, R. M. Torresi, *J. Power Sources* **2003**, *114*, 133. b) M. Malta, G. Louarn, N. Errien, R. M. Torresi, *J. Power Sources* **2006**, *156*, 533.

[21] Y. G. Wang, Y. Y. Xia, *Electrochem. Comm.* **2005**, *7*, 1138.

[22] W. Xing, S. Z. Qiao, R. G. Ding, F. Li, G. Q. Lu, Z. F. Yan, H. M. Cheng, *Carbon* **2006**, *44*, 216.

[23] D. W. Wang, F. Li, M. Liu, G. Q. Lu, H. M. Cheng, *Angew. Chem. Int. Ed.* **2008**, *47*, 373.

[24] D. Hulicova-Jurcakova, A. M. Puziy, O. I. Poddubnaya, F. Suárez-García, J. M. D. Tascón, G. Q. Lu, *J. Am. Chem. Soc.* **2009**, *131*, 5026.

[25] C. Gao, C. D. Vo, Y. Z. Jin, W. W. Li, S. P. Armes, *Macromolecules* **2005**, *38*, 8634.

[26] C. R. Xiong, A. E. Aliev, B. Gnade, K. J. Balkus Jr., *ACS NANO* **2008**, *2*, 293.

[27] J. B. Pang, Q. Y. Hu, Z. W Wu, J. E. Hampsey, J. B He, Y. F. Lu, *Micropor. Mesopor. Mater.* **2004**, *74*, 73.

[28] A. E. Fischer, K. A. Pettigrew, D. R Rolison, R. M. Stroud, J. W. Long, *Nano Lett.* **2007**, *7*, 281.

Chapter 6: Asymmetric Hybrid Lithium-ion Supercapacitors Based on Intertwined CNT/V_2O_5 Nanowire Composites

1. Introduction

An ideal electrical energy storage device provides both high energy and power density.[1,2] Supercapacitors exhibit significantly higher power densities compared to batteries and would be excellent candidates for numerous electronic devices and industrial applications if their energy density could be improved.[3,4] Since the energy density (E) of a capacitor is governed by $E=1/2\ CV^2$, where C is the capacitance and V is the cell potential, increasing the potential or capacitance leads to higher energy density.[5] In this context, the most commonly used electrode material (porous carbon) generally possesses double layer capacitances of around 100 F g^{-1}, which can provide a specific energy density up to 25 Wh kg^{-1} in an organic-electrolyte based symmetric device. Somewhat greater energy densities can be reached as specific capacitances of up to 150 F g^{-1} with carbide-derived carbon have been reported.[6] By comparison, transition-metal oxides possess significantly higher specific capacitance via pseudocapacitance. For example, RuO_2,[7] MnO_2[8] and NiO[9] have demonstrated specific capacitances up to 1300, 1200, and 940 F g^{-1}, respectively. Thus, an

asymmetric supercapacitor consisting of a carbon cathode and an oxide anode may provide a significantly higher energy density than symmetric capacitors based on carbon; asymmetric cells containing an anode of $Li_4Ti_5O_{12}$ and a cathode of activated carbon (AC) can provide an energy density in excess of 35 Wh kg^{-1}.[10,11] Nevertheless, building such high-energy density asymmetric devices has been highly challenging, mainly due to the kinetics of the pseudocapacitive electrode. In order to minimize the kinetic limitations, most of the pseudocapacitive electrodes made today are limited to sub-micron thin films.[8,12-15] Since the electrochemically inert components of a supercapacitor, including the current collectors, separator, and packaging, account for a large fraction of the total weight of the device, the use of thin electrodes results in a significantly lower energy density than what could be attained using thicker electrodes.[3] Therefore, the development of thick electrodes for supercapacitors represents an important direction for making high-energy supercapacitors for practical applications.

We have recently developed a class of pseudocapacitive anode materials for asymmetric supercapacitors composed of interpenetrating networks of carbon nanotubes (CNTs) and V_2O_5 nanowires.[16] The CNTs and nanowires were intimately intertwined into a hierarchically porous structure, enabling effective electrolyte access to the electrochemically

active materials without limiting charge transport. Such composites exhibited high specific capacitance (>300 F g^{-1}) at high current density (1 A g^{-1}) in aqueous electrolyte. In this paper we report the fabrication of high energy-density asymmetric supercapacitors containing thick-film electrodes (over 100 μm thick) of our CNT/V_2O_5 nanowire composite in combination with an organic electrolyte, which allows for a higher initial cell potential. The excellent conductivity, high specific capacitance, and large voltage window of the CNT/V_2O_5 nanocomposite enable the fabrication of devices with an energy density as high as 40 Wh kg^{-1} at a power density of 210 W kg^{-1}. Even at a high power density of 6300 W kg^{-1}, the device possesses an energy density of nearly 7.0 Wh kg^{-1}. Moreover, the resulting devices exhibit excellent cycling stability. This work demonstrates that the nanowire composite approach is an effective strategy towards high-energy and high-power density supercapacitors.

2. Results and Discussion

Figure 6.1A shows a representative scanning electron microscope (SEM) image of a nanocomposite with 18 wt-% of CNTs, demonstrating a continuous fibrous structure (**Figure 6.1A**). The intertwined networks of the CNTs and nanowires exhibit an electrical conductivity of ~3.0 S cm^{-1}, which is 80 times higher than that of V_2O_5 nanowires (0.037 S

cm^{-1}). **Figure 6.1B** is a transmission electron micrograph (TEM) of a V_2O_5 nanowire with a diameter of around 50 nm. The high-resolution TEM (HRTEM) image (inset) suggests the nanowire contains a layered crystalline structure; the small nanowire dimension allows effective Li^+ diffusion. Moreover, nitrogen sorption isotherms (**Figure 6.2**), and higher resolution SEM of the etched composite film (**Figure 6.1A**, inset) show that the composite possesses a hierarchically porous structure; the presence of large pores enables rapid electrolyte transport while the small pores provide large area of oxide surface. The latter is responsible for the surface area of 125 m^2 g^{-1} determined for the composite.

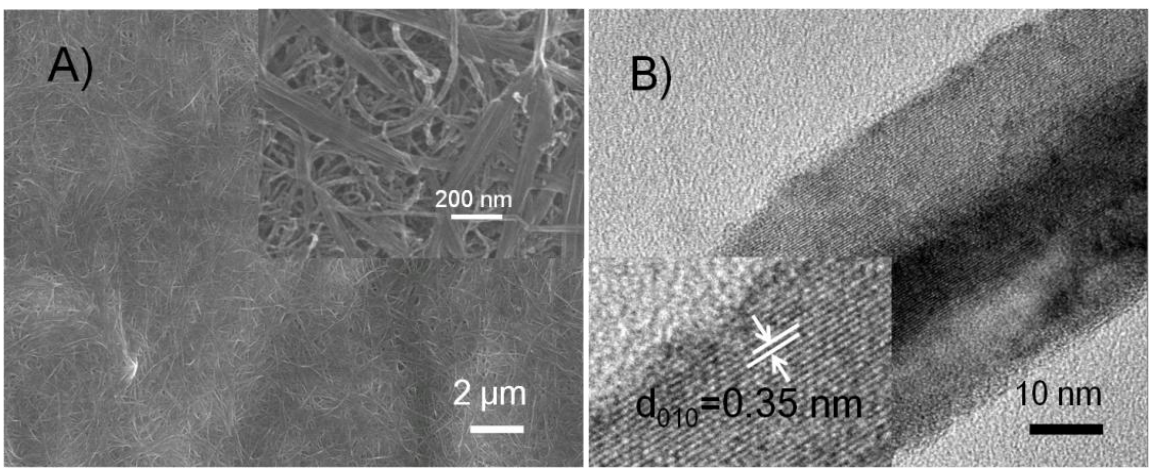

Figure 6.1 (A) SEM images of a representative CNT/V_2O_5 nanocomposite film containing 18 wt-% of CNTs, and the same film etched by 1 wt- % HF (inset); (B) TEM and HRTEM (inset) images of a V_2O_5 nanowire with a layered crystalline structure.

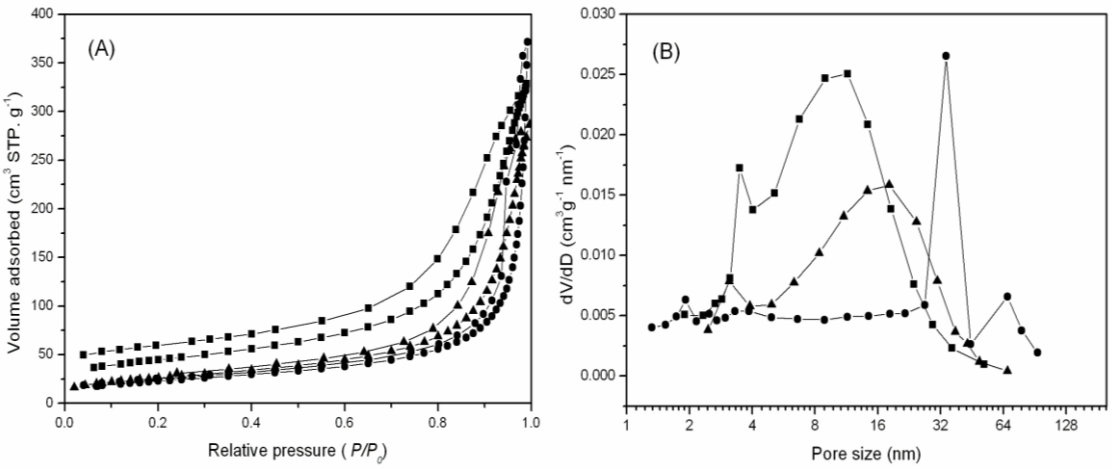

Figure 6.2 Nitrogen sorption isotherms (A) and pore size distributions (B) of CNTs (■), V_2O_5 nanowires (●) and CNT/V_2O_5 nanocomposites (▲).

The electrochemical behavior of the composite was investigated using three-electrode cells, in which lithium foils were used as both the counter and reference electrodes. Charge storage behavior was characterized by cyclic voltammetry (CV). The electrochemical Li^+ insertion process occurring at V_2O_5 electrodes can be expressed by $V_2O_5 + xLi^+ + xe^- \leftrightarrow Li_xV_2O_5$, where x is the mole fraction of inserted lithium ions.[17] **Figure 6.3A** compares the cyclic voltammograms of V_2O_5 nanowire, CNT and CNT/V_2O_5 nanocomposite electrodes. The nanowire electrode shows two pairs of broad, symmetric, and well-separated redox peaks, indicating sluggish lithium ion insertion/de-insertion kinetics.[18] In contrast, the nanocomposite electrode shows two pairs of well defined redox

peaks (anodic peaks at 2.8 and 3.0 V, with corresponding cathodic peaks at 2.4 and 2.7 V). The shift of anodic and cathodic peaks to the lower and higher potentials, respectively, is consistent with electrode polarization. The improved electrode kinetics observed in the nanocomposite electrode is associated with the presence of a hierarchical pore structure and more importantly, increased conductivity, which is strongly supported by recent studies on CNT-loaded V_2O_5 nano-crystals[19] and carbon nanofiber (CNF)-grafted nano-crystalline $Li_4Ti_5O_{12}$.[20] In comparing the cyclic voltammograms, it is evident that the charge storage behavior of the nanocomposite is not due to a simple addition of the current response of the CNT and nanowire electrodes. It is interesting to note that the peak potentials of the nanowire and nanocomposite electrodes are close to those reported for V_2O_5 aerogel- or xerogel-based thin film electrodes (anodic peaks at 2.8 V),[21,22] which are much lower than those of a crystalline V_2O_5 electrode (anodic peaks at 3.4 and 3.2 V respectively),[19] suggesting its application as an anode in asymmetric devices.

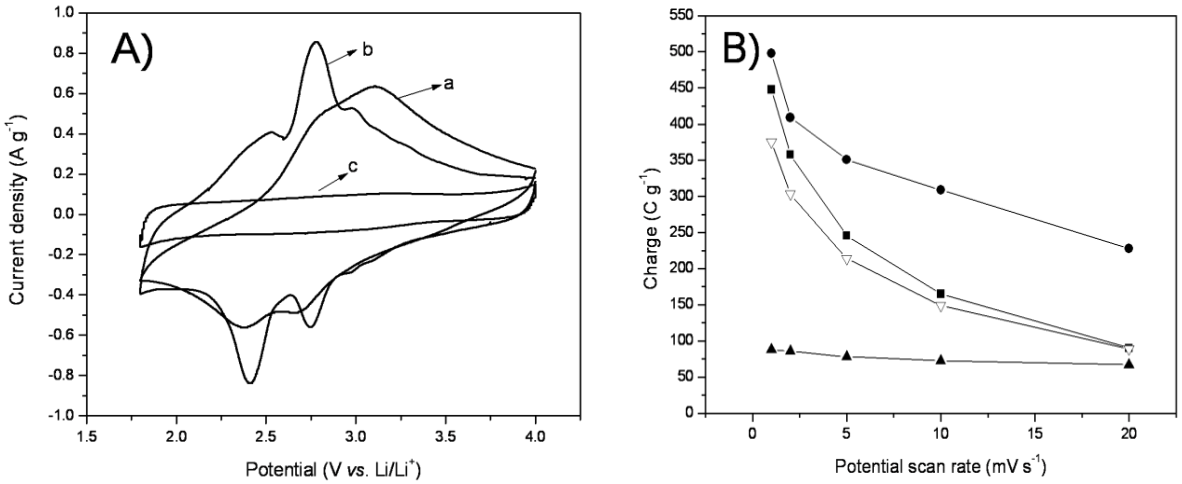

Figure 6.3 (A) Cyclic voltammograms of the electrodes made of (a) V_2O_5 nanowires, (b) CNT/V_2O_5 nanocomposite and (c) CNTs at a potential scan rate of 2 mV s^{-1}; (B) Comparison of the rate capability of V_2O_5 nanowires (■), CNT/V_2O_5 nanocomposite (●), CNTs (▲) based electrodes, and total charge storage by simply adding the capacity contribution of each constituent of the composite electrode (▽).

To further explore the charge storage ability, all the electrodes were first charged and discharged at slow rates. At a charge/discharge time of 2000 seconds, the CNT electrode gave a capacity of 86 C g^{-1} between 1.8 and 4.0 V (**Figure 6.4**). For the nanowire electrode, at a charge/discharge time of 4 hours (C/4 rate), the electrode provided a total charge storage of 792 C g^{-1}, which corresponds to a specific capacity of 220 mAh g^{-1}. This value is comparable to that of crystalline V_2O_5 prepared at higher temperatures.[19,23] Considering

that 18 wt-% of CNTs were incorporated into the composite, the nanocomposite electrode should exhibit a capacity of 663 C g^{-1} by simply adding the capacity contribution of each constituent. This behavior was observed in galvanostatic experiments which showed that the nanocomposite electrode exhibited a capacity of 650 C g^{-1} indicating that each constituent contributes independently to the total charge storage at slow charge and discharge rates.

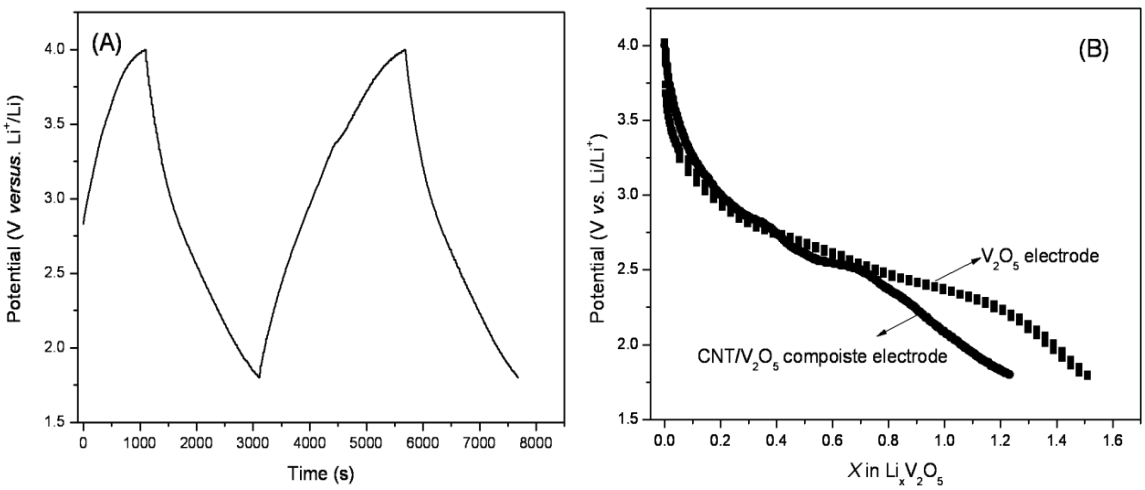

Figure 6.4 Galvanostatic experiments. (A) Charge-discharge curves of pretreated CNT electrode at a charge/discharge of 2000 seconds and (B) lithium insertion into V_2O_5 nanowire and the nanocomposite electrodes at a C/4 rate.

Much more interesting results were obtained in characterizing the rate capability of the nanocomposite electrode. In these experiments, CVs were carried out at different sweep rates with the areas under the curves used to determine the total electrode capacity.[24]

Figure 6.3B compares the charge storage of nanowire, CNT, and nanocomposite electrodes at sweep rates ranging from 1 to 20 mV s^{-1} (equal to charge/discharge times from 2200 to 110 s, respectively). As expected, the CNT electrode shows very high rate capability but low capacitance as there is only capacitive storage arising from the electrical double-layer (**Figure 6.5**). At 1 mV s^{-1}, the CNT and nanowire electrodes show capacities of 85 and 448 C g^{-1}, respectively. Simply adding the capacity contribution of each constituent at this sweep rate would give a capacity of 383 C g^{-1}, which is significantly lower than that measured for the composite electrode (498 C g^{-1}, x=0.89). Interestingly, the measured capacity of the nanocomposite electrode is even higher than that of the pure V_2O_5 nanowire electrode, suggesting that the addition of the CNTs leads to improved charge transfer for the V_2O_5 nanowires. This effect becomes more pronounced at higher scan rates. At 20 mV s^{-1} the V_2O_5 nanowire electrode exhibits only 20 % (90 C g^{-1}) of the capacity measured at 1 mV s^{-1}. In contrast, the CNT/V_2O_5 nanocomposite electrode exhibits substantially higher capacity (228 C g^{-1}) at 20 mV s^{-1}, which is nearly 50% of its value at 1 mV s^{-1}. This high rate capability is consistent with the notion that the CNTs effectively 'wire' the V_2O_5 to provide enhanced electronic conductivity, leading to increased rates of charge transfer, thus making these materials of potential interest for supercapacitor applications.

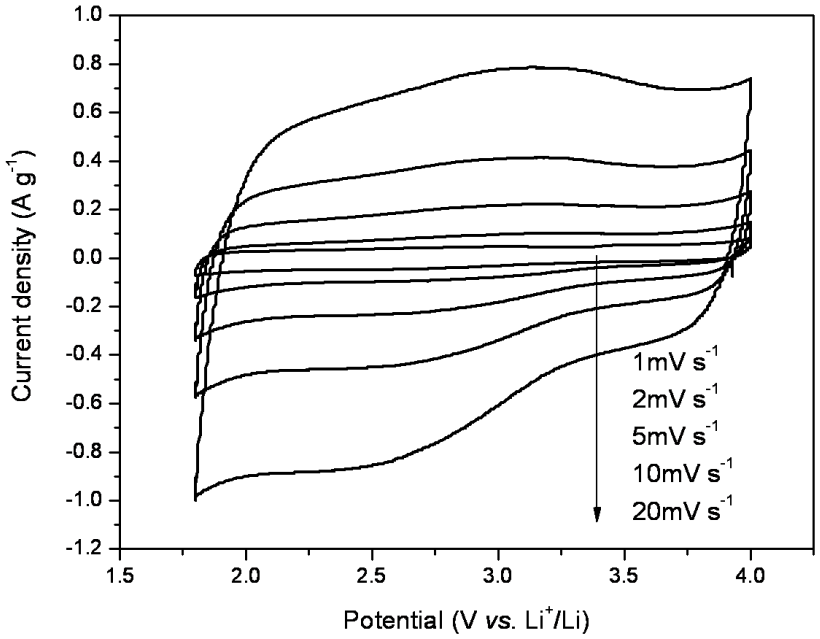

Figure 6.5 Cyclic voltammograms of the electrodes made of pure pretreated CNTs.

It is worth mentioning that the intercalation of Li^+ into the V_2O_5 solid phase is intrinsically slow, with a reported diffusion coefficient on the order of 10^{-13} cm^2 s^{-1}.[25] The maximum diffusion length of Li^+ at the time scale of 100 s is approximately 45 nm, which is close to the diameter of the V_2O_5 nanowires. However, our voltammetry results with the V_2O_5 nanowires show that insertion of one equivalent of lithium per vanadium requires a time scale longer than 2200 s. The poor rate capability observed for the nanowire electrode can arise from poor charge transfer. The low electrical conductivity of a thick electrode ($\sigma \approx 10^{-5}$-10^{-3} Ω^{-1} cm^{-1})[17] results in large uncompensated ohmic drops during fast charging and

discharging.[26] Intimately intertwining the nanowires with the highly conductive CNTs leads to composite electrodes which support high rate capability without compromising high energy density.

To assess the feasibility of using the composites for actual device fabrication, we assembled asymmetric supercapacitors using the CNT/V_2O_5 nanocomposite as an anode and a commercial AC as the cathode material. **Figure 6.6A** compares the Ragone plots derived from constant-current charge/discharge characteristics for different prototype supercapacitors (see **Figure 6.7**), along with symmetric supercapacitors made from AC for comparison. For the asymmetric device made from the nanocomposite anode, using a discharge current density of 0.5 mA cm^{-2} (corresponding to a power density of 210 W kg^{-1}) we obtain an energy density of 40 Wh kg^{-1}. Even at a power density of 6300 W kg^{-1} (charge and discharge time of 4 s), the device still possesses an energy density of 6.9 Wh kg^{-1}, an indication of its high-power performance. The energy and power performance of this asymmetric supercapacitor is competitive with that of graphitic carbon,[27] $Li_4T_5O_{12}$[28] or other metal oxide based hybrid systems[29], and represents a significant improvement over the current state-of-the-art electric double-layer capacitor (EDLC) technology. Also shown here are

recent results for CNF-grafted nano-crystalline $Li_4T_5O_{12}$-based hybrid supercapacitors. The improvement in energy and power density compared to other $Li_4T_5O_{12}$ electrodes is due to the increased electrical conductivity.[20]

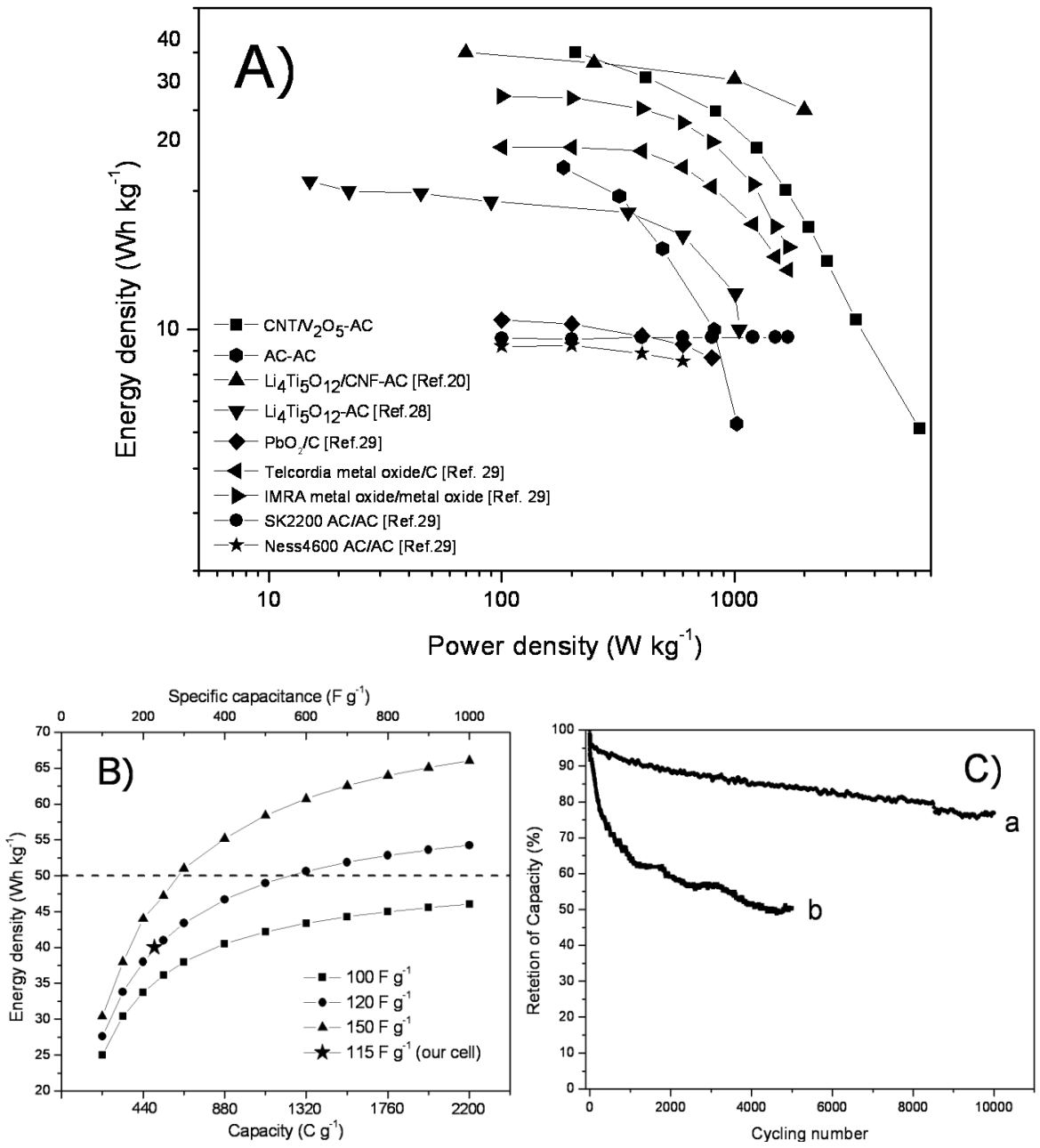

Figure 6.6 (A) Ragone plots of an asymmetric supercapacitor made from AC cathode and CNT/V_2O_5 nanocomposite anode, a symmetric supercapacitor made from the same AC, and various supercapacitor types developed recently. All the data is based on the mass of electrode materials. For the devices reported in Reference [29], the mass of the electrode materials was estimated to be 40% of the total device weight. A packaging factor on the order of 0.4 has been used by several authors [15, 30-31]; (B) Calculated maximum energy density *vs.* the anode capacitance at a cathode capacitance of 100, 120 and 150 F g^{-1}, respectively, at a cell voltage of 2.7 V; (C) Long-term cycling performance of the asymmetric devices based on (a) a nanocomposite anode and AC cathode and (b) a nanowire anode and AC cathode operated at cell potential of 2.7 V.

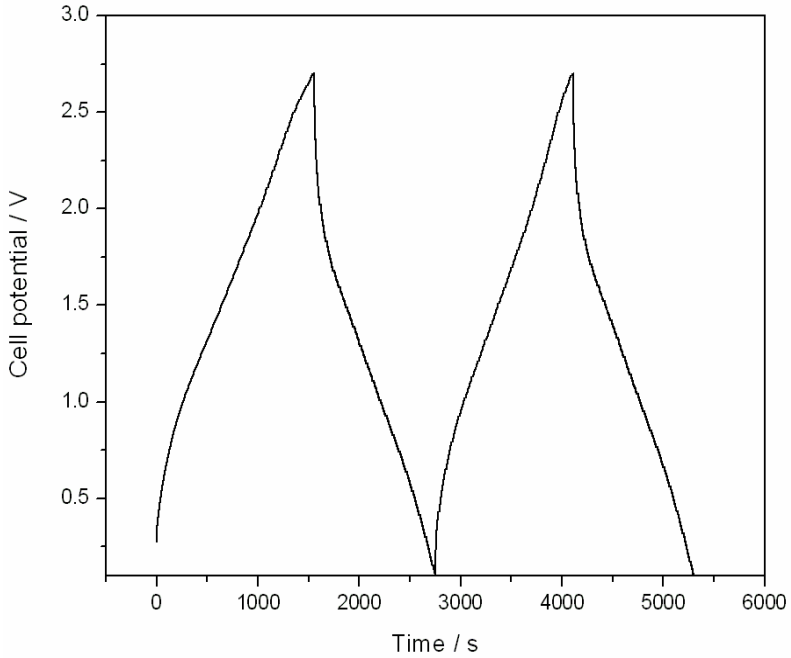

Figure 6.7 Constant current charge/discharge curves for an asymmetric CNT/V_2O_5-AC supercapacitor. The devices were discharged and charged at a power density of 210 W kg^{-1}.

An important question to address for this technology is what directions will be necessary to further improve energy density. As shown above, the energy density of a supercapacitor is governed by the overall capacitance (*C*) and the operating voltage (*V*). Assuming a fixed potential window of 2.7 V (a typical operating voltage for supercapacitors using organic electrolytes) and a specific capacitance for the AC cathode of 100, 120 or 150 F g^{-1}, the maximum energy densities (E_{max}) of the capacitors can be calculated by adjusting the mass ratio of the cathode and anode to achieve a balanced charge on both electrodes.[5,32] **Figure**

6.6B plots the E_{max} *vs.* the specific capacitance of the anode for the different cathode capacitances. The results indicate that an increase in E_{max} occurs with increasing specific capacitances for both electrodes. However, for a device built with a carbon cathode of specific capacitance less than 100 F g^{-1}, E_{max} is below 50 Wh kg^{-1} irrespective of how much charge can be stored in the anode. In our devices, the specific capacitances of the cathode and anode are considered to be 115 and 288 F g^{-1}, respectively, leading to a theoretical E_{max} of 42 Wh kg^{-1}. This value is in good agreement with the energy density measured (40 Wh kg^{-1}) for our asymmetric supercapacitor. In order to boost the energy density to 50 Wh kg^{-1}, the specific capacitance of the cathode has to be increased or the operating potential window has to be broadened.

In addition to demonstrating high energy density and high power, the asymmetric devices based on the CNT/V_2O_5 nanocomposite electrode also exhibit excellent cycling properties. **Figure 6.6C** shows the cycling behavior for asymmetric devices which use either a composite anode or a V_2O_5 nanowire anode. The device with the CNT/V_2O_5 nanocomposite electrode retained ~80% of the initial energy density after 10,000 cycles at a 30 C charge/discharge rate (power density of 820 W kg^{-1}), while the nanowire-based device retained only ~50% of its initial energy density after 5,000 cycles. The long cycling life

observed for the nanocomposite electrode is attributed to the unique intertwined CNT/nanowire structure. It has been commonly observed that nano-dimensional materials, such as MnO_2 nanoparticles, may lose most of their initial capacitance during cycling, mainly due to agglomeration and reduced surface area exposed to the electrolyte.[8] For the V_2O_5 nanowire electrode, the observed degradation in capacity may be attributed to a similar mechanism. However, the formation of intimately intertwined CNT/nanowire networks effectively provides the composite electrode with structural integrity, as agglomeration is suppressed and long-term charge storage is achieved.

3. Conclusion

In summary, we have designed and fabricated asymmetric supercapacitors based on using a thick-film CNT/V_2O_5 nanowire composite anode and commercial AC-based cathode in combination with an organic electrolyte. The nanocomposite electrode exhibits excellent rate capability, high capacity and cycling stability. A prototype asymmetric supercapacitor showed an energy density of 40 Wh kg^{-1} at a power density of 210 W kg^{-1}, and a maximum power density of 20 kW kg^{-1}. The overall energy and power performance of such an asymmetric cell is superior to the current technology based on electric double layer capacitors

(EDLCs). The improvement in energy density without compromising power density suggests that this supercapacitor approach may be attractive for a wide range of device applications. This work also validates the nanocomposite approach for the design and fabrication of new types of higher-energy and high-power electrochemical devices using heterogeneous nanocomposite materials.

4. Experimental

4.1 Synthesis of the CNT/V_2O_5 Composites

This CNT/V_2O_5 nanocomposite was synthesized through a one-pot hydrothermal process using aqueous vanadium-oxide precursors in the presence of pre-treated hydrophilic CNTs. Grams of this composite were produced using a lab-scale reactor. Details of the materials synthesis were described in our previous publication [16]. The composition of the CNT/V_2O_5 composite was determined by thermogravimetric analysis (TGA, **Figure 6.8**). Nitrogen sorption isotherms were measured at 77 K with a Micromeritics ASAP 2020 analyzer. The specific surface areas (S_{BET}) were calculated by the Brunauer-Emmett-Teller (BET) method using an adsorption branch in a relative pressure range from 0.04 to 0.25. Scanning electron microscopy (SEM) experiments were conducted on a JEOL JSM-6700

FE-SEM. Transmission electron microscopy (TEM) experiments were conducted on a Philips CM120 operated at 120 kV.

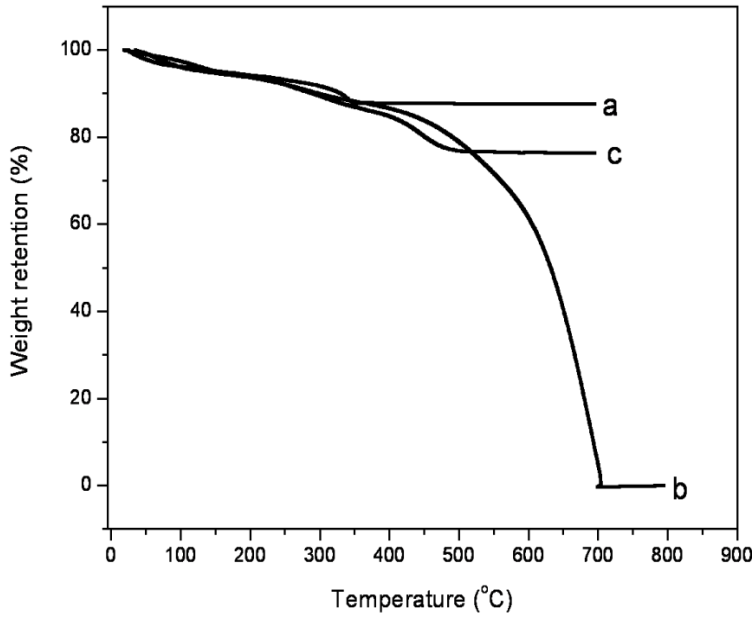

Figure 6.8 Thermogravimetric analysis for electrodes made of V_2O_5 nanowires (a), pre-treated CNTs (b) and CNT/V_2O_5 composites (c).

4.2. Electrode Fabrication and Electrochemical Measurements

The V_2O_5 nanowires, CNT/V_2O_5 nanowire composites or AC were assembled onto nickel foam current collectors. The AC (S_{BET} =1900 m^2 g^{-1}) has a gravimetric capacitance of 115 and 61 F g^{-1} at CV scan rates of 1 and 20 mV s^{-1} (**Figure 6.9**), respectively. Briefly, 80% of the electrochemically active material, 10% carbon black, and 10% poly(vinylidene fluoride) (PVDF) dispersed in N-methylpyrrolidinone (NMP) were mixed to form slurries. The

homogenous slurries were coated on a nickel foam substrate and dried at 80 ^{o}C for 10 min under vacuum. As formed electrodes were then pressed at a pressure of 2 MPa cm^{-2} and further dried under vacuum at 100 ^{o}C for another 12 h. Thick electrodes were obtained by coating an active mass of 3~5 mg on each current collector: a nanocomposite electrode with an active mass of 3.8 mg has a thickness of ~120 μm (**Figure 6.10**). The electrochemical measurements were carried out on a Solartron 1860/1287 Electrochemical Interface. The electrolyte solution was a 1 M $LiClO_4$ in propylene carbonate (PC) solution and lithium foils were used as both the counter and reference electrodes. CV measurements were carried out in an argon-filled glove box using cutoff voltages of 4.0 and 1.8 V versus Li/Li^{+}. To make 2032 type coin cells, glass fiber (GF/D) from Whatman was used as the separator. The cells were assembled in a glovebox under an argon atmosphere. The charge and discharge measurements were carried out by LAND CT2000 at different current densities. Asymmetric cells were charged and discharged between 2.7 and 0.1 V, and AC-based symmetric cells were charged and discharged between 2.7 and 0 V. The specific capacitance, power and energy density were calculated based on the total mass of anode and cathode materials.

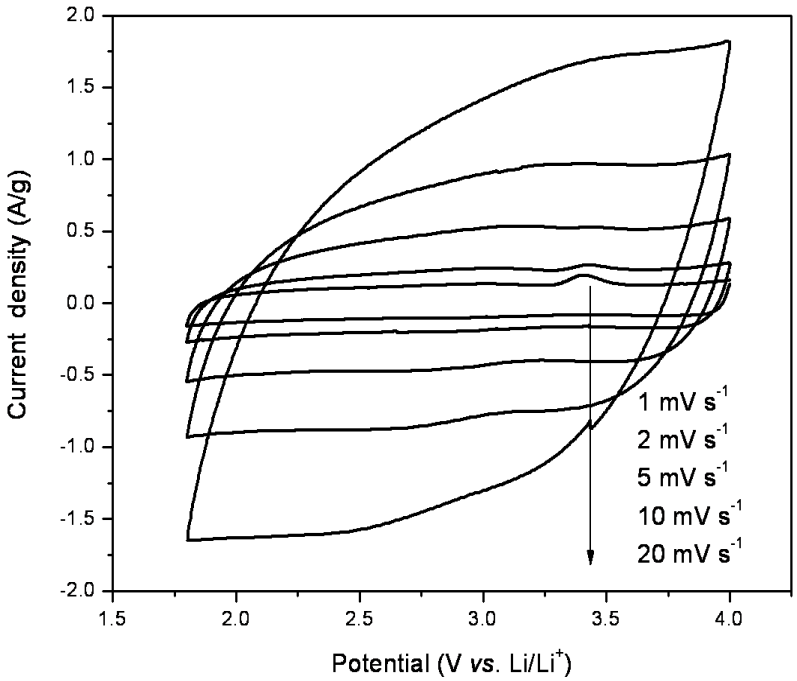

Figure 6.9 Cyclic voltammograms of the electrodes made of commercial activated carbon.

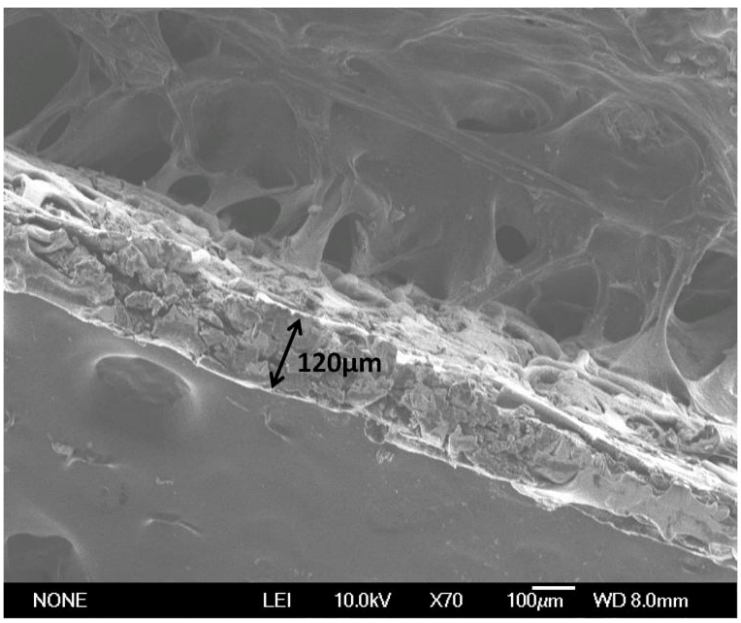

Figure 6.10 SEM image showing the thickness of the nanocomposite electrode to be over

100 μm.

Energy density is calculated using $E=1/2\ CV^2$, where C is the total cell capacitance and V is the maximum cell potential. For E_{max} calculation, the cell potential is considered as 2.7 V for all configurations. The charge stored by each electrode is determined by $q= C_s*m*\Delta U$, where C_s is the specific capacitance, ΔU the potential range for the charge/discharge process and m the mass of the single electrode. To obtain the maximum cell energy of the prototype supercapacitors, the cathode (represented by "ca") and anode (represented by "an") mass ratio was optimized according to $m_{ca}/m_{an}= (C_{an}*\Delta U_{an})/(C_{ca}*\Delta U_{ca})$. The total cell capacitance is calculated by $C= I/[-(dU/dt)*M]$, where I is the discharge current density and M the total mass of anode and cathode materials.

References:

[1] A. S. Arico, P. Bruce, B. Scrosati, J.-M. Tarascon, W. V. Schalkwijk, *Nat. Mater.* **2005**, *4*, 366.

[2] P. Simon, Y. Gogotsi, *Nat. Mater.* **2008**, *7*, 845.

[3] A. Burke, *J. Power Sources* **2000**, *91*, 37.

[4] J. R. Miller, P. Simon, *Science* **2008**, *321*, 651.

[5] R. Kötz, M. Carlen, *Electrochim. Acta* **2000**, *45*, 2483.

[6] J. Chmiola, G. Yushin, Y. Gogotsi, C. Portet, P. Simon, P. L. Taberna, *Science* **2006**, *313*, 1760.

[7] C. C. Hu, W. C. Chen, K. H. Chang, *J. Electrochem. Soc.* **2004**, *151*, A281.

[8] M. Toupin, T. Brousse, D. Belanger, *Chem. Mater.* **2002**, *14*, 3946.

[9] J. W. Lang, L. B. Kong, W. J. Wu, Y. C. Luo, L. Kang, *Chem. Commun.* **2008**, 4213.

[10] G. G. Amatucci, F. Badway, A. D. Pasquier, T. Zheng, *J. Electrochem. Soc.* **2001**, *148*, A930.

[11] J. P. Zheng, *J. Electrochem. Soc.* **2003**, *150*, A484.

[12] T. Brezesinski, J. Wang, J. Polleux, B. Dunn, S. H. Tolbert, *J. Am. Chem. Soc.* **2009**, *131*, 8.

[13] T. Brezesinski, J. Wang, S. H. Tolbert, B. Dunn, *Nat. Mater.* **2010**, *9*, 146.

[14] A. E. Fischer, K. A. Pettigrew, D. R. Rolison, R. M. Stroud, J. W. Long, *Nano Lett.* **2007**, *7*, 281.

[15] S. W. Lee, N. Yabuuchi, B. M. Gallant, S. Chen, B. S. Kim, P. T. Hammond, Y. Shao-Horn, *Nat. Nano.* **2010**, *5*, 531.

[16] Z. Chen, Y. C. Qin, D. Weng, Q. F. Xiao, Y. T. Peng, X. L. Wang, H. X. Li, F. Wei, Y. F. Lu, *Adv. Funct. Mater.* **2009**, *19*, 3420.

[17] J. Livage, *Chem. Mater.* **1991**, *3*, 578.

[18] W. Dong, A. N. Mansour, B. Dunn, *Solid State Ionics* **2001**, *144*, 31.

[19] Y. S. Hu, X. Liu, J.-O. Müller, R. Schlögl, J. Maier, D. S. Su, *Angew. Chem. Int. Ed.* **2009**, *48*, 210.

[20] K. Naoi, 'Nanohybrid Capacitor': The Next Generation Electrochemical Capacitors, *Fuel Cells* **2010**, 10, 825-833.

[21] S.-I. Pyun, J.-S. Bae, *J. Power Sources* **1997**, *68*, 669.

[22] W. Dong, J. Sakamoto, B. Dunn, *J. Sol-Gel Sci. Technol.* **2003**, *26*, 641.

[23] A. M. Cao, J. S. Hu, H. P. Liang, L. J. Wan, *Angew. Chem. Int. Ed.* **2005**, *44*, 4391.

[24] S. C. Pang, M. A. Anderson, T. W. Chapman, *J. Electrochem. Soc.* **2000**, *147*, 444.

[25] S. Passerini, J. J. Ressler, D. B. Le, B. B. Owens, W. H. Smyrl, *Electrochim. Acta* **1999**, *44*, 2209.

[26] F. Montilla, E. Morallon, A. De Battisti, J. L. Vazquez, *J. Phys. Chem. B* **2004**, *108*, 5036.

[27] Advanced Capacitor Techonologies, Inc., http://www.act.jp/-eng/premlis/- premlis.htm.

[28] Telcordia Energy Research group: http://www.argreenhouse.com/ESR/ah- main.html.

[29] A. F. Burke, Proc. IEEE Veh. Power Propulsion Conf. (VPPC"05), **2005**, 356.

[30] S. Eaves, J. Eaves, *J. Power Sources* **2004**, *130*, 208.

[31] G. B. Appetecchi, P. P. Prosini, *J. Power Sources* **2005**, *146*, 793.

[32] V. Khomenko, E. Raymundo-Piñero, F. Béguin, *J. Power Sources* **2006**, *153*, 183.

Chapter 7: Asymmetric Hybrid Sodium-Ion Pseudocapacitors Based on Intertwined CNT/V_2O_5 Nanowire Composites

1. Introduction

Electrical energy storage plays an increasingly important role in modern society. In our daily lives, a number of portable devices, as well as the development of electric vehicles and smart grid energy storage, are highly dependent on lithium-ion energy storage devices. However, extensive use of such devices is likely to affect existing lithium reserves.[1] Seeking alternative materials for sustainable energy storage is emerging as an essential topic within the electrochemical energy storage community.

Sodium, the second lightest metallic element after lithium, is four to five orders of magnitude more abundant than lithium. In this context, it holds great promise for economical and sustainable energy storage devices. Moreover, the standard Na/Na^+ electrode potential (2.71 V) is very close to that of Li/Li^+ (3.02 V), and sodium-based non-aqueous electrolytes generally exhibit stabilities, ionic conductivities, and electrochemical windows comparable to their lithium-ion counterparts.[2] These features make sodium-ion based electrochemical storage devices very attractive. A key requirement

for Na-ion based energy storage is finding suitable electrode materials in which to store sodium ions. Very recent studies show that sodium metal fluorophosphates,[3] lithium-sodium-mixed layered oxides[4] and sodium manganese oxide[5] store impressive amounts of sodium and may serve as cathode materials for Na-ion batteries. For anode materials, some hard-carbon materials could show reasonable sodium-storage capacities but their cycling stability is poor.[2,6] Some nanocrystalline iron oxides may reversibly store Na^+ ions with capacities of 100-130 mAh g^{-1}, however their charge/discharge process is characterized by slow electrode kinetics.[7] To date, there is a lack of suitable anode materials for Na-ion batteries.

An alternative to energy storage with batteries is electrochemical capacitive storage, which offers faster charge and discharge operation, longer cycle life and significantly higher power density than batteries.[8,9] Although most of this technology is based on carbon electrodes which store energy via an electrical double layer, there recently has been considerable interest in using pseudocapacitance, which is based on faradaic reactions, to store energy.[9,10] The specific capacitance for pseudocapacitive materials can be an order of magnitude larger than that of carbon because of the higher levels of charge storage from redox reactions.[9,11] The most common devices which incorporate pseudocapacitive

materials are hybrid asymmetric capacitors which typically have a carbon electrode as the cathode and the pseudocapacitor material as the anode.[12,13] Electrolytes can be aqueous or non-aqueous depending upon the pseudocapacitor material.[9-13]

In this work, we report a high-rate sodium-ion nanocomposite electrode material based on vanadium pentoxide (α-V_2O_5) nanowires. These materials can be used as a pseudocapacitive anode for an asymmetric electrochemical capacitor. α-V_2O_5 is a layered material that can accommodate a variety of metal ions, such as Li^+, Na^+ and K^+;[14-17] however, it generally exhibits poor electronic conductivity ($\sigma \approx 10^{-6}$-1 Ω^{-1} cm^{-1})[16] and slow ion-diffusion. Recently, it was shown that electrodeposited V_2O_5 thin-film electrodes can accommodate 2 Na/V_2O_5, achieving the theoretical capacity for sodium in vanadium oxide.[18] However, for device fabrication, thin films do not store adequate levels of energy and for this reason the electrode thickness should be at least in the micron range.[19] However, with such thicknesses, detrimental performance frequently occurs due to the increased electronic and ionic resistances. Fortunately, these technical barriers can be effectively circumvented by creating a porous composite architecture that integrates layer-structured V_2O_5 nanowires with carbon nanotubes (CNTs). As illustrated in **Figure 7.1**, such a composite architecture consists of interpenetrating networks of V_2O_5 nanowires and CNTs. The interpenetrating structure

leads to the formation of interconnected pore channels which are filled by the electrolyte, thus ensuring facile ion transport and providing access of the electrolyte to the redox-active material. Furthermore, the conductive CNT network enables effective electron transport, while the small dimension of the nanowires shortens ion diffusion paths. As a result, a fast pseudocapacitive charge storage process occurs, which seemingly avoids phase transformations during ion intercalation and de-intercalation, and enables enhanced cycling stability. Because of the electronic conduction of the CNT, it is possible to increase the mass loading of the nanocomposite electrodes to as much as 3 mg cm^{-2}. At this loading density, asymmetric devices produce practical levels of energy and power, unlike sub-micron thick electrodes.[19] The high rate capability, capacity, and cycling stability of our Na-ion electrodes and asymmetric capacitors have not been achieved by other Na-ion materials. This work provides a promising direction for high-performance and sustainable energy storage systems.

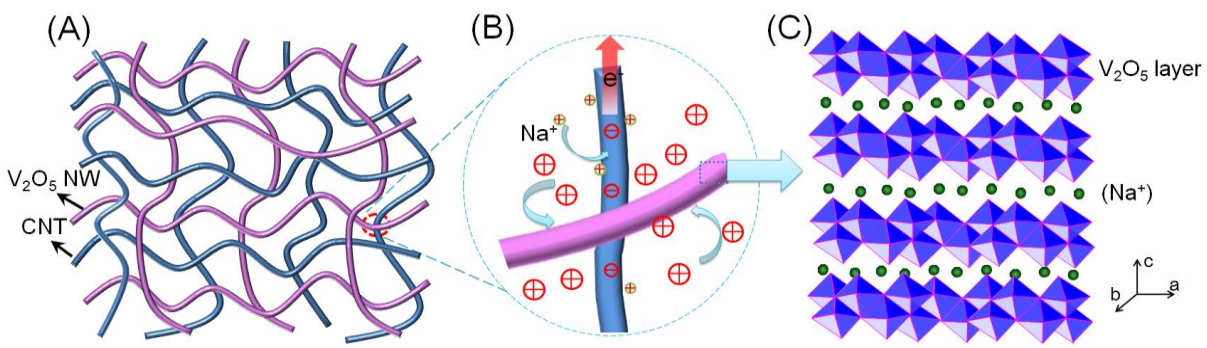

Figure. 7.1 Schematic of (A) a nanocomposite consisting of interpenetrating networks of V_2O_5 nanowires and CNTs, (B) Intimate contacts between the V_2O_5 nanowire and CNTs facilitating charge transport, and (C) Na^+ intercalation within the V_2O_5 layer structure.

2. Results and discussion

Figure 7.2A shows a representative scanning electron microscope (SEM) image of a nanocomposite obtained directly from the *in-situ* hydrothermal reaction, demonstrating nanowire V_2O_5 networks penetrated with CNTs. The V_2O_5 nanowires formed clusters due to the capillary force during water evaporation, while the CNTs are clearly observed penetrating through the nanowire network. **Figure 7.2B** shows a representative scanning electron microscope (SEM) image of the nanocomposite obtained from filtration and washing the as-synthesized product, which leads to the formation of a free-standing, flexible film (inset of **Figure 7.2B**). The nanocomposite, with 13 wt-% of CNTs (determined from thermogravimetric analysis, **Figure 7.3**A) demonstrates a continuous fibrous structure with abundant macropores formed by the network structure. A high-resolution SEM in **Figure 7.2C** shows a part of the composite film etched by 1% HF, indicating an intertwined porous network structure. The nanowires and CNTs possess an average diameter of ~50 and ~30

nm, respectively, and both of them have lengths of up to tens of micrometers. The formation of such interpenetrating networks relies on the dispersion of functionalized CNTs in solution followed by *in-situ* growth of V_2O_5 nanowires. The intertwined networks of the CNTs and nanowires exhibit an electrical conductivity of ~3.0 S cm^{-1}, which is substantially higher than that of bulk V_2O_5.[16,18]

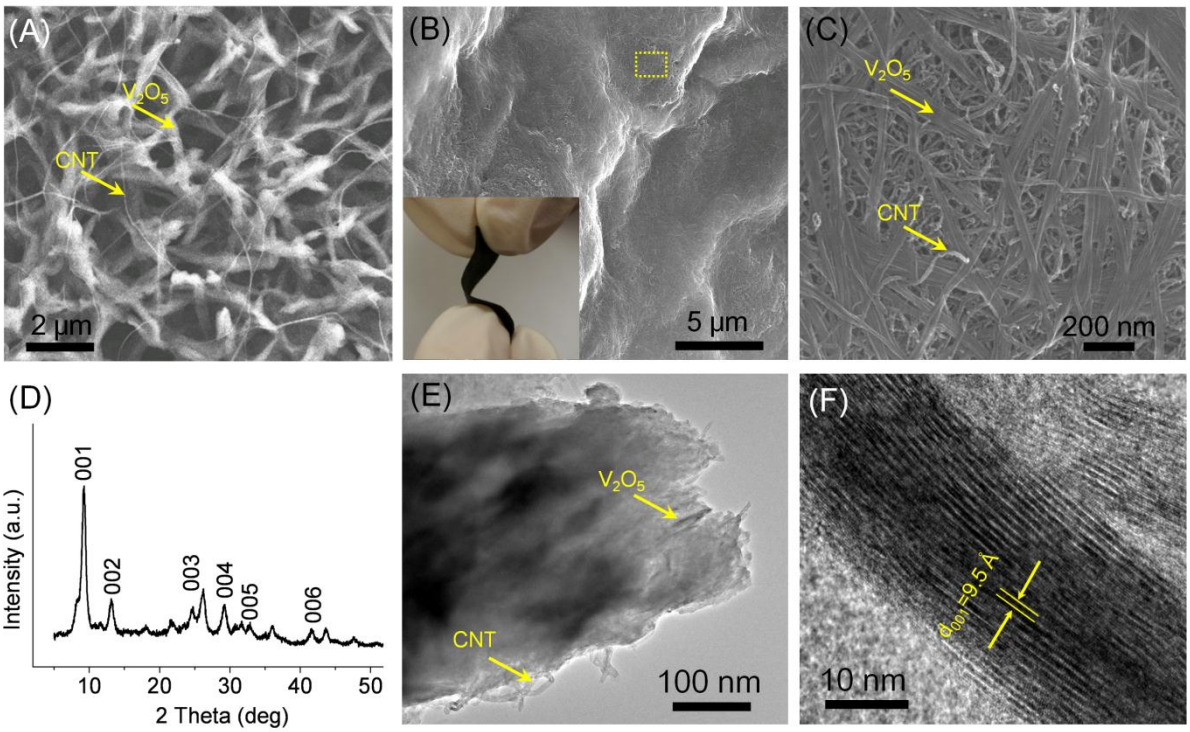

Figure 7.2 (A) SEM image of a V_2O_5/CNT nanocomposite demonstrating nanowire V_2O_5 networks penetrated with CNTs. The sample was obtained directly from the as-synthesized product. (B) Representative low-magnification SEM image of a V_2O_5/CNT nanocomposite

film obtained from filtration. Inset of Figure 7.2B presents a digital photograph of such a flexible nanocomposite film with a dimension of 1 cm×3 cm×130 μm. (C) High-magnification SEM image of the nanocomposites etched by 1 wt-% HF. The image corresponds to the selected area in Figure 7.2(B). (D) XRD patterns of the nanocomposite showing typical 00*l* diffraction. (E) TEM image of a nanocomposite showing embedded CNTs within the V_2O_5 nanowires. (F) HRTEM image of a V_2O_5 nanowire showing the layered structure with d_{001} spacing of 0.95 nm.

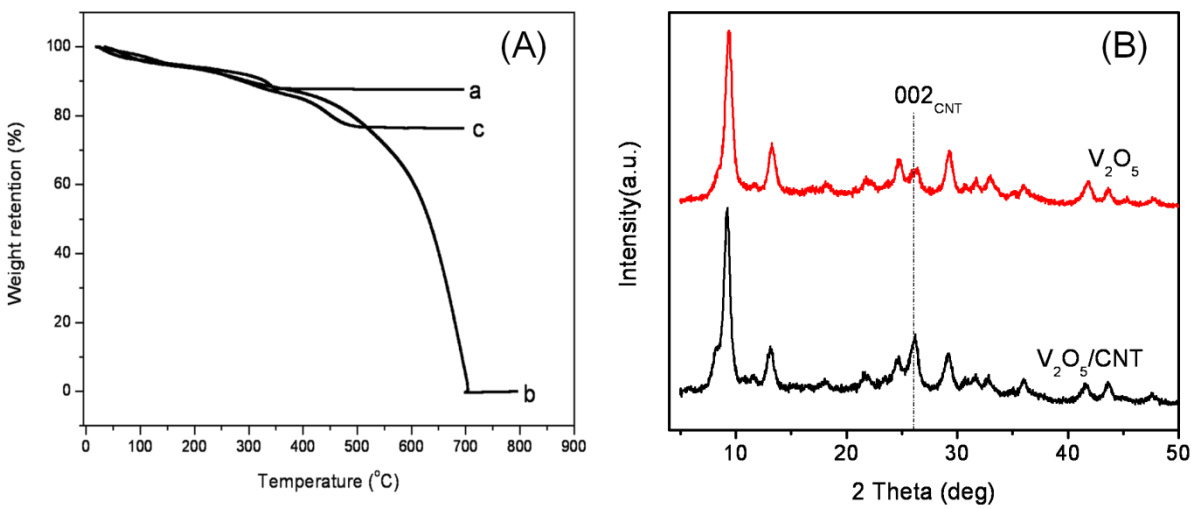

Figure 7.3 (A) Thermogravimetric analysis for V_2O_5 nanowires (a), functionalized CNTs (b) and V_2O_5/CNT nanocomposites (c). (B) XRD patterns of V_2O_5 and V_2O_5/CNT composite.

Figure 7.2D shows a representative x-ray diffraction (XRD) pattern of the

nanocomposite, suggesting a well-resolved layered structure with an interlayer spacing of ~1 nm. The layered structure supports Na-ion transport, thus enabling the material to reversibly intercalate Na-ions. The XRD pattern also suggests a small average crystallite grain size, which is calculated to be on the order of 9 nm using the Scherrer equation. The inappreciable diffraction peak of CNTs (at a 2 theta of ~26^{o}, **Figure 7.3B**) is mainly due to the acid-treatment of CNTs, which reduces the 002 ordering. In addition, the composite contains a relatively small mass fraction (~13%) of CNTs. **Figure 7.2E** shows a transmission electron microscope (TEM) image of V_2O_5 nanowires intertwined with CNTs. The nanowires and CNTs exhibit intimate interfaces due to the abundant hydrophilic groups (-OH and –COOH) on their surfaces, which form a strong interaction upon drying. In addition, the high-resolution TEM (HRTEM) image shown in **Figure 7.2F** further suggests that the nanowires are composed of a layered crystalline structure with a layer-to-layer distance (d_{001}) of ~9.5 Å, in good agreement with XRD results. This structure is similar to the hydrothermally synthesized V_2O_5 reported previously.[20] Besides the visible macroporous features observed from the microscopic images, nitrogen sorption isotherms (**Figure 7.4A**) suggest that such composites exhibit a hierarchically porous structure comprised of abundant micropores (~1.1 nm) and mesopores (3-50 nm). The calculated average pore size is around

12 nm (assuming slit pore geometry) and the porosity of the composite is ~58%. Moreover, such nanocomposites exhibit a high BET (Brunauer-Emmett-Teller) surface area of around 114 m^2 g^{-1}, which is substantially higher than bulk V_2O_5 crystals (~ 6 m^2 g^{-1}, **Figure 7.4B**). In short, the above physicochemical characterization indicates that the nanowire composite has a highly conductive, porous network structure with high surface area and hierarchical porosity, which are favorable features for fast electrode kinetics.

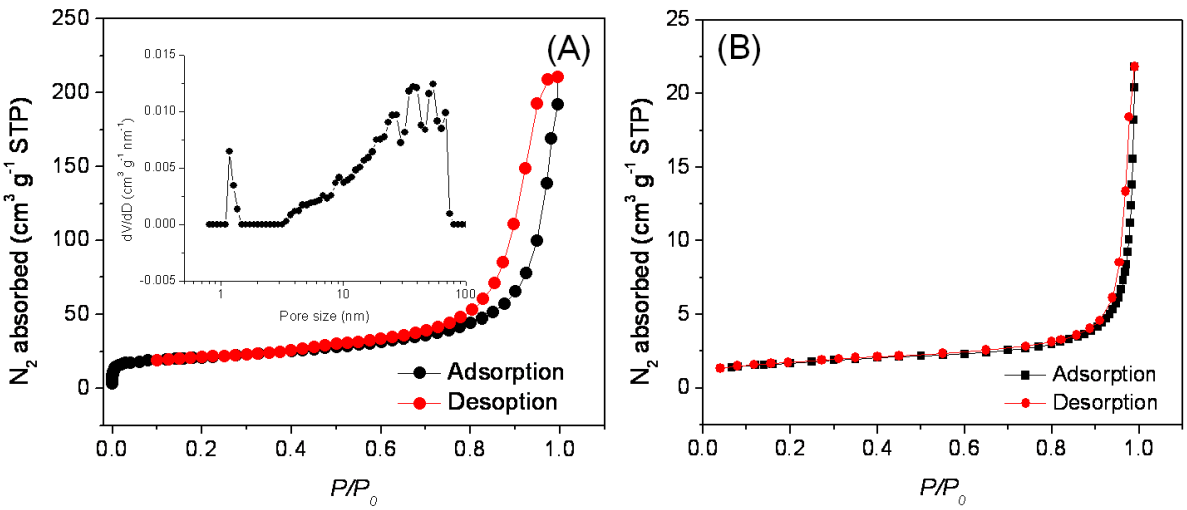

Figure 7.4. Nitrogen adsorption-desorption isotherms of the V_2O_5/CNT nanocomposite (A) and the commercial V_2O_5 (B). The isotherm of V_2O_5/CNT nanocomposite clearly shows the presence of both micropores and mesopores. Pore size distribution of the nanocomposite is also presented in the inset.

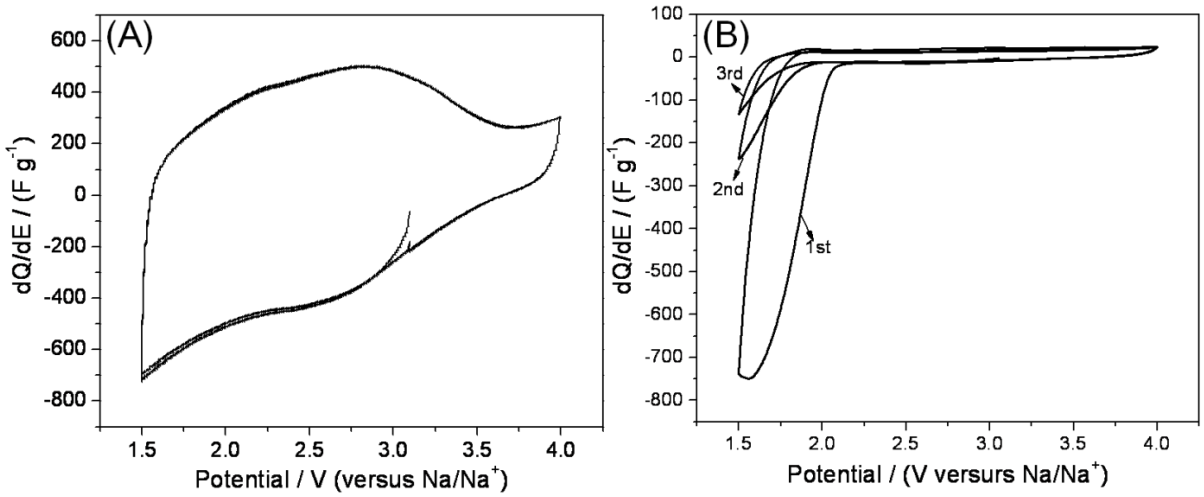

Figure 7.5 CV curves at 2 mV s^{-1} for the first three cycles of a V_2O_5/CNT nanocomposite electrode (A) and a commercial V_2O_5 electrode with orthorhombic structure (B).

The electrochemical behavior of the nanocomposites was investigated using three-electrode cells with 1 M $NaClO_4$ in propylene carbonate (PC) as an electrolyte, in which sodium foils were used as both the counter and reference electrodes. Charge storage behavior was characterized by cyclic voltammetry (CV). The electrochemical Na^+ insertion/extraction process occurring at the V_2O_5 electrodes can be represented by

$$V_2O_5 + xNa^+ + xe^- \leftrightarrow Na_xV_2O_5 \qquad (1)$$

where x is the mole fraction of inserted sodium ions.[21] Reversible charge storage is obtained by cycling the V_2O_5/CNT composite to 1.5 V, demonstrating that the structure is stable during Na^+ insertion and extraction. Further charging of the electrode to lower potentials is

possible, but the reaction might be less efficient due to irreversible structural changes.[22-26] A pure V_2O_5 nanowire electrode (i.e., without CNTs) shows appreciable capacity degradation during initial cycling (~30% capacity loss in the first 20 cycles), further confirming the advantage of utilizing V_2O_5/CNT nanocomposites for Na^+ electrodes. It is worth mentioning that commercial orthorhombic V_2O_5 materials are not feasible for Na^+ intercalation, possibly due to a rapid capacity degradation induced by structural changes (**Figure 7.5**).[18]

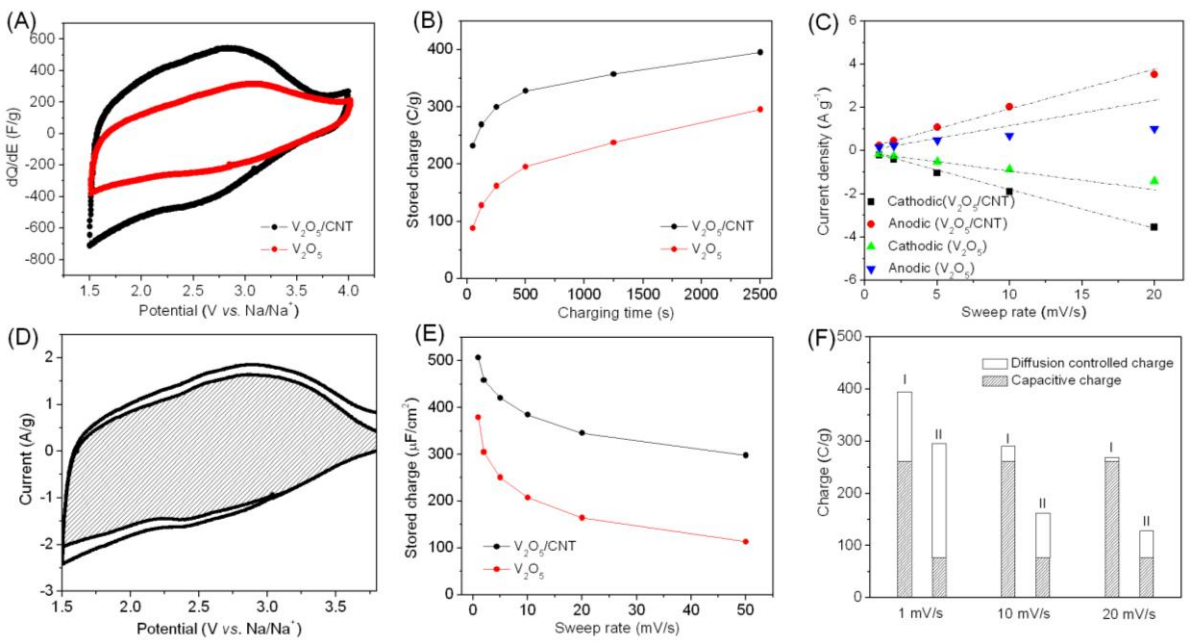

Figure 7.6 (A) Cyclic voltammograms (CVs) of V_2O_5/CNT and pure V_2O_5 electrodes at a potential scan rate of 2 mV s^{-1} in 1 M $NaClO_4$ in PC. The CV curves of the electrodes were

acquired after 10-15 cycles in order to obtain stable capacities. (B) Kinetic behavior of V_2O_5/CNT and pure V_2O_5 electrodes; (C) The voltametric current (at 2.5 V *vs.* Na/Na^+) dependence on the sweep rate. (D) Capacitive and diffusion-controlled contribution to charge storage. The capacitive current is shaded and compared with the total measured current. (E) The surface-area normalized capacitance for V_2O_5/CNT and pure V_2O_5 at different sweep rates. (F) Separation of contributions from capacitive and diffusion controlled capacities at different sweep rates (I: V_2O_5/CNT; II: pure V_2O_5).

Figure 7.6A compares the cyclic voltammograms of a V_2O_5/CNT nanocomposite electrode and a pure V_2O_5 nanowire electrode at a sweep rate of 2 mV s^{-1}. The nanocomposite electrode shows a pair of broad redox peaks between 2.4 and 2.8 V. The broad redox peaks arise from the large surface of the V_2O_5 crystal structure which lead to numerous active sites over a wide range of energy levels.[27-29] Sodium ion insertion/extraction into the V_2O_5/CNT nanocomposite occurs at similar potentials as lithium ions.[30] In contrast, the pure V_2O_5 nanowire electrode shows an almost featureless CV curve due to the relatively poor kinetics arising from slow diffusion and inefficient electron transfer. Using the CV curves to calculate the specific capacitances of V_2O_5/CNT and pure V_2O_5

electrodes (*vide infra)*, we find that the nanocomposite electrode provides a capacity of ~400 C g^{-1} between 1.5 and 3.5 V, which is higher than the V_2O_5 electrode (~300 C g^{-1}), and comparable to other high-performance Li-ion electrodes.[27-30]

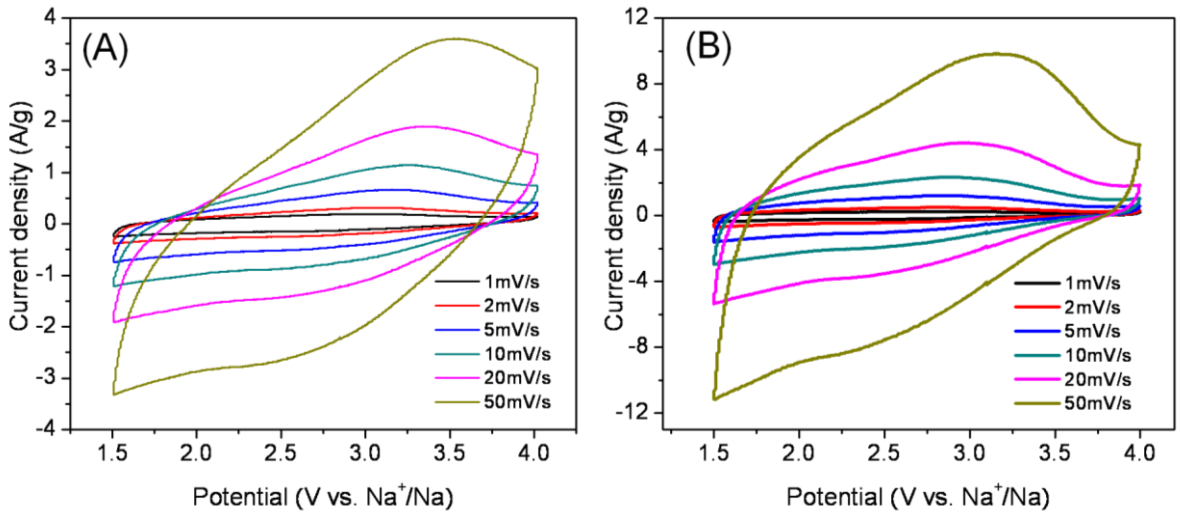

Figure 7.7 CV plots of a V_2O_5 nanowire electrode (A) and a V_2O_5/CNT nanocomposite electrode (B) at sweep rates of 1-50 mV s^{-1}.

To investigate the rate capability of the nanocomposite electrodes, CVs were carried out at different sweep rates and the areas under the CV curves were used to determine the total electrode capacity.[31] **Figure 7.6B** compares the capacities of the nanocomposite and pure V_2O_5 electrodes at sweep rates from 1 to 50 mV s^{-1} (**Figure 7.7**). For a typical voltage window at 1.5-4 V for V_2O_5 based electrodes, these rates correspond to a charge/discharge

time between 50 to 2500 s. Without a CNT network, the pure V_2O_5 nanowire electrode shows fast capacity degradation: the electrode loses ~70% of its initial capacity as the charging time decreases from 2500 to 50 s. In contrast, the nanocomposite electrode exhibits a substantially higher capacity (~400 C g^{-1}) at a charging time of 2500 s (1 mV s^{-1}), and still preserves 60 % of the total capacity (~240 C g^{-1}) as the charging time decreases to 50 s (50 mV s^{-1}). The substantial charge storage occurring on the order of a few minutes or less is a characteristic feature of capacitive storage. Such a high rate capability is consistent with the notion that the CNTs can effectively 'wire' the small V_2O_5 crystal domains and provide enhanced electronic conductivity, leading to an increased rate of charge transfer. While this behavior has been demonstrated with non-aqueous Li-ion electrolytes, the present work shows that comparable performance can be achieved with non-aqueous Na-ion electrolytes, thus making these materials of potential interest for high-rate sodium storage.[30,32]

In using CV to characterize the capacitive charge-storage, one assumes that the current response is proportional to the sweep rate according to:

$$i = \mathrm{d}q/\mathrm{d}t = C \cdot \mathrm{d}E/\mathrm{d}t = C \cdot v \qquad (2)$$

Where i is the current, q is the stored charge, C is the capacitance and $\mathrm{d}E/\mathrm{d}t$ is equal to the

sweep rate *v*. **Figure 7.6**C shows the voltammetric current (i.e., the current values at a potential of 2.5 V) dependence on the sweep rate (**Figure 7.7**). Note that the current response for the pure V_2O_5 nanowire electrode deviates from linearity as the sweep rate increases to 10 mV s^{-1}. This behavior is the result of slow charge transfer. This response was not observed for the V_2O_5/CNT electrode due to its better conductivity and hierarchical porosity. For both cathodic and anodic sweeps, a nearly perfect linear plot can be seen at sweep rates from 1 to 20 mV s^{-1}, confirming that the currents for the V_2O_5/CNT electrode are mainly capacitive in nature.

To quantitatively understand the charge storage mechanism for the nanocomposite electrode in the sodium-ion system, the measured current is separated into two components: 1) the capacitive contribution from pseudocapacitance and double-layer processes and 2) the contribution from diffusion-controlled current of Na^+ insertion. Using the previous approach developed by Dunn *et al*,[29,33] we were able to use the dependence of current on voltammetric sweep rate to quantitatively determine the capacitive contribution. **Figure 7.6D** shows the voltage profile at a sweep rate of 10 mV s^{-1} for the capacitive current (shaded region) in comparison to the total measured current. The capacitive contribution is 82 % for

the nanocomposite electrode, indicating that this is the dominant charge storage process. Since the surface areas of the nanocomposite and pure CNT are around 114 and 210 m^2 g^{-1}, respectively, the surface-area normalized specific capacitance for V_2O_5 in the composite is calculated to be approximately 380 μF cm^{-2} at 10 mV s^{-1} (**Figure 7.6E**). This value is substantially higher than the pure V_2O_5 electrode (205 μF cm^{-2}) and about one order of magnitude higher than pure double-layer based capacitances (5~20 μF cm^{-2}).[34-36] This calculation confirms that charge storage of the V_2O_5/CNT nanocomposites in Na-ion electrolyte is primarily associated with pseudocapacitance. Our results also agree well with previous studies, which suggested that pseudocapacitive effects play an increasing role as the metal oxide particle size decreases and/or the porosity increases.[27-29,33,37]

To further understand why such nanocomposites could store sodium ions with fast kinetics, we employed an analysis based on the work of Trasatti.[38-39] The total voltammetric charge (q_T) of the electrode materials was separated into two parts: surface capacitive charge (q_s) and diffusion controlled charge (q_d):

$$q_T = q_s + q_d \qquad (3)$$

Due to its faster kinetics, q_s can be correlated with double-layer capacitance and

pseudocapacitance, while q_d mainly depends on the slower diffusion process. Therefore, electrodes presenting a large fraction of q_s in the total capacity could exhibit a high rate capability. Assuming semi-infinite linear diffusion, within a reasonable range of sweep rates, q_s can be derived by plotting the total voltammetric charge q_T against the reciprocal of the square root of the potential sweep rate (v) and extrapolating v to ∞, according to the following equation (**Figure 7.8**):

$$q_T = q_s + cv^{-1/2} \qquad (4)$$

Deviation from the linearity of such a plot at high sweep rates is indicative of polarization effects that are ignored in the above equation.[38,39] The capacitive and diffusion controlled contributions to total capacity are displayed in **Figure 7.6F**. It clearly shows that capacitive charge storage plays a significant role in the total capacity of the nanocomposite electrode, and that this role increases as the sweep rate increases. Thus, at 1 mV s^{-1} capacitive processes account for some 70% of the charge storage, while at 20 mV s^{-1} it is 95%. This result is consistent with the capacitive current contribution shown in **Figure 7.6C-E**, strongly suggesting that most of the V_2O_5 intercalation sites within the nanocomposites are easily accessible to the electrolyte. In contrast, the pure V_2O_5 nanowire electrode has a significant diffusion contribution to charge storage at all sweep rates, implying difficult ion access and

charge transfer in the active material.

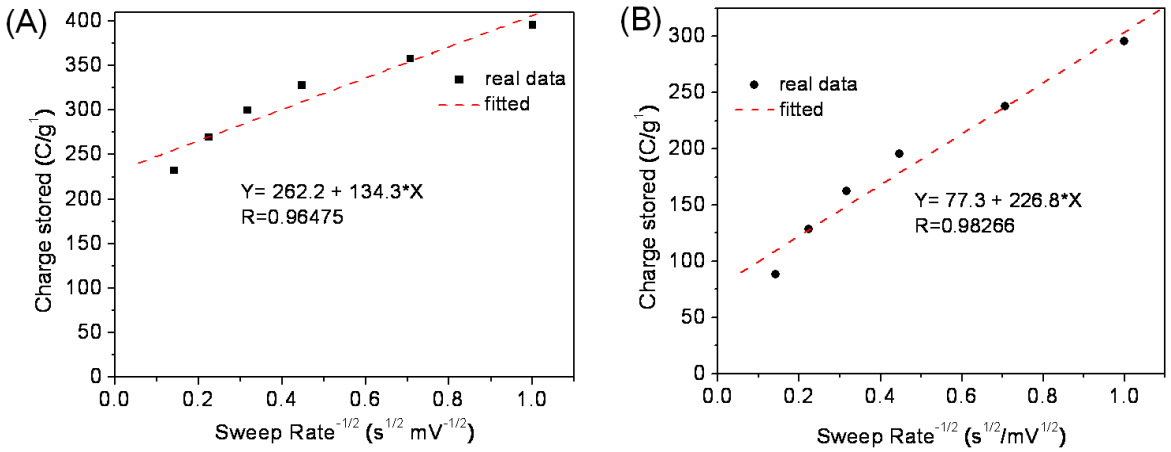

Figure 7.8 Examples of plotting the total voltammetric charge q_T against the reciprocal of the square root of the potential sweep rate (v) and extrapolating v to ∞ (A: V_2O_5/CNT nanocomposite electrode; B: pure V_2O_5 nanowire based electrode).

To assess the feasibility of using such nanocomposites for actual sodium-ion energy storage devices, we assembled coin-type asymmetric supercapacitors using the V_2O_5/CNT nanocomposite as an anode and a commercial activated carbon (with BET surface area of 2100 m^2 g^{-1}, **Figure 7.9**) as a cathode material. **Figure 7.10** shows a typical CV curve of the activated carbon (AC) electrode in the Na-electrolyte, indicating a pure double-layer charge storage process. In such asymmetric devices, the charging process involves sodium insertion into the anode and perchlorate anion absorption onto the carbon cathode. Sodium

extraction and perchlorate anion desorption occur on the anode and cathode, respectively, during a discharge process.[12] Due to the facile kinetics on both the anode and the cathode electrodes, this class of devices demonstrates high power and high energy density.

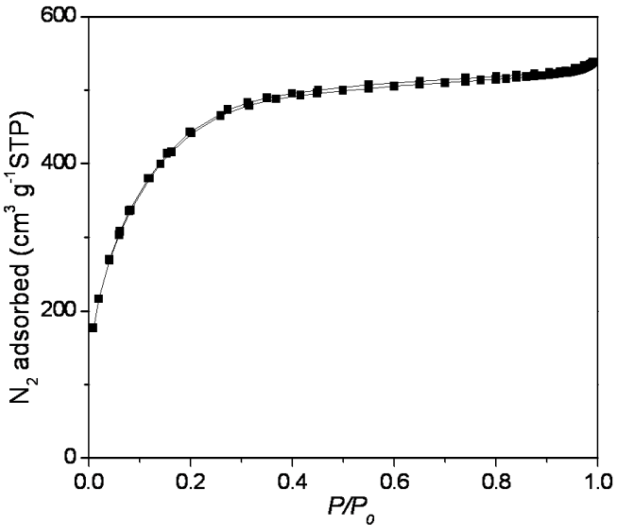

Figure 7.9 Nitrogen adsorption-desorption isotherms of the commercial activated carbon (AC) used for cathode in our hybrid asymmetric capacitors.

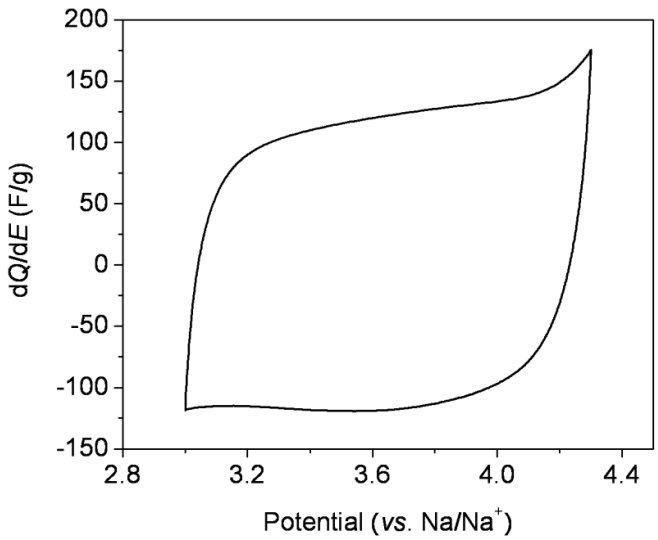

Figure 7.10 CV curve of an AC electrode at sweep rate of 2 mV s^{-1} in 1 M $NaClO_4$/PC.

We evaluated the asymmetric supercapacitor using several techniques. Based on the storage capacities and electrochemical windows of both materials, an optimal mass ratio between the cathode and anode is found to be 3.8 in an asymmetric cell.[13] The devices show an open circuit potential of ~0.1 V. Therefore, CV sweeps were performed from 0.1 V to different cell voltages to identify a suitable operating window. As shown in **Figure 7.11A**, the devices show rectangular CV curves at voltage windows up to 2.8 V, indicating an ideal capacitive behavior. However, further increasing the cell voltage caused appreciable irreversible capacitance, which should be avoided for long-term device operation. Galvanostatic cycling was also performed to evaluate the maximum voltage. **Figure 7.11B** (inset) shows the coulombic efficiency (η) of the prototypes at different maximum voltages. It is shown that devices operated over 2.8 V gave a coulombic efficiency lower than 98 %, probably due to irreversible reactions induced by overcharge. Therefore, the maximum cell voltage was controlled to 2.8 V for the device configuration.

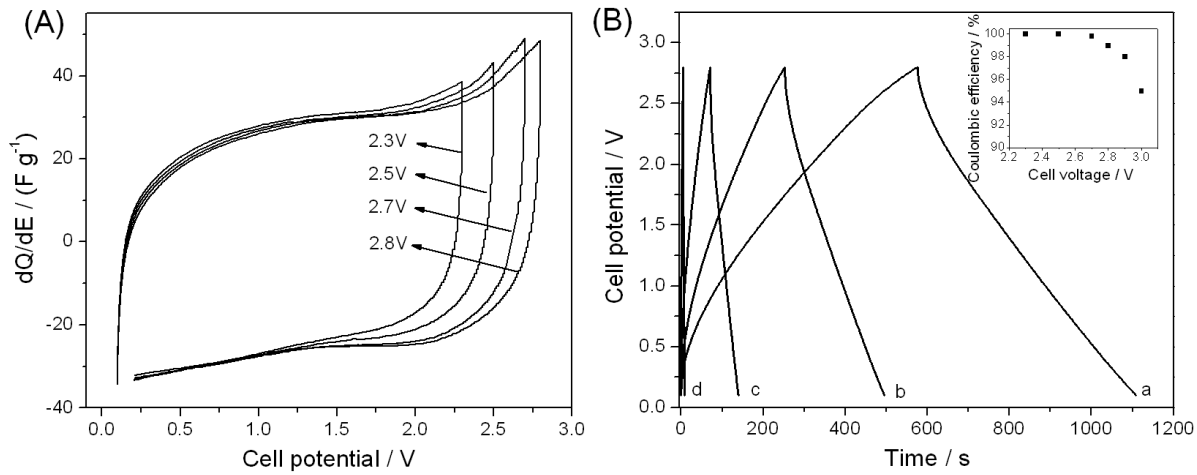

Figure 7.11 (A) CV curves of an asymmetric Na-ion supercapacitor device cycled in various potential windows at a sweep rate of 2 mV s^{-1}. (B) Galvanostaic charge/discharge curves from 0-2.8 V at different current densities in 1 M $NaClO_4$ in PC (a: 0.5 mA, b: 1 mA, c: 3 mA, d: 15 mA, the footprint areas of anode and cathode were about 0.4 and 1 cm^2, respectively). Inset shows the dependence of coulombic efficiency on the maximum charging voltage.

Representative galvanostatic charge/discharge curves for the asymmetric prototypes at different current densities are shown in **Figure 7.11B**. At a charge/discharge time of ~18 minutes, the devices provide an overall cell capacitance of ~35 F g^{-1} (capacitance was calculated based on the total mass of cathode and anode active materials), giving an energy density of 38 Wh kg^{-1} and a power density of 140 W kg^{-1}. The energy density is close to that of lithium-ion asymmetric devices.[30] Even at a power density of ~5 kW kg^{-1} (charge

and discharge time of 5.8 s), the devices still provide a cell capacitance of ~7 F g^{-1}, corresponding to an energy density of ~7.5 Wh kg^{-1}, an indication of the high power performance. From the internal resistance (*iR* drop) of the devices, a maximum power density was calculated to be 45 kW kg^{-1}. Moreover, the time constant ($\tau = RC$) was calculated to be ~2.0 s, which is comparable to conventional carbon-based supercapacitors (~1 s), further confirming the high power capability.

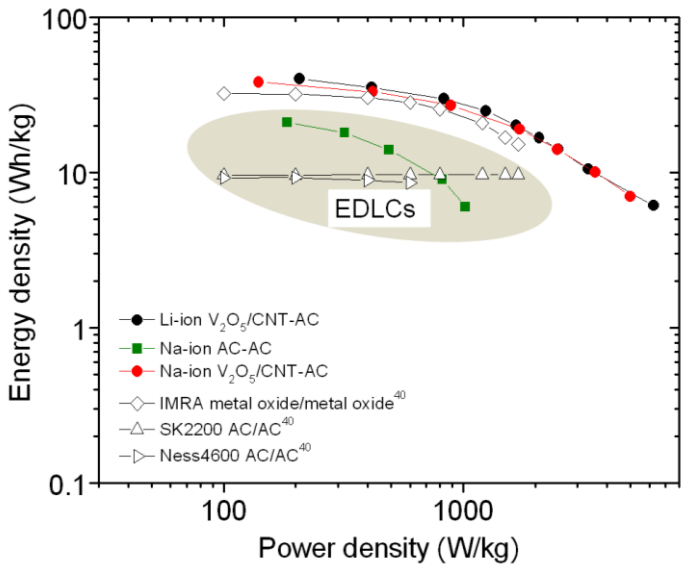

Figure 7.12 Ragone plots of Na-ion and Li-ion asymmetric supercapacitors made from a V_2O_5/CNT nanocomposite anode and an AC cathode, a symmetric supercapacitor made from the same AC, and various supercapacitor devices recently developed. All the data is based on the mass of electrode materials. For the devices reported,[40] the mass of the electrode materials was estimated to be 40% of the total device weight. A packaging factor on the

order of 0.4 was used.[41-43]

For another perspective of the Na-ion asymmetric devices, **Figure 7.12** compares the Ragone plots derived from galvanostatic cycling tests of different prototype supercapacitors. The power density is calculated based on the average power for each charge/discharge (**Figure 7.13**). Overall, the energy and power performance of the sodium-ion asymmetric supercapacitor is highly competitive with that of lithium-ion supercapacitors.[30] Moreover these devices offer significantly higher energy and power than that of AC-based symmetric cells (**Figure 7.14**) and the current state-of-the-art electrical double-layer capacitor (EDLC) technology. Considering that the specific capacitance of the cathode materials (AC) is still relatively low, an even higher energy density could be realized if a better cathode material was available.

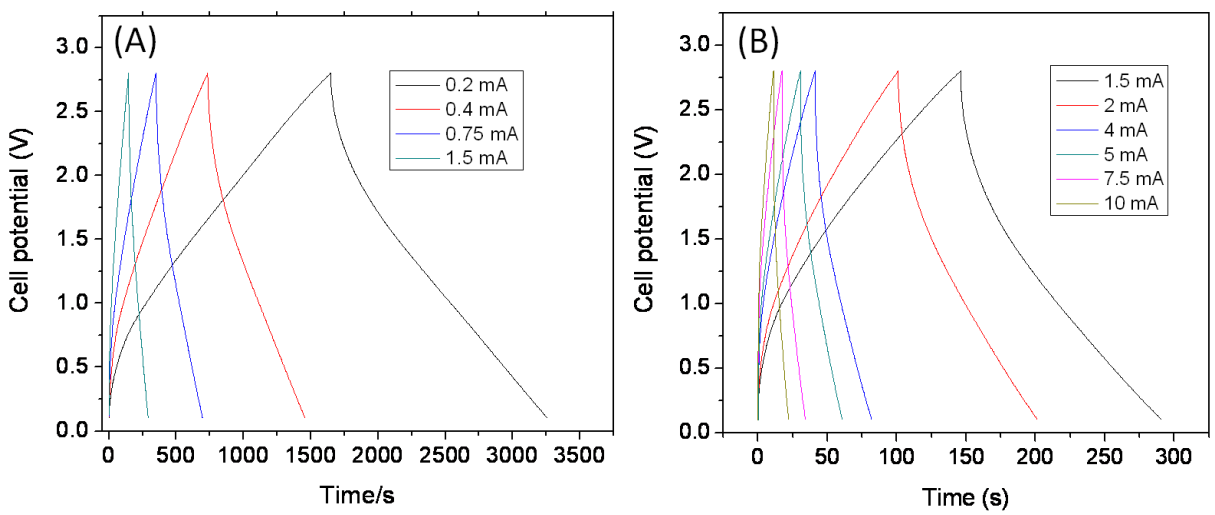

Figure 7.13 Galvanostatic charge/discharge curve of an asymmetric V_2O_5/CNT-AC device at different current rates (the footprint areas of anode and cathode were about 0.4 and 1 cm^2, respectively).

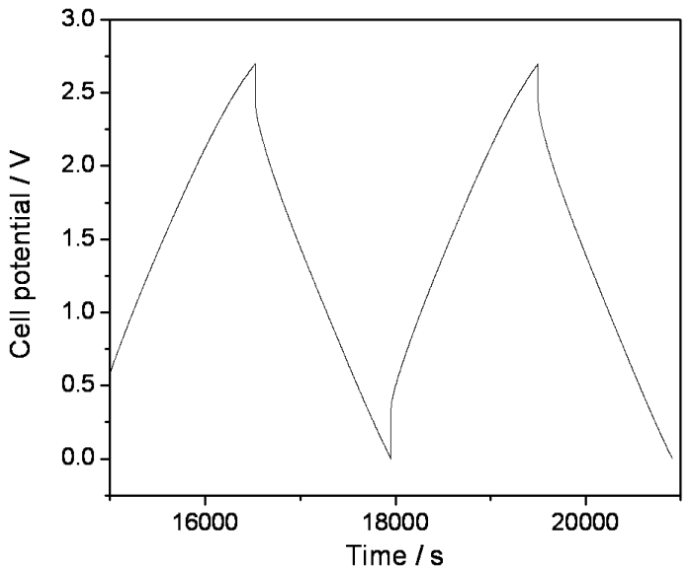

Figure 7.14 Representative galvanostatic charge/discharge curve of a symmetric AC-AC supercapacitor at a current density of 0.5 mA cm^{-2}.

The sodium-ion devices based on the V_2O_5/CNT nanocomposites retained ~80% of the initial capacity after 900 cycles at a charge/discharge rate of 60 C (power density of ~1700 W kg^{-1}, **Figure 7.15A**). Electrochemical impedance spectroscopy (EIS) was used to determine whether any structural or interfacial changes occurred upon cycling the electrodes. **Figure**

7.15B shows the Nyquist plots for a sodium-ion asymmetric supercapacitor as a function of cycling. The cell exhibited similar uncompensated resistances (R_s) from the electrolyte, current collectors and contacts before and after cycling, indicating a stable electrode structure. A slight decrease of R_s was measured after the first cycle, which could be due to the *in-situ* formation of a conductive sodium bronze ($Na_xV_2O_5$).[44] The observed semicircles are caused by polarization or charge transfer resistance (R_c) from both electrodes.[45-48] The R_c increased from ~10 to ~20 ohms after 900 cycles, which could be ascribed to an increased interfacial resistance due to interfacial changes or side reactions[49] occurring during the cycling process. The fact that R_c increased slowly in the first few cycles suggests that that no obvious structure change occurred on the Na-ion electrode, and that a robust electrode structure can be maintained.[50] In addition, the decrease in cell capacitance on cycling may also be due to slight dissolution of the V_2O_5 active material in the electrolyte.[51] The cycling results provide the insight that further improvements in cycling performance can be achieved by stabilizing the electrode interface and/or by judiciously choosing an electrolyte.

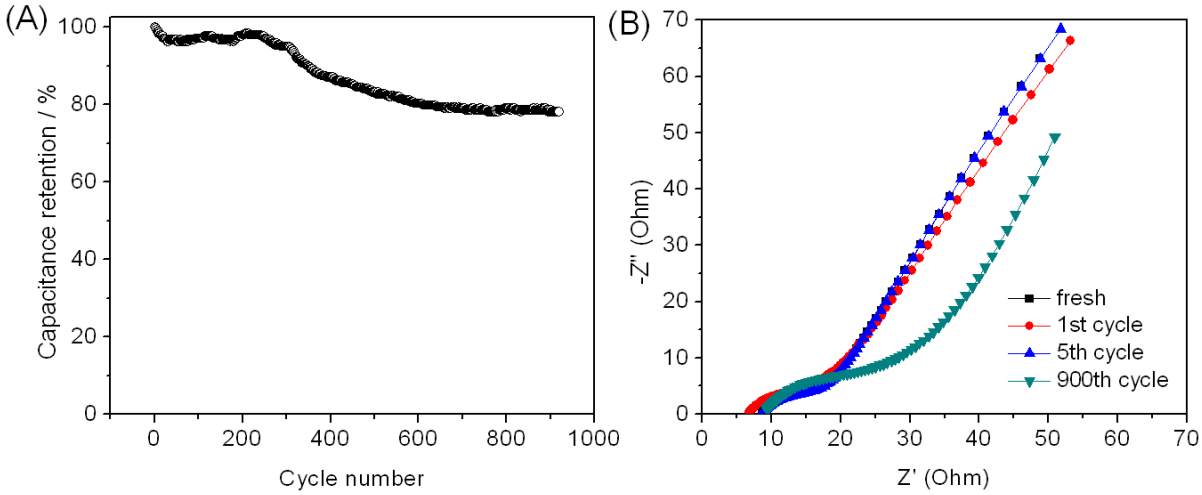

Figure 7.15 (A) Cycling performance of a V_2O_5/CNT-AC sodium-ion device for 900 cycles at a charge/discharge rate of 60 C. (B) Nyquist plots of the V_2O_5/CNT-AC hybrid sodium-ion device for different cycles (the plots of the fresh and 5th cycle electrode almost overlap).

3. Conclusions

In summary, we have demonstrated fast, reversible sodium-ion storage in V_2O_5/CNT nanocomposite electrodes. The V_2O_5/CNT nanocomposite exhibits far better rate capability and charge storage compared to V_2O_5 electrodes that do not contain CNTs. Various analytical methods show that charge storage in these materials arises from a pseudocapacitive process. Using the nanocomposite electrode as an anode and commercial AC as a cathode, we have demonstrated that sodium-ion asymmetric capacitors in organic electrolyte exhibit excellent energy and power densities. These results show that sodium-ion based energy

storage devices can exhibit comparable performance to lithium-ion devices, thus providing an attractive, cost-effective alternative for a wide range of applications.

4. Experimental

4.1 Synthesis of the V_2O_5/CNT Nanocomposites

The nanocomposites were synthesized through a one-pot hydrothermal process using aqueous vanadium-oxide precursors in the presence of pre-treated hydrophilic CNTs, which were synthesized by a mass production process with a capability of ~400 tons $year^{-1}$.[52] Grams of this composite were produced using a lab-scale reactor (volume of 120 mL). Details of the materials synthesis were described in previous publications.[20,53] The composition of the V_2O_5/CNT composite was determined by thermogravimetric analysis (TGA, Figure. S1). Nitrogen sorption isotherms were measured at 77 K with a Micromeritics ASAP 2020. The specific surface areas were calculated by the Brunauer-Emmett-Teller (BET) method using an adsorption branch in a relative pressure range from 0.04 to 0.25. SEM and TEM experiments were conducted on a JEOL JSM-6700 FE-SEM and FEI Titan S/TEM operated at 300 kV, respectively.

4.2 Electrochemical Characterization

To make electrodes, the V_2O_5/CNT nanocomposites, pure V_2O_5 nanowires or activated carbon (AC) were assembled onto stainless steel current collectors. Briefly, 80% of the electrochemically active material, 10% carbon black, and 10% poly(vinylidene fluoride) (PVDF) dispersed in N-methylpyrrolidinone (NMP) were mixed to form slurries. The homogenous slurries were coated on substrates and dried at 90 ^{o}C for 30 min. under vacuum. As-formed electrodes were then pressed at a pressure of 2 MPa and further dried for another 12 h. Typical mass loadings were 1-3 mg cm^{-2} of active material on each current collector. The electrochemical measurements were carried out on a Bio-Logic VMP3 or Solartron 1860/1287. The electrolyte was 1 M $NaClO_4$ in propylene carbonate (PC) solution and sodium foils were used as both the counter and reference electrodes. CV and EIS measurements were carried out in an argon-filled glovebox in three-electrode cells. To make 2032 type coin cells, glass fiber (GF/D) from Whatman was used as the separator. The cells were assembled under an argon atmosphere with moisture and oxygen levels of < 1 ppm. In asymmetric devices, the operation windows for the nanocomposite anode and AC cathode are 1.5-3.2 V and 3.3-4.3V, respectively, and the maximum operation window of whole devices is 2.8 V.

The specific capacitance, power and energy density were calculated based on the total masses of anode and cathode materials. The *iR* drop is used to calculate the cell's resistance using $R=U/I$ and the RC constant by using $\tau = R*C_t$, where C_t is the capacitance of the device and U is the maximum cell potential. The maximum power density is calculated based on $P_{max} = U^2/(4RM)$.[54] The device energy density is calculated using $E=1/2\ CU^2$, where C is the normalized cell capacitance. Asymmetric cells were charged and discharged between 2.8 and 0.1 V, and AC-based symmetric cells were charged and discharged between 2.8 and 0 V. The charge stored by each electrode is determined by $q= C_s*m*\Delta U$, where C_s is the specific capacitance, ΔU the potential range for the charge/discharge process and m the mass of a single electrode. To obtain the maximum cell energy of the prototype supercapacitors, the cathode (represented by "ca") and anode (represented by "an") mass ratio was optimized according to $m_{ca}/m_{an}= (C_{an}*\Delta U_{an})/(C_{ca}*\Delta U_{ca})$. The total cell capacitance is calculated by $C= I/[-(dU/dt)*M]$, where I is the discharge current density and M the total mass of anode and cathode materials.[55]

References

1 Tahil, W. *Meridian International Research*, **2007**, www.meridian-int-res.com.

2 Stevens, D. A; Dahn, J. R. High Capacity Anode Materials for Rechargeable Sodium-Ion Batteries. *J. Electrochem. Soc.* **2000**, *147*, 1271-1273.

3 Ellis, B. L.; Makahnouk, W. R. M.; Makimura, Y.; Toghill, K.; Nazar, L. F. A Multifunctional 3.5 V Iron-based Phosphate Cathode for Rechargeable Batteries. *Nat Mater.* **2007**, *6*, 749-753.

4 Kim, D.; Kang, S.-H.; Slater, M.; Rood, S.; Vaughey, J. T.; Karan, N.; Balasubramanian, M.; Johnson, C. S. Enabling Sodium Batteries Using Lithium-Substituted Sodium Layered Transition Metal Oxide Cathodes. *Adv. Energy Mater.* **2011**, *1*, 333-336.

5 Cao,Y.; Xiao, L.; Wang, W.; Choi, D.; Nie, Z.; Yu, J.; Saraf, L. V.; Yang, Z.; Liu, J. Reversible Sodium Ion Insertion in Single Crystalline Manganese Oxide Nanowires with Long Cycle Life. *Adv. Mater.* **2011**, *23*, 3155-3160.

6 Wenzel, S.; Hara, T.; Janek, J.; Adelhelm, P. Room-temperature Sodium-ion Batteries: Improving the Rate Capability of Carbon Anode Materials by Templating Strategies. *Energy Environ. Sci.* **2011**, *4*, 3342-3345.

7 Komaba, S.; Mikumo, T.; Yabuuchi, N.; Ogata, A.; Yoshida, H.; Yamada, Y.

Electrochemical Insertion of Li and Na Ions into Nanocrystalline Fe_3O_4 and α-Fe_2O_3 for Rechargeable Batteries. *J. Electrochem. Soc.* **2010**, *157*, A60-A65.

8 Miller, J. R.; Simon, P. Electrochemical Capacitors for Energy Management. *Science* **2008**, *321*, 651-652.

9 Simon, P.; Gogotsi, Y. Materials for Electrochemical Capacitors. *Nat. Mater.* **2008**, *7*, 845-854.

10 Zhang, L. L.; Zhao, X. S. Carbon-based Materials as Supercapacitor Electrodes. *Chem. Soc. Rev*. **2009**, *38*, 2520-2531.

11 Conway, B. E.; Birss, V.; Wojtowicz, J. The Role and Utilization of Pseudocapacitance for Energy Storage by Supercapacitors. *J. Power Sources* **1997**, *66*, 1-14.

12 Amatucci, G. G; Badway, F.; Pasquier, A. D; Zheng, T. An Asymmetric Hybrid Nonaqueous Energy Storage Cell. *J. Electrochem. Soc.* **2001**, **148**, A930-A939.

13 Khomenko, V.; Raymundo-Piñero, E.; Béguin, F. Optimisation of an Asymmetric Manganese Oxide/Activated Carbon Capacitor Working at 2 V in Aqueous Medium. *J. Power Sources* **2006**, *153*, 183-190.

14 Tang, P. E.; Sakamoto, J. S.; Baudrin, E.; Dunn, B. V_2O_5 Aerogel as a Versatile Host for Metal Ions. *J. Non-Cryst. Solids* **2004**, *350*, 67-72.

15 Livage, J. Vanadium Pentoxide Gels. *Chem. Mater.* **1991**, *3*, 578-593.

16 Badot, J. C.; Baffier, N. Ionic Conductivity and Dielectric Properties of Vanadium Pentoxide Xerogels. *J. Mater. Chem.* **1992**, *2*, 1167-1175.

17 Whittingham, M. S.; Song, Y.; Lutta, S.; Zavalij, P. Y.; Chernova, N. A. Some Transition Metal (oxy)phosphates and Vanadium Oxides for Lithium Batteries. *J. Mater. Chem.* **2005**, *15*, 3362-3379.

18 Tepavcevic, S.; Xiong, H.; Stamenkovic, V. R.; Zuo, X.; Balasubramanian, M.; Prakapenka, V. B.; Johnson, C. S.; Rajh, T. Nanostructured Bilayered Vanadium Oxide Electrodes for Rechargeable Sodium-Ion Batteries. *ACS Nano* **2012**, *6*, 530-538.

19 Gogotsi, Y.; Simon, P. True Performance Metrics in Electrochemical Energy Storage. *Science* **2011**, *334*, 917-918.

20 Xiong, C. R.; Aliev, A. E.; Gnade, B.; Balkus Jr.,;K. J.; Fabrication of Silver Vanadium Oxide and V_2O_5 Nanowires for Electrochromics. *ACS Nano* **2008**, *2*, 293-301.

21 Su, L.; Winnick, J.; Kohl, P. Sodium Insertion into Vanadium Pentoxide in Methanesulfonyl Chloride-Aluminum Chloride Ionic Liquid. *J. Power Sources* **2001**, *101*, 226-230.

22 Coustier, F.; Hill, J.; Owens, B. B.; Passerini, S.; Smyrl, W. H. Doped Vanadium Oxides

as Host Materials for Lithium Intercalation. *J. Electrochem. Soc.* **1999**, *146*, 1355-1360.

23 Leger, C.; Bach, S.; Soudan, P.; Pereira-Ramos, J. P. Structural and Electrochemical Properties of ω-$Li_xV_2O_5$ ($0.4 < x < 3$) as Rechargeable Cathodic Material for Lithium Batteries. *J. Electrochem. Soc.* **2005**, *152*, A236-A241.

24 Zhan, S. Y.; Wang, C. Z.; Nikolowski, K.; Ehrenberg, H.; Chen, G.; Wei, Y. J. Electrochemical properties of Cr doped V_2O_5 between 3.8 V and 2.0 V. *Solid State Ionics* **2009**, *180*, 1198-1203.

25 Hu, Y.-S.; Liu, X.; Müller, J.-O.; Schlögl, R.; Maier, J.; Su, D. S. Synthesis and Electrode Performance of Nanostructured V_2O_5 by Using a Carbon Tube-in-Tube as a Nanoreactor and an Efficient Mixed-Conducting Network. *Angew. Chem. Int. Ed.* **2009**, *48*, 210-214.

26 Mai, L.; Xu, L.; Han, C.; Xu, X.; Luo, Y.; Zhao, S.; Zhao, Y. Electrospun Ultralong Hierarchical Vanadium Oxide Nanowires with High Performance for Lithium Ion Batteries. *Nano Lett.* **2010**, *10*, 4750-4755.

27 Swider-Lyons, K. E.; Love, C. T.; Rolison, D. R. Improved Lithium Capacity of Defective V_2O_5 Materials. *Solid State Ionics.* **2002**, *152-153*, 99-104.

28 Brezesinski, T.; Wang, J.; Polleux, J.; Dunn, B.; Tolbert, S. H. Templated Nanocrystal-Based Porous TiO_2 Films for Next-Generation Electrochemical Capacitors.

J. Am. Chem. Soc. **2009**, *131*, 1802-1809.

29 Brezesinski, T.; Wang, J.; Tolbert, S. H.; Dunn, B. Ordered Mesoporous α-MoO_3 with Iso-oriented Nanocrystalline Walls for Thin-film Pseudocapacitors. *Nat. Mater*. **2010**, *9*, 146-151.

30 Chen, Z.; Augustyn, V.; Wen, J.; Zhang, Y.; Shen, M.; Dunn, B.; Lu, Y. High-Performance Supercapacitors Based on Intertwined CNT/V_2O_5 Nanowire Nanocomposites. *Adv. Mater.* **2011**, *23*,791-795.

31 Pang, S.-C.; Anderson, M. A.; Chapman, T. W. Novel Electrode Materials for Thin-Film Ultracapacitors: Comparison of Electrochemical Properties of Sol-Gel-Derived and Electrodeposited Manganese Dioxide. *J. Electrochem. Soc.* **2000**, *147*, 444-450.

32 Kim, I.-H.; Kim, J.-H.; Cho, B.-W.; Lee, Y.-H.; Kim, K.-B. Synthesis and Electrochemical Characterization of Vanadium Oxide on Carbon Nanotube Film Substrate for Pseudocapacitor Applications. *J. Electrochem. Soc.* **2006**, *153*, A989-A996.

33 Wang, J.; Polleux, J.; Lim, J.; Dunn, B. Pseudocapacitive Contributions to Electrochemical Energy Storage in TiO_2 (Anatase) Nanoparticles. *J. Phys. Chem. C.* **2007**, *111*, 14925-14931.

34 Frackowiak, E. Carbon Materials for Supercapacitor Application. *Phys. Chem. Chem.*

Phys. **2007**, *9*, 1774-1785.

35 Barbieri, O.; Hahn, M.; Herzog, A.; Kötz, R. Capacitance Limits of High Surface Area Activated Carbons for Double Layer Capacitors. *Carbon* **2005**, *43*, 1303-1310.

36 Chmiola, J.; Yushin, G.; Gogotsi, Y.; Portet, C.; Simon, P.; Taberna, P. L. Anomalous Increase in Carbon Capacitance at Pore Sizes Less Than 1 Nanometer. *Science* **2006**, *313*, 1760-1763.

37 Balaya, P.; Bhattacharyya, A.; Jamnik, J. J.; Zhukovskii, Y. F.; Kotomin, E. A.; Maier, J. Nano-Ionics in the Context of Lithium Batteries. *J. Power Sources* **2006**, *159*, 171-178.

38 Ardizzone, S.; Fregonara, G.; Trasatti, S. "Inner" and "Outer" Active Surface of RuO_2 Electrodes. *Electrochim. Acta.* **1990**, *35*, 263-267.

39 Baronetto, D.; Krstajic, N.; Trasatti, S. Reply to "Note on a Method to Interrelate Inner and Outer Electrode Areas" by H. Vogt. *Electrochim. Acta*. **1994**, *39*, 2359-2362.

40 Burke, A. F. Proc. IEEE Veh. Power Propulsion Conf. (VPPC"05). **2005**, 356-366.

41 Lee, S. W.; Yabuuchi, N.; Gallant, B. M.; Chen, S.; Kim, B. S.; Hammond, P. T.; Shao-Horn, Y. High-Power Lithium Batteries from Functionalized Carbon-Nanotube Electrodes. *Nat. Nano.* **2010**, *5*, 531-537.

42 Eaves, S.; Eaves, J. A Cost Comparison of Fuel-Cell and Battery Electric Vehicle. *J.*

Power Sources **2004**, *130*, 208-212.

43 Appetecchi, G. B.; Prosini, P. P. 0.4 Ah Class Graphite/$LiMn_2O_4$ Lithium-Ion Battery Prototypes. *J. Power Sources* **2005**, *146*, 793-797.

44 Bach, S.; Baffier, N.; Pereira-Ramos, J. P.; Messina, R.; Electrochemical Sodium Intercalation in $Na_{0.33}V_2O_5$ Bronze Synthesized by a Sol-Gel Process. *Solid State Ionics* **1989**, *37*, 41-49.

45 Fischer, A. E.; Pettigrew, K. A.; Rolison, D. R.; Stroud, R. M.; Long, J. W. Incorporation of Homogeneous, Nanoscale MnO_2 within Ultraporous Carbon Structures via Self-Limiting Electroless Deposition: Implications for Electrochemical Capacitors. *Nano Lett.* **2007**, *7*, 281-286.

46 Shaju, K. M.; Bruce, P. G. A Stoichiometric Nano-$LiMn_2O_4$ Spinel Electrode Exhibiting High Power and Stable Cycling. *Chem. Mater.* **2008**, *20*, 5557-5562.

47 Ma, H.; Zhang, S.; Ji, W.; Tao, Z.; Chen, J. α-CuV_2O_6 Nanowires: Hydrothermal Synthesis and Primary Lithium Battery Application. *J. Am. Chem. Soc.* **2008**, *130*, 5361-5367.

48 Brezesinski, T.; Wang, J.; Senter, R.; Brezesinski, K.; Dunn, B.; Tolbert, S. H. On the Correlation between Mechanical Flexibility, Nanoscale Structure, and Charge Storage in

Periodic Mesoporous CeO_2 Thin Films. *ACS Nano* **2010**, *4*, 967-977.

49 Kim, J. W.; Augustyn, V.; Dunn, B. The Effect of Crystallinity on the Rapid Pseudocapacitive Response of Nb_2O_5. *Adv. Energy Mater.* **2012**, *2*, 141-148.

50 Naoi, K. 'Nanohybrid Capacitor': The Next Generation Electrochemical Capacitors. *Fuel Cells*. **2010**, *5*, 825-833.

51 Sudant, G.; Baudrin, E.; Dunn, B.; Tarascon, J.-M. Synthesis and Electrochemical Properties of Vanadium Oxide Aerogels Prepared by a Freeze-Drying Process. *J. Electrochem. Soc.* **2004**, *151(5)*, A666-A671.

52 Wei, F.; Zhang, Q.; Qian, W. Z.; Yu, H.; Wang, Y.; Luo, G. H.; Xu, G. H.; Wang, D. Z. The Mass Production of Carbon Nanotubes Using a Nano-Agglomerate Fluidized Bed Reactor: A Multiscale Space-Time Analysis. *Powder Technol.* **2008**, *183*, 10-20.

53 Chen, Z.; Qin, Y.; Weng, D.; Xiao, Q.; Peng, Y.; Wang, X.; Li, H.; Wei, F.; Lu, Y. Design and Synthesis of Hierarchical Nanowire Composites for Electrochemical Energy Storage. *Adv. Funct. Mater.* **2009**, *19*, 3420-3426.

54 Burke, A. Ultracapacitors: Why, How, and Where Is the Technology. *J. Power Sources*. **2000**, *91*, 37-50.

55 Brousse, T.; Toupin, M.; Bélanger, D. A Hybrid Activated Carbon-Manganese Dioxide

Capacitor using a Mild Aqueous Electrolyte. *J. Electrochem. Soc.* **2004**, *151(4)*, A614-A622.

Chapter 8: Fabrication of Thin-Film Electrodes from Building Nanocrystals for Micro-Supercapacitors

1. Introduction

Micro-power-sources, which are commonly based on thin-film batteries and supercapacitors, are essential for micro-electronics, such as non-volatile memory, smart sensors, radio frequency identification tags (RFIT), implantable medical devices and micro-electromechanical systems (MEMS).[1] Their current fabrication mainly relies on complicated processes that often involve the use of expensive equipment with high operation cost, leading to solid-state devices often with low rate-capability and poor durability.[2] Although lower-cost micro-supercapacitors could also be made from activated carbons with higher power,[1c] activated carbons generally possess large particle size in the range of microns, which limits their use for thin devices. Note that thinner carbon-based devices may be made by controlled etching of metal carbide films.[1d] Such etching process, however, brings up the fabrication cost significantly. In addition, such carbon-based devices are generally operated based on double-layer capacitance, which offers energy densities that are much lower than those of micro-batteries.

Towards better micro-devices, one promising direction is to fabricate micro-pseudocapacitors using thin films of transition metal oxides. Compared with the carbon-based devices, such devices could store significantly larger amount of charge by fast redox reactions, providing new opportunities for high-energy and high-power micro-devices. For example, thin-films of RuO_2 and MnO_2 may provide specific capacitance up to 700 and 1200 F g^{-1},[3] respectively, which is an-order-of-magnitude larger than those of the carbon materials (~100-200 F g^{-1}).[4] However, current fabrication of such RuO_2-based thin films relies on the electrophoresis deposition techniques[3a] or an evaporation-induced self-assembly process with the aid of copolymers.[3b] Similarly, MnO_2 thin films were normally made by electrochemical deposition on porous metallic templates.[3c] Although other methods, including sputtering,[5a] pulse laser deposition[5b] and chemical vapor deposition,[5c] were also used to fabricate the oxide-based thin films, the processes developed so far are not effective enough for low-cost and large-scale device fabrication.

Herein, we report a facile coating technique that enables effective fabrication of high-performance micro-pseudocapacitor electrodes at low cost. Our strategy is based on a simple wet-chemical approach using nanocrystals (NCs) of transition metal oxides as the building materials. The past decade has witnessed a rapid advance in NCs synthesis;

large families of NCs were effectively synthesized with controlled structure, morphology, and composition,[6] which offers a large variety of building NCs for the fabrication of micro-pseudocapacitors. To demonstrate this concept, NCs of titanium dioxide (TiO_2) was used as the model system. TiO_2 has been extensively explored for energy storage applications partially due to its abundance, low cost and environmental benignity. Some high-rate electrodes were reported using nanoparticulate or mesoporous TiO_2 for lithium-ion anodes;[7] however, their rate-performances are still far below the requirement for supercapacitors. We note mesoporous TiO_2 thin films have been reported for pseudocapacitor electrodes; however, their fabrication highly is depended on the assembly of inorganic clusters with copolymers that are difficult to synthesize.[8]

2. Results and Discussions

To form the thin-film pseudocapacitor electrodes, monodispersed TiO_2 NCs were first synthesized using a simple two-phase thermal reaction method, where toluene and water were used as the reaction media and oleic acid (OA) was used as the capping agent. The resulting OA-capped TiO_2 NCs can be easily dispersed in toluene to form a nano-ink, which could be readily coated on conductive substrates such as indium-tin-oxide (ITO) glass and doped

silicon. Post-sintering treatment of the thin films in air removes the OA from the NCs, creating porous channels and networks of NCs for effective transport of charges, ions and electrolyte molecules. Compared with the current fabrication techniques, this simple coating technique enables effective fabrication of thin-film electrodes with controlled thicknesses at low cost.

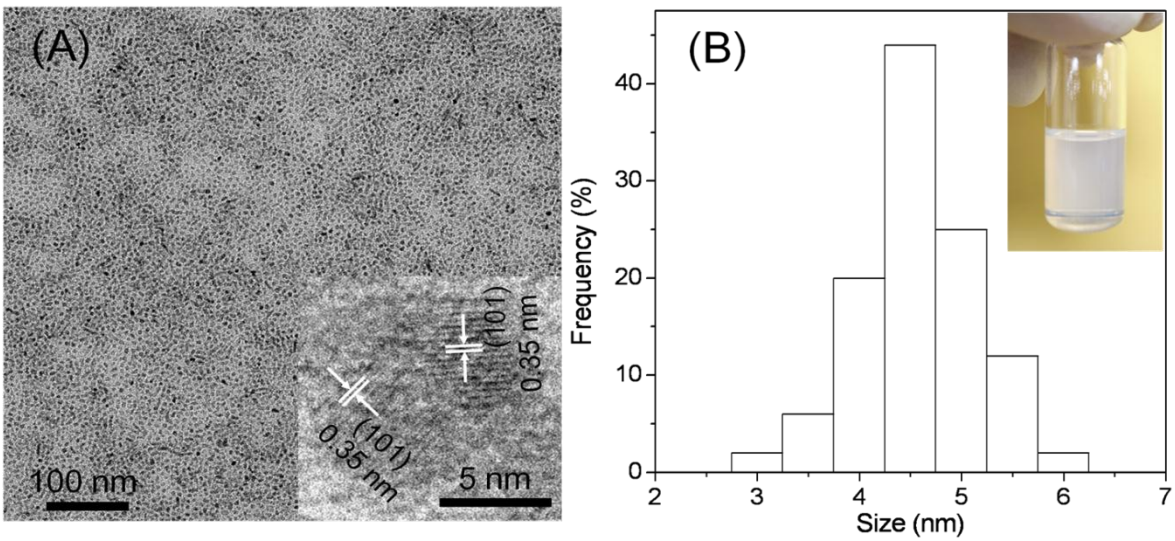

Figure 8.1 (A) Representative TEM image of TiO_2 nanocrystals. Inset showing a high-resolution TEM image of two closely attached TiO_2 nanocrystals with (101) plane and a lattice distance of 0.35 nm. (B) size-distribution of the TiO_2 nanocrystals. Inset showing a photograph of TiO_2-toluene solution containing 5 wt-% of TiO_2 nanocrystals.

Figure 8.1A displays a representative transmission electron microscopic (TEM) image of

the as-synthesized TiO_2 NCs. These nanocrystals are well dispersed and show narrow size-distribution as shown in **Figure 8.1B.** An average crystal size is calculated to be 4.9 nm. While the crystals are ultrafine, they are highly crystallized as shown in high-resolution TEM (inset, **Figure 8.1A**); well-defined lattices with distance of 0.35 nm are clearly observed. In addition, a toluene solution containing such TiO_2 NCs could be stable for a few months without any precipitation due to the presence of capping agents (inset, **Figure 8.1B**), which is favorable for large-scale fabrication.

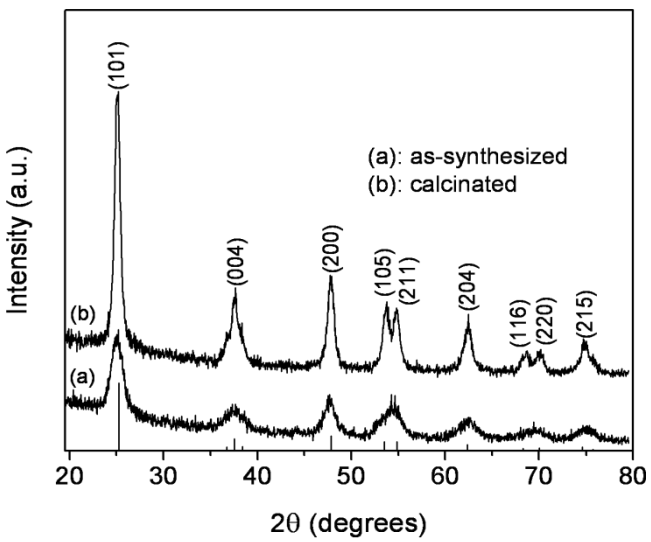

Figure 8.2 XRD patterns of TiO_2 nanocrystals before and after the sintering treatment that removed the capping agent.

Figure 8.2 shows the x-ray powder diffraction patterns of TiO_2 NCs before and after

sintering treatment to remove the capping ligands (oleic acid). The diffraction pattern of as-synthesized TiO_2 NCs matches well to that of tetragonal anatase TiO_2 (according to JCPDS reference card no. 21-1272) with no indication for either rutile or brookite phases. The broadening of peaks is originated from the small crystal size, which is calculated to be 5.3 nm from Scherrer equation and is close to the average size observed from TEM. Sintering treatment at 450 ^{o}C effectively removed the ligands (**Figure 8.3**) leading to slight increase of grain size (~ 8.2 nm), which is favorable for fast ion-storage kinetics.

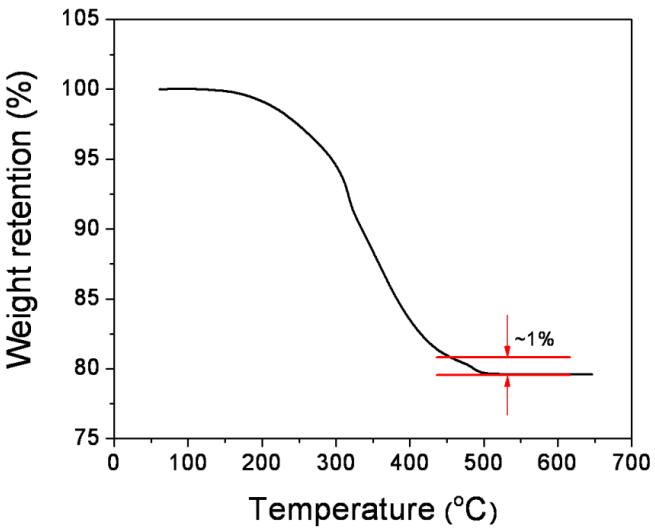

Figure 8.3 TGA plot of OA-capped TiO_2 NCs.

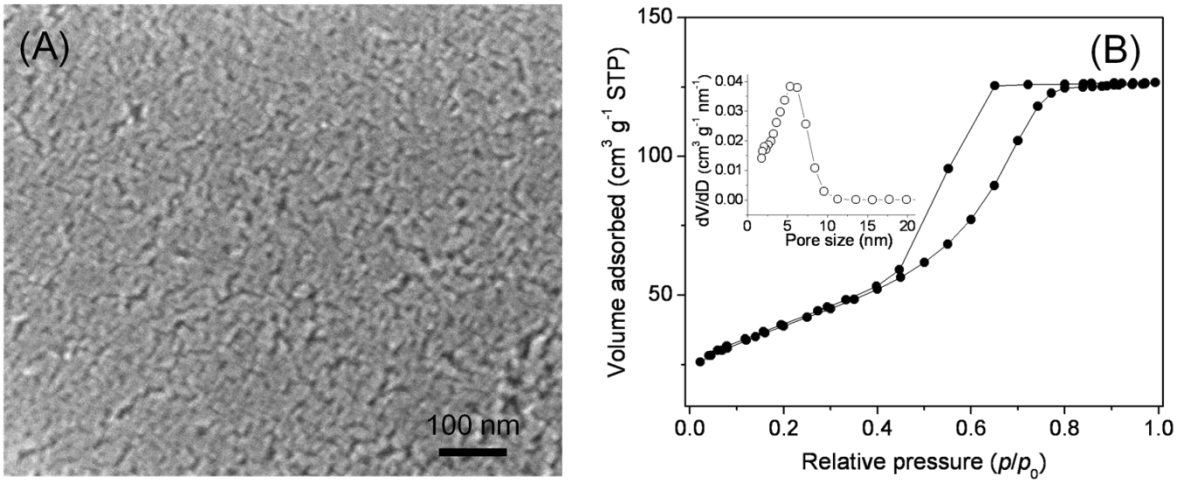

Figure 8.4 (A) Representative SEM image on the surface of a TiO_2 NCs thin-film and (B) Nitrogen adsorption isotherms of TiO_2 nanocrystals with sintering treatment (inset shows the corresponding pore-size distribution).

Figure 8.4A shows scanning electron microscopic (SEM) image of the calcined thin-film electrode, revealing porous networks of close-packed NCs. The porous structure was further confirmed by the nitrogen adsorption-desorption isotherms shown in **Figure 8.4B**. It gives a type-IV isotherm with an H_1-type hysteresis loop at a relative pressure between 0.45 and 0.8, which is typical of mesoporous structure. Such materials exhibit a high Brunauer–Emmett–Teller (BET) surface area of 140 m^2 g^{-1} and a narrow pore diameter distribution centered at about 6.5 nm.

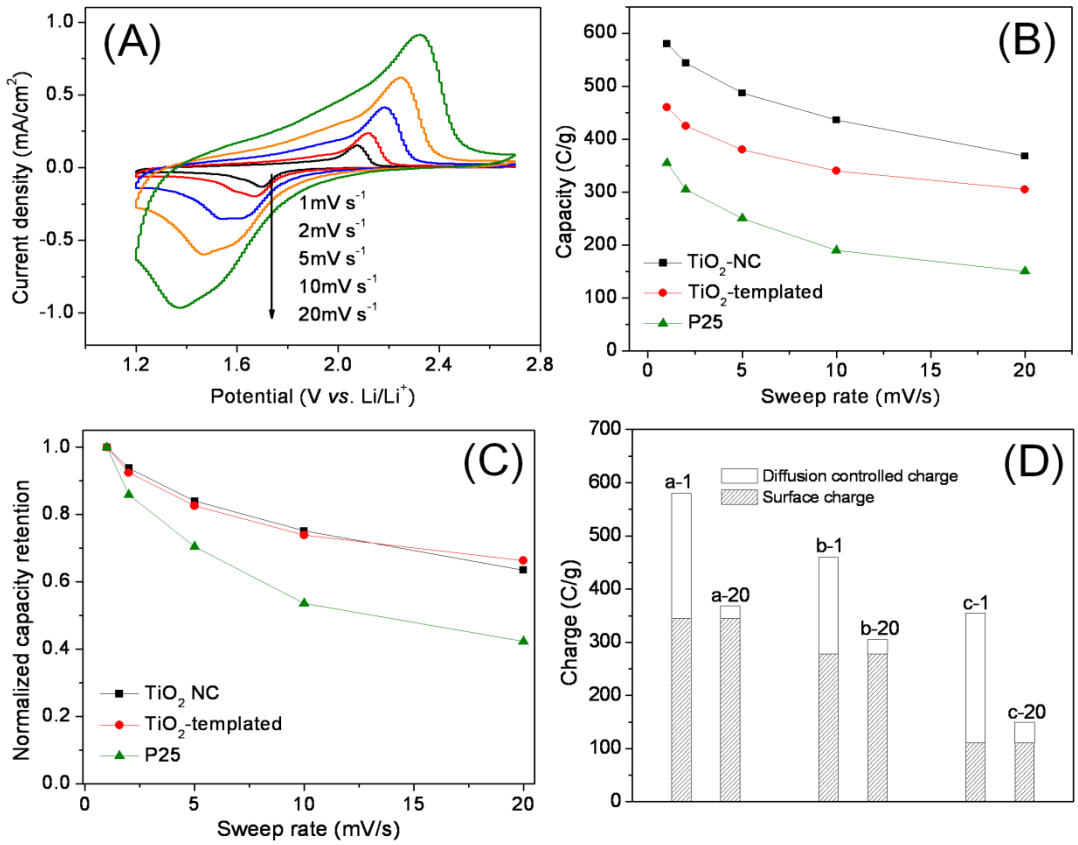

Figure 8.5 (A) Cyclic voltammograms of thin-film electrode based on TiO_2 nanocrystals (0.20 mg cm^{-2}); (B) Capacity dependence on sweep rate of different TiO_2 electrodes; (C) Normalized rate-capability of different TiO_2 electrodes; (D) Separation of surface charge and diffusion-controlled charge of different TiO_2 electrodes (a: TiO_2 NCs; b: templated mesoporous TiO_2, c: P25-TiO_2; "1" or "20" indicates a sweep rate of 1 or 20 mV s^{-1}).

The electrochemical behavior of the TiO_2 NCs-based thin-films was investigated using three-electrode cells, in which lithium foils were used as both the counter and the reference electrodes. Charge storage behavior was first characterized by cyclic voltammetry (CV).

Figure 8.5A shows typical cyclic voltammograms for the thin-film electrodes at various sweep rates. The area under the curves represents the total stored charge arising from both surface reaction and bulk diffusion processes. Generally, the electrochemical Li^+ insertion and extraction process occurring at anatase TiO_2 electrodes can be expressed by $TiO_2 + xLi^+ + xe^- \leftrightarrow Li_xTiO_2$, where x is the mole fraction of the inserted lithium ions.[9] The theoretical capacity is 168 mAh g^{-1} (605 C g^{-1}) based on x=0.5 for bulk anatase TiO_2. Consistent with the lithium insertion and extraction behavior of anatase TiO_2 at slow rates, two well-defined current peaks are observed at 1.7 V (cathodic sweep) and 2.0 V (anodic sweep), which are corresponding to the biphasic transition between tetragonal anatase (*I*41/*amd*) and orthorhombic lithium titanate (*Imma*). However, unlike the sharp lithium insertion and extraction peaks often observed for bulk anatase,[9c,d] the peaks on the CV curves show broad feature even at slow sweep rates, which indicates a pseudocapacitive effect arising from the ultra-small crystal size and high surface area. This effect has also been observed on a variety of templated mesoporous thin films.[8]

To further explore their lithium storage, **Figure 8.5B** compares the capacities of different TiO_2 thin-film electrodes made by P25-TiO_2 (a commercial TiO_2 with particle size of ~25

nm), templated mesoporous thin-film reported by Dunn[8] and ultrafine TiO_2 NCs at sweep rates from 1 to 20 mV s^{-1}. All these films have comparable thickness around submicron level. The P25 electrodes provide a capacity of ~355 and 190 C g^{-1} at 1 and 5 mV s^{-1}, respectively, indicating a moderate capacity and rate capability. The templated mesoporous thin films with pore size of ~20 nm and grain size of ~15 nm show a high capacity of ~460 at 340 C g^{-1} at 1 and 10 mV s^{-1} (corresponding to charging time of 1500 and 150 s), respectively. In contrast, the ultrafine NCs-based electrodes exhibit a substantially higher capacity, ~580 C g^{-1} at 1 mV s^{-1}, and still preserves ~370 C g^{-1} at 20 mV s^{-1} (a charge-discharge time of 75 s). It is noted that higher specific capacities (up to ~320 mAh g^{-1} or 1150 C g^{-1} at x=0.92) have been reported for TiO_2 previously, which relied on higher surface area, lower charging potential and longer charging time (**Figure 8.6**).

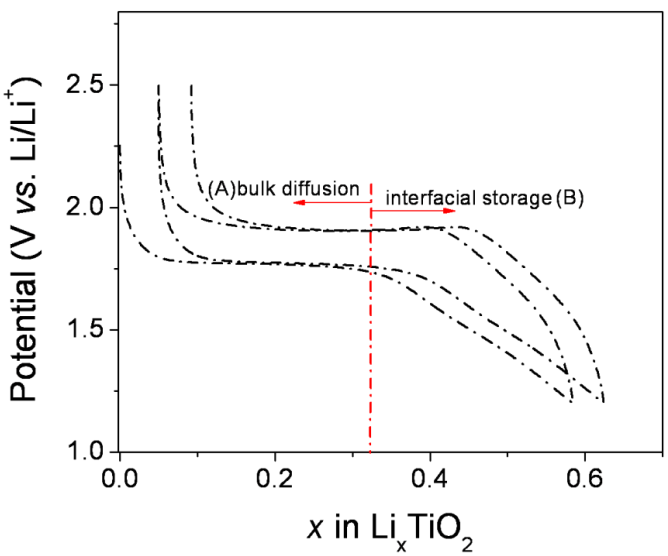

Figure 8.6 A representative galvanostatic charge/discharge plots of TiO_2 thin-film electrode at a rate of 0.5C. The plots show two regions, plateau region which is mainly associated with bulk diffusion process (A) and sloping region which is more likely related to interfacial charge storage (B),[10] which corresponds to different phase compositions and agrees well with CV measurement.

From CV and galvanostatic charge/discharge at a rate of 0.5C, we note a maximum specific capacity of ~ 200 mAh g^{-1} (x=0.59 in Li_xTiO_2) was achieved for the NC thin-film electrodes, close to most of anatase TiO_2 (150-230 mAh g^{-1})[11] but lower than the theoretical maximum capacity based on x=1 (~330 mAh g^{-1}) and some other high-surface-area nanoporous anatase electrodes.[10,12] In order to understand and explain the different charge storage behavior, we compared various anatase TiO_2 electrodes and found the following possible reasons leading to relatively lower capacity of the NC thin-film electrodes:

1) **Relatively small surface area**. For nanostructured anatase TiO_2 electrodes, various studies have revealed that the overall charge storage is contributed from two different storage modes: a) bulk diffusion-controlled insertion which relates to a charge/discharge plateau at ~1.75 V (vs. Li/Li^+), and b) interfacial storage which corresponds to a linear

charge/discharge region below 1.75 V.[10-12] Typically, the higher surface area enables shorter diffusion length and more surface active sites, which lead to larger overall capacity. For example, we note capacities of >300 mAh g^{-1} (close to theoretical capacity) for TiO_2 with surface area of over 200 m^2 g^{-1}.[10,12] For other nanostructured TiO_2 with moderate surface areas, the capacities range from 150-230 mAh g^{-1}.[11] Our NC TiO_2 has a surface area of ~140 m^2 g^{-1}, which provides a moderate capacity of ~200 mAh g^{-1}.

2) **High charge voltage**. The overall storage capacity strongly depends on the cut-off charge voltage (1.2V). The maximum TiO_2 capacity has been reported based on charging down to 1 V.[10,12] In such cases, much more interfacial storage was realized at the low voltage window. Our electrodes were charged to 1.2V, which further resulted in a lower capacity. It is worthwhile to mention that we emphasized the supercapacitor application, where the easy formation of solid-electrolyte-interface at ~1 V should be avoided. Therefore, we chose 1.2V as the cut-off voltage.

3) **Rapid charge/discharge rate**. The overall storage capacity also strongly depends on the charge/discharge rate. The largest TiO_2 capacity was achieved by charging/discharge for a few hours,[10,12] which allowed full Li-insertion in the anatase

framework, leading to high capacity. With regard to supercapacitor application in our case, much higher rates were used (charging/discharge in mins), which sacrificed some capacity simply due to less time for Li^+ to diffuse into the titania framework.

In addition, as far as the theoretical capacity concern, a lithium concentration of x=1 in Li_xTiO_2 will result in a maximum capacity of 336 mAh g^{-1} at cut-off charging voltage at 1.0 V. However, at x>0.5, the Li-rich titinia no longer reversibly dissolve Li and the diffusion kinetics is slow.[10] Although high capacity can be achieved at the first charge cycle, the capacity might decrease appreciably at the second cycle due to the irreversible reactions.[10,12] Similarly, for NC-based thin films, we noted a first-cycle charge capacity of ~220 mAh g^{-1} which decreased to ~200 mAh g^{-1} in the second cycle due to the similar reason.

A direct comparison of the rate-capability of three types of electrodes is shown in **Figure 8.5C**, where the capacities are normalized at 1 mV s^{-1}. Clearly, the NCs films present a similar rate-capability to those of templated mesoporous films, showing a ~70% capacity retention as sweep rate increased from 1 to 20 mV s^{-1}. Overall, the excellent lithium-storage performance of the NCs electrodes is attributed to their small crystal size and mesoporous architecture. Such high-capacity and high-rate performance has rendered such NCs films to

be one of the best lithium-storage electrodes for thin-film pseudocapacitors where high power is highly demanded. This result underscores the superiority of using NCs to make ultrafast thin-film pseudocapacitors since higher capacity can be achieved without sacrificing rate-capability. Moreover, such electrodes were fabricated by directly casting the NCs inks without using any scarce polymer template, making it more attractive towards low-cost energy storage devices.

It is also essential to understand how such ultrafine NCs could store lithium with high capacity and ultrafast kinetics. Recent studies on nanoscale energy storage reveals that thermodynamic and kinetics properties of particulate electrode materials could be strongly impacted by surface/interface effect, particularly, when the particles sizes approach certain critical values.[10] To study the possible surface/interface effects, we separated the surface- and bulk- contributions from the total charge storage based on the Trasatti method.[11] In this approach, the total voltammetric charge (q_T) was separated into surface-capacitive charge (q_s) and bulk-diffusion controlled charge (q_d) by:

$$q_T = q_s + q_d \quad (1)$$

where q_s is correlated with double-layer capacitance and pseudocapacitance, which are associated with surface lithium adsorption accompanied by a charge transfer process; while

q_d mainly depends on slow diffusion process followed by lithium intercalation within the bulk crystal. Due to faster kinetics associated with surface lithium adsorption, electrodes presenting a large fraction of q_s in the total capacity will exhibit a high rate-capability. In this context, reducing the particle size will enhance the surface contribution and improve electrode rate-capability.

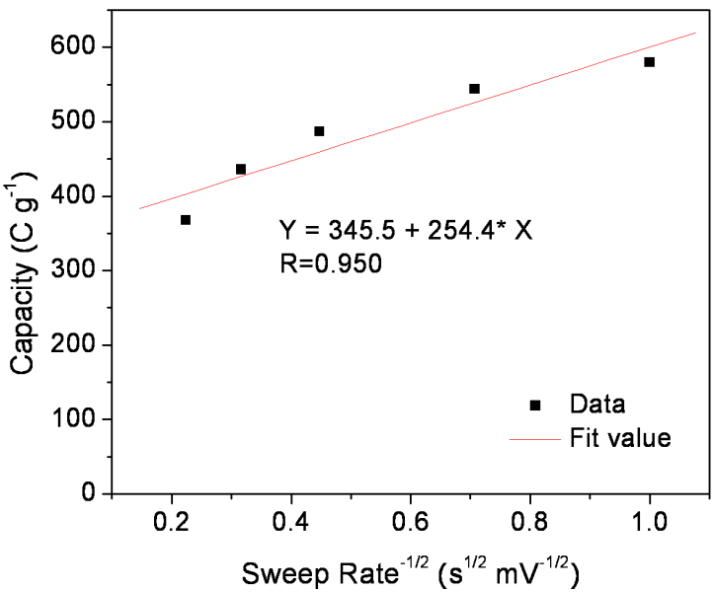

Figure 8.7 Example of plotting the total voltammetric charge q_T of TiO_2 NC thin-film electrode against the reciprocal of the square root of the potential sweep rate (v) and extrapolating v to ∞.

Based on the semi-infinite linear diffusion law, within a reasonable range of sweep rates, q_s can be derived by plotting the q_T against the reciprocal of the square root of the potential

sweep rate (v) and extrapolating v to ∞, according to the following equation (**Figure 8.7**):

$$q_T = q_s + cv^{-1/2} \quad (2)$$

A separation of surface (capacitive) and diffusion controlled charge contribution to total capacity is displayed in **Figure 8.5D.** It is clearly shown that the surface charge indeed plays an important part at various sweep rates for all electrodes, especially for templated mesoporous film and TiO_2 NCs electrodes. The templated mesoporous film electrodes show a surface contribution of 278 C g^{-1}, which accounts for 60 % of the total capacity at 1 mV s^{-1} and 91 % at 20 mV s^{-1}. Owing to their smaller crystal size, the NCs electrodes show even more surface contribution of 345 C g^{-1} (accounting for 60 % at 1 mV s^{-1} and 94 % at 20 mV s^{-1}), which is a ~25 % higher capacity than that of templated films. As a result, such large surface-capacity contribution endows electrodes with ultrafast charge and discharge capability since the slow diffusion process is no longer needed. The fast kinetics feature has also been confirmed by impedance study (**Figure 8.8**). Moreover, this effect results in a ~25 % higher total capacity than the templated mesoporous thin films, suggesting a larger portion of lithium titanate in the equilibrium composition where anatase TiO_2 and lithium titanate coexist.[10] While the dependence of particles size on the lithium storage performance has been investigated before,[9c,e] this result clearly discloses the significant

surface effect on the electrode kinetics and thermodynamics, providing better understanding on charge storage for thin film electrodes based on ultrafine NCs.

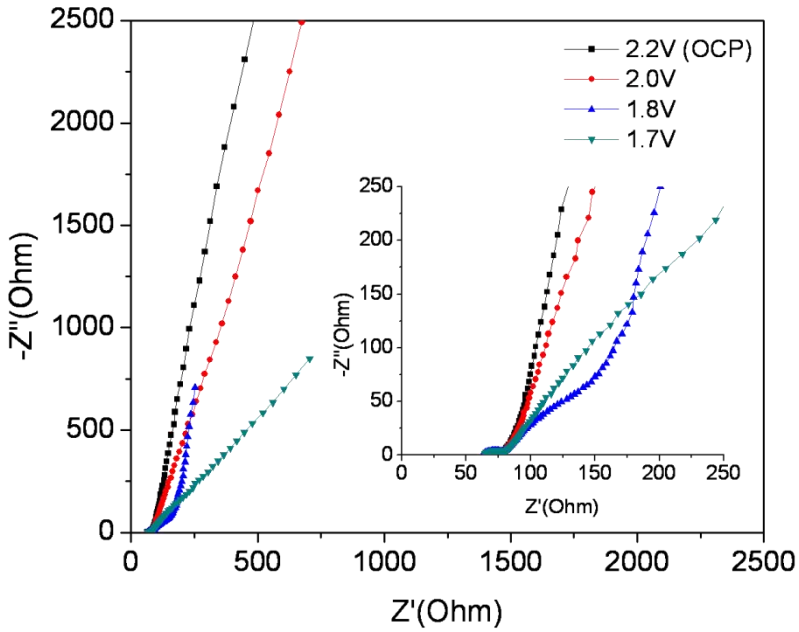

Figure 8.8 Nyquist representation of impedance spectra for the TiO_2 NC thin-film electrode (0.2 mg/cm^2) at four different potentials, before any lithiation at open-circuit (2.2 V) and after lithiating to 2.0, 1.8 and 1.7 V. Inset shows enlarged Nyquist plots. The electrode showed a typical capacitive feature as indicated by the close-to-vertical line at low-frequency region. The small semicircle at high-frequency region showed the charge-transfer resistance from electrode reaction. After slightly lithiating (at 1.8 V), the electrode showed a small Warburg region, which was associated with lithium diffusion in the titania framework. The electrode at 1.7 V showed a typical Warburg tail, indicating the electrode kinetics was then limited by

diffusion after substantial lithiating.

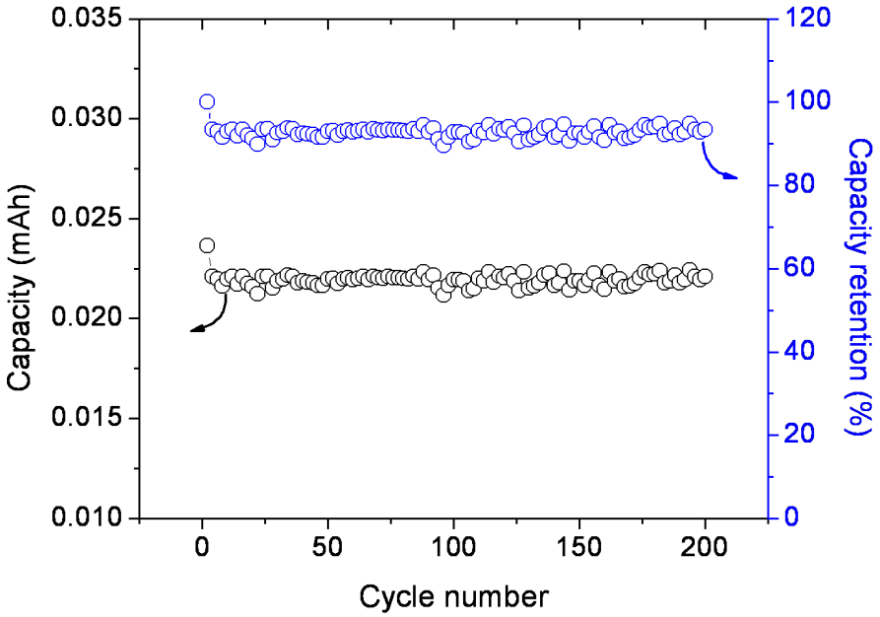

Figure 8.9 Cycling performance of a representative TiO_2 NC thin-film electrode with a mass loading of 0.16 mg.

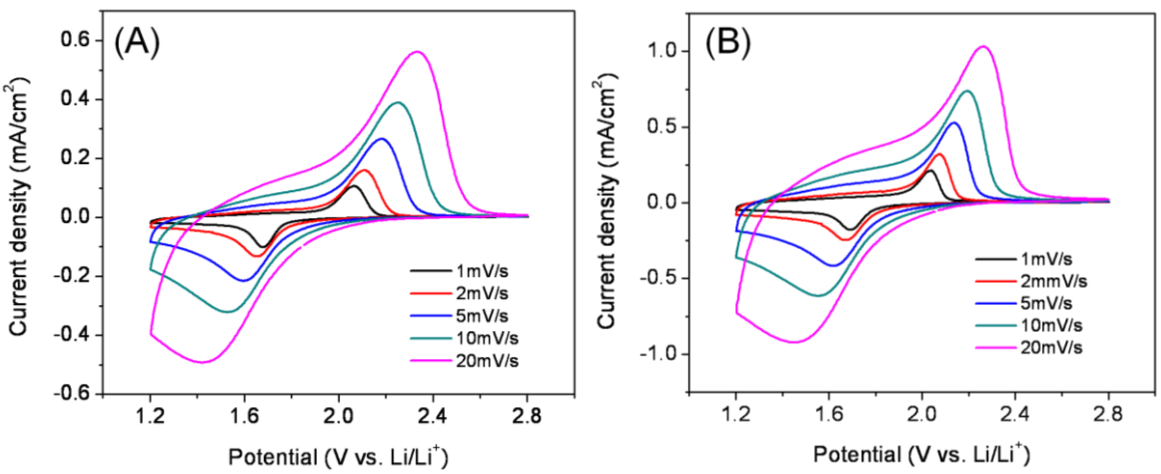

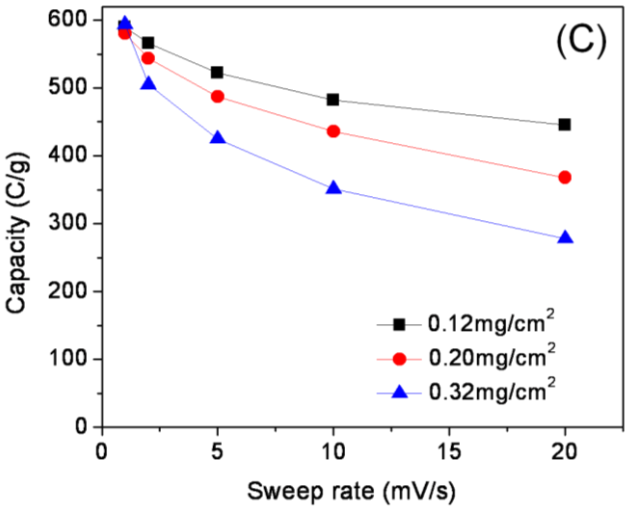

Figure 8.10 Cyclic voltammograms of TiO_2 NC thin-film electrodes at mass loading of 0.12 mg/cm^2 (A) and 0.32 mg/cm^2 (B); Capacity and rate dependence on the thickness of the NC thin-film electrodes (The electrodes with NC loading of 0.12, 0.20, and 0.32 mg/cm^2 showed thickness of 0.78, 1.3 and 2.1 μm, respectively).

Besides the fast kinetics observed, these NCs thin-films also show impressive cycling stability as evaluated from long-term galvanostatic cycling tests. **Figure 8.9** shows the cycling performance of a NC thin-film electrode at a rate of 10 C (1C=170 mA g^{-1}). The electrode could still preserve ~92% of its initial capacity after 200 cycles, indicating reliable structure stability of such binder-free NC thin-film electrodes. In addition, although we noted that the electrode performance was also affected by the film thickness (**Figure 8.10**), one typical thickness (~1 μm) was adapted to demonstrate the fabrication strategy and study

the storage property.

3. Conclusion

In summary, we have demonstrated a simple yet effective strategy towards high-performance thin-film pseudocapacitors using NCs of transition metal oxides as building blocks. These electrodes show high capacitance, excellent rate capability and reasonable stability. In light of recent advances in the synthesis of NCs with controlled structure and composition, this strategy provides a general fabrication approach towards NCs-based micro-pseudocapacitors. This strategy could also be extended to fabricate thin films for other applications such as anti-corrosion coatings and photocatalysis.

4. Experimental

4.1 Synthesis of TiO_2 NCs

The TiO_2 NCs were synthesized using a two-phase hydrothermal reaction.[9] In a typical synthesis, 0.4 mL of *tert*-butylamine was dissolved in 40 mL of de-ionized water and the solution was transferred into a 100 mL Teflon-line stainless-steel autoclave. Subsequently, 0.6 g of titanium (IV) n-propoxide (2 mmol) and 4.0 mL of oleic acid were dissolved in 40

mL of toluene in air and the solution was transferred into the autoclave without any stirring. The autoclave was sealed and maintained at 180 ^{o}C for 8 h and cooled to room temperature with tap water. The crude solution of TiO_2 NCs was precipitated with methanol and further isolated by centrifugation and decantation. The purified TiO_2 NCs were re-dispersed in toluene to form a NCs ink with desired concentration.

4.2 Fabrication of TiO_2 NCs thin-films

To make NC thin-films, different amounts of above NC solution were directly coated on clean indium tin oxide (ITO) substrates. After solvent evaporation at room temperature, the films were sintered at 450 ^{o}C for 1 hr at a ramp rate of 2 ^{o}C min^{-1}. The NC loading can be varied from μg to mg by controlling coating solution, though typical thin-films reported here have an active mass loading of 0.1-0.2 mg cm^{-2}.

4.3 Fabrication of P25 TiO_2-based thin-films

To make P25-based films, powder sample was dispersed in ethanol under sonication and stirring. The formed solution was directly coated on ITO substrates and thermal treated at 250 ^{o}C to removal solvent.

4.4 Material and Electrode Characterization

The X-ray diffraction measurements were taken on Panalytical X'Pert Pro X-ray powder diffractometer using the copper Kα radiation (λ=1.54 Å). Nitrogen sorption isotherms were measured at 77 K with a Micromeritics ASAP 2020 analyzer. The samples were degassed in vacuum at 200 ^{o}C for three hours. The specific surface areas (S_{BET}) were calculated by the Brunauer-Emmett-Teller (BET) method using adsorption branch in a relative pressure range from 0.04 to 0.25. The pore size distributions were derived from the adsorption branches of isotherms using the Barrett-Joyner-Halenda (BJH) model. Scanning electron microscopy (SEM) experiments were conducted on a JEOL JSM-6700 FE-SEM. Transmission electron microscopy (TEM) experiments were conducted on a Philips CM120 operated at 120 kV.

To test thin-film electrodes, CV and galvanostatic charge/discharge measurements were carried out in three-electrode flood cells in an argon-filled glove box. The measurements were carried out on a Solartron 1860/1287 electrochemical interface. The electrolyte solution was a 1 M $LiClO_4$ in propylene carbonate (PC) solution and lithium foils were used as both the counter and reference electrodes.

References

1. (a) J. W. Long, B. Dunn, D. R. Rolison and H. S. White, *Chem. Rev.*, 2004, **104**, 4463; (b) N. J. Dudney, *Mater. Sci. Eng. B*, 2005, **116**, 245; (c) D. Pech, M. Brunet, P. L. Taberna, P. Simon, N. Fabre, F. Mesnilgrente, V. Conedera and H. Durou, *J. Power Sources*, 2010, **195**, 1266; (d) J. Chmiola, C. Largeot, P.-L. Taberna, P. Simon and Y. Gogotsi, *Science*, 2010, **328**, 480.
2. M. Baba, N. Kumagai, N. Fujita, K. Ohta, K. Nishidate, S. Komaba, H. Groult, D. Devilliers and B. Kaplan, *J. Power Sources*, 2001, **97-98**, 798.
3. (a) J. H. Jang, A. Kato, K. Machida and K. Naoi, *J. Electrochem. Soc.*, 2006, **153**, A321; (b) S. Capucine, L. Christel, K. Hung Le, C. Sophie, B. Cédric, A. Markus and S. Clément, *Adv. Funct. Mater.*, 2009, **19**, 1922; (c) X. Lang, A. Hirata, T. Fujita and M. Chen, *Nat Nano*.,2011, **6**, 232.
4. J. Chmiola, G. Yushin, Y. Gogotsi, C. Portet, P. Simon and P. L. Taberna, *Science*, 2006, **313**, 1760.
5. (a) J. Xie, T. Tanaka, N. Imanishi, T. Matsumura, A. Hirano, Y. Takeda and O. Yamamoto, *J. Power Sources*, 2008, **180**, 576; (b) S. B. Tang, M. O. Lai and L. Lu, *Mater. Chem. Phys.*, 2008, **111**, 149; (c) S. W. Jin and H. N. G. Wadley, *J. Vac. Sci.*

Tech. A, 2008, **26**, 114.

6. (a) J. Park, J. Joo, S. G. Kwon, Y. Jang and T. Hyeon, *Angew. Chem. Int. Ed.*, 2007, **46**, 4630; (b) N. Zhao, W. Nie, J. Mao, M. Yang, D. Wang, Y. Lin, Y. Fan, Z. Zhao, H. Wei and X. Ji, *Small*, 2010, **6**, 2558.

7. (a) I. Moriguchi, R. Hidaka, H. Yamada, T. Kudo, H. Murakami and N. Nakashima, *Adv. Mater.*, 2006, **18**, 69; (b) R. Yu, J. H. Laurence and G. B. Peter, *Angew. Chem. Int. Ed.*, **49**, 2570; (c) D. Wang, D. Choi, J. Li, Z. Yang, Z. Nie, R. Kou, D. Hu, C. Wang, L. V. Saraf, J. Zhang, I. A. Aksay and J. Liu, *ACS Nano*, 2009, **3**, 907.

8. T. Brezesinski, J. Wang, J. Polleux, B. Dunn and S. H. Tolbert, *J. Am. Chem. Soc.*, 2009, **131**, 8.

9 D. Pan, N. Zhao, Q. Wang, S. Jiang, X. Ji and L. An, *Adv. Mater.*, 2005, **17**, 1991.

10 J.-Y. Shin, D. Samuelis and J. Maier, *Adv. Funct. Mater.*, 2011, **21**, 3464.

11 a) I. Moriguchi, R. Hidaka, H. Yamada, T. Kudo, H. Murakami and N. Nakashima, *Adv. Mater.*, 2006, **18**, 69; b) Y.-G. Guo, Y.-S. Hu, W. Sigle and J. Maier, *Adv. Mater.*, 2007; **19**, 2084; c) C. Jiang, M. Wei, Z. Qi, T. Kudo, I. Honma and H. Zhou, *J. Power Sources*, 2007, **166**, 239; d) T. Brezesinski, J. Wang, J. Polleux, B. Dunn and S. H. Tolbert, *J. Am. Chem. Soc.*, 2009, **131**, 8.; e) D. Wang, D. Choi, J. Li, Z. Yang, Z. Nie, R.

Kou, D. Hu, C. Wang, L. V. Saraf, J. Zhang, I. A. Aksay and J. Liu, *ACS Nano*, 2009, **3**, 907.

12 Y. Ren, L. J. Hardwick and P. G. Bruce, *Angew. Chem. Int. Ed.*, 2010, **49**, 2570.

Chapter 9: Flexible Energy Storage Architectures from Carbon Nanotubes and Nanocrystal Building Blocks

1. Introduction

High-rate energy storage devices have been attracting tremendous interest due to their promising applications, such as cordless power tools, hybrid electric vehicles (HEVs) and renewable energy storage. Current lithium-ion batteries have been widely employed for small electronic devices; however, their application in HEVs and other fields are still limited by low power and energy densities. Developing high-performance electrodes and devices has been an essential component of the current endeavor in energy storage.[1-3]

Fundamentally, lithium-ion batteries rely on shuttling of lithium ions and electrons between the cathodes and anodes. To realize high power and energy densities, sufficient number of lithium ions and electrons need to be rapidly shuttled between the electrodes, which implies that high-performance architectures should possess effective ion- and electron-transport pathways and high active-material loading. In this context, much efforts have been devoted to the synthesis of low-dimensional active materials (e.g., nanoparticles,[3-5] nanowires,[6-8] and nanosheets[9, 10]) with high surface area and shortened lithium-diffusion

length. However, the use of such low-dimensional materials often leads to decreased volumetric density and increased contact resistance. To ensure good conductivity, significant fractions of conductive agent and binder were used, which inevitably sacrifices overall energy storage capacity. For example, high-rate electrodes of lithium iron phosphate ($LiFePO_4$)[3] and titanium dioxide (TiO_2)[4] were fabricated from their ultrafine particles. Such electrodes may use up to 70- and 50- wt% of carbon and binder (vs. the total weight of electrode materials), respectively, which led to electrodes with less than half of the capacity based on pure active materials. To circumvent this problem, one promising strategy is to construct conductive scaffolds and subsequently deposit active electrode materials on these scaffolds. Recently, several high-performance electrodes have been reported based on this approach using porous copper,[11] nickel[12] and gold[13] as the conductive scaffolds. However, the fabrication of such electrodes was inefficient with extremely low active-material loading in the form of ultra-thin coating.

Herein, we report a general fabrication strategy towards high-performance electrodes from conductive scaffolds of carbon nanotubes (CNTs) and the nanocrystals (NCs) of active materials. To demonstrate this concept, anatase TiO_2 NCs were used as a model material due to its abundance, low cost and environmental benignity. TiO_2 has been extensively

explored for lithium anode applications and high-rate anodes based on low-dimensional TiO_2 were also reported.[4, 9, 14-16] However, similar to the fabrication of other high-rate electrodes, large fractions of conducting agents and binders were used in these electrodes.

2. Results and Discussions

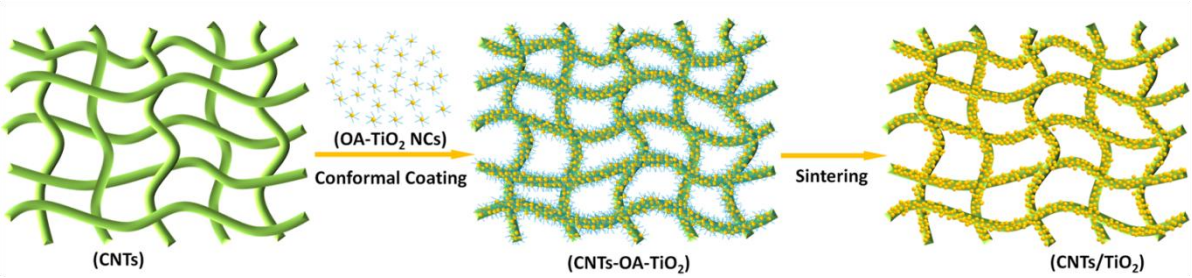

Figure 9.1 Schematic of preparing binder-free high-rate electrodes through the formation of conformal TiO_2 nanocrystals (OA-TiO_2 NCs) coatings on a CNTs scaffold followed by a sintering process that removes the capping agents on the NCs.

Figure 9.1 illustrates our strategy towards the binder-free high-rate electrodes. Uniform TiO_2 NCs capped with oleic acid (OA) (OA-TiO_2 NCs) were first synthesized and dispersed in nonpolar solvent such as toluene. Upon dropping the NCs solution to a CNTs paper prepared from unmodified ultra-long CNTs, the NCs solution rapidly spread throughout the CNTs scaffold owning to its excellent wettability with the CNTs. Subsequent solvent

evaporation enriches the NCs; driven by the hydrophobic interactions, the NCs spontaneously assemble on the CNTs.[17] A subsequent sintering process removes the capping ligands from the NCs assemblies, creating conformal mesoporous TiO_2 coatings on the CNTs. Such a hydrophobic-interaction driven process provides two key features required for high-rate electrode:

1. Effective transport of electrons and ions. The conformal coatings ensure intimate contacts and effective electron transport between the CNTs scaffold and the NCs coatings. Besides the NCs with shortened ion-diffusion length, the conformal coating process also retains the scaffold's porous channels, providing hierarchical pathways for effective ion transport.
2. High loading of active materials. Compared with the metallic scaffolds, CNTs scaffolds possess high porosity, low density and large thickness, which enable the fabrication of electrodes with high loading of active materials. For example, coating the CNTs scaffold with 5 nm- and 20 nm-thick of NCs could result in an active material loading ~ 20 wt-% and 100 wt-% (*vs.* the weight of the CNTs), respectively (see **Figure 9.6**).

In the light of recent advances in the synthesis of NCs with controlled structure and composition,[18] this strategy provides a general fabrication approach towards CNTs-NCs

based high-rate electrodes through judicious choice of building NCs. We noticed that CNTs were commonly used to fabricate the electrodes for energy storage and other applications. Their use often requires surface functionalization to improve their dispersion; however, the functionalization process also reduces their conductivity and structure stability. Moreover, such electrodes were often prepared by simply mixing active materials with the functionalized CNTs, where the interfaces between the active materials and the CNTs were poorly controlled.[14, 19-22] Although some ultra-thin coatings (~5 nm) were also applied to the surface of functionalized CNTs, the materials rendered poor stability and mass loading was difficult to control.[23, 24] By comparison, the strategy presented here utilizes the hydrophobic interactions between the NCs and the unmodified CNTs, which enables the efficient assembly of the NCs confined around CNTs and the formation of CNTs/NCs composite electrodes with the abovementioned outstanding features.

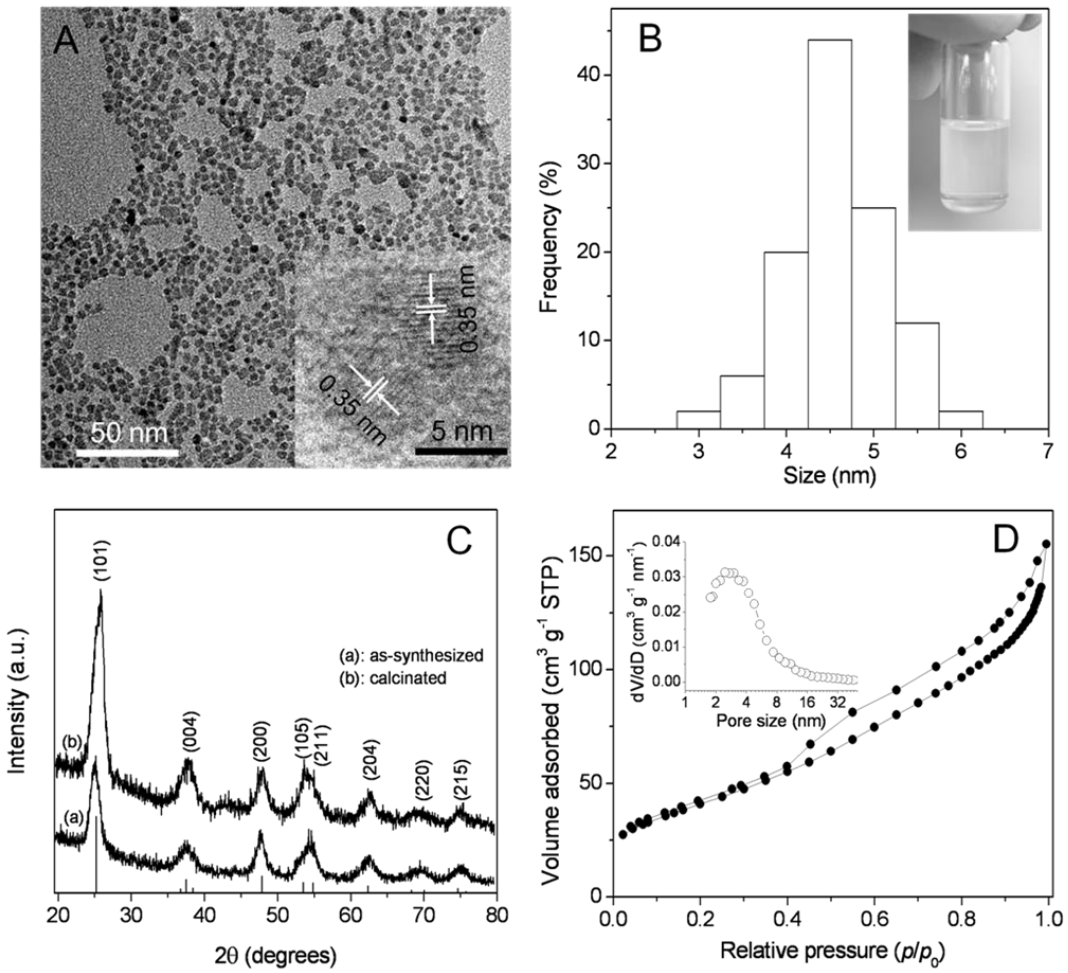

Figure 9.2 Representative TEM image of TiO_2 NCs (inset, high-resolution TEM of two closely attached TiO_2 NCs showing 101 (0.35 nm) lattice) (A) and corresponding size distribution of the NCs (inset, a photograph of TiO_2-toluene solution containing 5 wt-% of TiO_2 NCs in a 4 mL glass vial) (B). (C) XRD patterns of the NCs before and after sintering treatment. (D) Nitrogen adsorption isotherms and pore size distribution (inset) of CNT/NCs nanocomposites after the sintering treatment.

Figure 9.2A displays a representative transmission electron microscopic (TEM) image of the NCs, suggesting a narrow size distribution with an average diameter of 4.9 nm (**Figure 9.2B** and **Figure 9.7**). While the NCs are ultrafine, they are highly crystallized as shown in the high-resolution TEM image (inset, **Figure 9.2A**). In addition, since these NCs are capped with capping agents, they are stable in solvent (toluene) for a few months without precipitation (inset, **Figure 9.2B**). **Figure 9.2C** shows x-ray powder diffraction patterns of the NCs before and after removal of the capping agents. The diffraction pattern of as-synthesized NCs matches well to that of anatase TiO_2 (JCPDS reference card no. 21-1272). The peak broadening originates from their small crystallite size, which is calculated to be 5.3 nm from the Scherrer equation and consistent with those observed from TEM. Heating the CNT/NCs composites in air at 450 $^{\circ}$C removes the capping agent (**Figure 9.8**). We noticed that such a heat treatment did not lead to noticeable growth of grain size; the NCs kept an average size of 5.3 nm after the removal of the capping agent.

As expected, removal of the capping agent creates a hierarchically porous structure confirmed by the nitrogen adsorption-desorption isotherms shown in **Figure 9.2D**. A type-IV isotherm with significant nitrogen uptake from the relative pressure 0.45 is consistent with a hierarchically porous network (see pore size distribution in the inset). Note that the

presence of macropores cannot be seen from the pore size distribution due to the intrinsic instrumental limitation. The calcined nanocomposite exhibits a Brunauer–Emmett–Teller (BET) surface area of 148 m^2 g^{-1} and a pore diameter distribution centered at ~ 3 nm. Interestingly, without the CNT scaffold, sintered NCs gave a similar BET surface area (~140 m^2 g^{-1}) but slightly larger pore size (~ 6.5 nm) (**Figure 9.9**).

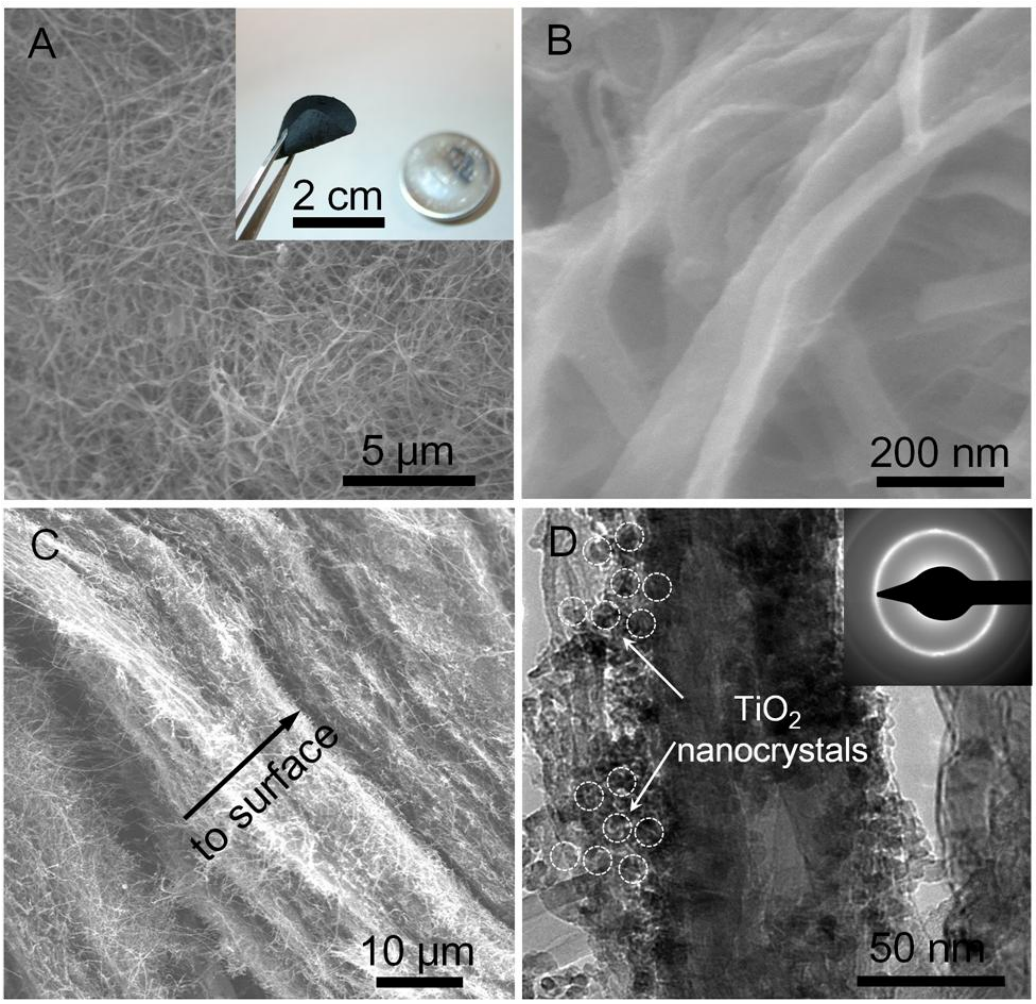

Figure 9.3 (A) Low magnification SEM image of a 3D CNT/NCs electrode showing the CNTs scaffold coated with TiO_2 NCs. Inset shows a digital photograph of a freestanding

flexible CNT/NCs electrode. (B) High magnification SEM image confirming the conformal coating of NCs on CNT surface. (C) Representative cross-section SEM image of the CNT/TiO_2 NCs electrode. (D) TEM image showing TiO_2 NCs coated on CNTs.

Inset of **Figure 9.3A** shows a freestanding flexible electrode with a thickness of ~ 100 μm. **Figure 9.3A** presents a scanning electron microscopic (SEM) image of the CNT/NCs electrode, clearly showing a macroporous 3D network structure with uniform NCs coating, which is further confirmed by the high-magnification SEM in **Figure 9.3B**. **Figure 9.3C** shows a SEM image of cross-section view of the electrode, further confirming that the super-long CNTs are intertwined through the whole electrode without obvious NCs aggregation. The successful formation of conformal NC coatings on the CNTs is further confirmed by TEM observation in **Figure 9.3D**. Layers of NCs coatings on the CNTs with thickness of ~20 nm are clearly shown. Such structure ensures short diffusion length, continuous conductive pathway, and intimate interface contacts between the NCs and the CNTs, which endows the electrodes with excellent lithium storage performance.

As mentioned above, making high-rate bulk electrodes has been an essential topic due to their broad uses in high-energy and high-power energy storage. This strategy enables us to

effectively construct bulk electrodes with high loading of active materials without additional binder and conductive-agent. For example, the CNTs scaffold used here (~ 100 μm thick) has a density of ~3 mg cm^{-2} (equivalent to a volumetric density of 0.3 g cm^{-3}), which is about two orders of magnitude lighter than that of copper foil (~ 9 g cm^{-3}) commonly used in the commercial lithium-ion anodes. Directly measuring the mass of the CNT scaffold and that of the CNT/TiO_2 NCs electrode shows that the NCs loading is ~ 130 wt% (4 mg cm^{-2}) of the CNT's weight, which is consistent with the estimation shown in Figure 9.6. Such an effective loading results in an overall volumetric density of the CNT/TiO_2 NCs hybrid electrode to be ~ 0.7 g cm^{-3}, which is close to the common tap density (< 1 g cm^{-3}) of many nano-powder-based electrodes (e.g. nano-sized $LiFePO_4$[25]). In contrast, previous 3D porous metal-based thin electrodes normally present active-material loadings far below 1 mg cm^{-2}.[11-13] Moreover, our electrode is based on a 3D continuous conductive pathway with intimate contacts between active materials and current collector.

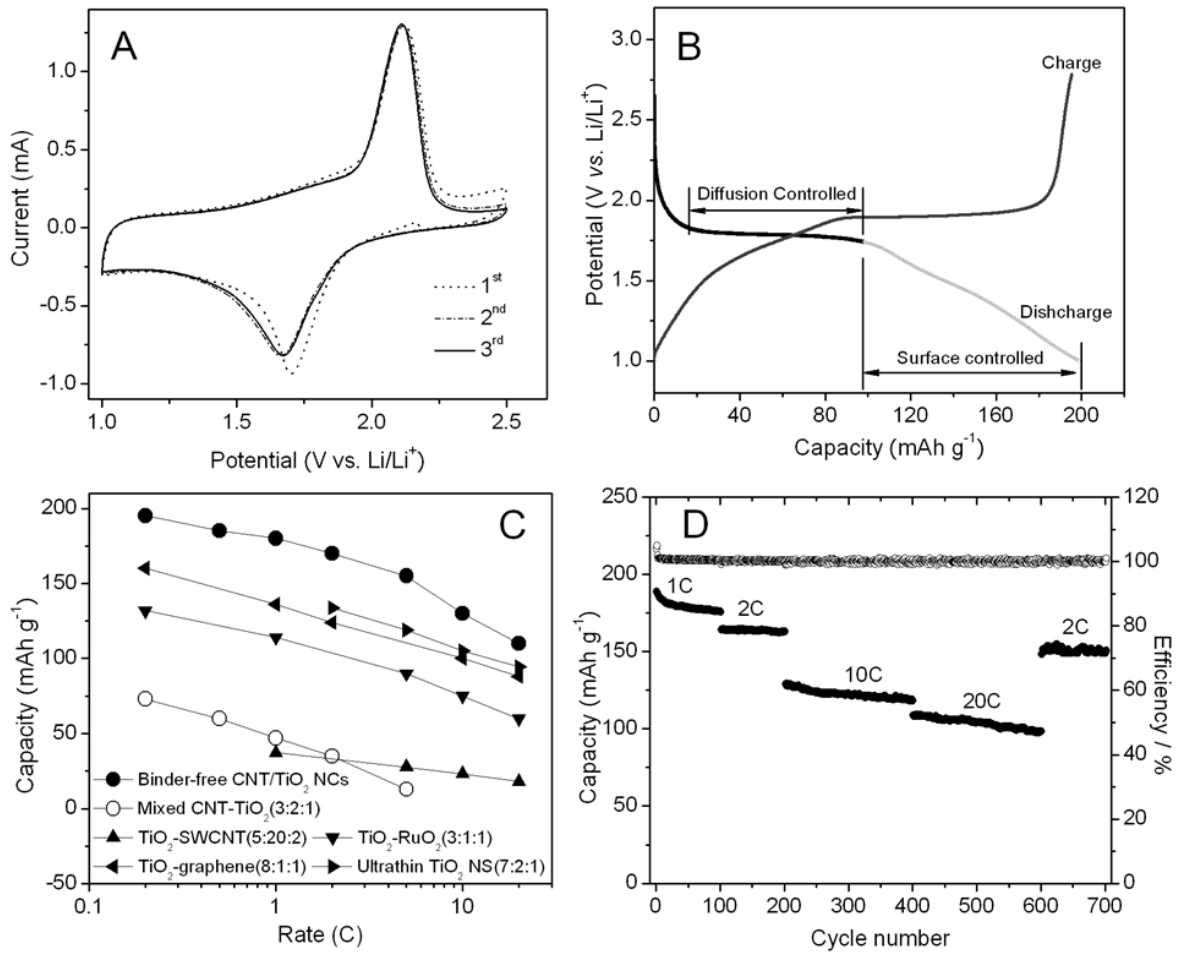

Figure 9.4 (A) CV plots of the CNT/NCs electrode for the first three cycles at a sweep rate of 0.2 mV s^{-1}, (B) Typical charge-discharge curves of the hybrid electrode at a current rate of 0.25 C, (C) Comparison of rate-capability of a variety of TiO_2-based high-rate electrodes reported recently. The capacities were estimated based on their effective mass of the whole electrodes. Their electrode compositions are listed using the mass ratio of active materials: conductive carbon: binder (TiO_2-SWCNT,[14] TiO_2-graphene,[15] TiO_2-RuO_2,[16] ultrathin TiO_2 NS[9]). (D) Long-term cycling performance of the hybrid electrode at different C-rates.

The electrochemical behavior of the electrodes was investigated using coin-cell devices, in which lithium foils were used as both the counter and the reference electrodes. Charge storage behavior was first characterized by cyclic voltammetry (CV) studies. **Figure 9.4A** shows representative cyclic voltammograms for the hybrid electrodes at a sweep rate of 0.2 mV s^{-1}. The electrochemical Li^+ insertion and extraction process occurring at anatase TiO_2 electrodes can be expressed by $TiO_2 + xLi^+ + xe^- \leftrightarrow Li_xTiO_2$, where x is the mole fraction of the inserted lithium ions ($x \leq 1$).[26] Slight shift of the CV curves were observed during the first three scans (especially cathodic scans) due to some irreversible reactions. Consistent with the insertion and extraction of lithium in anatase TiO_2, two well-defined current peaks are observed at 1.7 V (cathodic sweep) and 2.0 V (anodic sweep), corresponding to the biphasic transition between tetragonal anatase and orthorhombic lithium titanate. However, unlike the sharp insertion and extraction peaks observed in bulk anatase,[27, 28] these electrodes show broad feature, which is consistent with the pseudocapacitive effect arising from their small crystallites and high surface area (see supporting information and **Figure 9.10**). In addition, the cathodic curves are broader than the anodic ones, suggesting the insertion and extraction kinetics may be slightly different. Such effects were also observed

in mesoporous thin films.[29-31]

Figure 9.4B shows typical charge/discharge curves of CNT/NCs electrodes at 0.25C (1C = 170 mA g^{-1}) with a total capacity of ~ 200 mAh g^{-1}. A distinct voltage plateau can be first observed for the discharge plot, indicating coexisting of anatase and lithium titanate phases. A capacity of ~ 95 mAh g^{-1} can be estimated from this plateau region, which is controlled by the bulk diffusion and insertion process. The slope voltage region in the discharge plot accounts for a surface lithium storage process, which contributes a capacity of ~ 103 mAh g^{-1}. This region agrees well with the broad feature of the CV curves, and is similar to a typical capacitive discharge profile. For the charging process, a slope region followed by a voltage plateau at higher voltage was also observed, indicating a similar lithium extraction feature. Note the CNT scaffold only provides a capacity of ~15 mAh g^{-1} in this potential range. Such high capacity is among the highest ones achieved from a variety of TiO_2 electrodes.[4, 9, 14-16]

To investigate the rate-capability, electrodes were charged and discharged at different C-rates. **Figure 9.4C** shows the rate performance of the CNT/NCs electrodes in comparing with several high-rate TiO_2 electrodes from recent literature.[9, 14-16] As discussed above, traditional TiO_2-based high-rate electrodes often utilized a large fraction of binders and

conductive agents that do not contribute to the overall capacity. For example, an ultrathin TiO_2 nanosheet electrode (20 μm thick) could deliver a capacity (based on its TiO_2 loading) of 191- and 135- mAh g^{-1} at 2C and 20C, respectively.[9] Taking the total electrode mass (excluding the current collector) into consideration, its capacity deceases to 134 and 95 mAh g^{-1}, respectively. Similarly, the composites of TiO_2 with single-wall CNTs,[14] graphene[15] and RuO_2[16] exhibit enhanced rate-capability but also with reduced capacity for whole electrodes. By comparison, the CNT networks serve as both the conductive agent and the current collector in these electrodes, which respectively provides a capacity of 170- and 110- mAh g^{-1} at 2C and 20C based on the total weight of the materials, which is similar to the best nanostructured or hybrid TiO_2 electrodes reported so far. In addition, the area-normalized capacity reaches ~ 1 mAh cm^{-2}; further increasing the NC coating thickness to 40 nm will result in such capacity comparable to those of practical batteries (~2 mAh cm^{-2}). If the mass of current collectors were further considered, such 3D NC/CNT hybrid electrodes may show more significant advantage in terms of specific capacities than those of the traditional TiO_2 electrodes reported.

Besides their outstanding capacity and rate performance, these composited electrodes also exhibit impressive cycling stability. **Figure 9.4D** displays a long-term cycling performance

at different charge-discharge rates. In spite of the capacity drops in the initial cycles that are commonly observed,[32-34] the electrodes show stable capacity at 1C and 2C. The capacity faded gradually at high rates (e.g., capacity loss of 10 mAh g^{-1} for 200 cycles at 10C or 9 mAh g^{-1} for another 200 cycles at 20C), which might be caused by increased loss of active materials and irreversible reactions. Upon returning to 2C, a stable capacity of 150 mAh g^{-1} was resumed and negligible capacity loss was observed after another 100 more cycles. Overall, the electrode retained ~90% of the capacity over 700 cycles, which has never been achieved for electrodes made with nanostructured TiO_2, binder and conductive agent (usually less than 100 cycles).[4, 9, 14-16].

The durable performance of the electrodes is attributed to their robust structure, which can be probed using electrochemical impedance spectroscopy (EIS) study. Nyquist plots of the CNT/NCs electrodes at different cycling status are shown in **Figure 9.11**. It was found that the fresh electrode exhibits a relatively large single semicircle and an intercept at high frequency range, which is associated with a combination of ohmic and charge transfer resistance. The low-frequency Warburg tail presents a relatively low slope, implying a surface-wetting process is required for such thick electrodes (over 100 μm). The diameter of the semicircle decreases and the slope of the Warburg tail increases dramatically after 10

cycles at 1C, indicating a decreased charge-transfer resistance and improved lithium-diffusion rate (see insets). The impedance behavior shows similar features after 400 cycles, confirming the robust electrode structure. After cycling at high rate (20C) for 200 cycles followed by 100 cycles at 2C, slight increase of diffusion resistance can be detected from the Warburg region. Nevertheless, the total electrode resistance remains small due to the robust CNT network, which is consistent with its excellent long-term cycling stability.

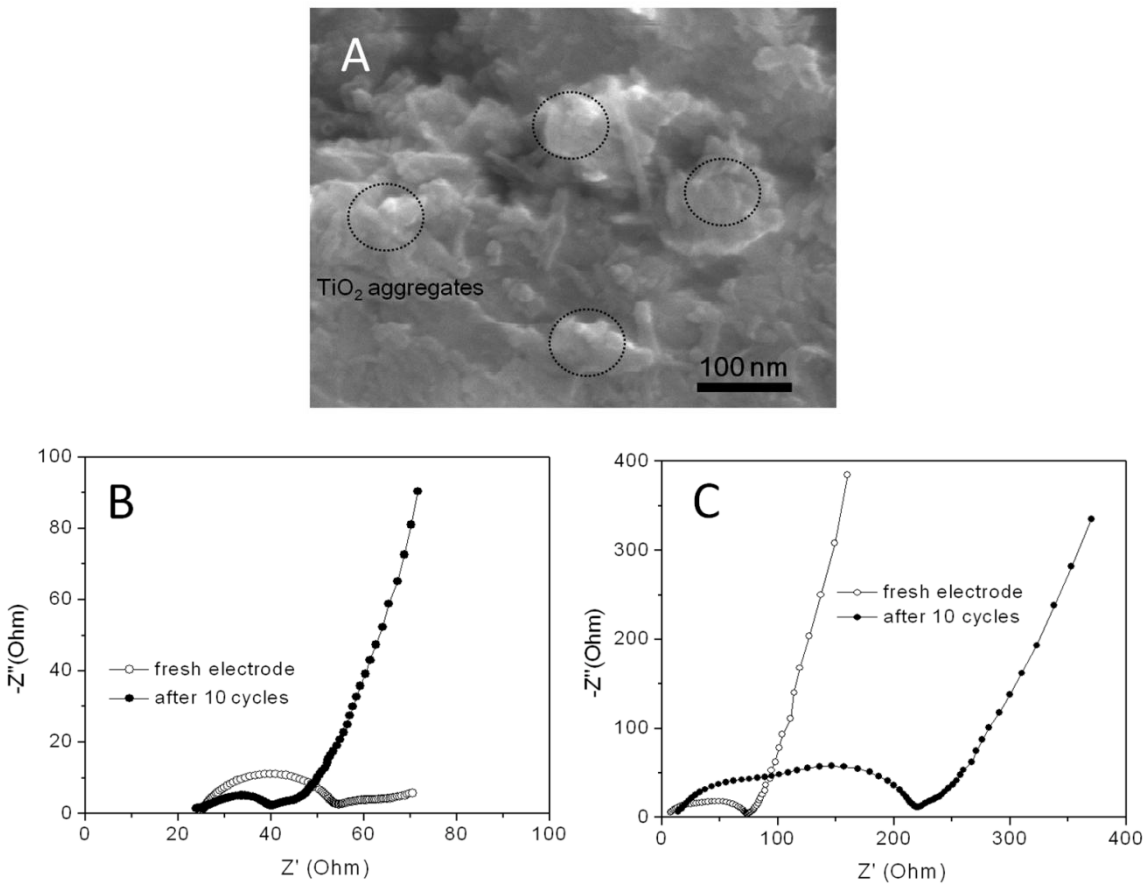

Figure 9.5 (A) Representative SEM image of the simply mixed CNT-TiO_2 composite. Nyquist plots of a 3D binder-free (B) and a binder-containing electrode (C) at fresh state and

after 10 cycles of galvanostaic charge/discharge at 2C-rate.

To further verify the role of the CNT/NCs intimate structure in the electrode performance, we also made electrodes using the traditional process in which binder was used. In this work, TiO_2 NC powders were mixed with CNTs at a mass ratio of 3:1; the mixture was sintered at the same condition as that used for the CNT/NCs hybrid electrode. The resulted powder was used to fabricate the electrodes with TiO_2, CNTs, carbon and binder at a mass ratio of 3:1:1:1, which provided comparable TiO_2 content with the 3D CNT/NCs electrodes. **Figure 9.5A** shows a representative SEM image of this electrode. Significantly different from the conformal CNT/NCs electrodes, such electrodes display appreciable NCs aggregation without a clear CNTs conductive scaffold. Consistently, such electrodes show much larger impedance (~ 80 Ω) than those of the conformal electrodes (55 Ω) in the first cycle **(Figure 9.5B**). After 10 cycles of galvanostaic charge/discharge, the total resistance of the binder-containing electrode increases to 220 Ω **(Figure 9.5C**), while the electrode with the conformal coating only exhibit an resistance of ~ 40 Ω, which is ~5 time less than that the binder-containing electrode. This experiment fully proves that the conformal coating of the NCs onto the preformed CNTs scaffold indeed provide the electrodes with cycling stability.

Consistently, such binder-containing electrode exhibits a low capacity of 73- and 13- mAh g^{-1} at 0.2C and 5C, respectively (**Figure 9.4**C), which are significantly lower than that of the conformal CNT/NCs electrode (200- and 162- mAh g^{-1}). These results strongly highlight the importance of building a 3D continuous conductive architecture for high-performance electrodes.

In addition, it is important to point out that the CNT/NCs electrodes are highly flexible (Figure 9.2A), which is of interest for rollup displays, smart electronics, wearable devices and other applications.[35] Recently, several flexible anodes have been reported, such as the composites of CNTs or graphene with active anode materials,[36-38] and the composites of graphite with fibrillated cellulose.[39] However, rate-capability of these flexible anodes are rather low. Our electrode design combines both high-rate and flexibility, holding great promise for flexible device application.

3. Conclusions

In summary, using TiO_2 NCs and ultra-long CNTs, we have demonstrated an effective conformal coating strategy to fabricate flexible lithium electrodes with high capacity, high rate, and cycling stability. The high performance arises from their small building NCs,

effective pathways for charge and ion transport, and robust scaffold structure. Considering the vast library of NCs that have been synthesized (eg. Fe_2O_3 NCs, Figure 9.12), such a strategy may be extended to fabricate various high-performance architectures for energy storage, catalysis, sensing, photo-synthesis and other applications.

4. Experimental Section

4.1 Synthesis of TiO_2 NCs

The TiO_2 NCs were synthesized using a two-phase hydrothermal reaction. In a typical synthesis, 0.4 mL of *tert*-butylamine was dissolved in 40 mL of water and the solution was transferred into a 100 mL Teflon-line stainless-steel autoclave. Subsequently, 0.6 g of titanium (IV) n-propoxide (2 mmol) and 4.0 mL of oleic acid were dissolved in 40 mL of toluene in air and the solution was transferred into the autoclave without any stirring. The autoclave was sealed and maintained at 180 ^oC for 8 h and cooled down to room temperature with tap water. The crude solution of TiO_2 NCs was precipitated with methanol and further isolated by centrifugation and decantation. The purified TiO_2 NCs were re-dispersed in toluene to form a NCs solution with desired concentration.

4.2 Fabrication of binder-free CNT/TiO_2 electrodes

To fabricate the binder-free CNT/TiO_2 NC hybrid electrodes, as-grown super-long CNTs (diameters of ~ 30-80 nm and length of ~5 mm, Figure 9.13) were dispersed in N-methylpyrrolidinone (NMP) and filtrated to make CNT papers that were cut into discs. ~50 μL of 5 wt- % NCs solution was dropped onto a CNT disc while the solvent evaporates rapidly in air. The coating process was repeated to tune the TiO_2 loading. The discs were then sintered at 450 ^{o}C for 1 h in air at a ramp rate of 2 ^{o}C min^{-1}, resulting in flexible electrodes. The loading of TiO_2 was further determined by comparing the mass difference between the original CNT sheet and the composites and confirmed by TGA. Electrodes with different NCs loadings were fabricated and tested (Figure 9.14); yet the 130 wt% NC/CNT was mainly used for all the characterization and measurement.

4.3 Fabrication of binder-containing electrodes

As synthesized TiO_2 NCs were dispered and isolated for three times and dried under vacumm to get NC powders. Then TiO_2 NCs and CNTs (3:1 w/w ratio) were milled to fully disperse CNTs with NCs. Such TiO_2 NCs/CNTs mixture, carbon black and poly(vinylidene fluoride) (PVDF) binder were mixed in a mass ratio of 4:1:1 and homogenized in NMP to

form slurries. The homogenous slurries were coated on Cu foil substrates and dried at 100 ^{o}C for 30 min under vacuum. As formed electrodes were then pressed at a pressure of 2 MPa and further dried under vacuum at 100 ^{o}C for another 12 h. The mass loading was controlled to be ~4 mg cm^{-2} on each current collector. Such electrodes present comparable loading and TiO_2 content with above binder-free CNT/TiO_2 NC electrodes.

4.4 Synthesis of Fe_2O_3 NCs

The synthesis of Fe_2O_3 was similar to ref.[40].

4.5 Material and Electrode Characterization

The x-ray diffraction measurements were taken on Panalytical X'Pert Pro x-ray powder diffractometer using the copper Kα radiation (λ=1.54 Å). Nitrogen sorption isotherms were measured at 77 K with a Micromeritics ASAP 2020 analyzer. The samples were degassed in vacuum at 200 ^{o}C for three hours. The specific surface areas (S_{BET}) were calculated by the Brunauer-Emmett-Teller (BET) method using adsorption branch in a relative pressure range from 0.04 to 0.25. The pore size distributions were derived from the adsorption branches of isotherms using the Barrett-Joyner-Halenda (BJH) model. Scanning electron microscopy (SEM) experiments were conducted on a JEOL JSM-6700 FE-SEM. Transmission electron

microscopy (TEM) experiments were conducted on a Philips CM120 operated at 120 kV.

To test electrodes, 2032-type coin cells were assembled in the glovebox, using glass fiber (GF/D) from Whatman as the separator. Lithium discs were used as both the counter and the reference electrodes and 1 M $LiPF_6$ in a 1:1 (w/w) mixture of ethylene carbonate and diethyl carbonate was used as the electrolyte. The CV measurements were performed on a Bio-Logic VMP3 electrochemical workstation at a scan rate of 0.2 mV s^{-1} in a voltage range between 2.6 and 1.0 V (vs. Li/Li^+). Galvanostatic charge-discharge measurements were carried out by a LAND CT2000 battery tester at different current rates. EIS tests were carried out on a Solartron 1860/1287 Electrochemical Interface.

5. Supporting Materials

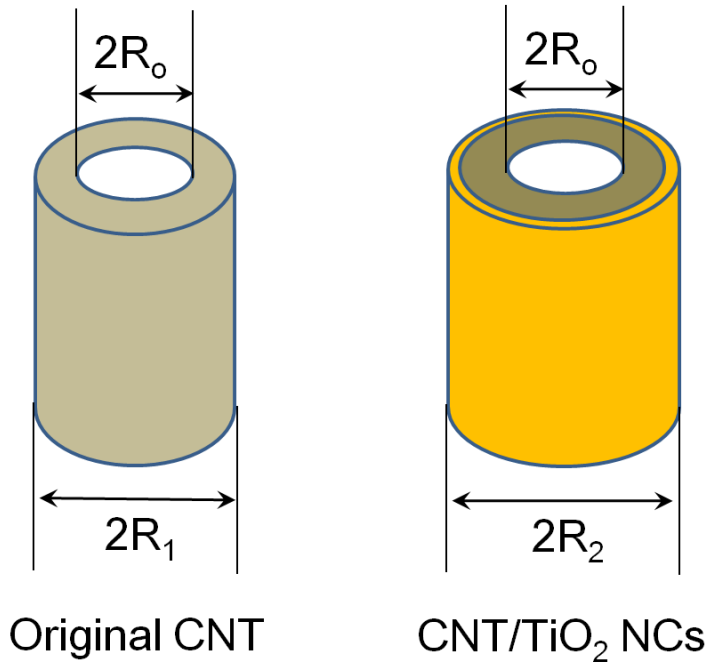

Figure 9.6A A Schemetic of CNT structure before (left) and after (right) NC coating ($2R_o$ and $2R_1$: inner and outside diameter of CNT; $2R_2$: outside diameter of CNT/NCs hybrid.)

From SEM and TEM, we can use R_o= 30 nm and R_1=60 nm for the super-long CNT. The density of wall of CNT is 2.1 g cm^{-3} and bulk density of anatase TiO_2 is 4.2 g cm^{-3}. The nitrogen adsorption test shows that the TiO_2 NCs have a mesoporous structure with a pore volume of 0.236 cm^3 g^{-1}. Therefore, a porosity of 50 % should be considered to caculate the effective mass of NC coating layer. If assuming a leght of L for a CNT, the mass of CNT and TiO_2 NC layer can be respectively expressed by:

$$M_{CNT}=2.1*2\pi L(R_1^2-R_o^2)=4.2\pi L(R_1^2-R_o^2)$$

$$M_{NC}=0.5*\ 4.2\ *\ 2\pi L*(R_2^2-R_1^2) = 4.2\pi L(R_2^2-R_1^2)$$

therefore, the loading ratio of the TiO_2 NCs to CNT can be expressed by:

$M_{NC}/M_{CNT}=[4.2\pi L(R_2^2-R_1^2)]/[4.2\pi L(R_1^2-R_o^2)]=(R_1^2-R_2^2)/(R_1^2-R_o^2)$. Using different coating thicknesses, we can get various loading ratios as shown in **Figure S1B** below.

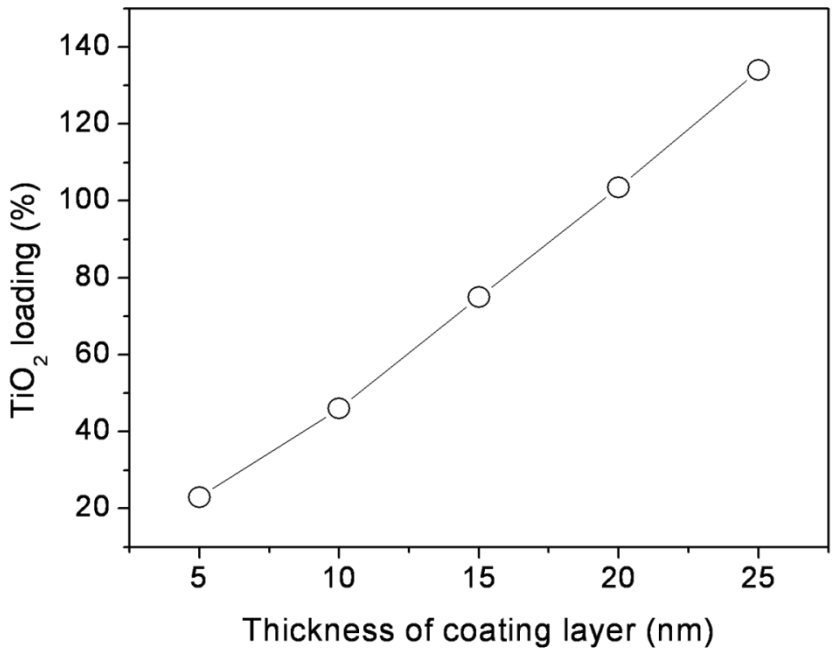

Figure 9.6B Dependence of TiO_2 NCs loading on the coating layer thickness.

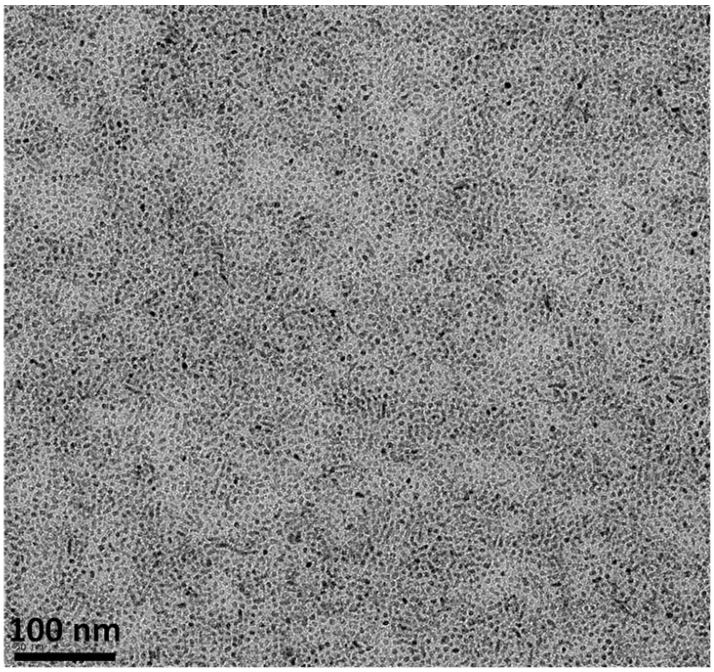

Figure 9.7 Low magnification TEM of monodisperse TiO_2 NCs.

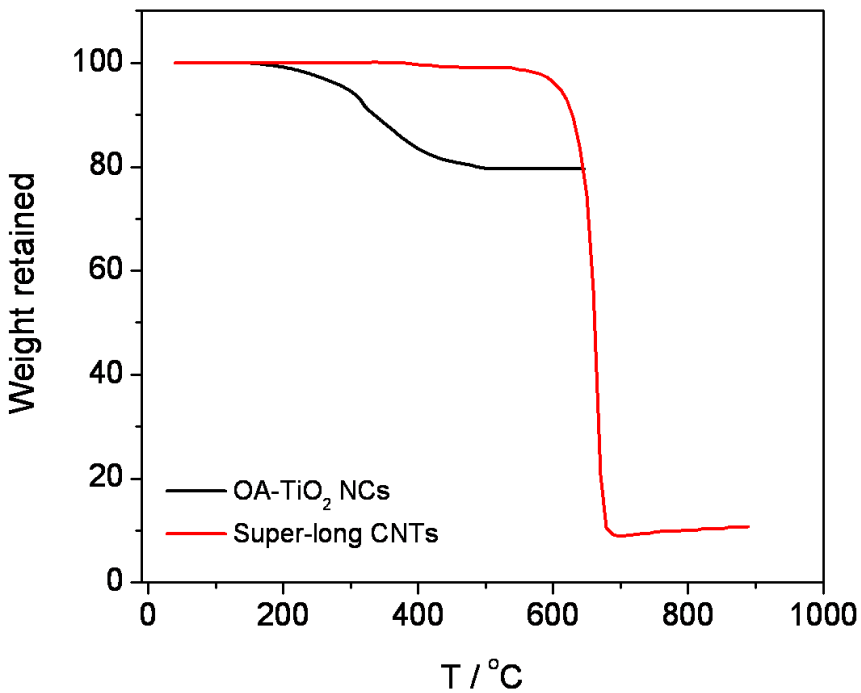

Figure 9.8 TGA plots of OA-capped TiO_2 NCs and Super-long CNTs.

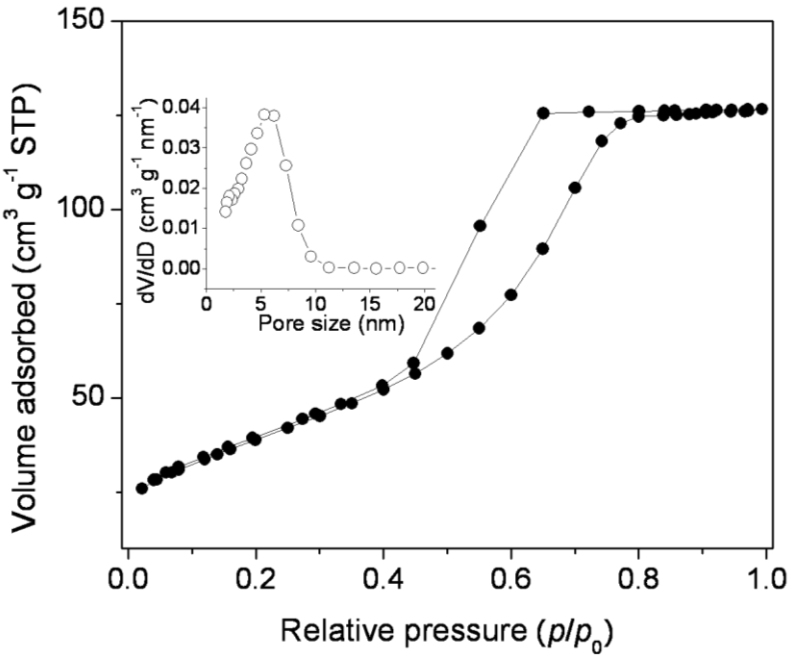

Figure 9.9 Nitrogen adsorption isotherms and pore size distribution (inset) of TiO_2 NCs after sintering.

To study the pseudocapacitive property (from surface/interface effect) of ultrafine TiO_2 NCs, we tested CV behavior of pure NCs based thin film electrodes. We separated the pseudocapacitive and bulk- diffusion contributions from the total charge storage based on the Trasatti method.[41] In this approach, the total voltammetric charge (q_T) was separated into surface-capacitive charge (q_s) and bulk-diffusion controlled charge (q_d) by:

$$q_T = q_s + q_d \quad (1)$$

where q_s is correlated with double-layer capacitance and pseudocapacitance, which are

associated with surface lithium adsorption accompanied by a charge transfer process; while q_d mainly depends on slow diffusion process followed by lithium intercalation within the bulk crystal. Due to faster kinetics associated with surface lithium adsorption, electrodes presenting a large fraction of q_s in the total capacity will exhibit a high rate-capability. In this context, reducing the particle size will enhance the surface contribution and improve electrode rate-capability.

Based on the semi-infinite linear diffusion law, within a reasonable range of sweep rates, q_s can be derived by plotting the q_T against the reciprocal of the square root of the potential sweep rate (v) and extrapolating v to ∞, according to the following equation:

$$q_T = q_s + cv^{-1/2} \quad (2)$$

A separation of surface and diffusion controlled charge contribution to total capacity is displayed in Figure S5. It is clearly shown that the pseudocapacitive (surface charge) indeed plays an important part at various sweep rates for the NC electrodes. For example, the electrodes show pseudocapacitive contribution of 60 % at 1 mV s^{-1} and 94 % at 20 mV s^{-1}.

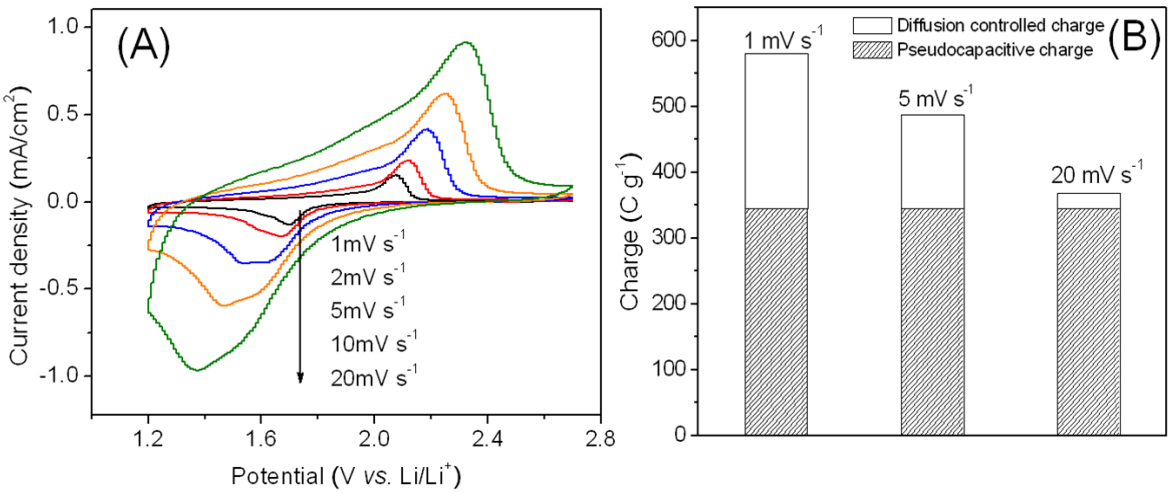

Figure 9.10 (A) Cyclic voltammograms of thin-film electrodes based on TiO_2 nanocrystals. (B) Separation of pseudocapacitive charge and diffusion-controlled charge of TiO_2 electrodes at different sweep rates.

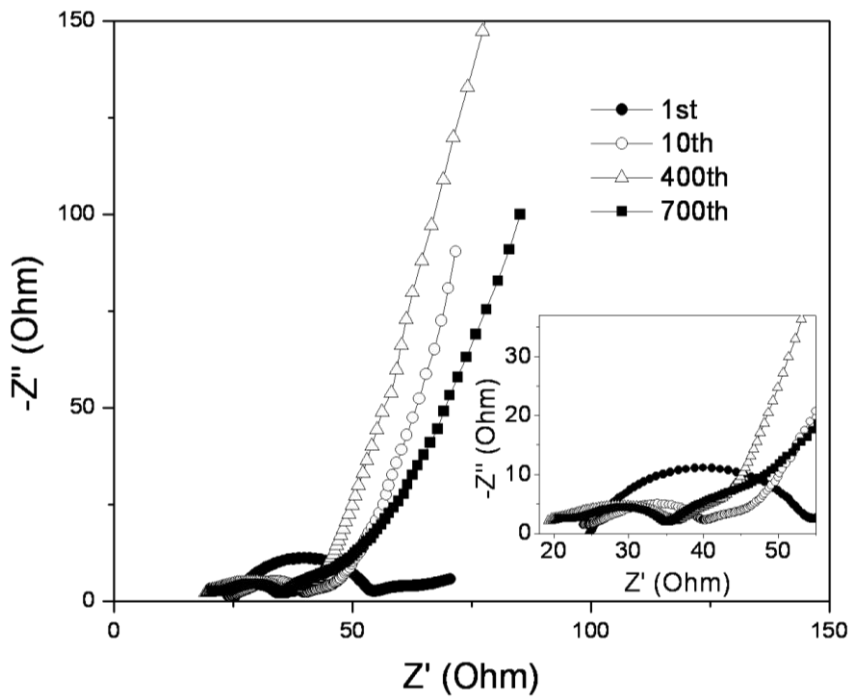

Figure 9.11 Nyquist plots of the binder-free CNT/ TiO_2 NCs hybrid electrode at different cycling status.

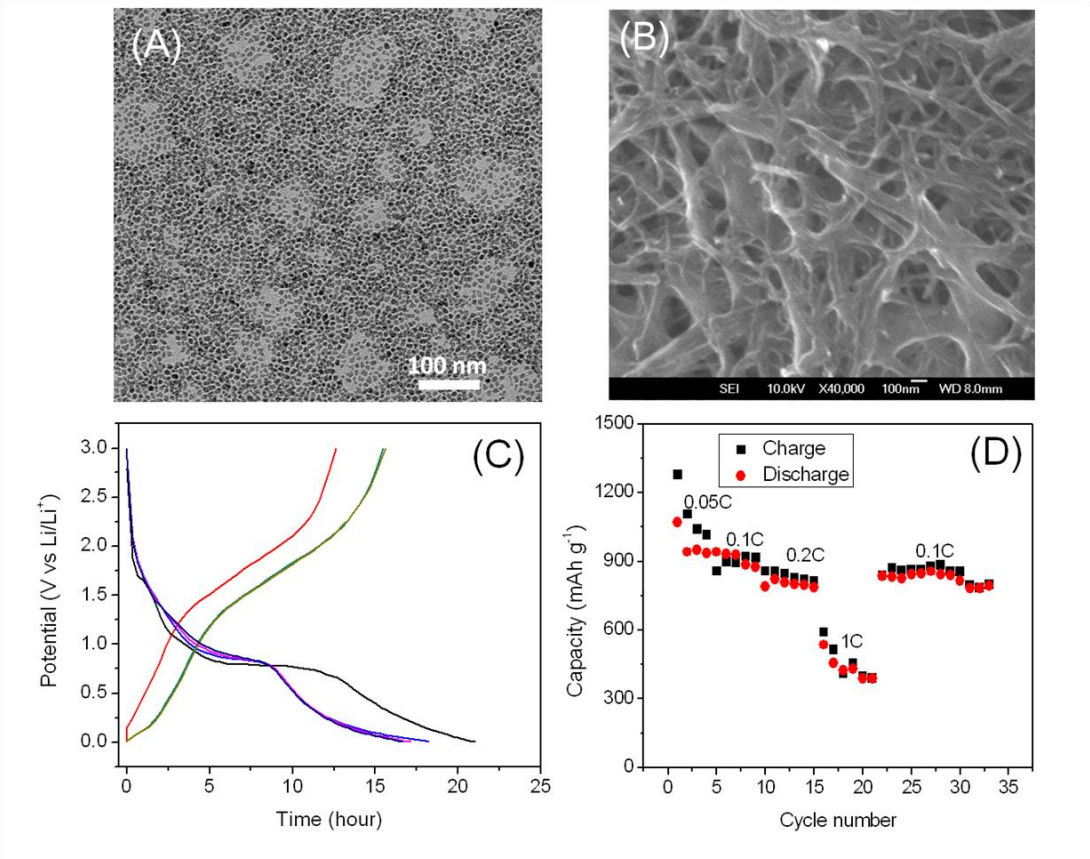

Figure 9.12 (A) TEM image of hydrophobic monodispersed Fe_2O_3 NCs with diameter of 6-7 nm. (B) SEM image of Fe_2O_3 NC/CNT composite electrode (the Fe_2O_3 NC loading was ~100 % vs. the mass of the CNT scaffold) made from the same method of fabricating TiO_2 NC/CNT electrode. (C) First four cycles of charge/discharge curves of the Fe_2O_3 NC/CNT electrode at a rate of ~0.05C. (D) Cycling performance of the Fe_2O_3 NC/CNT electrode at different rates.

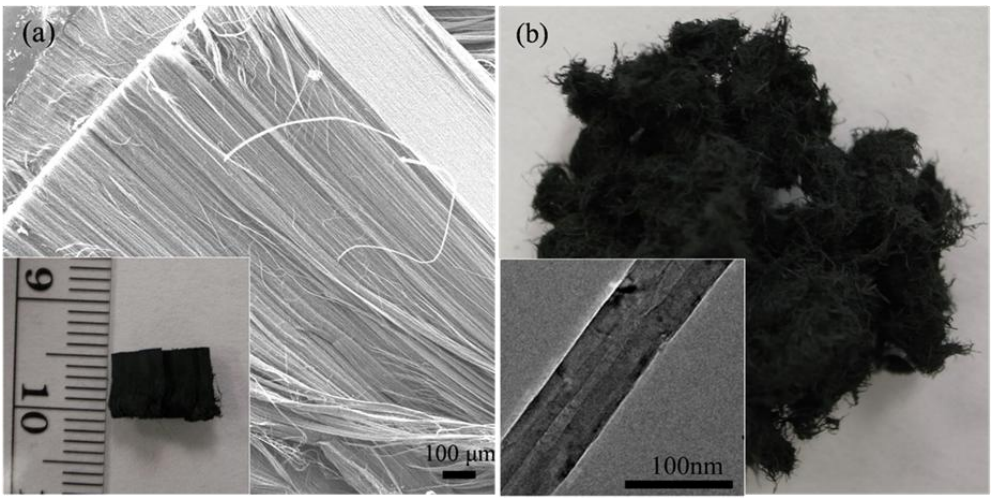

Figure 9.13 (a) SEM image and digital photograph (inset) of pristine ultra-long CNT arrays. (b) Digital photograph of dispersed ultra-long CNT; inset shows a TEM image of a single CNT.

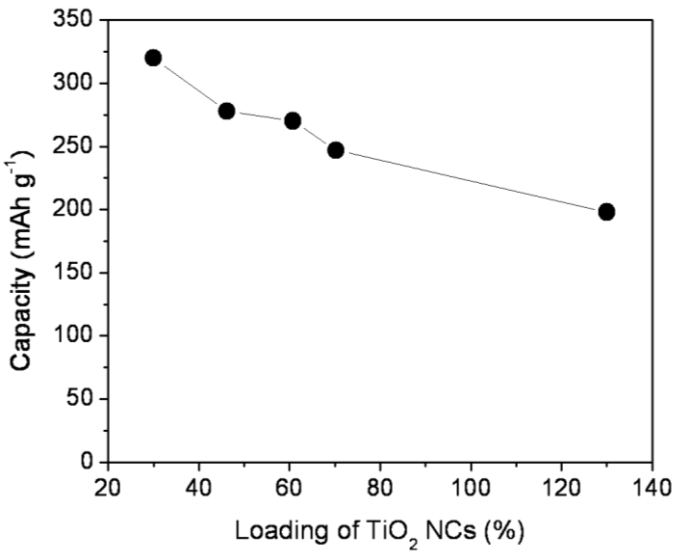

Figure 9.14 The dependence of specific capacity on the loading of TiO_2 NCs (wt-% vs. the mass of the CNT scaffold).

References

[1] P. Bruce, B. Scrosati, J. M. Tarascon, *Angew. Chem. Int. Ed.* **2008**, *47*, 2930.

[2] Y.-G. Guo, J.-S. Hu, L.-J. Wan., *Adv. Mater.* **2008**, *20*, 2878.

[3] B. Kang, G. Ceder, *Nature* **2009**, *458*, 190.

[4] C. Jiang, M. Wei, Z. Qi, T. Kudo, I. Honma, H. Zhou, *J. Power Sources* **2007**, *166*, 239.

[5] K. Naoi, S. Ishimoto, Y. Isobe, S. Aoyagi, *J. Power Sources*, **2010**, *195*, 6250.

[6] M.-S. Park, G.-X. Wang, Y.-M. Kang, D. Wexler, S.-X. Dou, H.-K. Liu, *Angew. Chem. Int. Ed.* **2007**, *46*, 750.

[7] Z. Chen, V. Augustyn, J. Wen, Y. Zhang, M. Shen, B. Dunn, Y. Lu, *Adv. Mater.* **2011** *23*, 791.

[8] A. R. Armstrong, G. Armstrong, J. Canales, P. G. Bruce, *Angew. Chem. Int. Ed.* **2004**, *43*, 2286.

[9] J. Liu, J. S. Chen, X. Wei, X. W. Lou, X.-W. Liu, *Adv. Mater.* **2011**, *23*, 998.

[10] J. S. Chen, Y. L. Tan, C. M. Li, Y. L. Cheah, D. Luan, S. Madhavi, F. Y. C. Boey, L. A. Archer, X. W. Lou, *J. Am. Chem. Soc.* **2010** *132*, 6124.

[11] P. L. Taberna, S. Mitra, P. Poizot, P. Simon, J. M. Tarascon, *Nat. Mater.* **2006**, *5*, 567.

[12] H. Zhang, X. Yu, P. V. Braun, *Nat. Nano.* **2011**, 6, 277.

[13] X. Lang, A. Hirata, T. Fujita, M. Chen, *Nat. Nano.* **2011**, 6, 232.

[14] I. Moriguchi, R. Hidaka, H. Yamada, T. Kudo, H. Murakami, N. Nakashima, *Adv. Mater.* **2006**, *18*, 69.

[15] Y.-G. Guo, Y.-S. Hu, W. Sigle, J. Maier, *Adv. Mater.* **2007**, *19*, 2087.

[16] D. Wang, D. Choi, J. Li, Z. Yang, Z. Nie, R. Kou, D. Hu, C. Wang, L. V. Saraf, J. Zhang, I. A. Aksay, J. Liu, *ACS Nano* **2009**, *3*, 907.

[17] Z. Hui, N. Du, P. Wu, B. Chen, D. Yang, *Nanotechnology* **2008**, *19*, 315604.

[18] J. Park, J. Joo, S. G. Kwon, Y. Jang, T. Hyeon, *Angew. Chem. Int. Ed.* **2007**, *46*, 4630.

[19] J. H. Park, J. M. Ko, O. O. Park, *J. Electrochem. Soc.* **2003**, *150*, A864.

[20] J. Li, S. Tang, L. Lu, H. C. Zeng, *J. Am. Chem. Soc.* **2007**, *129*, 9401.

[21] C. Ban, Z. Wu, D. T. Gillaspie., L. Chen, Y. Yan, J. L. Blackburn, A. C. Dillon, *Adv. Mater.* **2010**, *22*, E145.

[22] C. Ban, Z. Li, Z. Wu, M. J. Kirkham, L. Chen, Y. S. Jung, E. A. Payzant, Y. Yan, M. S. Whittingham, A. C. Dillon, *Adv. Energy Mater.* **2011**, *1*, 58.

[23] I. H. Kim, J. H. Kim, B. W. Cho, Y. H. Lee, K. B. Kim, *J. Electrochem. Soc.* **2006**, *153*, A989.

[24] M. Sathiya, A. S. Prakash, K. Pamesha, J-M. Tarascon, A. K. Shukla, *J. Am. Chem. Soc.*

2011, *133*, 16291.

[25] S. W. Oh, S.-T. Myung, S.-M. Oh, K. H. Oh, K. Amine, B. Scrosati, Y.-K. Sun, *Adv. Mater*, **2010**, *22*, 4842.

[26] M. Wagemaker, W. J. H. Borghols, F. M. Mulder, *J. Am. Chem. Soc.* **2007**, *129*, 4323.

[27] H. Lindström, S. Södergren, A. Solbrand, H. Rensmo, J. Hjelm, A. Hagfeldt, S.-E. Lindquist, *J. Phys. Chem. B* **1997**, *101*, 7717.

[28] M. Mancini, P. Kubiak, J. Geserick, R. Marassi, N. Hüsing, M. Wohlfahrt-Mehrens, *J. Power Sources* **2009**, *189*, 585.

[29] J. Wang, J. Polleux, J. Lim, B. Dunn, *J. Phys. Chem. C* **2007**, *111*, 14925.

[30] T. Brezesinski, J. Wang, J. Polleux, B. Dunn, S. H. Tolbert, *J. Am. Chem. Soc.* **2009**, *131*, 8.

[31] T. Brezesinski, J. Wang, S. H. Tolbert, B. Dunn, *Nat. Mater.* **2010**, *9*, 146.

[32] W. J. H. Borghols, D. Lützenkirchen-Hecht, U. Haake, W. Chan, U. Lafont, E. M. Kelder, E. R. H. van Eck, A. P. M. Kentgens, F. M. Mulder, M. Wagemaker, *J. Electrochem. Soc.*, **2010**, *157*, A582.

[33] Y. Chang, H. Li, L. Wu, T. Lu, *J. Power Sources* **1997**, *68*, 187.

[34] G. Ning, B. Haran, B. N. Popov, *J.Power Sources* **2003**, *117*, 160.

[35] V. L. Pushparaj, M. M. Shaijumon, A. Kumar, S. Murugesan, L. Ci, R. Vajtai, R. J. Linhardt, O. Nalamasu, P. M. Ajayan, *P. Natl Acad. Sci.USA* **2007**, *104*, 13574.

[36] S. Y. Chew, S. H. Ng, J. Wang, P. Novák, F. Krumeich, S. L. Chou, J. Chen, H. K. Liu, *Carbon* **2009**, *47*, 2976.

[37] L. Hu, H. Wu, F. L. Mantia, Y. Yang, Y. Cui, *ACS Nano*, **2010**, *4*, 5843.

[38] H. Gwon, H.-S. Kim, K. U. Lee, D.-H. Seo, Y. C. Park, Y.-S. Lee, B. T. Ahn, K. Kang, *Energy Environ. Sci*. **2011**, *4*, 1277.

[39] L. Jabbour, C. Gerbaldi, D. Chaussy, E. Zeno, S. Bodoardo, D. Beneventi, *J. Mater. Chem.* **2010**, *20*, 7344.

[40] N. Zhao, W. Nie, J. Mao, M. Yang, D. Wang, Y. Lin, Y. Fan, Z. Zhao, H. Wei and X. Ji, *Small*, **2010**, 6, 2558.

[41] S. Ardizzone, G. Fregonara and S. Trasatti, *Electrochim. Acta*, **1990**, 35, 263.

Chapter 10: Carbon-Nanotube-Threaded Nanocrystal Architecture for Lithium-ion Pseudocapacitors

1. Introduction

Supercapacitors hold great promise for energy storage owing to their high power density and long cycling life; however, broader application of supercapacitor has been hampered by low energy density.[1-3] To address this challenge, extensive effort has been devoted to developing better electrode materials with controlled architecture, such as high-surface-area carbons and low-dimension redox-active metal oxides.[3-6] However, despite much progress made, capacitances of the current-state-of-art carbons are still less than 150 F g^{-1} in an organic electrolyte [7-8] or 300 F g^{-1} in aqueous electrolytes,[9] which can only provide moderate energy density (~10 Wh kg^{-1}). Transition-metal oxides, on the other hand, possess significantly higher capacitance (up to 1000 F g^{-1});[10-12] however, it is difficult to harvest such high capacitance due to their slow ion diffusion and poor electronic conductivity.

To circumvent this limitation, the most effective strategy is to form the nanocomposites of conductive agents (e.g., carbon black,[13, 14] carbon nanotubes (CNTs) [15,16] and graphene[17]) and the low-dimension oxide materials, such that the low-dimension structure

shortens ion-diffusion length while the conductive agents construct electron conductive pathways. Synthesizing such nanocomposites with effective structure and interface control is therefore essential to ensure effective electron and ion transports.

Towards this aim, nanocomposites with various structures have been explored, such as the cable-like structure formed by coating CNTs with active oxide layers, the interpenetrative network structure constructed by intertwining growth of nanowires within CNTs networks, and the sandwich structure made by alternative stacking of oxide particles and graphene layers. The cable-like structure facilitates effective charge transport locally; the oxide layers, however, increase the CNT contact resistance resulting in mediocre rate performance. For example, electrodes prepared by coating CNTs with TiO_2 exhibit improved rate performance in comparison with those made by physical mixing of TiO_2 and CNTs; their charge/discharging time, however, is still more than 10 mins.[18] The interpenetrative network structure, on the other hand, provides better network conductivity; the loose CNTs-nanowire interface, however, reduce the electrode stability. Accordingly, electrodes based on interpenetrative V_2O_5 nanowires and CNTs exhibit excellent rate performance but lose more than 10% of their capacity in the first 20 cycles.[19] Compared with the former structure, the sandwich structure enables intimate contact between the graphene and the

active materials; their two-dimensional structure, however, intrinsically limits three-dimensional mass and charge transport. Consistently, sandwich-structure electrodes made from graphene and Fe_3O_4 show good cycling performance but still with mediocre rate performance.[17]

Herein, we report a novel three-dimensional (3D) architecture for high-performance pseudocapacitive electrodes by solvation-induced assembly. Note that hydrophobic nanocrystals (NCs) of oxides can be homogenously dispersed within non-polar solvent in the presence of CNTs. We hypothesize that, upon addition of polar solvent, solvation force will induce the NCs to assemble around the CNTs, which results in the formation of nanocrystal spheres threading through by the CNTs. Subsequent calcination will remove the capped ligands on the NCs and convert the composite spheres into robust CNT-threaded mesoporous particles.

Unlike the aforementioned structures, this architecture not only enables intimate contact locally between the oxide and the CNTs scaffold, but also provides excellent electrode conductivity through the CNTs networks formed in the process. In the aspect of ion transport, the mesoporous structure provides effective channels for electrolyte transport, while the nanocrystal structure retains the shortened ion-diffusion length. In the aspect of

electrode stability, the porous network structure also helps to buffer the stress during charge and discharge. More importantly, such compact spherical structure offers mechanical robustness and minimizes the electrode-electrolyte interface, which will render the electrodes with better stability. Note that the past two decades have witnessed incredible development in the synthesis of nanocrystals, which make this strategy a versatile approach towards high-performance pseudocapacitive storage.

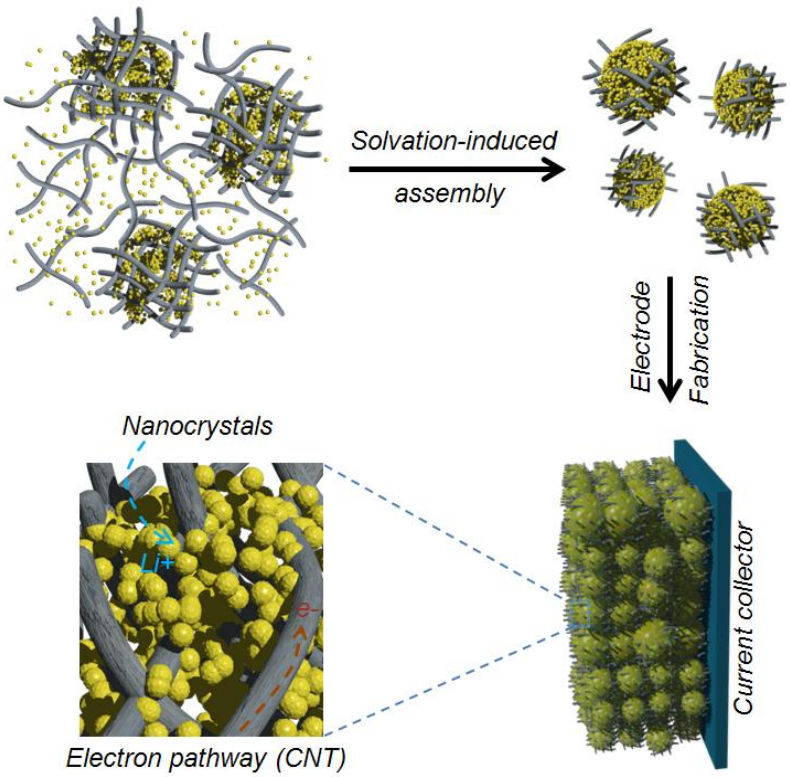

Figure 10.1 Schematic of forming 3D spherical NC/CNT nanocomposite and electrode.

Figure 10.1 illustrates the synthesis of such composite architecture using anatase TiO_2

nanocrystals (NCs) and massively produced cluster-like CNTs as an example. Monodispersed TiO_2 NCs were synthesized using oleic acid (OA) as the capping ligand, which allows their uniform dispersion in toluene. TiO_2 has been long considered as a promising energy storage material owning to its impressive lithium-storage capacity, low cost and superior safety;[20] however, despite the great efforts made, current TiO_2-based electrodes still exhibit moderate rate performance and cycling stability. It is also important to point out that the CNTs used herein were massively produced with low cost; moreover, such CNTs contain intertwined network structures, allowing efficiently encaging the NCs. The nanocomposites were prepared by simply adding methanol into the mixture of CNTs and NCs in toluene, which generates the spherical composites of NCs and CNTs precipitated out from the mixture. Subsequent annealing process creates a class of mesoporous TiO_2/CNTs spherical composites for high-performance pseudocapacitive electrode.

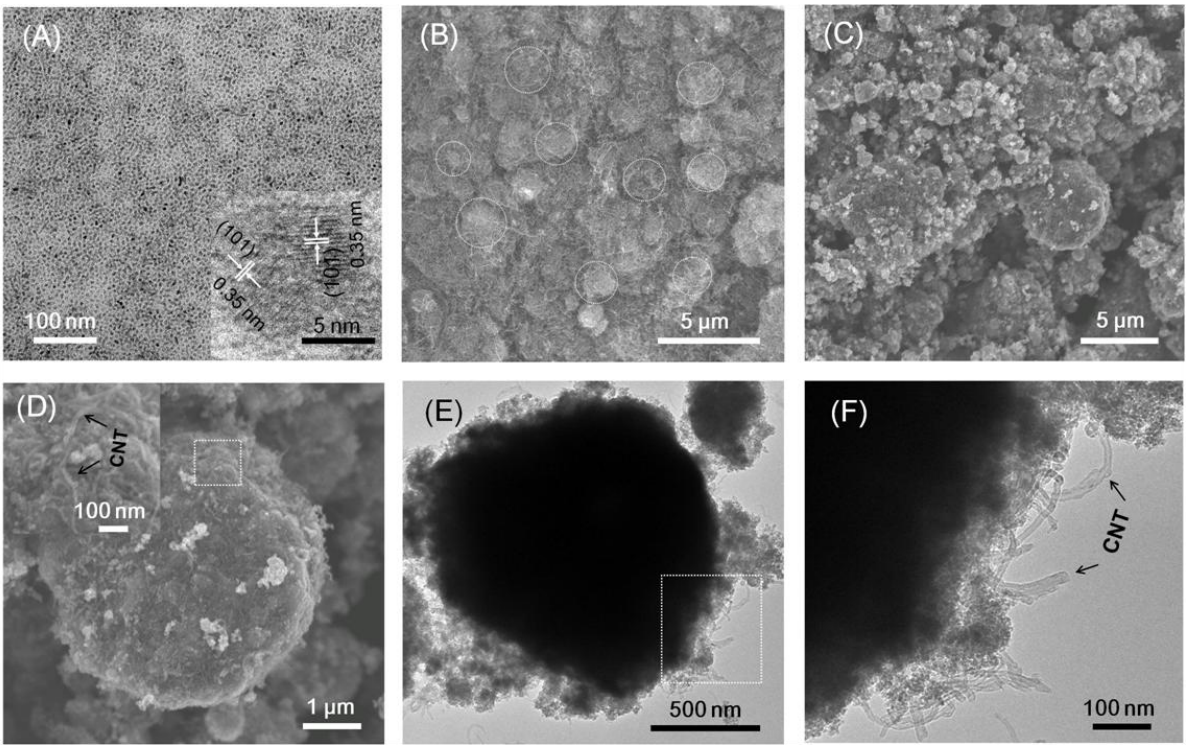

Figure 10.2 (A) Representative TEM image of TiO_2 NCs (inset, HRTEM of two TiO_2 NCs showing 101 (0.35 nm) lattice). (B) SEM image of CNT used in the experimental. Some examples of cluster structures are shown in the circled areas. (C) and (D) SEM images of TiO_2 NC/CNT composites presenting sphere-like shape. Inset of D shows high-resolution SEM image of selected area of a typical composite sphere. (E) TEM image of a typical NC/CNT sphere. (F) HRTEM image of selected area of the sphere in (F). The linked NCs and CNT network can be clearly distinguished from the image.

Figure 10.2A shows a representative transmission electron microscopic (TEM) image of the NCs, which possess a narrow size distribution with an average diameter of ~5 nm (**Figure 10.6A**). The NCs are highly crystallized as revealed in the high-resolution TEM image (HRTEM, inset in **Figure 10.2A**). In addition, since these NCs are capped with OA ligand, they can be stable in solvent (toluene) for a few months without appreciable precipitation (**Figure 10.6B**). **Figure 10.2B** presents a scanning electron microscopic (SEM) image of the CNTs used for building 3D spherical NC/CNT architectures. The CNTs, with diameter of 20-30 nm and length of 5-10 μm, intrinsically show intertwined network structures. **Figure 10.2C** shows a SEM image of the as-prepared NC/CNT composites, presenting a spherical morphology with size ranging from a few hundred nm to a few μm. A representative spherical composite particle is presented in **Figure 10.2D**, in which an inset high-magnification SEM clearly shows the CNTs threading through the NC networks. **Figure 10.2E** and 1F show TEM images of a typical composite particle with mesoporous NCs penetrated through by CNTs, further confirming the formation of CNT-threaded nanocrystal particles.

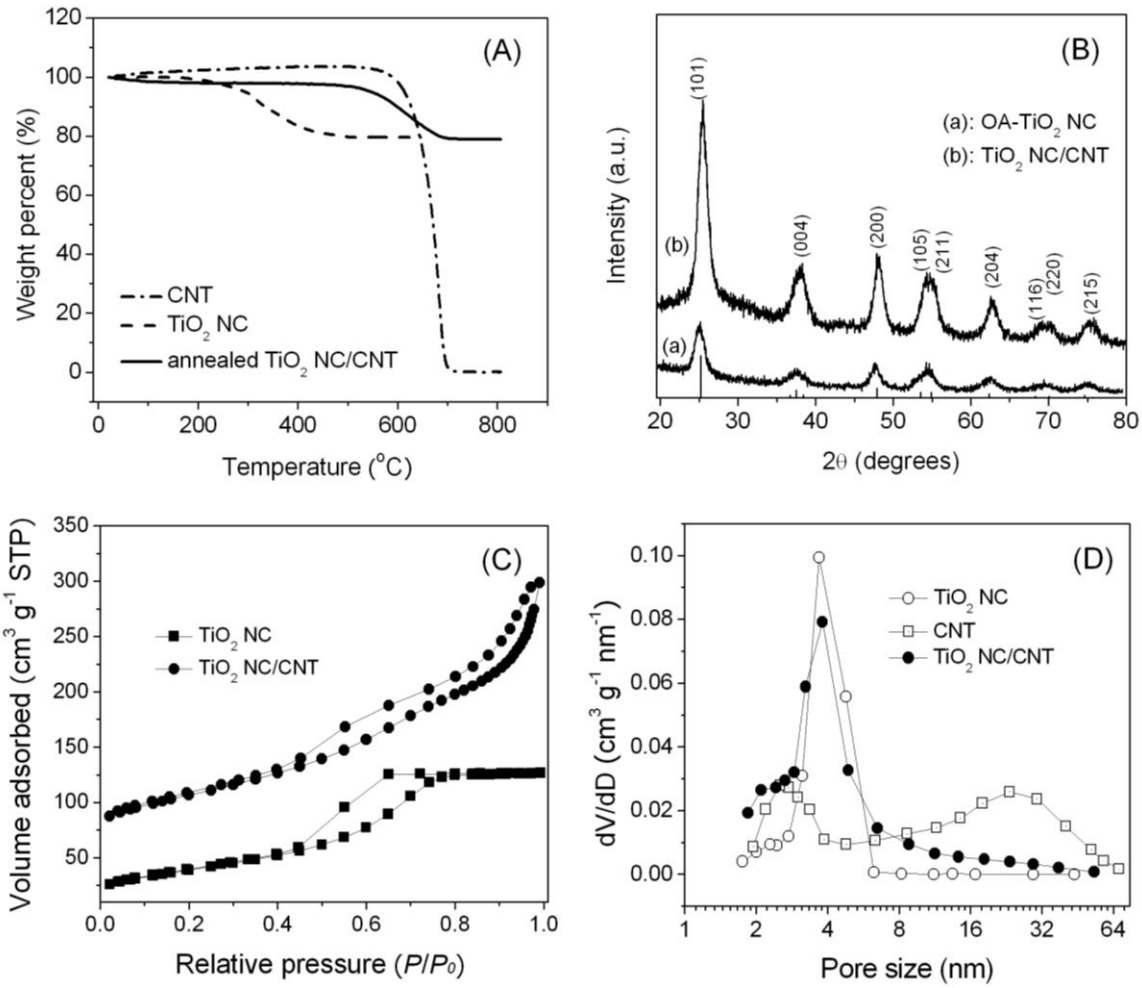

Figure 10.3 (A) TGA curves of CNTs, as-synthesized OA-capped TiO_2 NCs and annealed TiO_2 NC/CNT. (B) XRD patterns and of as-synthesized TiO_2 NCs and NC/CNT composites. (C) Nitrogen adsorption isotherms of TiO_2 NCs and NC/CNT composite after annealing. (D) Pore-size distribution of CNTs, annealed TiO_2 NCs and annealed NC/CNT.

Figure 10.3A shows thermogravimetric analysis (TGA) curves of TiO_2 NCs, CNTs, and the NC/CNT composite. No appreciable weight loss can be observed for the CNTs at

temperature below 600 ^{o}C, indicating a superior thermal stability of these CNTs. The weight loss of NCs is ~20%. Accordingly, the sintered NC/CNT composite consists of ~80 wt-% of TiO_2 and 20 wt-% of CNT. The mass ratio of TiO_2 and CNT in the composite can be easily tuned, while we mainly focused on the composite with 20 wt-% of CNT in this work. **Figure 10.3B** shows x-ray diffraction (XRD) patterns of as-synthesized TiO_2 NCs and the NC/CNT composite after removal of capping agents. The diffraction pattern of as-synthesized NCs matches well to that of anatase TiO_2 (JCPDS card No. 21-1272). The peak broadening originates from their small crystallite size, which is calculated to be 5.3 nm from the Scherrer equation and consistent with the TEM observation. Sintering the NC/CNT composites in air successfully removed the capping agent (**Figure 10.3A**) and led to unnoticeable growth of grain size; TiO_2 NCs retained the anatase phase with an average size of ~5.5 nm.

The pore structure of the composite was further probed using nitrogen sorption technique. The CNTs show a macroporous structure according to the tremendous nitrogen update at relative pressures above 0.85 (**Figure 10.7**), which agrees with the open network structure observed in SEM (**Figure 10.2B**). The sintered TiO_2 NCs display a type-IV isotherm (**Figure 10.3C**) with appreciable nitrogen uptake at the relative pressures below 0.45, which

implies micropores or small mesopores formed by NCs. The hysteresis loop at relative pressures between 0.45 and 0.75 indicates the presence of larger mesopores. By comparison, NC/CNT composites presented a hierarchically porous structure. Besides significant amount nitrogen uptake at relative pressures below 0.4, the NC/CNT composites also showed co-existence of mesopores and macropores revealed from two substantial hysteresis loops at higher relative pressures. Pore-size distributions shown in **Figure 10.3D** further confirms the hierarchical porosity of the NC/CNT composites. Note that the presence of macropores may not show in the distribution due to the intrinsic instrumental limitation. In addition, CNTs and sintered TiO_2 NCs exhibited a surface area of 212 and 140 $m^2\ g^{-1}$, respectively. Remarkably, the NC/CNT composites with 20 wt-% of CNT had a surface area of 204 $m^2\ g^{-1}$, significantly higher than the sum (146 $m^2\ g^{-1}$) of contributions from CNT and NC constituents. This result indicates that threading NCs with CNTs can also effectively prevent nanocrystal fusion during sintering process. Such a hierarchical porosity and high surface-area provide the NC/CNT electrodes with fast kinetics due to efficient ion transport and abundant surface active sites.

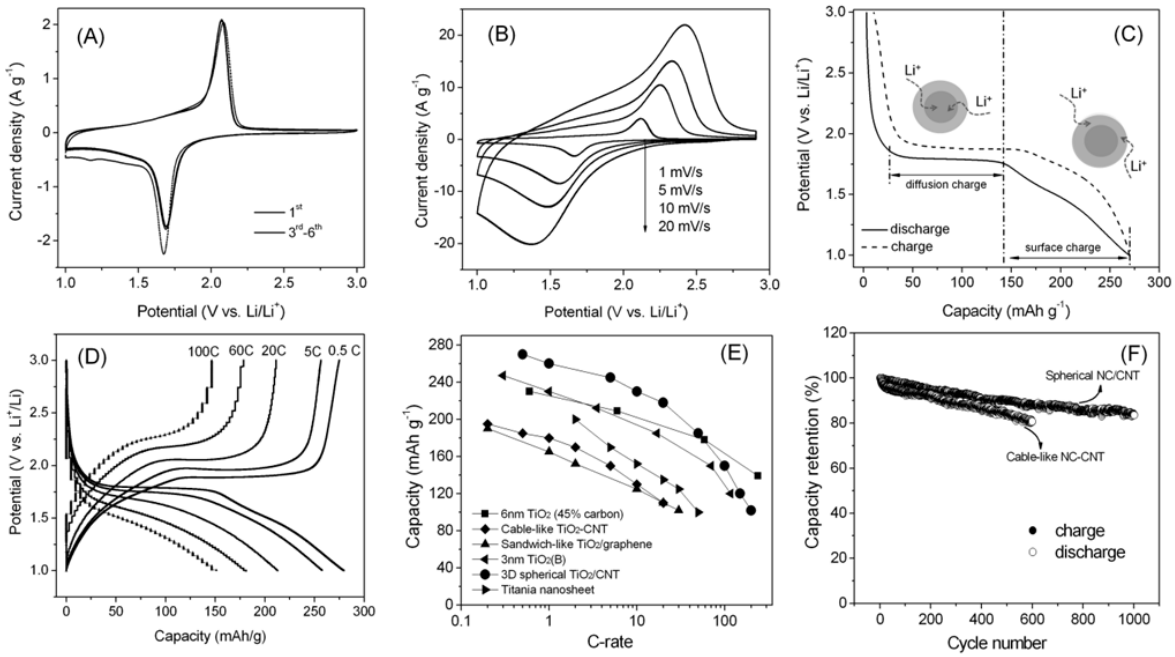

Figure 10.4 (A) CV plots of the CNT-threaded TiO_2 NC/CNT composite electrode on the first a few cycles at a sweep rate of 0.5 mV s^{-1}. (B) CV plots of the TiO_2 NC/CNT composite electrodes at various sweep rates. (C) Typical charge/discharge curves of the TiO_2 NC/CNT electrodes at a current rate of 0.25C, and (D) from 0.5C to 100C. (E) Comparison of rate-capability of a variety of TiO_2-based high-rate electrodes reported recently (TiO_2-CNT,[18] 6 nm TiO_2 with 45% carbon black,[28] cable-like titania nanosheet,[29] sandwich-like TiO_2/graphene,[30] 3 nm TiO_2 particles[31]). The capacities were estimated based on the effective mass of TiO_2 in electrodes. (F) Comparison of long-term cycling performance of the CNT-threaded TiO_2 NC/CNT electrode and cable-like TiO_2-CNT electrode at a rate of 20C.

Charge storage behavior was first characterized by cyclic voltammetry (CV) using coin-type half cells. **Figure 10.4A** presents representative cyclic voltammograms for the spherical NC/CNT composite electrodes at a sweep rate of 0.5 mV s^{-1}. The electrochemical Li^+ insertion/extraction processes occurring at anatase TiO_2 electrodes can be expressed by [21]

$$TiO_2 + xLi^+ + xe^- \leftrightarrow Li_xTiO_2 \qquad (1)$$

where *x* is the mole fraction of the inserted lithium ions ($x \leq 1$). Slight shift of the CV curves were observed during the first a few cycles (especially cathodic scans) due to irreversible reactions. The observed capacity loss from initial scans may be ascribed to irreversible replacement of absorbed protons on composite surface by lithium ions and other electrolyte-related surface reactions. Nevertheless, the charge/discharge efficiency increased from 90% to 100% after first five cycles. Two well-defined current peaks are observed at 1.7 V (cathodic sweep) and 2.1 V (anodic sweep), corresponding to the biphasic transition between tetragonal anatase and orthorhombic lithium titanate, which is consistent with typical insertion/extraction behavior of lithium in anatase TiO_2.[22, 23]

CV measurement at different sweep rates was performed to evaluate the rate behavior. **Figure 10.4B** shows cyclic voltammograms of NC/CNT electrodes at various sweep rates.

Although slight peak shift can be observed due to increased rates, the current peaks corresponding to characteristic lithium reactions were well retained as sweep rates increased from 1 to 20 mV s^{-1}. The decreased peak intensity suggests that the bulk lithium reaction were retarded. Nevertheless, the broad CV curves with large symmetric under-curve areas at high sweep rates indicate significant charge storage from surface reactions. Such a fast voltametric response was only achieved by ultra-thin-film (~200 nm) TiO_2 electrodes,[21] while our electrodes had typical thickness of 15-20 μm, indicating fast electrode kinetics enabled by the CNT-threaded architecture.

Typical galvanostatic charge/discharge curves of TiO_2 NC electrodes at a rate of 0.25C (1C = 170 mA g^{-1}) are shown in **Figure 10.4C**. The electrodes delivered a reversible charge storage capacity of ~270 mAh g_{TiO2}^{-1}, which is amongst the highest TiO_2 capacities reported so far. Note that the CNTs are only responsible for a small portion of capacity (~20 mAh g^{-1}) in the composite electrodes. Distinct voltage plateaus can be observed for both the charge and discharge plots, indicating coexistence of anatase and lithium titanate phases during charge/discharge process. A capacity of ~130 mAh g^{-1} can be estimated from this plateau region in the discharge plot, which can be ascribed to diffusion-controlled intercalation capacity in the crystal structure. The following slope voltage region accounts for a surface

lithium storage process, which contributes a capacity of ~140 mAh g^{-1}.[21, 24] This charge storage process agrees well with the small TiO_2 NC size and high surface area which provides abundant surface active sites for fast surface/interfacial lithium reaction. This behavior represents a typical capacitive feature where surface process significantly contributes to total charge storage. During the charging process, a slope region followed by a voltage plateau at higher voltage was also observed, indicating a lithium extraction process also involving diffusion and surface processes.

Figure 10.4D shows charge/discharge curves of TiO_2 NC/CNT electrodes at different C-rates. The TiO_2 in electrodes delivered a reversible capacity of ~265 and 220 mAh g^{-1} at a rate of 1 C and 20 C, respectively. Remarkably, even at an extremely high rate of 100C and 200C (charge/discharge in 22 and 11s), the electrodes still retained a capacity of ~150 and 104 mAh g^{-1}, respectively, showing super-fast electrode kinetics. The significant charge storage occurs in charging time of less than a minute also represents a typical capacitive behavior. It should be noted that previous application of TiO_2 for lithium-ion capacitors has been only achieved in ultra-thin films due to its poor electronic conductivity (10^{-8}-10^{-11} s cm^{-1}) [25, 26] and low lithium diffusion coefficient (10^{-11}-10^{-13} cm^2 s^{-1}).[22, 27] Here, the realization of super-fast charge storage in bulk TiO_2 electrodes with hierarchical spherical NC/CNT

architecture should be attributed to the efficient ion transport, high electronic conductivity and large surface active sites.

To better evaluate the charge storage behavior of the TiO_2 NC/CNT electrodes, various high-rate nanostructured TiO_2 composite electrodes reported recently are compared in **Figure 10.4E**. As shown, the CNT-threaded NC/CNT architecture is amongst the best hybrid TiO_2 electrodes reported so far.[18, 28, 29-31] Essentially, compared with cable- or sandwich-like TiO_2 structures, this new 3D spherical architecture showed dramatically enhanced rate capability. Some electrodes fabricated with a simple mixture of 6-nm anatase and carbon black showed slightly higher rate capability but with an extremely high content of carbon (45 wt-%) and very low densities (0.15 g cm^{-3}),[28] while our NC/CNT electrodes contain much less carbon and present a high density of ~1.1 g cm^{-3} due to effectively assembly of NCs and CNTs into spherical structures. The CNT-threaded NC/CNT may show more advantage if considering the charge storage of the whole electrodes since less amount of inert component was adopted. Moreover, due to the robust 3D spherical architecture, the NC/CNT electrodes kept 87% of its initial capacity after 1000 cycles (**Figure 10.4F**), which is even much better than the cable-like structure reported recently.[18] In contrast, the simple mixture of 6-nm

anatase and carbon black led to electrodes fast capacity loss due to randomly formed conductive network and poor electrode/electrolyte interface.[28]

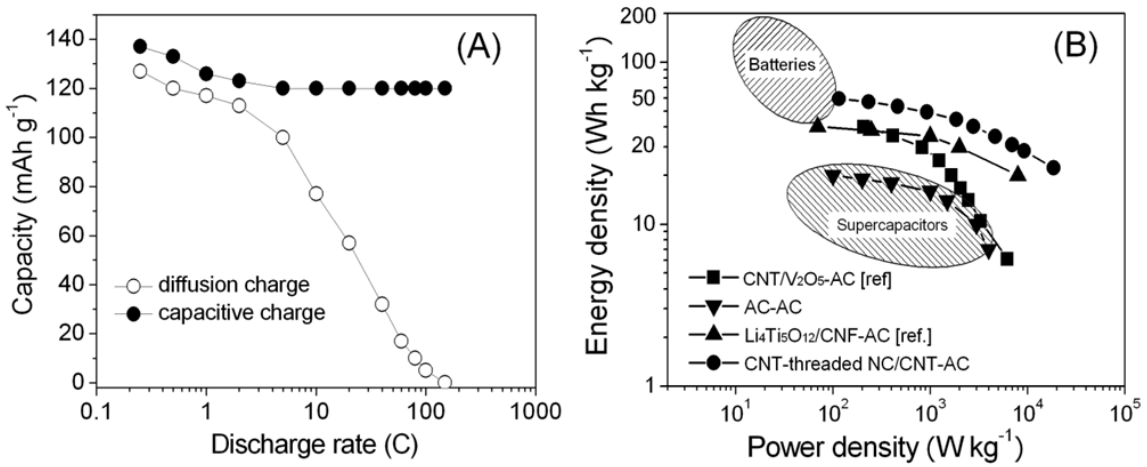

Figure 10.5 (A) Capacity dependence of diffusion and capacitive charge on the discharge rate. (B) Comparison of Ragone plots of asymmetric supercapacitors made from a TiO_2/CNT nanocomposite anode and AC cathode, a symmetric supercapacitor made from the same AC, and asymmetric supercapacitor devices recently developed (CNT/V_2O_5-AC,[19] $Li_4Ti_5O_{12}$/CNF-AC [34]). All the data is based on the mass of electrode materials.

To further understand the effect of capacitive charge storage on the high rate performance of TiO_2 NC/CNT composite, the stored charges were further analyzed based on Trasatti method.[32, 33] The capacitive and diffusion controlled contributions to total capacity are displayed in **Figure 10.5A**. It clearly shows that capacitive storage plays a significant part

in the total capacity of the nanocomposite electrode, and that this part increases as the charging rate increases. For example, capacitive contribution accounted for about 60% of the total charge at 0.25C and increased to 95% at 100 C. This result strongly suggests that effective utilization of capacitive charge storage could enable significant charge capacity even using materials with poor intrinsic kinetics.

Moreover, taking into account of the surface area (212 m^2 g^{-1}), the surface-normalized specific capacitance of TiO_2 in the NC/CNT composite was calculated to be ~150 μF cm^{-2} at a rate of 100C. This value is about one order of magnitude higher than those normally observed for double-layer capacitance (5~15 μF cm^{-2}),[7] further confirming that charge storage occurs in the NC/CNT electrodes is strongly associated with pseudocapacitance. This result agrees well with previous studies which suggest that surface pseudocapacitive effect plays an essential role as the metal oxide particle size decreases and electronic conductivity increases.

The high-capacity and high-rate TiO_2 NC/CNT provides as an ideal candidate for high-energy asymmetric supercapacitors by replacing carbon-based anodes. To assess actual capacitive devices application, asymmetric supercapacitor prototypes were assembled using the NC/CNT composite as the anode and a commercial activated carbon (AC) electrode as

the cathode. Representative galvanostatic charge/discharge curves at different rates are shown in **Figure 10.8**. At a current of 0.25 A g^{-1}, the devices provided a maximum cell capacitance of ~54 F g^{-1}, giving an energy density of 59.6 Wh kg^{-1} at a power density of 120 W kg^{-1}. This energy density is about two time that of double-layer capacitors and close to that of lithium-ion capacitors. Even at a power density of about 7 kW kg^{-1} or 18.6 kW kg^{-1} (charge/discharge in 16 or 2.3 s), the devices still provided an energy density of 31.2 or 22.3 Wh kg^{-1}, an indication of the ultrahigh power performance.

For another perspective of the asymmetric lithium-ion devices, **Figure 10.5B** compares the Ragone plots of different prototype supercapacitors.[19, 34] Overall, our devices offer significantly higher energy and power densities than that of carbon-based symmetric cells and the current state-of-the-art EDLC technology. Moreover the energy and power performance of the TiO_2 NC/CNT-carbon asymmetric supercapacitor is also superior to other lithium-ion supercapacitors reported recently. Such excellent performance provides our materials with great promise for many critical applications where both high energy and high power are needed. Considering that the specific capacitance of the cathode materials is still relatively low, an even higher energy density could be realized if a better cathode material was available.

3. Conclusions

In summary, we have demonstrated an effective design and fabrication of high-performance pseudocapacitive architecture. By threading active nanocrystals with CNT network, we fabricated 3D composite architecture providing efficient charge transport, large active surface and high durability, which enabled ultrafast electrode kinetics with tremendous pseudocapacitive charge storage and excellent cycling stability. Using the composite electrode as an anode and commercial AC as a cathode, we also demonstrated asymmetric capacitors with energy and power densities superior to current supercapacitor devices. The materials strategy developed in this work may be extended to fabricate other functional architectures for high-performance energy storage, catalyst, sensing and other emerging application.

4. Experimental

4.1 Synthesis of TiO_2 NCs

The TiO_2 NCs were synthesized using a two-phase hydrothermal reaction. In a typical synthesis, 0.4 mL of *tert*-butylamine was dissolved in 40 mL of water and the solution was transferred into a 100 mL Teflon-line stainless-steel autoclave. Subsequently, 1.0 g of

titanium (IV) n-propoxide and 4.0 mL of oleic acid were dissolved in 40 mL of toluene in air and the solution was transferred into the autoclave without any stirring. The autoclave was sealed and maintained at 180 ^{o}C for 8 h and cooled down to room temperature with tap water. The crude solution of TiO_2 NCs was precipitated with methanol and further isolated by centrifugation and decantation. The purified TiO_2 NCs were re-dispersed in 20 mL of toluene to form a TiO_2 NC solution for future use.

4.2 Synthesis of CNT-threaded 3D spherical architectures

CNT-threaded 3D spherical architectures were fabricated through a solvation-induced assembly process. Controlled amount of CNTs were dispersed into a pre-formed TiO_2 NC solution under ultrasonication and stirring. 25 mL of methanol was added into the above mixture with agitation. The TiO_2 NCs precipitated within CNT networks and the product was further separated by centrifuge or filtration. A composite of TiO_2 NCs/CNT with capping agents on NC surface was obtained after drying at 50 ^{o}C. Finally, an annealing treatment of the composite at 450 ^{o}C for 2 hrs in air removed the capping agents and resulted in the CNT-threaded 3D NC/CNT architecture. While the composition of the composite can be easily tuned by changing the amount of CNTs used in the preparation, the sample with 20

wt-% of CNTs content was mainly investigated. Details of the chemicals, TiO_2 NCs synthesis, electrode fabrication and charizations are provided in the Supporting Information.

4.3 Fabrication of electrodes

A convential slurry-coating process was used to fabricate electrodes. The TiO_2 NC/CNT composite was first pulverized into fine powders. This TiO_2 NC/CNT power, carbon black and poly(vinylidene fluoride) (PVDF) binder were mixed in a mass ratio of 8:1:1 and homogenized in N-Methyl-2-pyrrolidone (NMP) to form slurries. The homogenous slurries were coated on Cu foil substrates and dried at 100 ^{o}C for 30 min under vacuum. As formed electrodes were then pressed at a pressure of 2 MPa and further dried under vacuum at 100 ^{o}C for another 12 h. The mass loading was controlled to be 1.5~2 mg cm^{-2} on each current collector. The electrode loadings corresponded to active layers with thickness of 15-20 μm and density of ~1.1 g cm^{-3} according to the mass loading.

4.4 Single-Electrode test (half-cell)

To test electrodes, 2032-type coin cells were assembled in the glovebox, using Celgard 2500 membrane as the separator. Lithium discs were used as both the counter and the

reference electrodes and 1 M $LiPF_6$ in a 1:1 (w/w) mixture of ethylene carbonate and diethyl carbonate was used as the electrolyte. The CV and galvanostatic charge/discharge measurements were performed on a Bio-Logic VMP3 electrochemical workstation at different scan rates (0.5-20 mV s^{-1}) or C-rates (0.25-200C) in a voltage range between 3.0 and 1.0 V (vs. Li/Li^+). EIS tests were carried out on a Solartron 1860/1287 Electrochemical Interface.

4.5 Material and Electrode Characterization

The x-ray diffraction measurements were taken on Panalytical X'Pert Pro x-ray powder diffractometer using the copper Kα radiation (λ=1.54 Å). Nitrogen sorption isotherms were measured at 77 K with a Micromeritics ASAP 2020 analyzer. The samples were degassed in vacuum at 200 ^oC for three hours. The specific surface areas (S_{BET}) were calculated by the Brunauer-Emmett-Teller (BET) method using adsorption branch in a relative pressure range from 0.04 to 0.25. The pore size distributions were derived from the adsorption branches of isotherms using the Barrett-Joyner-Halenda (BJH) model. Scanning electron microscopy (SEM) experiments were conducted on a JEOL JSM-6700 FE-SEM. Transmission electron microscopy (TEM) experiments were conducted on a Philips CM120 operated at 120 kV.

4.6 Assembly of Asymmeric Supercapacitors

To assess actual capacitive devices application, we assembled asymmetric supercapacitors using the NC/CNT composite as the anode and a commercial activated carbon electrode (with a typical thickness of 80 μm) as the cathode. In such asymmetric devices, the charging process involves lithium ions insertion into the anode and hexafluorophosphate anions absorption onto the carbon cathode. Lithium extraction and hexafluorophosphate anions desorption occur on the anode and cathode, respectively, during a discharge process. Moreover, according to the operation potential windows of anode (1-3 V vs. Li/Li^+) and cathode (3-4 V Li/Li^+), such devices possess a maximum cell potential of 3 V, which is higher than that of typical EDLCs (2.3-2.7 V). Thus higher device energy density can be achieved. The overall cell capacitance was calculated based on the total mass of cathode and anode active materials. The power density is calculated based on the average power for each charge/discharge. From the internal resistance (*iR* drop) of the devices, a maximum power density was calculated to be 120 kW kg^{-1}. Moreover, the time constant ($\tau = RC$) was calculated to be ~0.11 s, which is significantly lower than many conventional carbon-based supercapacitors (~1 s), further confirming the high rate capability.

5. Supporting Materials

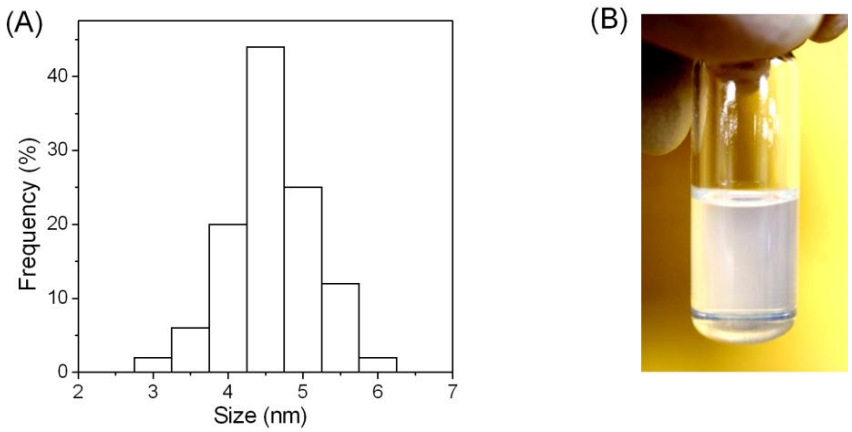

Figure 10.6 (A) Size distribution of the TiO_2 NCs, (B) A photograph of TiO_2-toluene solution containing 5 wt-% of TiO_2 NCs in a glass vial.

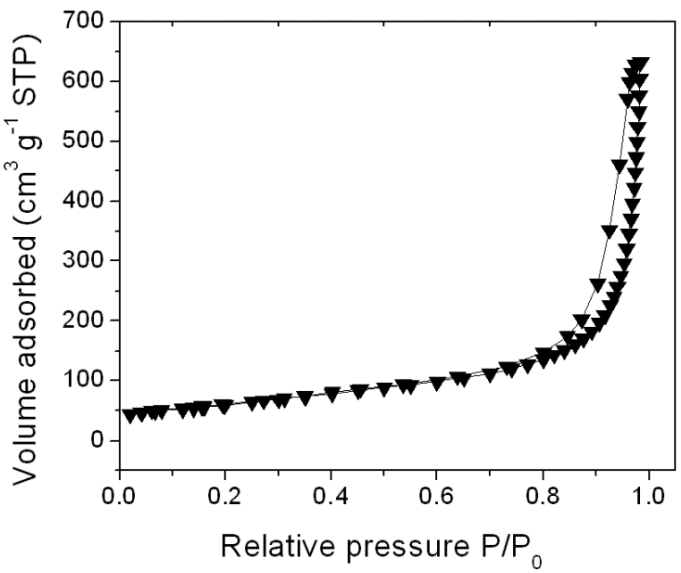

Figure 10.7 Nitrogen adsorption isotherms of CNTs.

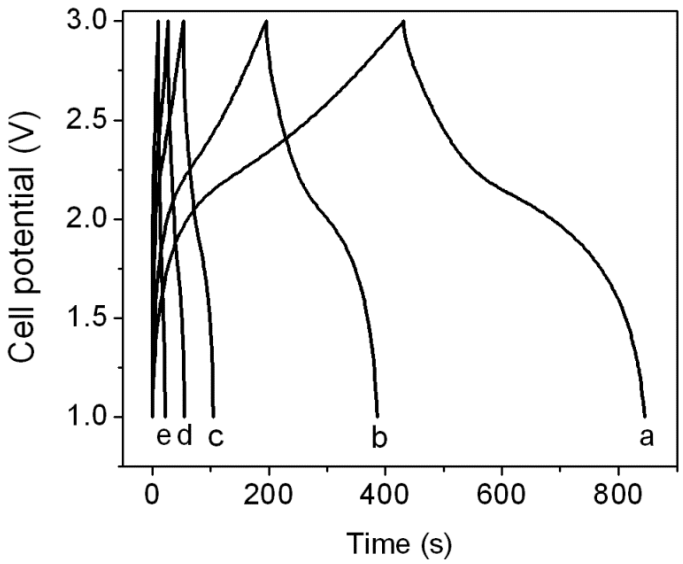

Figure 10.8 Galvanostaic charge/discharge curves of TiO_2/CNT-AC asymmetric supercapacitors from 1.0-3.0 V at different current densities in 1 M $LiPF_6$ in EC/DMC (a-e: 1, 2, 6, 10, 15 A g^{-1}, the current density is based on the mass of TiO_2/CNT electrode).

The analysis of capacitive charge storage:

The total charge storage (q_T) of the electrode materials was separated into two parts: capacitive charge (q_s) and diffusion controlled charge (q_d):

$$q_T = q_s + q_d \qquad (2)$$

Due to its faster kinetics feature, q_s can be correlated with EDL capacitance and pseudocapacitance, while q_d mainly depends on the slower diffusion process. Therefore, electrodes presenting a large fraction of q_s in the total capacity could exhibit a high rate

capability. Assuming semi-infinite linear diffusion, within a reasonable range of charging rates, q_s can be derived by plotting the total charge q_T against the square root of the charging time (t) and extrapolating t to zero, according to the following equation (Figure S4):

$$q_T = q_s + ct^{1/2} \qquad (3)$$

Deviation from the linearity of such a plot at very high charging rates is indicative of polarization effects that could be ignored in the above equation.

References

[1] A. F. B. John R. Miller, *The Electrochemical Society Interface* **2008**, 53.

[2] J. R. Miller, P. Simon, *Science* **2008**, *321*, 651.

[3] P. Simon, Y. Gogotsi, *Nat Mater* **2008**, *7*, 845.

[4] A. F. B. J. R. Miller, *The Electrochemical Society Interface* **2008**, *17*.

[5] P. S. Katsuhiko Naoi, *The Electrochemical Society Interface* **2008**, *17*.

[6] G. Wang, L. Zhang, J. Zhang, *Chemical Society Reviews*, *41*, 797.

[7] J. Chmiola, G. Yushin, Y. Gogotsi, C. Portet, P. Simon, P. L. Taberna, *Science* **2006**, *313*, 1760.

[8] Y. Zhu, S. Murali, M. D. Stoller, K. J. Ganesh, W. Cai, P. J. Ferreira, A. Pirkle, R. M.

Wallace, K. A. Cychosz, M. Thommes, D. Su, E. A. Stach, R. S. Ruoff, *Science* **2011**, *14*, B70.

[9] A. Kajdos, A. Kvit, F. Jones, J. Jagiello, G. Yushin, *Journal of the American Chemical Society* **2010**, *132*, 3252.

[10] J. P. Zheng, T. R. Jow, *Journal of The Electrochemical Society* **1995**, *142*, L6.

[11] M. Toupin, T. Brousse, D. Belanger, *Chemistry of Materials* **2002**, *14*, 3946.

[12] T.-Y. Wei, C.-H. Chen, H.-C. Chien, S.-Y. Lu, C.-C. Hu, *Advanced Materials* **2010**, *22*, 347.

[13] C.-C. Hu, W.-C. Chen, K.-H. Chang, *Journal of The Electrochemical Society* **2004**, *151*, A281.

[14] M. Min, K. Machida, J. H. Jang, K. Naoi, *Journal of The Electrochemical Society* **2006**, *153*, A334.

[15] J. M. K. Jong Hyeok Park, and O. Ok Park, *J. Electrochem. Soc.* **2003**, *150*, 4.

[16] T. Bordjiba, D. Belanger, *Journal of The Electrochemical Society* **2009**, *156*, A378.

[17] Q. Qu, S. Yang, X. Feng, *Advanced Materials*, **2011**, *23*, 5574.

[18] Z. Chen, D. Zhang, X. Wang, X. Jia, F. Wei, H. Li, Y. Lu, *Advanced Materials*, **2012**, *24*, 2030.

[19] Zheng Chen, Veronica Augustyn, Jing Wen, Yuewei Zhang, Meiqing Shen, Bruce Dunn, Y. Lu, *Advanced Materials* **2011**, *23*, 791.

[20] D. Deng, M. G. Kim, J. Y. Lee, J. Cho, *Energy & Environmental Science* **2009**, *2*, 818.

[21] T. Brezesinski, J. Wang, J. Polleux, B. Dunn, S. H. Tolbert, *Journal of the American Chemical Society* **2009**, *131*, 8.

[22] H. Lindstrom, S. Sodergren, A. Solbrand, H. Rensmo, J. Hjelm, A. Hagfeldt, S.-E. Lindquist, *The Journal of Physical Chemistry B* **1997**, *101*, 7717.

[23] M. Wagemaker, W. J. H. Borghols, F. M. Mulder, *Journal of the American Chemical Society* **2007**, *129*, 4323.

[24] J.-Y. Shin, D. Samuelis, J. Maier, *Advanced Functional Materials*, **2011**, *21*, 3464.

[25] M. Z. M. M. S. P. Sarah, M. N. Asiah and M. Rusop, *2010 Internatinal Conference on Electronic Devices, Systems and Applications (ICEDSA2010)* **2010**, 361.

[26] R. A. Shriram Ramanathan, David C. Bell, Annamalai Karthikeyan and Michael Aziz, *Journal of Materials Science* **2009**, *44*, 4613.

[27] J. Wang, J. Polleux, J. Lim, B. Dunn, *The Journal of Physical Chemistry C* **2007**, *111*, 14925.

[28] C. Jiang, M. Wei, Z. Qi, T. Kudo, I. Honma, H. Zhou, *Journal of Power Sources* **2007**, *166*, 239.

[29] J. Liu, J. S. Chen, X. Wei, X. W. Lou, X.-W. Liu, *Advanced Materials* **2011**, *23*, 998.

[30] D. Wang, D. Choi, J. Li, Z. Yang, Z. Nie, R. Kou, D. Hu, C. Wang, L. V. Saraf, J. Zhang, I. A. Aksay, J. Liu, *ACS Nano* **2009**, *3*, 907.

[31] Y. Ren, Z. Liu, F. Pourpoint, A. R. Armstrong, C. P. Grey, P. G. Bruce, *Angewandte Chemie International Edition* **2012**, *51*,2164.

[32] Z. Chen, V. Augustyn, X. Jia, Q. Xiao, B. Dunn, Y. Lu, *ACS Nano* **2012**, 6(5), 4319.

[33] S. Ardizzone, G. Fregonara, S. Trasatti, *Electrochimica Acta* **1990**, *35*, 263.

[34] K. Naoi, *Fuel Cells*, **2010**, *10(5)*, 825.

Chapter 11: Conclusion

Energy storage performance of current batteries and ECs are constrained by poor material properties. The work in this dissertation is to address the limitation of current energy storage materials by rational structure designs according to well-recognized principles and criteria. The overall research strategy is to design and fabricate multifunctional architectures by integrating distinct material structures and properties to create a new family of high-performance energy materials with desired performance.

Different types of energy storage architectures were investigated and compared with conventional structures to demonstrate such design concepts. First, hierarchically porous carbon particles with graphitized structures were designed and synthesized with an efficient aerosol-spray process. By comparison with commercially available activated carbon and CNTs, it was found that hierarchical pore architecture is important for providing high surface area and fast ion transport, which leads to high capacitance and high power EDLC materials. Secondly, MnO_2/mesoporous carbon nanocomposites were designed. MnO_2 layers with different thicknesses were deposited on mesoporous carbon scaffolds with hierarchical pore structure and the charge storage performance of the composites was correlated to MnO_2 layer thickness. It was determined that a suitable thickness is critical to ensure good electronic

conductivity, electrolyte diffusion and high capacitance. Thirdly, interpenetrating oxide nanowire/CNT network structures were designed and fabricated by an *in situ* hydrothermal reaction. The composition, CNT length, pore structure, V_2O_5 structure, electrode thickness and architecture are critical factors. Synergistic effects obtained between V_2O_5 nanowires and CNTs resulted in an optimal composition with the highest storage performance. Long CNTs led to robust flexible electrodes, while a hierarchical V_2O_5 structure enabled storage of both lithium and sodium ions at high rate. Thus, electrode architectures can be engineered and led to high-rate, thick electrodes for bulk energy storage. Last, various architectures obtained through integrating nanocrystals and CNTs were designed and fabricated using ultrafine TiO_2 nanocrystals as a model system. Electrodes were fabricated by directly coating thin film TiO_2 on conductive Indium-Tin-Oxide (ITO) glass, by conformably coating nanocrystals on pre-formed CNT papers, or by solvation induced assembly between nanocrystals and CNTs. It was demonstrated that thick electrodes with high charge capacity, high rate performance and cycling stability rely on functional architecture that simultaneously provides high electronic conductivity, easy ion diffusion, abundant surface actives sites and robust structure and interfaces.

The general conclusion derived from these studies is that the energy storage performance

of electrode materials can be significantly improved by constructing rational architectures that provide effective ion diffusion, good electronic conductivity, fast electrode reaction, robust structure and a stable interface, which normally cannot be obtained with conventional materials. This strategy also can be extended to other devices, such as batteries and fuel cells, providing a general design platform for high performance energy materials. Further exploration in this research direction will ultimately lead to high energy, high power, and long life energy storage devices for many applications, including portable electronics, EVs and grid-scale energy storage.